

ISTANBUL TECHNICAL UNIVERSITY ★ ENERGY INSTITUTE

FRANCIS TURBINE DESIGN AND OPTIMIZATION BY USING CFD



M.Sc. THESIS

Berk Can DUVA

Energy Science and Technology Division

Energy Science and Technology Program

Thesis Advisor: Prof. Dr. Habil Mete ŞEN

JUNE 2016

ISTANBUL TECHNICAL UNIVERSITY ★ ENERGY INSTITUTE

FRANCIS TURBINE DESIGN AND OPTIMIZATION BY USING CFD



M.Sc. THESIS

**Berk Can DUVA
(301131005)**

Energy Science and Technology Division

Energy Science and Technology Program

Thesis Advisor: Prof. Dr. Habil Mete ŞEN

JUNE 2016

İSTANBUL TEKNİK ÜNİVERSİTESİ ★ ENERJİ ENSTİTÜSÜ

**HAD ANALİZLERİ YARDIMI İLE FRANCİS TÜRBİN TASARIMI VE
OPTİMİZASYONU**

YÜKSEK LİSANS TEZİ

**Berk Can DUVA
(301131005)**

Enerji Bilim ve Teknoloji Anabilim Dalı

Enerji Bilim ve Teknoloji Programı

Tez Danışmanı: Prof. Dr. Habil Mete ŞEN

HAZİRAN 2016

Berk Can DUVA, a M.Sc. student of ITU Institute of Energy student ID 301131005, successfully defended the thesis entitled "FRANCIS TURBINE DESIGN AND OPTIMIZATION BY USING CFD", which he prepared after fulfilling the requirements specified in the associated legislations, before the jury whose signatures are below.

Thesis Advisor : **Prof. Habil Mete ŞEN**
Istanbul Technical University

Co-advisor : **Prof. Erkan AYDER**
Istanbul Technical University

Jury Members : **Prof. Filiz BAYTAŞ**
Istanbul Technical University

Assoc. Prof. Deniz ULUSARSLAN
Yildiz Technical University

Asst. Prof. Ümit KURŞUN
Istanbul University

Date of Submission : 12 April 2016

Date of Defense : 07 June 2016





To my beloved family,



FOREWORD

The studies presented in this thesis were supported by Electric Generation Company (EÜAŞ); therefore, I would like to thank EÜAŞ for its financial support. I also thank Energy Institute of The Scientific and Technological Research Council of Turkey (TUBITAK) Marmara Research Center, where I conducted my studies, and my colleagues in Electrical Power Technology Group who have persistently contributed my technical knowledge and created chances to improve myself.

I wish to express my gratitude to people at Hydraulic Fluid Machinery of Graz University of Technology for their contributions and supports. Furthermore, I owe Prof. Mehmet Haluk Aksel a debt of gratitude for encouraging me to push the limits. Finally, I would like to thank my family and my wife for being always there for me with their endless support and love. And, my grandfather who always believed in me will be in my heart forever.

June 2016

Berk Can DUVA
Mechanical Engineer

TABLE OF CONTENTS

	<u>Page</u>
FOREWORD	ix
TABLE OF CONTENTS	xi
SYMBOLS AND ABBREVIATIONS	xiii
LIST OF TABLES	xv
LIST OF FIGURES	xvii
SUMMARY	xxiii
ÖZET	xxvii
1. INTRODUCTION	1
1.1 Purpose of Thesis	1
1.2 Literature Review	2
1.2.1 History of Francis turbine	2
1.2.2 Numerical investigation of fluid flow inside a Francis turbine.....	2
1.2.3 Validation of CFD results in hydraulic power plant applications	3
1.2.4 Design of a Francis turbine by using CFD	4
1.2.5 Optimization of a Francis turbine by using CFD	4
1.3 Hypothesis	6
2. DETERMINATION OF THE OVERALL DIMENSIONS AND BLADE GEOMETRY OF FRANCIS TURBINE	7
2.1 Design of the Runner.....	10
2.1.1 Main parametrization of De Siervo and De Leva	11
2.1.2 Main parametrization of United States Department of the Interior Bureau of Reclamation	12
2.1.3 Main parametrization of Giesecke and Leeb.....	14
2.1.4 Main parametrization of Schweiger and Gregori	16
2.1.5 Main parametrization of Thomann.....	17
2.1.6 Main parametrization of Raabe	19
2.1.7 Main parametrization of Chapallaz	20
2.1.8 Main parametrization of Bovet	22
2.1.9 General main parametrization	25
2.1.10 Determination of blade angles and profiles of runner.....	26
2.1.11 X – Blade technology.....	31
2.2 Design of the Draft Tube	33
2.2.1 Main parametrization of De Siervo and De Leva	33
2.2.2 Main parametrization of United States Department of the Interior Bureau of Reclamation	35
2.2.3 Main parametrization of Lugaresi and Massa	38
2.2.4 Main parametrization of Gubin	39
2.2.5 General main parametrization	42
2.2.6 Cross sectional design of draft tube	44
2.3 Design of the Spiral Case	45

2.3.1 Main parametrization of De Siervo and De Leva.....	46
2.3.2 Main parametrization of United States Department of the Interior Bureau of Reclamation	47
2.3.3 General main parametrization	50
2.3.4 Cross sectional design of spiral case	52
2.4 Design of the Stay Vanes and Guide Vanes	55
3. CAVITATION PHENOMENON IN FRANCIS TURBINE	59
3.1 Definition of Cavitation.....	59
3.2 Types of Cavitation in Francis Turbine	61
3.2.1 Leading edge cavitation.....	61
3.2.2 Travelling bubble cavitation.....	61
3.2.3 Vortex rope.....	62
3.2.4 Inter – blade vortex cavitation.....	62
3.2.5 Von Karman vortex cavitation	63
3.3 Evaluation of Cavitation Behavior – Histogram Method.....	65
4. CFD ANALYSIS OF EXISTING UNIT	69
4.1 Description of Power Plant.....	69
4.2 Geometry of Main Components	74
4.2.1 Laser scanning	74
4.2.2 CAD modelling	77
4.3 Meshing	78
4.4 CFD Model.....	82
4.4.1 Governing equations and turbulence modelling.....	82
4.4.2 Chosen methodology	86
4.4.3 Boundary conditions.....	88
4.5 Evaluation of the CFD Results	93
4.5.1 Overall performance definitions.....	93
4.5.2 Evaluation of CFD results at design head	94
4.5.3 Spiral case.....	97
4.5.4 Stay vanes	102
4.5.5 Guide vanes	106
4.5.6 Runner	110
4.5.7 Draft tube.....	114
4.5.8 Numerical hill chart.....	119
4.6 Validation of CFD	121
5. OPTIMIZATION OF RUNNER	125
5.1 Existing Situation	125
5.2 Method of Optimization	127
5.3 Reconstruction of Original Runner.....	128
5.4 Optimization of Runner	133
5.4.1 Optimization with traditional methods.....	136
5.4.2 Optimization with X – Blade technology.....	139
5.5 Results of Proposed Designs	142
5.5.1 Results of traditional design	142
5.5.2 Results of X–Blade design	148
6. CONCLUSIONS AND RECOMMENDATIONS	155
REFERENCES	161
APPENDICES	169
CURRICULUM VITAE	181

SYMBOLS AND ABBREVIATIONS

A	: Area [m^2]
ANN	: Artificial Neural Network
c	: Absolute Velocity [m/s]
c_m	: Meridional Velocity [m/s]
c_u	: Circumferential Velocity [m/s]
CFD	: Computational Fluid Dynamics
D_{gv}	: Rotation Axis of Guide Vane [m]
$D_{gv,o}$: Guide Vane Outlet Diameter [m]
D_{LE}	: Diameter of Leading Edge [m]
D_{TE}	: Diameter of Trailing Edge [m]
g	: Gravitational Acceleration [m/s^2]
GA	: Genetic Algorithms
H_{net}	: Net Head [m]
H_{loss}	: Head Loss [m]
HAD	: Hesaplamalı Akışkanlar Dinamiği
HES	: Hidroelektirik Santral
HPP	: Hydraulic Power Plant
k_u	: Peripheral Velocity Coefficient
L_{gv}	: Guide Vane Length [m]
MFR	: Multiple Frame of Reference
n	: Rotational Speed [rpm]
N_{gv}	: Number of the Guide Vane
n_s	: Specific Speed
n_q	: Specific Speed
NPSH	: Net Positive Suction Specific Head
NPSE	: Net Positive Suction Specific Energy
P	: Power
P_{abs}	: Absolute Pressure [Pa]
P_{amb}	: Ambient Pressure [Pa]
P_{his}	: Histogram Pressure [Pa]
P_s	: Static Pressure [Pa]
P_t	: Total Pressure [Pa]
P_{va}	: Vapor Pressure [Pa]
Q	: Flowrate [m^3/s]
Q_{max}	: Maximum Flowrate [m^3/s]
Q_{opt}	: Optimum Flowrate [m^3/s]
T	: Tork [Nm]
u	: Peripheral Velocity [m/s]
w	: Relative Velocity [m/s]
Z_M	: Machine Axis Level [m]
Z_T	: Tail Water Level [m]

Greek Letters

β_1	: Inlet Blade Angle – Runner [deg]
β_2	: Outlet Blade Angle – Runner [deg]
φ	: Cover (Wrap) Angle [deg]
η_u	: Circumferential Hydraulic Efficiency
ρ	: Density [kg/m^3]
σ_P	: Plant Cavitation Number (Thoma Number of Plant)
σ_{rez}	: Reserve Cavitation Coefficient
σ_T	: Turbine Cavitation Number (Thoma Number of Turbine)
ω	: Rotational Speed [rad/s]
Ω	: Speed Number



LIST OF TABLES

	<u>Page</u>
Table 2.1 : Specific speed definitions.	9
Table 2.2 : Geometrical parameters of De Siervo and De Leva for runner.	12
Table 2.3 : Geometrical parameters of United States Department of the Interior Bureau of Reclamation for runner.	13
Table 2.4 : Geometrical and hydraulic parameters of Giesecke and Leeb for runner.	16
Table 2.5 : Geometrical and hydraulic parameters of Schweiger and Gregori for runner.....	17
Table 2.6 : Geometrical and hydraulic parameters of Thomann for runner.....	19
Table 2.7 : Geometrical and hydraulic parameters of Raabe for runner.	20
Table 2.8 : Geometrical and hydraulic parameters of Chapallaz for runner.	22
Table 2.9 : Geometrical parameters of Bovet for runner.	24
Table 2.10 : Main parameters of various scientists for runner of Kadincik I HPP. ...	27
Table 2.11 : Calculated velocities and blade angles for Kadincik I HPP.....	30
Table 2.12 : Geometrical parameters of De Siervo and De Leva for draft tube.	35
Table 2.13 : Geometrical parameters of United States Department of the Interior Bureau of Reclamation for draft tube.	37
Table 2.14 : Geometrical and hydraulic parameters of Lugaresi and Massa for draft tube.	39
Table 2.15 : Geometrical parameters of Gubin for draft tube.	41
Table 2.16 : Main parameters of various scientists for draft tube of Kadincik I HPP.	43
Table 2.17 : Geometrical parameters of De Siervo and De Leva for spiral case.	47
Table 2.18 : Geometrical parameters of United States Department of the Interior Bureau of Reclamation for spiral case.....	50
Table 2.19 : Main parameters of various scientists for spiral case of Kadincik I HPP.	51
Table 4.1 : Characteristics of Kadincik I HPP.	70
Table 4.2 : Commissioning test results of Kadincik I HPP (single unit).	72
Table 4.3 : Commissioning test results of Kadincik I HPP (two units).	72
Table 4.4 : Calculated shaft power for Kadincik I HPP.....	73
Table 4.5 : Guide vane flow angles for Kadincik I HPP.....	76
Table 4.6 : Number of the mesh nodes for Kadincik I HPP.	82
Table 4.7 : Number of the mesh elements for Kadincik I HPP.....	82
Table 4.8 : Numerical results for different outlet boundary conditions.	91
Table 4.9 : Recalculated shaft power for commissioning test and CFD results.....	123
Table B.1 : Mesh statistics of guide vanes.	171
Table B.2 : Mesh statistics of runner.	172
Table B.3 : Mesh statistics of draft tube.	172
Table B.4 : Mesh statistics of spiral case.	172

Table E.1 : Numerical hill chart data for Kadincik I HPP.....	176
Table F.1 : Numerical hill chart data for Kadincik I HPP with tradionally optimized runner.....	177
Table F.2 : Numerical hill chart data for Kadincik I HPP with tradionally optimized runner (continued).	178
Table G.1 : Numerical hill chart data for Kadincik I HPP with X-Blade optimization.....	179
Table G.2 : Numerical hill chart data for Kadincik I HPP with X-Blade optimization (continued).....	180



LIST OF FIGURES

	<u>Page</u>
Figure 2.1 : Suggestions on the type of the turbine according to head and discharge values.....	7
Figure 2.2 : Diagram for types of turbines.....	10
Figure 2.3 : Geometrical parameter definition of De Siervo and De Leva for runner	12
Figure 2.4 : Geometrical parameter definition of United States Department of the Interior Bureau of Reclamation.....	13
Figure 2.5 : Correlation of parameters for runner (United States Department of the Interior Bureau of Reclamation)	14
Figure 2.6 : Correlation of parameters for runner (United States Department of the Interior Bureau of Reclamation)	14
Figure 2.7 : Correlation of parameters for runner (Giesecke).....	15
Figure 2.8 : Correlation of parameters for runner (Thomann).....	18
Figure 2.9 : Correlation of parameters for runner (Raabe)	20
Figure 2.10 : Correlation of parameters for runner (Chapallaz).....	21
Figure 2.11 : Geometrical parameter definition of Bovet for runner.....	23
Figure 2.12 : Designation of main parameters of runner for Table 2.10	25
Figure 2.13 : Velocity angle in Francis turbine	28
Figure 2.14 : Blade angle distribution of Kadincik I HPP	29
Figure 2.15 : Leading (top) and trailing (bottom) edge geometries.....	31
Figure 2.16 : Reversed leading edge geometry (Left) – meridional view of X-Blade (Right)	32
Figure 2.17 : Inlet cavitation erosion in conventional design.....	32
Figure 2.18 : Pressure distribution along the runner.....	33
Figure 2.19 : Geometrical parameter definition of De Siervo and De Leva for draft tube	34
Figure 2.20 : Geometrical parameter definition of United States Department of the Interior Bureau of Reclamation.....	36
Figure 2.21 : Geometrical parameter definition of Lugaresi and Massa for draft tube	39
Figure 2.22 : Geometrical parameter definition of Gubin for draft tube	40
Figure 2.23 : Empirical Correlations between Runner Dimensions (Gubin).....	40
Figure 2.24 : Correlation of parameters for draft tube (Gubin)	41
Figure 2.25 : Designation of the main parameters of draft tube for Table 2.16	42
Figure 2.26 : Meridional view of Kadincik I HPP draft tube in comparison with literature.....	44
Figure 2.27 : Spiral casing types	45
Figure 2.28 : Cross sectional shape of the spiral casing	45
Figure 2.29 : Geometrical parameter definition of De Siervo and De Leva for spiral case	46

Figure 2.30 : Correlation of parameters for spiral case (United States Department of the Interior Bureau of Reclamation).....	48
Figure 2.31 : Geometrical parameter definition of United States Department of the Interior Bureau of Reclamation	49
Figure 2.32 : Designation of the main parameters of spiral case for Table 2.19	51
Figure 2.33 : Meridional view of spiral case.....	52
Figure 2.34 : Overlap of stay vanes over spiral case.....	54
Figure 2.35 : Area distribution of spiral case of Kadincik I HPP	54
Figure 2.36 : Meridional view of a radial machine	56
Figure 3.1 : Machine levels of Francis turbine.....	60
Figure 3.2 : Reservoir levels of Francis turbine	60
Figure 3.3 : Leading edge cavitation – on pressure side (left) - on suction side (right)	61
Figure 3.4 : Travelling bubble cavitation	61
Figure 3.5 : Vortex rope and velocity triangles in the entrance of draft tube – part load (left) – overload (right)	62
Figure 3.6 : Inter – blade vortex cavitation	63
Figure 3.7 : Von Karman vortex cavitation	63
Figure 3.8 : Cavitation limits	64
Figure 3.9 : Cavitation regions	64
Figure 3.10 : Francis turbine machine and tail water level definitions for Thoma number calculations	66
Figure 3.11 : Comparison of numerical simulation with model test results	67
Figure 4.1 : Schematic view of Kadincik I and II power plants.....	71
Figure 4.2 : Net head vs shaft power.....	73
Figure 4.3 : Laser scanning studies in Kadincik I HPP.....	74
Figure 4.4 : Wicket gate opening	75
Figure 4.5 : Guide vane angle and inflow angle definition.....	75
Figure 4.6 : Scanned geometry of runner blade	76
Figure 4.7 : Cutwater region of spiral case (left – reality, right – CAD model)	77
Figure 4.8 : CAD model of Kadincik I HPP	79
Figure 4.9 : Unstructured mesh of spiral case.....	78
Figure 4.10 : Structural mesh of draft tube	80
Figure 4.11 : H -, J-, L-, C- Topologies (from left to right)	80
Figure 4.12 : Guide vane mesh	81
Figure 4.13 : Runner mesh	81
Figure 4.14 : Boundary layer illustration	84
Figure 4.15 : Kadincik I HPP CFD flow domain.....	88
Figure 4.16 : Streamlines and static pressure distribution at the draft tube outlet for different outlet boundary conditions at best efficiency point (15° guide vane angle).....	91
Figure 4.17 : Streamlines and static pressure distribution at the draft tube outlet for different outlet boundary conditions at extreme part load (7.5° guide vane angle).....	92
Figure 4.18 : Streamlines and static pressure distribution at the draft tube outlet for different outlet boundary conditions at over load (22.5° guide vane angle)	92
Figure 4.19 : The overall CFD performance of Kadincik I HPP at design head	95
Figure 4.20 : CFD percentage head losses of mechanical components	96
Figure 4.21 : CFD single component efficiencies for Kadincik I HPP.....	97

Figure 4.22 : Post processing planes of spiral case.....	98
Figure 4.23 : Swirl contours at different spiral case planes	99
Figure 4.24 : Velocity components in a radial machine	99
Figure 4.25 : Static pressure distribution in front of the stay vanes.....	100
Figure 4.26 : c_u velocity distribution in front of the stay vanes	100
Figure 4.27 : Total pressure distribution in front of the stay vanes	101
Figure 4.28 : c_r velocity distribution in front of the stay vanes	101
Figure 4.29 : Static pressure distribution at the outlet of the stay vanes.....	102
Figure 4.30 : c_r velocity distribution at the outlet of the stay vanes	103
Figure 4.31 : c_u velocity distribution at the outlet of the stay vanes	103
Figure 4.32 : Total pressure distribution at the outlet of the stay vanes	104
Figure 4.33 : Static pressure contour of stay vanes at $z=0$ meter	105
Figure 4.34 : Velocity vectors for first stay vanes	104
Figure 4.35 : Total pressure distribution at the outlet of the guide vanes.....	106
Figure 4.36 : Velocity vectors and pressure contours of guide vanes.....	107
Figure 4.37 : Static pressure distribution at the outlet of the guide vanes	108
Figure 4.38 : c_u velocity distribution at the outlet of the guide vanes.....	109
Figure 4.39 : c_r velocity distribution at the outlet of the guide vanes	109
Figure 4.40 : Normailize mass flow through the guide vanes	110
Figure 4.41 : Velocity distributions at the inlet of the runner.....	111
Figure 4.42 : Velocity distributions at the outlet of the runner.....	111
Figure 4.43 : Static pressure distribution on the runner blades.....	112
Figure 4.44 : Blade Loading at Span 5 % (close to hub)	112
Figure 4.45 : Blade Loading at Span 50 % (mid plane).....	113
Figure 4.46 : Blade Loading at Span 95 % (close to shroud)	113
Figure 4.47 : Cavitation damages at the runner, leading edge (left), trailing edge (right).....	113
Figure 4.48 : Draft tube post processing planes.....	114
Figure 4.49 : c_u velocity contour at meridional cross section of draft tube	115
Figure 4.50 : c_u velocity contours at plane 1 and 2	115
Figure 4.51 : Absolute velocity contour at meridional cross section of draft tube.	116
Figure 4.52 : Static pressure distribution at meridional cross section of draft tube.	116
Figure 4.53 : Total pressure distribution at meridional cross section of draft tube..	117
Figure 4.54 : Absolute velocity contours at plane 1, 2, 3 and 4.....	117
Figure 4.55 : Static pressure contours at plane 1, 2, 3 and 4.....	118
Figure 4.56 : Total pressure contours at plane 1, 2, 3 and 4	118
Figure 4.57 : Static and total pressure distributions at the outlet of draft tube	119
Figure 4.58 : Absolute velocity distribution at the outlet of the draft tube.....	119
Figure 4.59 : Francis turbine losses as a function of the specific speed	120
Figure 4.60 : Numerical hill chart of Kadincik I HPP	121
Figure 4.61 : Comparison of CFD results with measurements	122
Figure 5.1 : Averaged yearly power production of Kadincik I HPP	126
Figure 5.2 : Segmented annual production for one unit operation.....	126
Figure 5.3 : Segmented annual production for two unit operation	126
Figure 5.4 : 10 year-averaged power production per year	127
Figure 5.5 : Workflow of optimization process	128
Figure 5.6 : Meridional view of the original runner of Kadincik I HPP with the layers for the geometry definition	129

Figure 5.7 :	Blade sections of the original runner of Kadincik I HPP	130
Figure 5.8 :	“Theta vs M” curves of the original runner of Kadincik I HPP	130
Figure 5.9 :	Thickness distribution of the original runner of Kadincik I HPP.....	131
Figure 5.10 :	CAD model of reconstructed original runner of Kadincik I HPP	132
Figure 5.11 :	Angle definition of radial turbomachines	132
Figure 5.12 :	“Beta vs M” curves of the original runner of Kadincik I HPP	133
Figure 5.13 :	Static pressure distribution on the original runner blades at best efficiency point ($H_{net}=155$ m and $Q=17$ m ³ /s).....	134
Figure 5.14 :	Blade loadings of the original runner for various span values at best efficiency point ($H_{net}=155$ m and $Q=17$ m ³ /s).....	135
Figure 5.15 :	c_m and c_u distribution at the outlet of the original runner of Kadincik I HPP at best efficiency point ($H_{net}=155$ m and $Q=17$ m ³ /s).....	135
Figure 5.16 :	Meridional view of optimized runner with traditional design methods	136
Figure 5.17 :	“Theta vs M” curves of optimized runner with traditional design methods.....	137
Figure 5.18 :	Thickness distribution of optimized runner with traditional design methods.....	137
Figure 5.19 :	“Beta vs M” curves of optimized runner with traditional design methods.....	138
Figure 5.20 :	CAD model of optimized runner with traditional design methods ...	138
Figure 5.21 :	Meridional view of optimized runner with X-Blade design method..	140
Figure 5.22 :	“Theta vs M” curves of optimized runner with X-Blade design method	140
Figure 5.23 :	Thickness distribution of optimized runner with X-Blade design method	141
Figure 5.24 :	“Beta vs M” curves of optimized runner with X-Blade design method	141
Figure 5.25 :	CAD model of optimized runner with X-Blade design method.....	142
Figure 5.26 :	Numerical hill chart for traditional optimization of Kadincik I HPP..	143
Figure 5.27 :	CFD percentage head losses for mechanical components of conventionally optimized turbine	144
Figure 5.28 :	The overall CFD performance of conventionally optimized turbine at design head	145
Figure 5.29 :	Blade loading comparison of the original runner and traditional optimization version at their best efficiency points.....	146
Figure 5.30 :	Pressure contours of the original runner (left) and traditional optimization version (right) at their best efficiency points (view from upstream)	147
Figure 5.31 :	Pressure contours of the original runner (left) and traditional optimization version (right) at their best efficiency points (view from downstream)	147
Figure 5.32 :	Velocity distributions at the outlet of the runner for the original blade and traditional optimization version at their best efficiency points... ..	147
Figure 5.33 :	Numerical hill chart for X-Blade optimization of Kadincik I HPP... ..	149
Figure 5.34 :	CFD percentage head losses for mechanical components of X-Blade optimization	149

Figure 5.35 : The overall CFD performance of X-Blade optimization at design head...	150
Figure 5.36 : Blade loading comparison of the original runner and optimization versions at their best efficiency points	151
Figure 5.37 : Pressure contours of the original runner (left) and X-Blade optimization version (right) at their best efficiency points (view from upstream)	152
Figure 5.38 : Pressure contours of the original runner (left) and X-Blade optimization version (right) at their best efficiency points (view from downstream)	152
Figure 5.39 : Velocity distributions at the outlet of the runner for the original blade and optimization versions at their best efficiency points	153
Figure A.1 : Commissioning test results of Kadincik I HPP (single unit operation)	170
Figure A.2 : Commissioning test results of Kadincik I HPP (two unit operation)	170
Figure C.1 : Mesh independency study for Kadincik I HPP	173
Figure C.2 : Hydraulic losses for different mesh densities	174
Figure D.1 : y^+ at runner for medium grid CFD results	175



FRANCIS TURBINE DESIGN AND OPTIMIZATION BY USING CFD

SUMMARY

Hydraulic power is a vital component of the power production in Turkey. Approximately 34 % of the installed capacity belongs to the hydraulic power plants. However, almost half of the hydraulic power plants in Turkey are older than 40 years and after the commissioning, they have not undergone a comprehensive refurbishment. This suggests that not only the old technology was utilized in the hydropower plants in Turkey, but also these power plants are not operated effectively due to the aging effect.

This thesis aims to explain the optimization of the Francis turbine runner according to the operation conditions of the power plants by using CFD. Improvements in the turbine efficiency, cavitation behavior, pressure distribution at the runner blades and velocity distributions at the outlet of the runner can be listed as optimization targets. The hypothesis is that all these targets can be achieved only with the adjustment of the hydraulic shape of the runner with respect to the fluid flow.

This thesis starts with the brief history of the Francis turbine and first attempts to investigate the fluid flow inside a Francis turbine numerically. With the improvements in technology and increased experiences on numerical investigations and Francis turbines, CFD has become an integral part of the Francis turbine design and optimization.

After the introduction, design procedure of a Francis turbine is investigated in detail. All mechanical parts are under consideration. First step in hydraulic turbine design is the determination of the specific speed, which depends on the nominal operation conditions. Then, design is followed by the designation of main geometrical parameters regardless of which mechanical component is considered. In literature, there are various empirical correlations between specific speed and dimensions of the turbine, some of which are widely utilized in Francis turbine design.

For most of the designers, runner is considered as the starting point of the design because the geometrical dimensions of the other mechanical parts are calculated by taking the runner inlet or discharge diameter into account. Main parametrization is followed by detection of blade angles with the help of the velocity triangles at the inlet and outlet of the runner. The crucial part is to satisfy constant meridional velocity throughout the blade and zero circumferential velocity at the outlet of the runner. After the preliminary design of all mechanical components, CFD takes the stage for fine-tuning.

After the explanation of the design procedure for each component, preliminary design parameters are calculated for specific speed of Kadincik I HPP, which is utilized as case study in this thesis. Findings from the empirical correlations, which are widely accepted in literature, are compared with the geometrical dimensions of

the existing turbine. Therefore, some of the possible optimization potentials are revealed before the CFD analysis of the actual turbine.

A comprehensive CFD analysis is performed in order to investigate the performance of Kadincik I HPP at different operation conditions. The study starts with the laser scanning of guide vane and runner geometries and followed by the computer aided modeling of mechanical parts of the turbine with the help of the point clouds and technical drawings. Subsequently, structural meshes are generated for guide vanes, runner and draft tube in different mesh densities in order to conduct mesh independency study. On the other hand, the spiral case (including the stay vanes) is meshed using unstructured grids due to its complex shape.

Navier-Stokes equations are solved with Reynolds Averaged Navier Stokes (RANS) formulation using commercial CFD software, ANSYS CFX, in order to evaluate the performance of the existing turbine unit. Menter's SST turbulence model with automatic wall functions is applied. For the runner, an additional approach called Multiple Frame of References (MFR) with the assumption of steady state flow and incompressible fluid is utilized.

Boundary conditions are defined as total pressure at the inlet and the static pressure at the outlet. In order not to cause secondary flows and perturbations, additional out block is inserted at the end of the draft tube and outlet boundary condition is introduced at the outlet surface of the out block as one bar. Then, inlet total pressure is adjusted with respect to the desired net head level, which is the difference between inlet and outlet total pressures according to IEC standards. Different discharges are realized with different guide vane openings.

At the design operation point of the turbine, detailed investigation is performed for the performance of each mechanical component by using CFD in order to determine the optimization potential of the existing unit. Economic feasibility, hydraulic shape, efficiency and cavitation performance are used for the evaluation process. Cavitation phenomenon is examined with a steady state histogram method. In the end, numerical hill chart of the Kadincik I HPP are obtained with the help of the CFD results for different net head and flow rate values. This part of the study shows that peak efficiency of the existing turbine is so far away from the nominal operation condition.

After many studies on blade leaning angle, Francis turbine design with X-Blade technology, which has a reversed leading edge, was introduced in 1998 during Three Gorges Project. Since then, it has been proposed that X-Blade design has higher peak and off-design efficiencies, more uniform blade loading, better cavitation performance and wider range of stability than conventional design.

According to the feasibility studies, new best efficiency point of the turbine is determined. With the help of the CFD results, existing runner geometry is optimized according to the flow conditions. Among the various optimization versions, conventional and X-Blade designs with best performances are chosen as final runner geometries and these new runner designs are got involved in CFD analyses. Numerical results of both optimized turbine are compared with original turbine geometry and each other. In the end, it is concluded that an improvement is achieved in peak efficiency, cavitation performance, velocity distribution and blade loading with each of the optimized runner with respect to the original turbine. Furthermore, best efficiency point is shifted through the operation points only with the modifications in the hydraulic shape of the runner. However, whereas improvements

in peak efficiency and blade loading are more severely felt in X-Blade optimization version than the conventional one, both optimization versions show adequate performance in cavitation and velocity distribution. Moreover, CFD results prove that X-Blade design offers wider high efficiency region, which is significant when discharge and net head of the power plant are changing considerably throughout the year.





HAD ANALİZLERİ YARDIMI İLE FRANCİS TÜRBİN TASARIMI VE OPTİMİZASYONU

ÖZET

Hidroelektrik santraller, Türkiye'nin kurulu gücünün % 34 'ünü oluşturmaktadır. Ülkemizin jeolojik yapısı ve su kaynaklarının karakteristik özelliğinden dolayı hidroelektrik santrallerimizde çoğunlukla Francis tipi türbin üniteleri kullanılmıştır. Fakat enerji üretiminin dörtte birinden daha büyük bir bölümü su kaynaklarına dayanan Türkiye'de hidroelektrik santrallerin neredeyse yarısı 40 yıl ve üstü bir geçmişe sahiptir. Bu santrallerin hemen hemen hiçbirinde devreye alındıktan sonra kapsamlı bir rehabilitasyon projesi gerçekleştirilmemiştir. Bu nedenle santraller sadece eski teknolojiyle tasarlanmış olmakla kalmayıp zaman içerisinde yıpranmalarından dolayı performansları hatırı sayılır seviyede düşmüştür.

Bu tezin amacı, Francis türbin çarkının santral çalışma koşullarına göre HAD analizleri yardımı ile nasıl optimize edilebileceğini anlatmaktır. Optimizasyon hedefleri türbin ve kavitasyon performansında artış, çark kanadı üzerindeki basınç dağılımı ve çark giriş ve çıkışındaki hız bileşenlerinin dağılımında iyileşme olarak listelenebilir. Tezin hipotezi bu optimizasyon hedeflerinin yalnızca çark geometrisinin akış koşullarına göre modifiye edilmesi sonucunda elde edilebileceğidir. Türbinin diğer mekanik ekipmanlarında herhangi bir değişiklik yapılmayacaktır.

Tezin giriş bölümü Francis türbininin tarihçesi ve geçmişten günümüze Francis türbini içerisindeki akışın numerik olarak modellenme çabaları ile başlar. Bu gün sahip olduğumuz teknoloji, su türbinleri içindeki akış için üç boyutlu Navier-Stokes denklemlerini numerik olarak çözmeye imkan sağlar. Yıllar içinde HAD analizlerinin türbin performansının tespitindeki doğruluğu birçok kez ispatlanmıştır. Bu sayede HAD analizleri artık Francis türbin tasarımı ve optimizasyonunun ayrılmaz bir parçası haline dönüşmüştür. Model testlerin pahalı oluşu ve proje sürelerini hatırı sayılır ölçüde uzatması nedeniyle birçok türbin firması tasarıma son halini verene kadar HAD analizlerinden aktif olarak faydalanır.

Giriş bölümünün ardından Francis türbinin her bir mekanik parçası için tasarım süreci ayrıntılı şekilde incelenmiştir. Hidrolik türbinlerin tasarımında ilk adım özgül hızın hesaplanmasıdır. Bu değer santralin tasarım düşüsü, debisi, gücü ve dönme hızına bağlıdır. Dönme hızı seçilen generatörün kutup sayısı ile doğrudan ilişkilidir. Düşü, debi ve güç değerleri ise nehirde yıllar boyunca yapılan gözlemler sonucunda karar verilen büyüklüklerdir. Özgül hız değeri santralde kullanılması gereken türbin tipi ile ilgili bilgi vermektedir. Türbin tipinin belirlenmesinin ardından ise tasarıma çoğu zaman çark ile başlanır çünkü çark giriş veya çıkış çapı diğer mekanik ekipmanların geometrik boyutlarının hesaplanmasında kullanılır.

Francis türbinin her bir mekanik parçasında olduğu gibi çark tasarımı da ana boyutların belirlenmesi ile başlar. Fakat türbin parçalarının ana boyutlarını veren

genel geçer formüller bulunmamaktadır. Literatürde birçok tasarımcı kendi ampirik formüllerini ileri sürmüştür. Bu ampirik formüller, genellikle var olan hidroelektrik santrallerde yapılan çalışmalara dayanmaktadır. Türbinin özgül hız değerini kullanarak ana boyutların hesaplanmasına yardımcı olan bu korelasyonlardan en çok kabul görenleri tezde sunulmuştur. Ana boyutların belirlenmesini çark kanat açılarının hesaplanması takip eder. Francis türbininin çark açıları hız üçgenleri yardımı ile saptanır. Bu hesaplar sırasında çark giriş ve çıkışında sabit meridyonel hız kabulü yapılır. Ayrıca çarkın suyun bütün enerjisini mekanik enerjiye dönüştürdüğü düşünülerek çark çıkışındaki çevresel hız bileşeni sıfır olarak kabul edilir.

Emme borusu ve salyangoz ana boyutları için de literatürde ampirik korelasyonlar mevcuttur. Emme borusunda akış ayrılmalarının oluşmaması için kesit alanları arasında yumuşak geçişler yapılmalıdır. Öte yandan salyangoz kesitlerinin geometrileri için literatürde kabul gören üç adet yöntem mevcuttur. Bu yöntemler tez içerisinde ayrıntılı şekilde açıklanmıştır. Sabit kanat ve ayar kanadı geometrileri ile ilgili sınırlı sayıda tasarım yöntemi yayınlanmıştır ve bu yöntemler tasarımın her adımını kapsamamaktadır. Bu nedenle sabit ve ayar kanadı geometrileri çoğunlukla tasarımcının tecrübesi ile belirlenmektedir. Bütün mekanik parçaların ön tasarımlarının tamamlanmasının ardından HAD analizleri devreye girer ve akış koşullarına göre ekipmanların hidrolik geometrilerinde değişikliğe gidilir.

Kadıncık I Hidroelektrik Santrali, bu tezde sunulan incelemelerde vaka çalışması olarak kullanılmıştır. Santralin mekanik parçalarının ana boyutları ve çark kanat açılarının santral çalışma koşullarına uygunluğunun test edilmesi amacıyla Kadıncık I HES türbininin özgül hızı hesaplanmıştır. Literatürde sıklıkla kullanılan ampirik formüller ana boyutların hesabında kullanılmıştır. Bu çalışma sonucunda çark, salyangoz, sabit kanat ve ayar kanadı geometrilerinin ana boyutlarında herhangi bir problemle karşılaşılmazken Kadıncık I HES'in emme borusunun yataydaki çıkış bölümünün literatüre göre gereğinden çok daha uzun olduğu tespit edilmiştir. Uzun emme borusu geometrisi kayıpları arttırarak türbin performansını düşürmektedir. Öte yandan, çark kanat açıları incelendiğinde Kadıncık I HES çarkının giriş kanat açıları literatürde belirtilen değerlerden daha yüksek iken çıkış kanat açıları ise literatürden düşük olduğu belirlenmiştir.

Kadıncık I HES'in farklı çalışma koşullarındaki performansını incelemek için türbin HAD analizlerine tabi tutulmuştur. Bu amaçla çark ve ayar kanatlarının lazer tarama cihazı ile nokta bulutları oluşturulmuş ve bu nokta bulutları 3 boyutlu geometrilere dönüştürülmüştür. Daha sonra salyangoz, sabit kanatlar ve emme borusunun geometrileri teknik çizimler baz alınarak çizilmiş ve 3 boyutlu modele eklenmiştir. Ünite içinde yapılan gözlemler sonunda geometrideki son eksik noktalar da tamamlanmış ve HAD analizlerine başlamak için çözüm ağları oluşturulmuştur. Çark, ayar kanadı ve emme borusu için farklı yoğunluklarda yapısal çözüm ağları tercih edilmiştir. Çark ve ayar kanadında H-J-C-L topolojisinden yararlanılırken emme borusunda "O-grid" yapısı hakimdir. Öte yandan salyangoz sahip olduğu kompleks geometriden dolayı yapısal olmayan çözüm ağı ile örülmüştür. Salyangoz için de dört farklı yoğunlukta ağı oluşturulmuş ve bu çözüm ağları ağı bağımsızlığı çalışmalarında kullanılmıştır.

Reynolds ortalamalı Navier-Stokes formülasyonu yardımı ile üç boyutlu Navier-Stokes denklemleri ANSYS-CFX HAD analizi çözücüsünde analitik olarak çözülmüştür. Menter'in ileri sürdüğü ve otomatik duvar fonksiyonu avantajı sağlayan

SST türbülans modeli kullanılmıştır. Bu otomatik fonksiyonlar çözüm ağlarının sahip olduğu $y+$ değerlerinin önemini büyük ölçüde kaybetmesini sağlamaktadır. Ayrıca dönen komponentlerin sabit parçalarla etkileşimlerini kararlı analizlerde modelleyebilmek için çoklu referanslar çerçevesi yaklaşımı kullanılmıştır. HAD analizi kodu, hız ve basınç için, özdeş noktalarla hücre merkezli kontrol hacmi kullanılmaktadır. Konvektif terimlerin konumsal ayrıklaştırılmasında hibrit şemanın kullanılması ile lokal olarak hesaplanan “blend” faktörü çözümlerin ikinci dereceden hassas olmasını sağlamıştır.

Sınır koşulları girişte toplam basınç ve çıkışta statik basınç olacak şekilde tanımlanmıştır. İkincil ve geri akışları engellemek adına emme borusunun sonuna bir çıkış bloğu yerleştirilmiş ve bloğun sonundaki statik basınç bir bar olarak belirtilmiştir. Çıkış bloğu akışın emme borusunu santralde olduğu gibi özgürce terk etmesine izin vermektedir. Çıkış sınır koşulunun emme borusunun sonuna tanımlanması, radyal denge opsiyonu kullanılsın veya kullanılsın, emme borusundaki akış koşullarını bozmaktadır. Net düşü hesabında salyangoz girişi ve emme borusu çıkışındaki toplam basınç farkının baz alınması ve çıkış bloğunun büyük geometrisi sayesinde sürtünme kayıplarını ve ikincil akışları minimuma indirmesi HAD analizi sonuçlarına olan güveni arttırmaktadır. Giriş toplam basınç değeri ile istenen net düşü elde edilene kadar HAD analizleri iteratif olarak yenilenmektedir. Farklı debi değerleri ayar kanadı geometrilerinin açılıp kapanması ile sağlanmaktadır.

Kavitasyon performansının çift fazlı kararsız HAD analizleri ile saptanmasının analiz sürelerini ciddi miktarda uzatmasından ve bu durumda numerik metotların deneysel çalışmalara göre avantajını kaybetmesinden dolayı kararlı HAD analizlerinden yararlanılarak kavitasyon performansı incelenmiştir. Bu incelemeler esnasında santral çalışma koşulları ile hesaplanan santral kavitasyon kat sayısı, IEC 60041 standardında belirtilen türbin kavitasyon kat sayısı (Thomann sayısı) ile karşılaştırılmıştır. Santralin kavitasyon kat sayısının türbininkinden büyük olduğu çalışma koşullarında kavitasyonun gözlenmediğini söylemek mümkündür. Türbin kavitasyon kat sayısında kullanılan minimum kanat basıncının belirlenmesinde statik histogram metodundan yararlanılmıştır.

Kadıncık I HES’in tasarım noktasında yapılan HAD analizleri sayesinde türbin mekanik parçalarının ayrı ayrı performansları incelenmiştir. Düşü cinsinden kayıp analizi çalışmaları her bir mekanik parçadaki minimum kaybın farklı debilerde gerçekleştiğini göstermektedir. Bu durum mekanik parçaların birbirleri ile bir uyum içinde tasarlanmadığı sonucunu ortaya koyar. Salyangoz kesitleri sabit girdap prensibine uygun olarak tasarlanmıştır. İlk sabit kanatlarda akış kanadın basınç kenarına çarpıyor olsa da dil bölgesine yaklaştıkça akışın durma noktası sabit kanatların giriş kenarına doğru çekilir. Dil bölgesi ayrı tutulmak kaydı ile akış ayar kanatlarına kadar çevresel yönde düzgün bir dağılım göstererek ulaşır. Fakat her bir ayar kanadının arasından çarka ulaşan su miktarı çevresel yönde çok farklıdır ve bu farklılıklar çark şaftında radyal kuvvetlere ve dolayısıyla titreşime neden olur. Çark giriş ve çıkışındaki hız uçgenleri literatürdeki tavsiyelerle paralellik göstermektedir. Giriş ve çıkış kanat açılarındaki bozukluklar basınç dağılımında sorunlara neden olmaktadır. Özellikle çark kanadı girişinin alt gövdeye yakın bölümlerinde düşük basınç bölgeleri gözlenmektedir. Emme borusundaki akış incelendiğinde çarkın hemen altında iç içe geçmiş iki adet girdap yapısı görülmektedir. Tasarım noktasında gözlenmesi beklenmeyen bu girdaplar çark kanadından emme borusuna bırakılan çevresel hız bileşeninin bir sonucudur. Çark çıkışında önemsenmeyecek büyüklüğe

sahip olan bu girdaplar emme borusu konisinin sonuna doğru emme borusu duvarlarına yaklaşır. Bu olay çalışma sırasında vuruntulara ve titreşime neden olur. Emme borusunun literatürdeki benzerlerine göre neden bu denli uzun olduğu HAD analizleri sonucuna bakılarak anlaşılabilir. Literatür emme borusu çıkışındaki mutlak hızın 2 m/s'nin altında olması gerektiğini savunur. Kadıncık I HES'te 2 m/s mutlak hız seviyesine ancak bu kadar uzun bir emme borusu ile inilebilmiştir.

Kadıncık I HES'in farklı operasyon noktalarındaki performansını görmek için farklı düşü ve debi değerlerinde analizler atılmıştır. Bu analizler türbinin maksimum verimine çalışma koşullarından ve tasarım noktasından çok daha uzak bir noktada ulaştığını göstermektedir. Bu durumda ikinci paragrafta listelenen optimizasyon hedeflerinin yanına türbin maksimum veriminin yıllık çalışma noktalarına kaydırılması da eklenmelidir. Yapılan HAD analizi sonuçları türbinin devreye alınması sırasında gerçekleştirilen test sonuçları ile karşılaştırılmış ve shaft güçleri arasında oldukça tutarlı grafikler elde edilmiştir.

Francis türbin kanadının giriş ve çıkış kenarı eğimleri üzerine yapılan çalışmalar sonunda 1998 yılında Three Gorges projesinde zıt yönlü giriş kenarı eğimine sahip X-Blade çark tasarımı kullanılmıştır. Geleneksel Francis çarkı tasarımının aksine X-Blade teknolojisi zıt yönde uzanan giriş kenarı geometrisine ve daha eğimli çıkış kenarına sahiptir. Çarkın hidrolik tasarımındaki bu değişim X-Blade teknolojisine sahip çarkların daha dengeli basınç dağılımına sahip olmalarını mümkün kılar. Ayrıca bu tasarımla çark giriş ve çıkışındaki hız dağılımlarında da iyileşme yaşanmıştır. 1998 yılından beri bu teknolojide kazanılan tecrübeler sayesinde X-Blade tasarımının daha yüksek verim, daha iyi kavitasyon performansı ve daha geniş çalışma aralığı sağladığı ispatlanmıştır.

Santral personelinden temin edilen yıllık düşü, debi ve enerji üretimi değerlerinin yardımıyla ekonomik fizibilite hesapları yapılmıştır. Bu hesaplar sonucunda optimizasyon sonrası türbinin maksimum verim noktası belirlenmiştir. HAD analizleri yardımı ile var olan türbin çarkı akış koşullarına göre optimize edilmiştir. Bu optimizasyon çalışmaları sırasında bir yandan geleneksel tasarım metodu takip edilirken bir yandan da X-Blade teknolojisinden yararlanılmıştır. Kanat geometrisinde yapılan modifikasyonlar sonunda iki tasarım metodunun da en iyi performansa sahip çark geometrileri seçilmiş ve geleneksel metotlarla optimize edilen çark ile X-Blade tasarım yöntemine sahip çarkın geometrileri belirlenmiştir. Bu iki optimizasyon versiyonunun dahil edildiği HAD analizi sonuçları kendi aralarında ve var olan türbinin numerik analiz sonuçları ile karşılaştırılmıştır. Bu karşılaştırma, sadece türbin çarkında yapılan değişikliklerle, maksimum verim değerinin artırılabilceği, optimum çalışma noktasının başka düşü-debi değerlerine kaydırılabileceği, kavitasyon performansının, kanat üzerindeki açı dağılımının ve çark giriş ve çıkışındaki hız bileşenlerinin dağılımlarının iyileştirilebileceğini ispatlamıştır.

İki optimizasyon versiyonuyla da optimum çalışma noktası türbinin operasyon noktalarına yaklaştırılmıştır. Bu versiyonlar kavitasyon ve hız dağılımları açısından yeterli performansı gösterirken, maksimum verimdeki artış ve basınç dağılımlarındaki iyileşme X-Blade tasarımında kendini daha çok hissettirmiştir. Ayrıca X-Blade ile optimize edilen türbin yüksek verimlerde daha geniş bir operasyon aralığı sunmaktadır.

1. INTRODUCTION

1.1 Purpose of Thesis

Total capacity of the hydraulic power plants in Turkey equals to 34 % of installed capacity of Turkey [1]. Hydraulic power does not face with the stability problems that occur frequently in solar and wind power. Besides, hydraulic power plants are much more environmental friendly than thermal and nuclear power plants. With the establishment of pump storage technology, energy storage capacity has been available in hydraulic energy sources. When all these issues are considered, significance of waterpower in power production of Turkey will be understood once again.

The geological structure of Turkey and characteristics of water sources make the Francis turbine a good option for many of the hydraulic power plants. This is also a result of the fact that Francis turbines can operate in wide range of head and discharge. Furthermore, if head and discharge values are not changing dramatically throughout the year for a certain power plant, designers mostly prefer Francis turbines because they have higher peak efficiency than the other hydraulic turbine types, but they are not so adaptable to divergent conditions. Fortunately, only 30 % of the hydraulic power plants are run of river type [1]. This means 70 % of the plants have a dam to compensate sudden and notable changes in head and discharge. Finally, Francis turbines are the most commonly utilized turbines in the world and consequently, they have undertaken more improvement than Kaplan and Pelton turbines.

Although Turkey has produced 34 % of its power from water sources, approximately 45 % of the power plants are older than 40 years and there has been no rehabilitation from start-up in almost all of them. These power plants were not only designed with old technology but also their efficiency has been lowered in considerable amount due to the aging effect. These factors bring the need of refurbishment in most of the hydraulic power plants of Turkey.

This thesis aims to show how hydraulic design of a Francis turbine runner can be optimized according to operation conditions by using CFD analysis. The word of optimization here means an improvement in turbine performance. For illustration, Kadincik I HPP is chosen as a case study and all the explained methodologies are applied to the runner geometry of this power plant. The results of the changes are examined and generally valid statements are issued.

1.2 Literature Review

1.2.1 History of Francis turbine

As one of the most commonly preferred hydraulic turbine, Francis turbine was invented by James B. Francis in 1848. According to Madsen [2], almost two centuries have been passed without any considerable innovation since the development of Francis turbine. Although there have been very valuable contributions to the improvement of performance and flow prediction, same turbines are still utilized as before. In fact, all researches have been focused on the understanding of turbomachinery behavior and increase the turbine efficiency rather than making severe changes in hydraulic design.

The success of the design is judged with satisfaction of desired power, efficiency and stability. Before 1980s, turbine designs heavily depended on theoretical knowledge and model test experiments. Experimental approach of predicting the performance of water turbines, i.e. testing of physical turbine models, is costly, time consuming and limited with the means of laboratory [3][4]. Therefore, understanding the behavior of fluid flow inside the Francis turbine became a must.

1.2.2 Numerical investigation of fluid flow inside a Francis turbine

The first comprehensive attempt to explain flow through radial machines was made by Lorenz in 1906 [5]. Bauersfeld [6] continued his theory for Francis turbines in 1912. Subsequently, Dreyfus [7] published remarkable theories on fluid flow inside the Francis turbine unit in 1946. However, mathematical cost of his studies was too high even for today's computers to carry out such calculations [2]. The studies of Professor Wu [8] have ushered in a new age in prediction of turbine flow. His works have served as a base for a lot of computer algorithms which are developed by Katsanis and McNally [9] in 1969, Kirsch [10] in 1970, Katsanis and McNally [11]

in 1974, Chauvin [12] in 1977, Hirsch and Warzee [13] in 1978, Keck and Haas [14] in 1982, Gjerde in [15] 1988 etc. In 1993, Jocabesen [16] left the quasi 3D approach of Professor Wu and focused on the non-viscous fully 3D Euler equations. Subsequently, viscous flow solutions based upon the full Navier-Stokes equations have been developed thanks to the increased capacity of contemporary computers [17][18].

1.2.3 Validation of CFD results in hydraulic power plant applications

Today, CFD is a powerful tool to predict flow behavior. It is able to give accurate information about the essential design and performance parameters, such as flow angles, head losses, guide vane torques, discharge, efficiency, pressure distribution etc. Throughout the years, CFD results of a Francis turbine unit have been validated with several case studies include both model turbines and prototypes. For instance, Shukla [19] conducted 3-D CFD analysis in commercial software CFX for a model turbine of an actual Francis turbine at an Indian hydraulic power plant. She observed that steady state CFD analysis results were inside the error limits of efficiency measurement. Lain [20] made a similar study for a power plant in Colombia to understand the operation conditions of the system. He experienced that numerical hill chart of the Francis turbine derived with steady state CFD analysis in CFX were in a good agreement with the results of the efficiency measurement test at site. Nonetheless, he stated that although steady state analysis is adequate for determination of turbine performance, transient CFD analysis is needed for clarification of the unsteady phenomena inside the unit, such as pressure pulsations, vortex rope and Von Karman vortexes. Furthermore, Čarija [21] validated his CFD results for a 20 MW Francis turbine (Rijeka HPP) with an efficiency measurement. Apart from the previous examples, he utilized commercial software Fluent for his steady state analysis.

CFD validation studies are not only limited with commercial softwares. Open source codes are also tested for commonly known test cases. The studies of Nilsson [22] can be shown as an example for this. He tested his open source code in GAMM Francis turbine runner and concluded that his steady state CFD solutions fitted to the experimental findings.

The accuracy of the steady state CFD analysis for prediction of turbine performance has been proved. Nowadays, even CFD analysis by itself becomes determinative for improvement in performance without any validation with experimental studies. For instance, Choi [23] conducted a project to enhance performance of 500 kW Francis turbine. By depending on the CFD results of original and final turbine geometries, he demonstrated the improvement in the turbine performance.

1.2.4 Design of a Francis turbine by using CFD

Thanks to its good presume of turbomachinery performance, CFD started to get involved into the design procedure of Francis turbine. Design of a Francis turbine starts with main parametrization and is followed by blade angle determination. However, there is no complete design methodology that covers every detail and results as a final geometry. After the preliminary design, turbine geometry should be modified according to the flow conditions. CFD is benefitted at this stage. All designers utilize CFD analysis together with the model tests to reach the optimum Francis turbine design. For example, Neopane [24] suggested using numerical methods for final tuning of the prototype Francis runners. This expresses the iterative design method of Norwegian University of Science & Technology, which is combined with CFD. Similar examples of the usage of CFD in Francis turbine design can be seen in the studies of Odesola [25], Patel [26], Okyay [27], Hellström [28] etc. CFD has contributed to the improvement of design methodologies, also. Due to the unfavorable pressure distribution, low hydraulic efficiencies at off-design conditions and instabilities of conventional designs, negative lean angle approach was introduced in 1982 [44]. This design method has been enhanced with CFD analysis and model tests. In the end, runners with reversed leading edge have been widely accepted and called X-Blade after it was proved that this technology is able to solve the problems faced in the conventional designs.

1.2.5 Optimization of a Francis turbine by using CFD

The design methodologies have not been dramatically changed for many years and main researches have been focused on optimization of existing turbines [2]. This has resulted in several rehabilitation projects in existing hydraulic power plants. The refurbishment of the plant machinery poses very specific challenges; therefore, only the key components of the existing turbines are replaced [29]. In most of the cases,

all rotating components, like runner, synchronous generator and guide vanes, are under the consideration of the replacement, whereas stationary parts, like spiral case, stay vanes and draft tube, are preserved [30]. The reason behind this approach is that the hydraulic performance of a Francis turbine strictly depends on shape of the runner [31] [32]. Moreover, stationary parts are immobilized by putting them under the concrete. Therefore, changing these components is very costly, extends the pay-back periods of projects and consequently is not preferred.

A joint project of U.S. and Japan shows that 3 % relative increase can be achieved in the Francis turbine peak efficiency by optimizing only the runner and guide vane geometries [33]. On the other hand, the rehabilitation project of VA TECH HYDRO in Taloro II power plant, Italy, proves that runner replacement can result in not only an increase in peak efficiency but also a shift of the position of best efficiency point [34]. Moreover, Huang [35] conducted a case study in a real hydraulic power plant in order to solve its cavitation problems. Only the runner was replaced in the scope of the project and it was observed that new runner optimized by using commercial CFD software CFX eliminated the cavitation phenomenon at overload. Thum [36] benefited from multilevel CFD techniques to demonstrate the potential of development by only adjusting runner blading of a Francis turbine. In the end, she also concluded that runner blade geometry has a great influence on the turbine performance. Toshiba Corporation is another company that utilizes CFD in refurbishment projects frequently. Enomoto [37] optimized the runner geometry of a real HPP by steady state simulations, validated the results with model test for this high specific speed Francis turbine and observed that optimized runner solved the instability vibrations with transient CFD analysis and model test. Tsinghua University, China, uses their open source CFD software for adaptation of runner geometry of a Francis turbine. For a test case, they achieved to increase the turbine efficiency by 1 % (from 93 % to 94 %) only with optimized runner [38]. Similar studies were conducted by Wang [39] for Xiluodu Hydropower Station, Kaewnai [40] for Eglisu Electrical Plant, Sotnikov [41] for Bratskaya HPP (Russia) and Pamilo II HPP (Finland) and Henggeler [29] for Rempen Pumped Storage Plant. Finally, Gray [42], EPRI project manager, published a life extension and modernization program and projects for hydraulic power plants in U.S. and Canada.

It is consistent with previous examples to see that most of the refurbishment projects consist of only runner replacement.

CFD became an integral part of the optimization in hydraulic turbines. In addition to the hand-made optimization approach, some scientists proposed automatic optimization codes coupled with CFD. Cherny [43] and Derakhshan [31] utilized global optimization methods based on artificial neural networks (ANN) and genetic algorithms (GA) compatible with 3D Navier-Stokes flow solver in order to enhance Francis turbine performance.

1.3 Hypothesis

In the refurbishment projects, it is really hard to change spiral case and draft tube of a turbine unit since they are inside the concrete most of the time. Therefore, although their performances are highly poor, implementation of new designs are avoided. Nevertheless, it is widely accepted that turbine performance is mostly governed by runner component. In fact, only change in hydraulic shape of the runner design can considerably improve the turbine performance. Especially, introduction of X-Blade technology can provide much better cavitation behavior and higher peak and off design condition efficiencies. This study will prove these statements by taking Kadincik I HPP as an illustration.

2. DETERMINATION OF THE OVERALL DIMENSIONS AND BLADE GEOMETRY OF FRANCIS TURBINE

In this chapter, design procedure of a Francis turbine is explained in detail. Suggestions in the literature for the designs of all mechanical parts (runner, draft tube, spiral case, stay vanes and guide vanes) are discussed and geometrical parameters determined according to the commonly used design approaches are compared with the prototype of Kadincik I HPP turbine.

After the determination of the nominal head, flow rate and rotational speed, most proper hydraulic turbine for corresponding power plant can be selected according to specific speed, although there is a general suggestion for what kind of a turbine should be utilized for a certain head and discharge values (Figure 2.1).

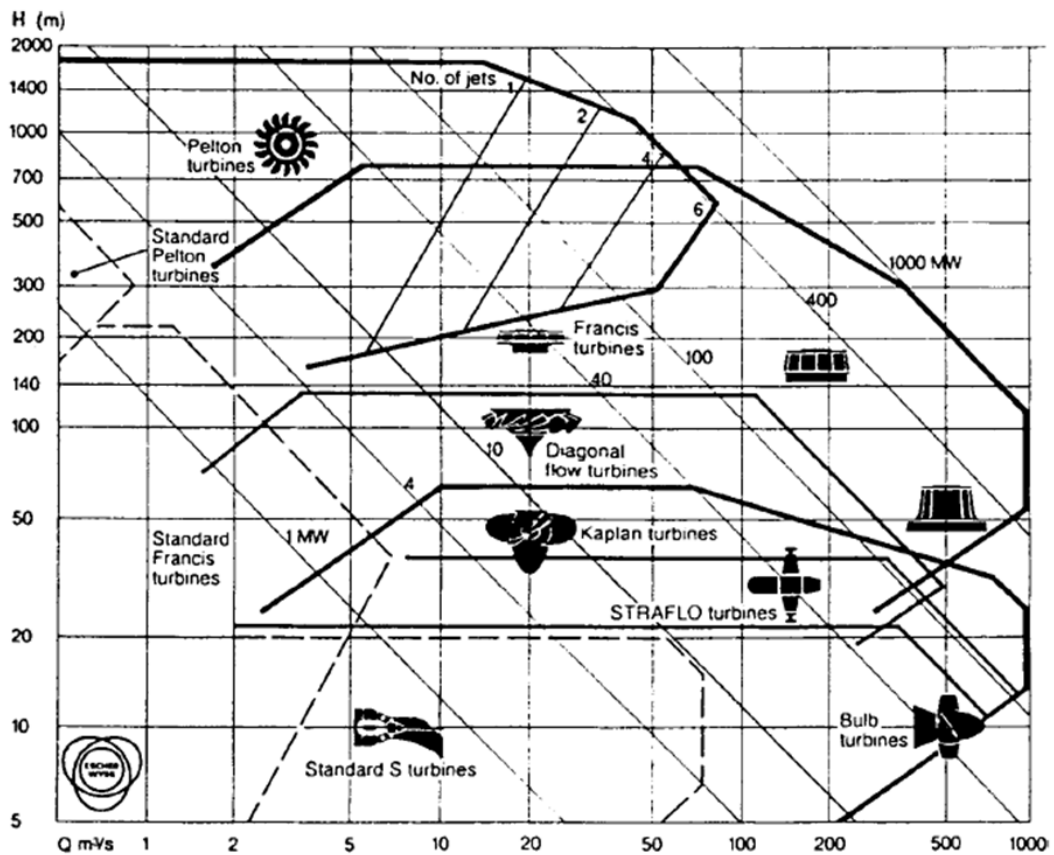


Figure 2.1 : Suggestions on the type of the turbine according to head and discharge values, adapted from [45].

Though there are some commonly accepted formulations for specific speed, its definition varies among some authors. In fact, IEC standard already established a formula for specific speed (n_s - Equation (2.1)). This formula is frequently utilized especially in American literature. There is also a non-dimensional alternative of this definition (n_s' - Equation (2.3)). Another widely-used formulation for specific speed is presented in Equation (2.2) which is very popular in German speaking countries.

In addition to these three well known specific speed equation, some designers have tried to find a correlation directly between specific speed and design net head. Whereas Siervo and Leva established a relation between dimensional n_s and net head, Schweiger – Gregori and Lugaresi – Massa conducted similar studies for n_q . Resulting empirical Equations (2.4) - (2.6) give the specific speed values very close to original equations.

After the calculation of the specific speed, proper type of the turbine can be selected from Figure 2.2 regardless of which definition of specific speed is utilized. As it is seen in Figure 2.2, Francis turbine can be a good option for dimensional n_s between 80 and 330, non-dimensional n_s between 0.12 and 0.60 and n_q between 30 and 110. Furthermore, Francis turbines are capable of operating in a head level range between 30 and 700 meter. This wide range of operation and its higher efficiency values than other types of turbines make Francis turbine to be widely preferred. Especially, if the head and discharge values are not changing dramatically throughout the year, Francis turbines fit this power plant perfectly; otherwise, Kaplan turbine may be a better option due to its adjustable blade configuration.

When Kadincik I HPP is under examination for specific speed, it is seen that its dimensional n_s number is 126.615 whereas corresponding non-dimensional version of this value is 0.259. On the other hand, n_q is calculated for Kadincik I as 38.811 by using the 428.6 rpm rotational speed, 35 MW maximum power, 25 m³/s maximum flow rate and 194 meter net head. Note that optimum discharge is accepted as 80 % - 90 % of maximum flowrate.

Figure 2.2 concludes that for the calculated specific speeds, Francis turbine preference in Kadincik I HPP is quite reasonable. In addition, around this specific speed, it is expected to have a net head between 150 and 200 meter. Therefore, no defect is seen in the turbine selection for Kadincik I HPP.

Table 2.1 : Specific speed definitions.

Designation	Definition	Utilized by	Units	Equation Number
n_s	$\frac{n * \sqrt{P}}{H_{net}^{5/4}}$	<ul style="list-style-type: none"> • IEC Standards • United States Department of the Interior Bureau of Reclamation [46] • Gubin [47] • Brekke [48] 	<p>n:rotational speed [rpm]</p> <p>P: power [HP]</p> <p>H_{net}: net head [m]</p>	(2.1)
n_q	$\frac{n * \sqrt{Q_{opt}}}{H_{net}^{3/4}}$	<ul style="list-style-type: none"> • Thomann [49] • Chapallaz [50] • Giesecke [51] • Raabe [52] • Leeb [53] • Pfleiderer [54] 	<p>n:rotational speed [rpm]</p> <p>Q_{opt}: optimum discharge [m³/s]</p> <p>H_{net}: net head [m]</p>	(2.2)
n'_s	$\frac{\omega * \sqrt{Q/\pi}}{(2 * g * H_{net})^{3/4}}$	<ul style="list-style-type: none"> • Bovet [55] • Miloš [56] • Morales [57] • Razavi [58] 	<p>ω: rotational speed [rad/s]</p> <p>Q: discharge [m³/s]</p> <p>g: gravitational acceleration [m/s²]</p> <p>H_{net}: net head [m]</p>	(2.3)
n_s	$\frac{3470}{H_{net}^{0.625}}$	<ul style="list-style-type: none"> • Siervo and Leva [59] 	<p>H_{net}: net head [m]</p>	(2.4)
n_q	$\left(\frac{58369.7}{H_{net}}\right)^{1/1.53}$	<ul style="list-style-type: none"> • Schweiger and Gregori [60] 	<p>H_{net}: net head [m]</p>	(2.5)
n_q	$\frac{2419}{3 * H_{net}^{0.489}}$	<ul style="list-style-type: none"> • Lugaresi and Massa [61] 	<p>H_{net}: net head [m]</p>	(2.6)

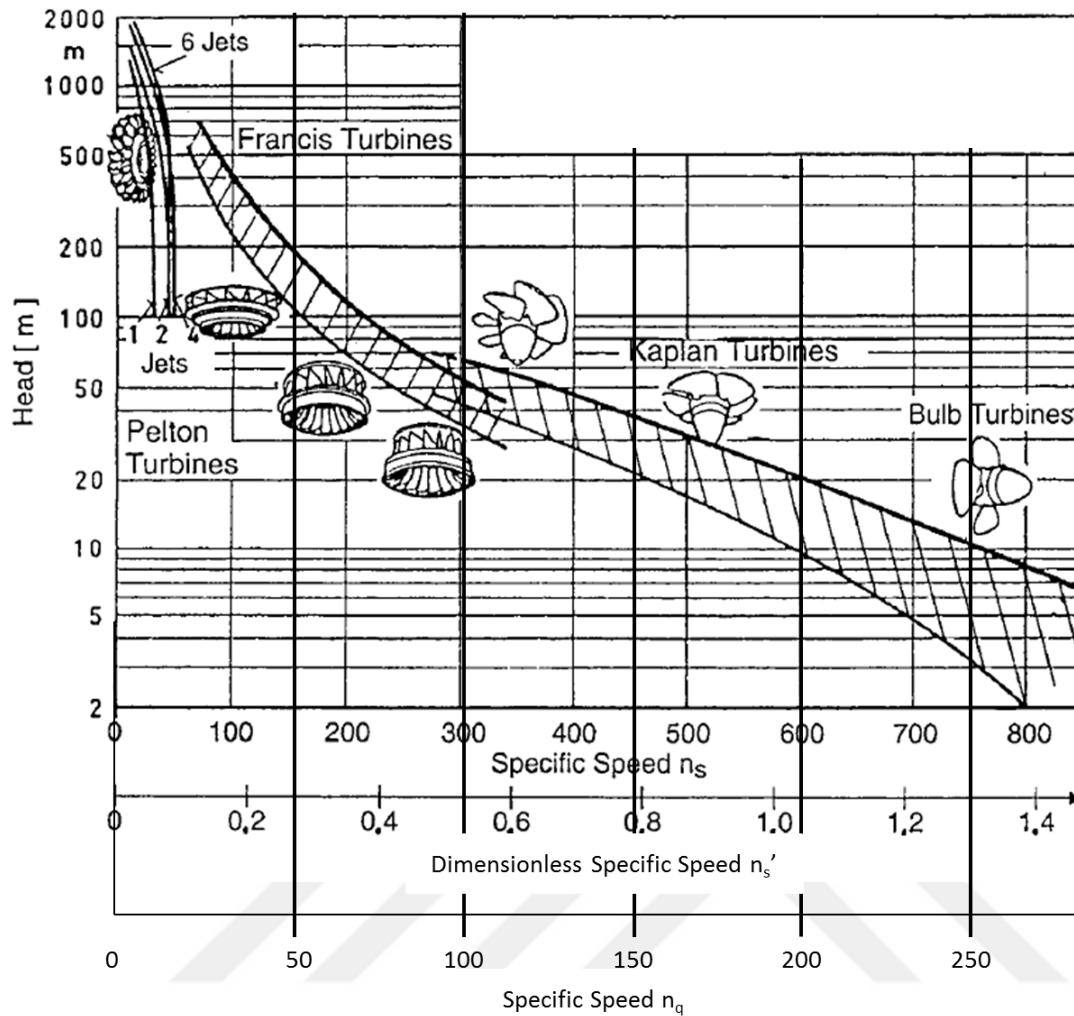


Figure 2.2 : Diagram for the types of hydraulic turbines, adapted from [62].

After determination of turbine type, design procedure goes on with the calculation of the main dimensions for all mechanical parts of turbine. Some designers established empirical correlations between main turbine parameters and specific speed. In the following sub-chapters, design methodologies for all mechanical parts are explained.

2.1 Design of the Runner

Francis turbine design starts with runner after the determination of the specific speed because most of the designers have published empirical correlations between geometrical parameters of turbine and runner design diameter. Nevertheless, definition of runner design diameter changes from author to author. Some designers, like De Siervo - De Leva [59] and Bovet [55], identify it as runner outlet diameter (runner discharge diameter), whereas some of the others assume that this dimension refers to the point where runner leading edge touches to the shroud (runner inlet

diameter). Nevertheless, in the end, they all define other turbine parameters with respect to this runner design diameter. This part of the design procedure is called main parametrization and followed by the determination of blade angles and fine tuning of geometry by CFD.

2.1.1 Main parametrization of De Siervo and De Leva

One of the most widely accepted main parametrization was established by De Siervo and De Leva because these scientists made recommendations also for draft tube and spiral case. They utilized specific speed definition presented in Equation (2.4). With the help of the Equation (2.7), peripheral velocity coefficient (k_u) is calculated. This coefficient also depends on the runner discharge diameter. From this dependency, Equation (2.8), outlet diameter (D_3) is obtained and other geometrical parameters of runner are correlated with D_3 (Equations (2.9) - (2.12)). These parameters and their designations are shown in Figure 2.3. Note that designations for runner main parameters are not same for all authors. In this chapter, each geometrical parameter definition is presented with a figure for all designers.

$$k_u = 0.31 + 0.0025 * n_s \quad (2.7)$$

$$D_3 = \frac{84.5 * k_u * \sqrt{H_{net}}}{n} \quad (2.8)$$

$$D_1 = \left(0.4 + \frac{94.5}{n_s}\right) * D_3 \quad (2.9)$$

$$D_2 = \frac{D_3}{0.96 + 0.00038 * n_s} \quad (2.10)$$

$$H_1 = (0.094 + 0.00025 * n_s) * D_3 \quad (2.11)$$

$$H_2 = \frac{D_3}{3.16 - 0.0013 * n_s} \quad (2.12)$$

De Siervo and De Leva obtained these equations by examining 105 different hydropower plants. And, the results of these equations for the condition of Kadincik I HPP are compared with the actual parameters in Table 2.2. As it is seen, runner outlet diameter of Kadincik I HPP is very close to recommendation of De Siervo and De Leva, which is important since all other dimensions depend on this value. However, difference between actual and proposed D_1 and D_2 show that hub and shroud extends in horizontal direction more than they should be, although they show

a favorable manner in vertical direction. At this point, it should not be forgotten that maximum difference between the values in Table 2.2 is 25 cm and it is negligibly small when compared with runner discharge diameter.

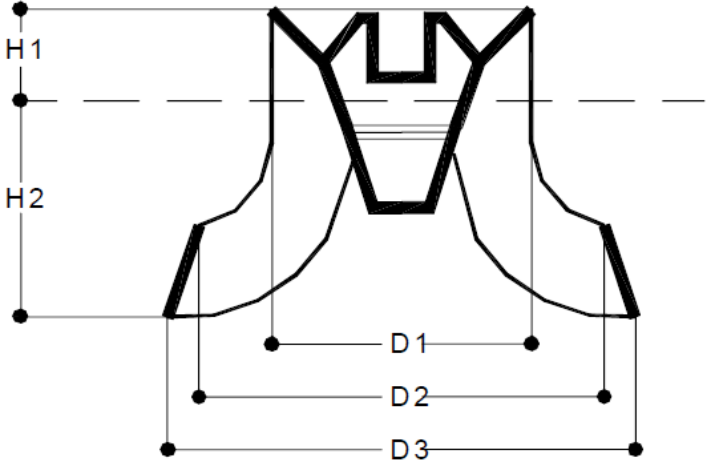


Figure 2.3 : Geometrical parameter definition of De Siervo and De Leva for runner, adapted from [59].

Table 2.2 : Geometrical parameters of De Siervo and De Leva for runner.

Designation of Dimensions (based on Figure 2.3)	De Siervo and De Leva Recommendation		Actual Situation in Kadincik I HPP	
	Value	Unit	Value	Unit
D ₃	1.740	meter	1.700	meter
D ₁	1.979	meter	1.840	meter
D ₂	1.725	meter	1.975	meter
H ₁	0.219	meter	0.220	meter
H ₂	0.581	meter	0.565	meter

2.1.2 Main parametrization of United States Department of the Interior Bureau of Reclamation

A similar parametrization approach with De Siervo and De Leva was utilized by United States Department of the Interior Bureau of Reclamation. It also advises to get benefit from a term related with velocity in order to calculate the runner discharge diameter. Nonetheless, different than De Siervo and De Leva, this parametrization uses dimensional form of n_s , Equation (2.1), and velocity ratio (ϕ_3 – Equation (2.13)) to determine outlet diameter (D_3) with the help of Equation (2.14). Other parameters, whose recommendations are stated by United States Department of the Interior Bureau of Reclamation, D_1 and b , are decided according to Figure 2.5 and Figure 2.6 (definitions of these parameters in Figure 2.4).

$$\phi_3 = 0.0211 * (n_s)^{2/3} \quad (2.13)$$

$$D_3 = \frac{84.47 * \phi_3 * \sqrt{H_{net}}}{n} \quad (2.14)$$

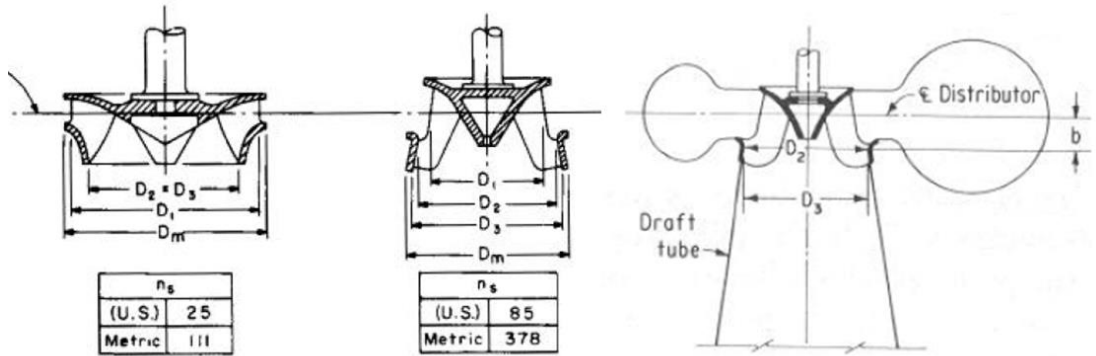


Figure 2.4 : Geometrical parameter definition of United States Department of the Interior Bureau of Reclamation for runner, adapted from [46].

As it is noticed, suggestions of United States Department of the Interior Bureau of Reclamation on main parameters of runner do not cover most of the geometrical dimensions, but it gets respect from majority because it gives also information about draft tube and spiral case. The values coming from Figure 2.5 and Figure 2.6 are compared with the actual geometry of Kadincik I HPP in Table 2.3. Except from D_1 and D_m , other parameters better matches with De Siervo and De Leva rather than this methodology. This recommendation suggests smaller outlet diameter and therefore closer D_1 and D_m values to actual case. Moreover, only a few geometrical dimensions are indicated with this method; therefore, further design considerations are needed to complete meridional view of runner.

Table 2.3 : Geometrical parameters of United States Department of the Interior Bureau of Reclamation for runner.

Designation of Dimensions (based on Figure 2.4)	United States Department of the Interior Bureau of Reclamation Recommendation		Actual Situation in Kadincik I HPP	
	Value	Unit	Value	Unit
$D_3 = D_2$	1.468	meter	1.700	meter
D_m	1.908	meter	1.975	meter
D_1	1.835	meter	1.840	meter
b	0.426	meter	0.565	meter

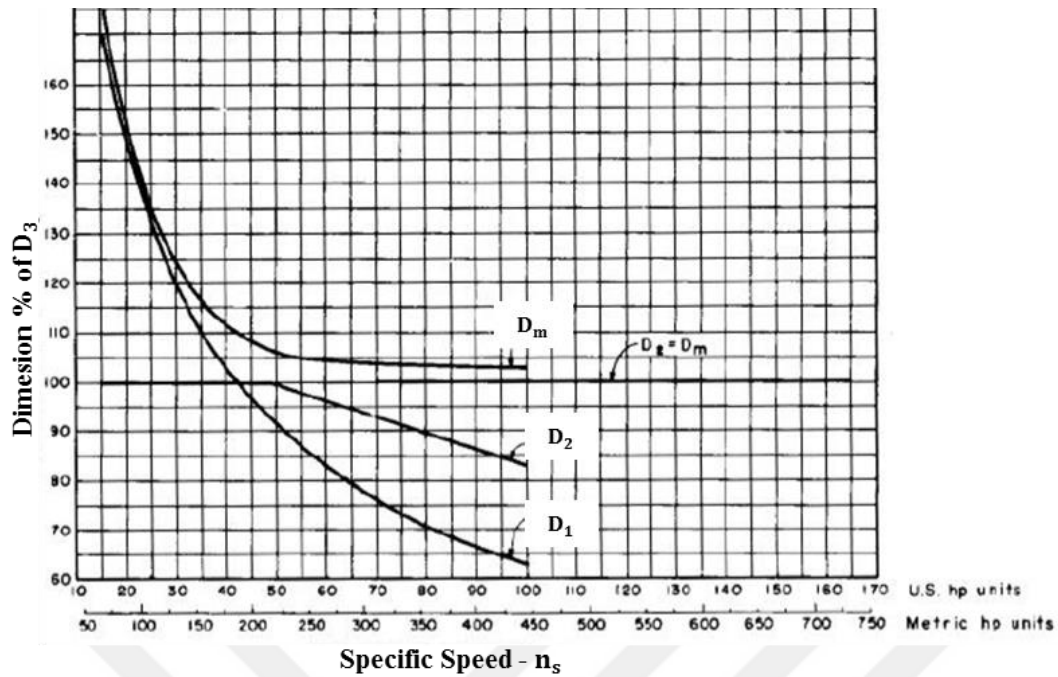


Figure 2.5 : Correlation of parameters for runner (United States Department of the Interior Bureau of Reclamation), adapted from [46].

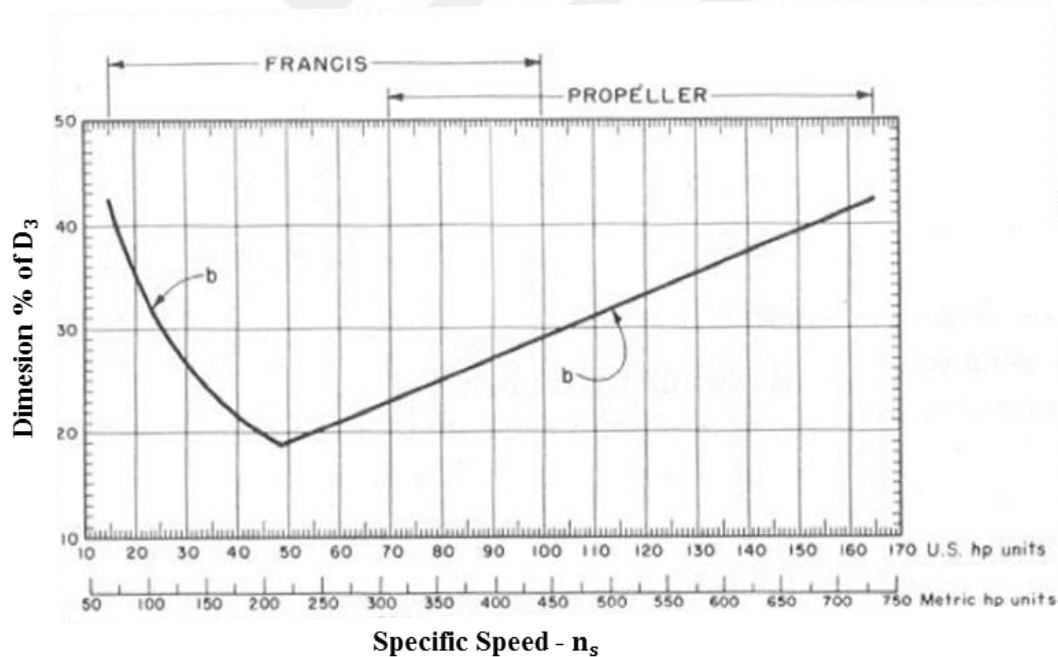


Figure 2.6 : Correlation of parameters for runner (United States Department of the Interior Bureau of Reclamation), adapted from [46].

2.1.3 Main parametrization of Giesecke and Leeb

Velocity coefficient concept is used by Giesecke [51] and Leeb [53] in order to find runner inlet diameter, which is defined as the diameter corresponds to the point

where the leading edge touches to shroud (D_{1a} in Figure 2.7). As a result, different velocity coefficient (k_{u1a}) is provided for runner inlet. Giesecke suggested determining k_{u1a} from Figure 2.7 with the help of the n_q , Equation (2.2). Then, D_{1a} can be calculated with Equation (2.15) and other parameters can easily be decided in Figure 2.7.

$$D_{1a} = \frac{84.6 * k_{u1a} * \sqrt{H_{net}}}{n} \quad (2.15)$$

Apart from the previously discussed parametrizations, Giesecke and Leeb provide a chance to find out all the points of leading and trailing edges that touch to the hub and shroud. When the results of this design methodology are compared with the actual situation in Kadincik I, it is seen that dimensions have a good agreement between each other (Table 2.4). The only little problem can be detected in D_{2i} , which suggests that the blade profile may be a little bit long around the hub.

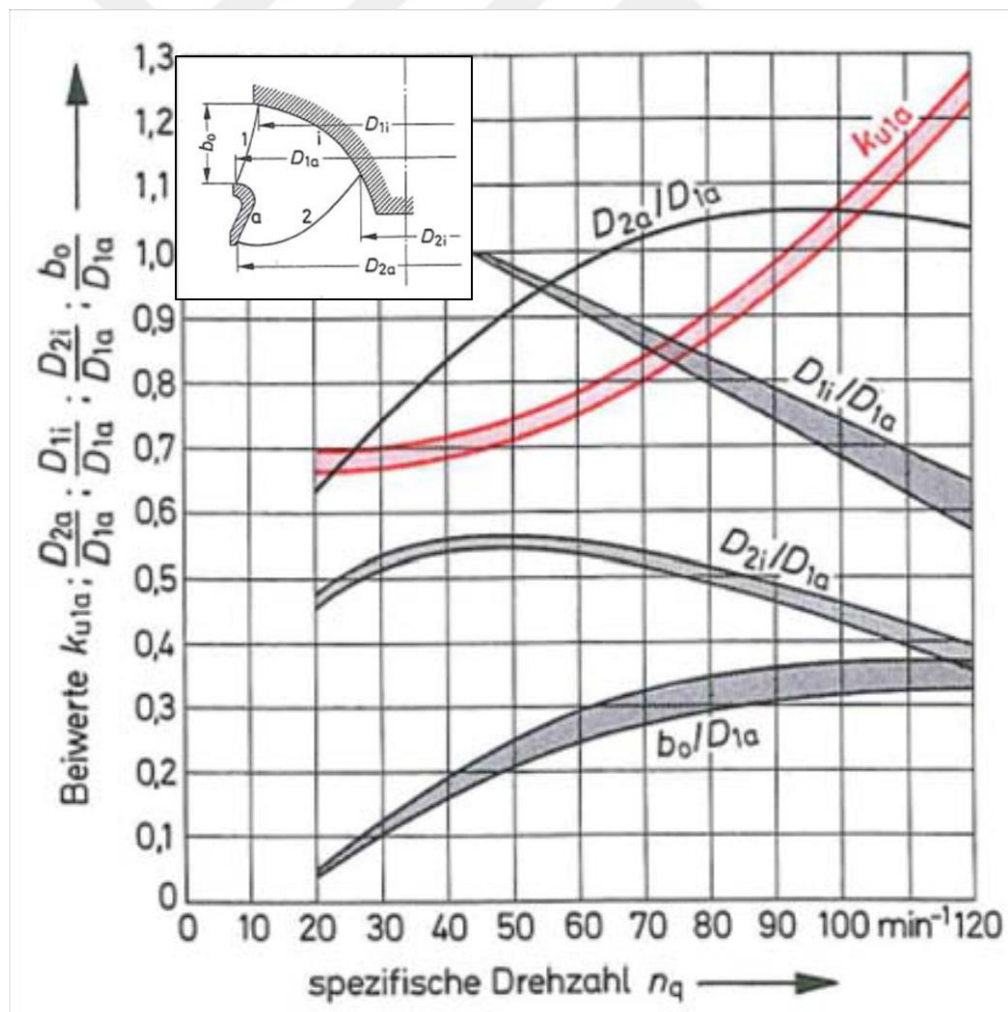


Figure 2.7 : Correlation of parameters for runner (Giesecke), adapted from [53].

Table 2.4 : Geometrical and hydraulic parameters of Giesecke and Leeb for runner.

Designation of Dimension (based on Figure 2.7)	Giesecke and Leeb Recommendation		Actual Situation in Kadincik I HEP	
	Value	Unit	Value	Unit
k_{u1a}	0.700	-	-	-
D_{1a}	1.934	meter	1.975	meter
D_{2a}	1.606	meter	1.700	meter
D_{1i}	1.934	meter	1.840	meter
D_{2i}	1.064	meter	0.867	meter
b_o	0.339	meter	0.360	meter

2.1.4 Main parametrization of Schweiger and Gregori

Schweiger and Gregori [60] conducted a very similar study with Giesecke in 1985. They tried to link some runner parameters to their specific speed definition, Equation (2.5), and runner inlet diameter, whose definition is same with Giesecke. They also utilized inlet peripheral velocity coefficient (k_{u1a}), which is this time determined by Equation (2.16). Subsequently, D_{1a} , runner inlet diameter, is calculated with Equation (2.17), which is nothing but the same formula with Equation (2.15). The other dimensions, such as runner outlet diameter (D_{2a}), height of the guide vane (b_o) and guide vane rotation axis (D_{gv}), are obtained with the following formulas, Equations (2.18) - (2.20).

$$k_{u1a} = 0.75019 - 0.003154 * n_q + 0.00006361 * n_q^2 \quad (2.16)$$

$$D_{1a} = \frac{60 * k_{u1} * \sqrt{2 * g * H_{net}}}{\pi * n} \quad (2.17)$$

$$D_{2a} = (0.46 + 0.00829 * n_q) * D_{1a} \quad (2.18)$$

$$b_o = (-0.00702 + 0.003798 * n_q) * D_{1a} \quad (2.19)$$

$$D_{gv} = (1.19985 - 0.0002495 * n_q) * D_{1a} \quad (2.20)$$

Schweiger and Gregori give information about not only the runner but also the guide vanes. They made some recommendations about guide vane height and position of the guide vane rotation axis. They concluded empirical formulas listed above after a detail study with big companies in hydro business. Their design suggestions show similarity with Giesecke and Leeb. Furthermore, results are very consistent with geometry of Kadincik I HPP (Table 2.5). Nevertheless, number of the dimensions

provided is limited in the study of Schweiger and Gregori. This makes the further considerations on main parametrization of runner a must.

Table 2.5 : Geometrical and hydraulic parameters of Schweiger and Gregori for runner.

Designation of Dimensions	Schweiger and Gregori Recommendation		Actual Situation in Kadincik I HPP	
	Value	Unit	Value	Unit
k_{u1}	0.725	-	-	-
D_{1a}	2.003	meter	1.975	meter
D_{2a}	1.609	meter	1.700	meter
b_o	0.301	meter	0.360	meter
D_{gv}	2.383	meter	2.300	meter

2.1.5 Main parametrization of Thomann

Empirical correlations put forward by Thomann [49] are also one of the most commonly utilized main parametrization in Francis turbine because he provides considerable amount of information on hydraulic shape of the runner. Although Thomann started with well-known n_q definition, Equation (2.2), he constructed his parametrization plot (Figure 2.8) according to n_s' , which is 3.652 times n_q (Equation (2.21)). He has the same runner inlet diameter definition with Giesecke and Schweiger. However, he calculates this dimension with the help of the pressure coefficient (ψ) rather than peripheral velocity coefficient, Equation (2.22). Afterwards, all the other parameters can be determined from Figure 2.8.

$$n_s = 3.652 * n_q \quad (2.21)$$

$$D_{2a} = \frac{60}{\pi * n} * \sqrt{\frac{2 * g * H_{net}}{\psi}} \quad (2.22)$$

One of the advantages of Thomann on other parametrization methods is that he gives information of both geometrical and hydraulic parameters, such as maximum head and optimum discharge. When Table 2.6 is observed, it can be concluded that design head of Kadincik I HPP is too high for Thomann; although, it is inside the permissible region according to Figure 2.1 and Figure 2.2. Furthermore, parametrization of Thomann suggests that best efficiency point should occur around 84 % of maximum flowrate which corresponds to 21 m³/s. This percentage is also supported with different sources that claim Francis turbines should reach the peak

efficiency between 80 % and 90 % of their maximum discharges. In fact, Kadincik I HPP attains its maximum efficiency at 21 m³/s for 194 meter design net head. The consistency in the optimum flow rate continues in geometrical dimensions. Only notable difference can be seen in D₄ and this parameter belongs to guide vane apparatus.

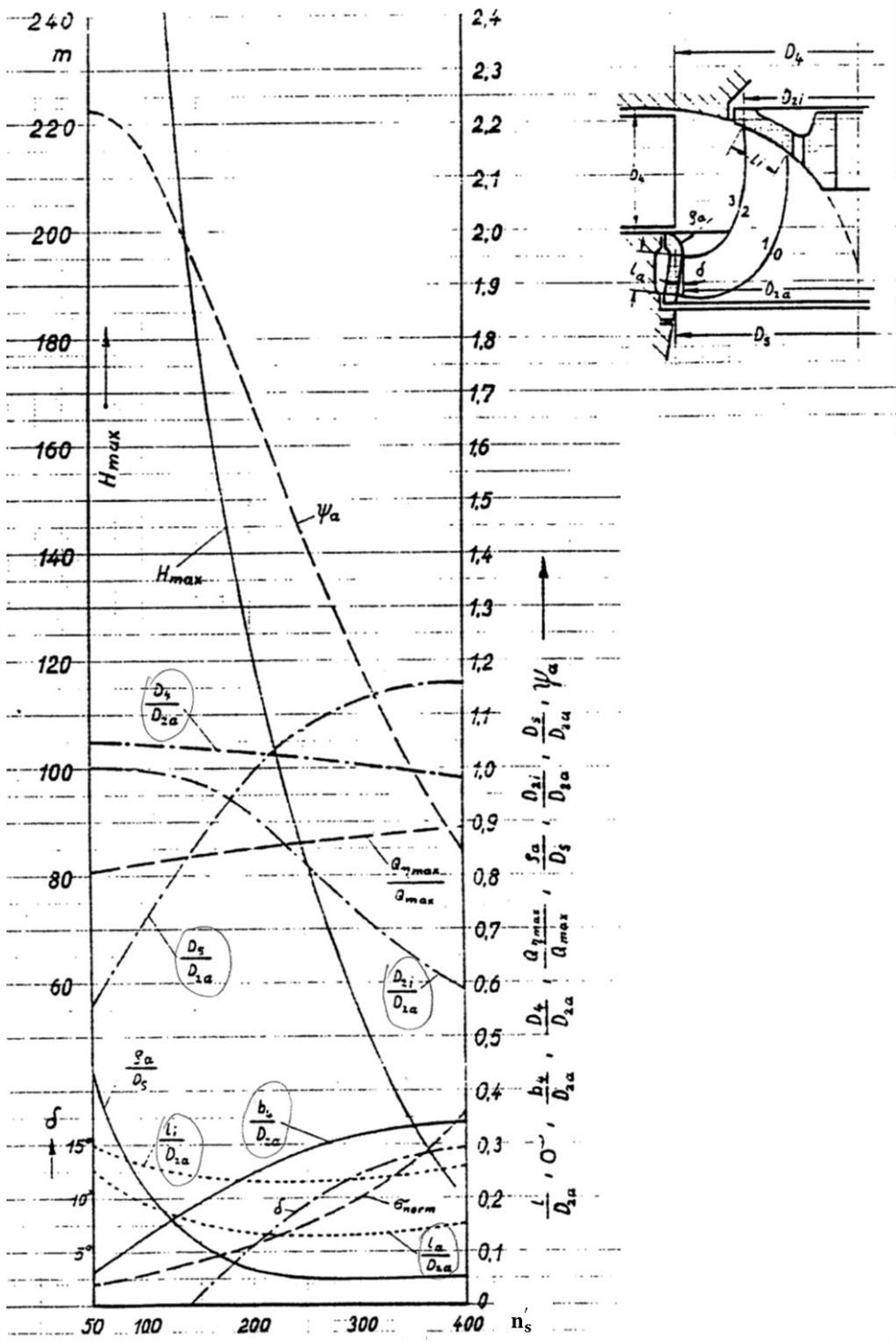


Figure 2.8 : Correlation of parameters for runner (Thomann), adapted from [49].

Table 2.6 : Geometrical and hydraulic parameters of Thomann for runner.

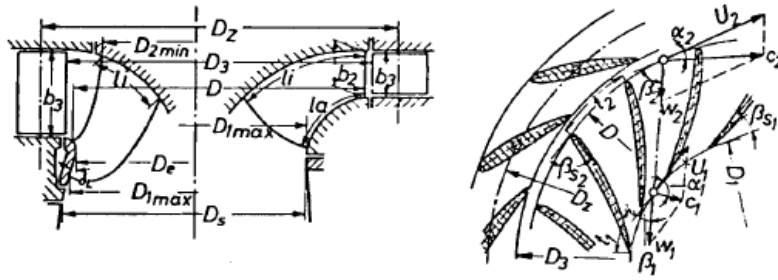
Designation of Dimensions (based on Figure 2.8)	Thomann Recommendation		Actual Situation in Kadincik I HPP	
	Value	Unit	Value	Unit
n_s	141.737	-	141.737	-
ψ	1.950	-	1.950	-
H_{max}	185.000	meter	194.000	meter
Q_{opt}	21.000	m ³ /s	21.000	m ³ /s
D_{2a}	1.979	meter	1.975	meter
D_4	2.572	meter	2.000	meter
D_{2i}	1.919	meter	1.840	meter
D_s	1.682	meter	1.700	meter
l_i	0.495	meter	0.609	meter
b_4	0.356	meter	0.360	meter
l_a	0.317	meter	0.337	meter
g_a	0.247	meter	0.158	meter
δ	0.000	degree	0.000	degree

2.1.6 Main parametrization of Raabe

Up to this point, all the parametrization methodologies explained use peripheral velocity coefficient, velocity ratio or pressure ratio in order to calculate runner design diameter. Nevertheless, Raabe introduces a new term called unit speed in rpm (n_{11}) and gets benefit from it to determine the diameter corresponds to the point where leading edge touches to the shroud (D in Equation (2.23)). Determination of unit speed and other geometrical parameters of runner is done with the linear interpolation of the values presented in a table established by Raabe. He provides main parameters for various n_q numbers and advices to use linear interpolation if one has a turbine whose specific speed is in between these values. This table and geometrical parameter definition of Raabe is presented in Figure 2.9.

$$D = n_{11} * \frac{\sqrt{H_{net}}}{n} \quad (2.23)$$

First thing which can be noticed in Table 2.7 is that the maximum head recommended by Raabe is much higher than other references. Moreover, higher values can also be seen in diameters suggested by him. However, Raabe provides smaller value for the distance between trailing edges of guide vanes in meridional view than Thomann, but this recommendation is still higher than the actual dimension.



n_1	rpm	17	29	43	57	70	85	100
max H	m	700	520	300	180	120	80	64
$Q_{11 \ 1/1}$	m^3/s	0,123	0,230	0,466	0,715	0,948	1,166	1,280
n_{11}	rpm	61	62,5	65,3	70	75,5	82,5	92,2
max n_{11}	rpm	106	107	117	131	146	161	180
$Q_{11 \ 1}/Q_{11 \ 1/1}$		0,81	0,81	0,82	0,84	0,87	0,88	0,88
$\eta_{i \ 2}$		0,88	0,885	0,90	0,905	0,905	0,905	0,90
$\eta_{i \ 1/1}$		0,845	0,855	0,87	0,88	0,885	0,88	0,875
$c_{1 \ 1}^2/2gH$		0,024	0,033	0,049	0,065	0,082	0,098	0,115
ϵ		0,045	0,055	0,075	0,1	0,14	0,195	0,27
D_{2i}/D		1,0	1,0	0,98	0,92	0,85	0,775	0,695
D_3/D		1,04	1,052	1,054	1,02	1,03	1,03	0,99
D_s/D		0,6	0,68	0,825	0,955	1,06	1,12	1,15
b_3/D		0,055	0,1	0,167	0,23	0,288	0,326	0,327
l_j/D		0,36	0,32	0,28	0,26	0,25	0,26	0,28
l_a/D		0,27	0,22	0,17	0,14	0,13	0,14	0,15

Figure 2.9 : Correlation of parameters for runner (Raabe), adapted from [52].

Table 2.7 : Geometrical and hydraulic parameters of Raabe for runner.

Designation of Dimensions (based on Figure 2.9)	Raabe Recommendation		Actual Situation in Kadincik I HPP	
	Value	Unit	Value	Unit
n_{11}	64.500	rpm	-	rpm
H_{max}	362.000	meter	194.000	meter
D	2.107	meter	1.975	meter
D_{2i}	2.077	meter	1.840	meter
D_3	2.219	meter	2.000	meter
D_s	1.652	meter	1.700	meter
b_3	0.312	meter	0.360	meter
l_i	0.611	meter	0.609	meter
l_a	0.379	meter	0.337	meter

2.1.7 Main parametrization of Chapallaz

In Figure 2.9, Raabe gives a range for n_{11} , which is utilized for the calculation of runner inlet diameter, from 61 to 92.2 rpm. On the other hand, Chapallaz [50] uses almost the same formula, Equation (2.23), but to obtain diameter corresponds to the point where leading edge touches to the hub (D_{li} in Figure 2.10 - Equation (2.24)). Instead of n_{11} he yields a constant in the calculation of his runner design diameter.

Furthermore, he suggests another formula for runner discharge diameter, Equation (2.25). Finally, with the help of the three figures he provided for different n_q numbers (Figure 2.10), he recommends making linear interpolation to find out guide vane height and the diameter corresponds to the point where leading edge touches to the shroud.

$$D_{1i} = 64.4 * \frac{\sqrt{H_{net}}}{n} \quad (2.24)$$

$$D_{2e} = 4.44 * \left(\frac{Q_{max}}{n}\right)^{1/3} \quad (2.25)$$

Chapallaz provides only four geometrical parameters for turbine and all belong to runner. He predicts the longer blade profiles at the inlet close to the hub than the actual blade geometry of Kadincik I HPP. Other dimensions have a good conformity as it is seen in Table 2.8.

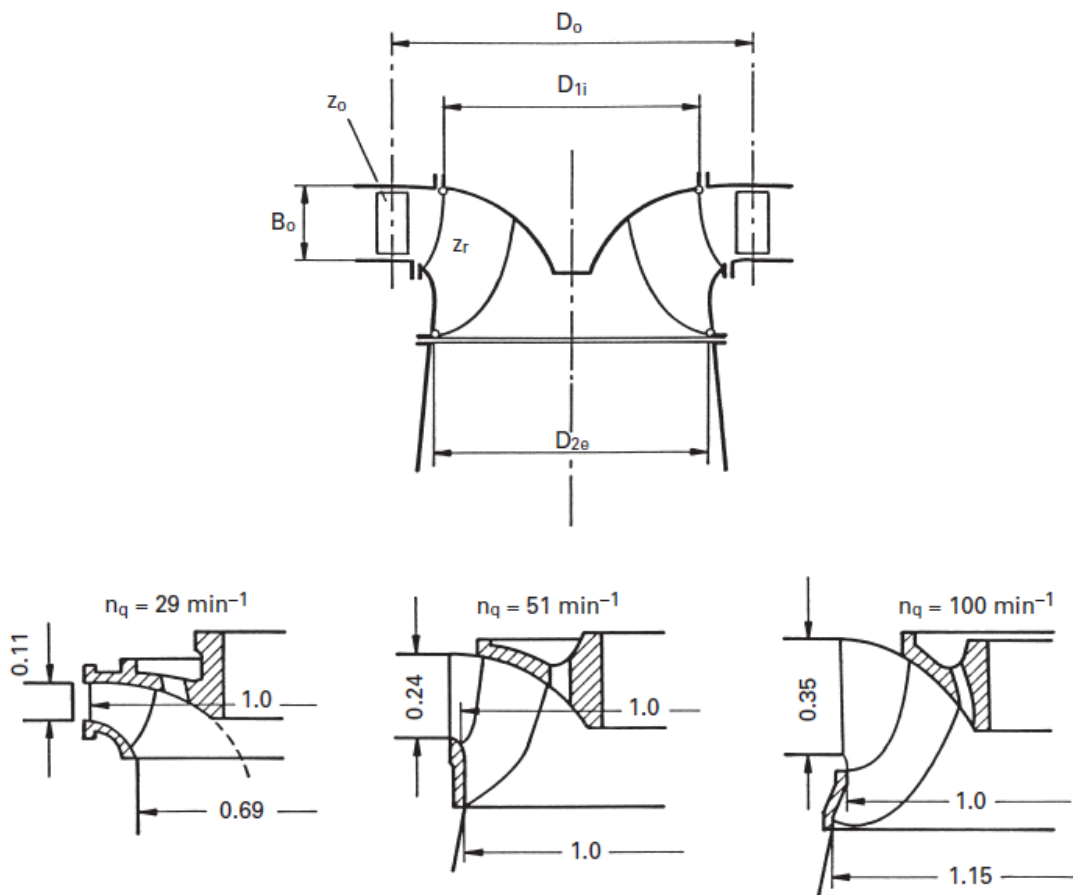


Figure 2.10 : Correlation of parameters for runner (Chapallaz), adapted from [50].

Table 2.8 : Geometrical and hydraulic parameters of Chapallaz for runner.

Designation of Dimensions (based on Figure 2.10)	Chapallaz Recommendation		Actual Situation in Kadincik I HPP	
	Value	Unit	Value	Unit
D _{1i}	2.104	meter	1.840	meter
D _{2e}	1.722	meter	1.700	meter
D _{2i}	2.075	meter	1.975	meter
b _o	0.353	meter	0.360	meter

2.1.8 Main parametrization of Bovet

Bovet establishes a full design guideline for Francis turbine runner, starting from main parametrization to 3D blade profile generation. He utilizes the non-dimensional form of the specific speed, Equation (2.3), and states that turbines with n_s between 0.1 and 0.8 can be chosen as Francis type. Bovet takes the runner outlet diameter as base and calculates it with Equation (2.26). In this formula, v_{2e} corresponds to specific discharge, which represents the peak point of the efficiency vs flowrate plot. Bovet states that this value should be in between 0.26 and 0.275 according to his experience. He also believes that specific discharge can be considered as independent from the specific speed. In the design of a Francis turbine, he prefers to choose this value as 0.27. Another critical dimension for Bovet is R_{1i} (Figure 2.11), which is obtained with Equation (2.27). In this formula, he gets benefit from a term called as specific head (h_{1i}). He claims that h_{1i} is also independent from specific speed and should vary between 1.65 and 1.8. Although there may be some extreme cases like $h_{1i}=2.0$, recent experiences of Bovet shows that specific head can be assumed as 1.72 for Francis turbines. Other parameters in Figure 2.11 are correlated only with non-dimensional specific speed and runner discharge diameter (Equations (2.28) to (2.36)).

$$R_{2e} = \left(\frac{Q_{\max}}{\pi * \omega * v_{2e}} \right)^{1/3} \quad (2.26)$$

$$R_{1i} = \sqrt{\frac{2 * g * H_{\text{net}}}{\omega^2 * h_{1i}}} \quad (2.27)$$

$$B_o = [0.8 * (2 - n_s) * n_s] * R_{2e} \quad (2.28)$$

$$R_{oi} = Y_{mi} = \left(0.7 + \frac{0.16}{n_s + 0.08} \right) * R_{2e} \quad (2.29)$$

$$R_{oe} = \left(\frac{0.493}{(n_s)^{2/3}} \right) * R_{2e} \quad (2.30)$$

$$\frac{L_i}{4} = [3.2 + 3.2 * (2 - n_s) * n_s] * \frac{R_{2e}}{4} \quad (2.31)$$

$$L_e = [2.4 - 1.9 * (2 - n_s) * n_s] * R_{2e} \quad (2.32)$$

$$X_{2e} = 0.5 * R_{2e} \quad (2.33)$$

$$Y_{2e} = [0.255 - 0.3 * n_s] * R_{2e} \quad (2.34)$$

$$Y_{me} = \frac{Y_{2e}}{3.08 * \left(1 - \frac{X_{2e}}{L_e}\right) * \sqrt{\frac{X_{2e}}{L_e} * \left(1 - \frac{X_{2e}}{L_e}\right)}} \quad (2.35)$$

$$R_{me} = R_{oe} - Y_{me} \quad (2.36)$$

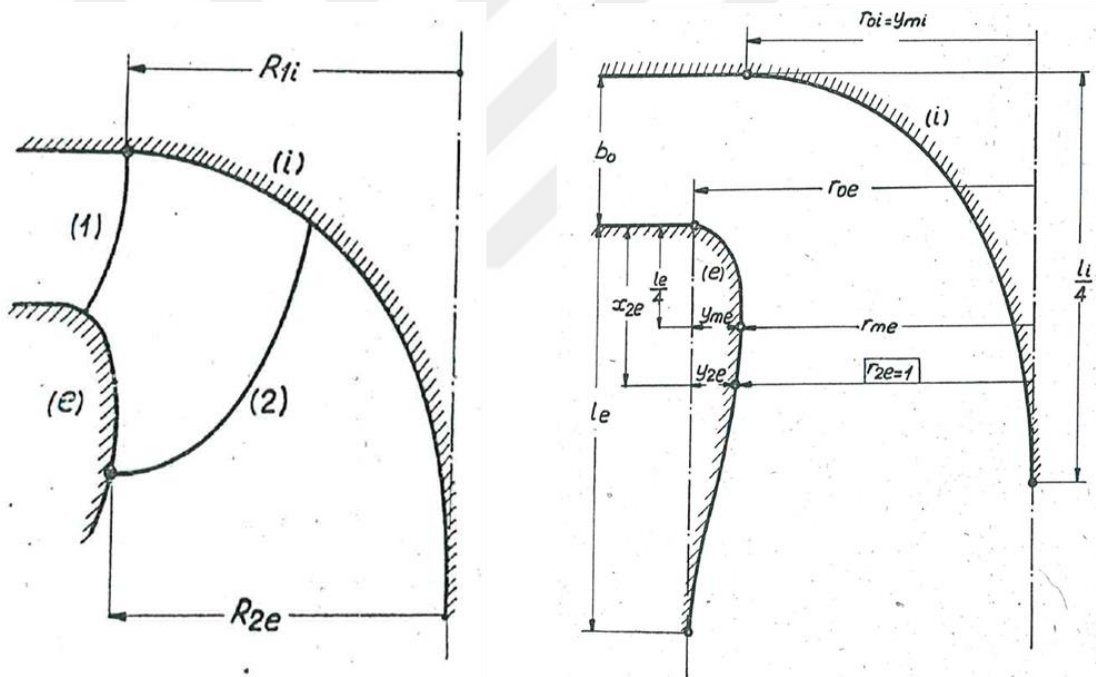


Figure 2.11 : Geometrical parameter definition of Bovet for runner, adapted from [55].

Main parametrization of Bovet is commonly applied in literature. For instance, Morales [57] wrote a code to design runner based on the information provided by Bovet. Furthermore, Bovet suggests two formulas for hub and shroud contours in meridional view (Equations (2.37) and (2.38)). However, these equations are not preferred in today's designs. Instead, an arc of a circle which passes all the points determined during parametrization is fitted for crown and band [48]. Table 2.9

compares the recommendations of Bovet on geometrical parameters with the actual dimensions of Kadincik I HPP. Except from the $L_i/4$ and L_e values, dimensions show similarity with recommendation. As it can be noticed from Figure 2.11 and Table 2.9, Bovet suggests more extended hub and shroud contour than other authors. Most of the designers think that the portion of the shroud after the runner outlet diameter should be included in draft tube domain and hub contour is cut with a cone before it touches to rotation axis. Therefore, the information on hub and shroud contours provided by Bovet is not got enough credit.

$$Y_i = \left[3.08 * \left(1 - \frac{X_i}{L_i} \right) * \sqrt{\frac{X_i}{L_i} * \left(1 - \frac{X_i}{L_i} \right)} \right] * Y_{mi} \quad (2.37)$$

$$Y_e = \left[3.08 * \left(1 - \frac{X_e}{L_e} \right) * \sqrt{\frac{X_e}{L_e} * \left(1 - \frac{X_e}{L_e} \right)} \right] * Y_{me} \quad (2.38)$$

Table 2.9 : Geometrical parameters of Bovet for runner.

Designation of Dimension (based on Figure 2.11)	Bovet Recommendation		Actual Situation in Kadincik I HPP	
	Value	Unit	Value	Unit
v_{2e}	0.270	-	-	-
h_{1i}	1.720	-	-	-
R_{2e}	0.869	meter	0.850	meter
R_{1i}	1.053	meter	0.908	meter
B_o	0.314	meter	0.360	meter
$R_{oi} = Y_{mi}$	1.018	meter	0.920	meter
R_{oe}	1.054	meter	0.988	meter
$L_i/4$	1.009	meter	0.505	meter
L_e	1.341	meter	1.962	meter
X_{2e}	0.435	meter	0.337	meter
Y_{2e}	0.185	meter	0.138	meter
Y_{me}	0.190	meter	0.137	meter
R_{me}	0.864	meter	0.851	meter

After the determination of the main dimensions, Bovet advice to draw 2D-streamlines in meridional view. In 1963s technology, he drew the streamlines in paper with the help of the principle that same amount of water should pass between each streamlines. Miloş [56] followed the same design methodology in his paper but he utilized FEM to find out the streamlines in 2004. And, in 2007, Razavi [58] repeated the same procedure with FDM.

2.1.9 General main parametrization

Up to this point, numerous main parametrization approaches are listed above. All authors use their special designations for dimensions and this can cause confusion while comparing the recommendations with each other. Therefore, all parametrization methodologies are summarized in Table 2.10 together with the actual dimensions of Kadincik I HPP. Figure 2.12 is taken as a reference to specify the symbols of the dimensions. Moreover, an average is calculated for each value by taking available recommendations into account.

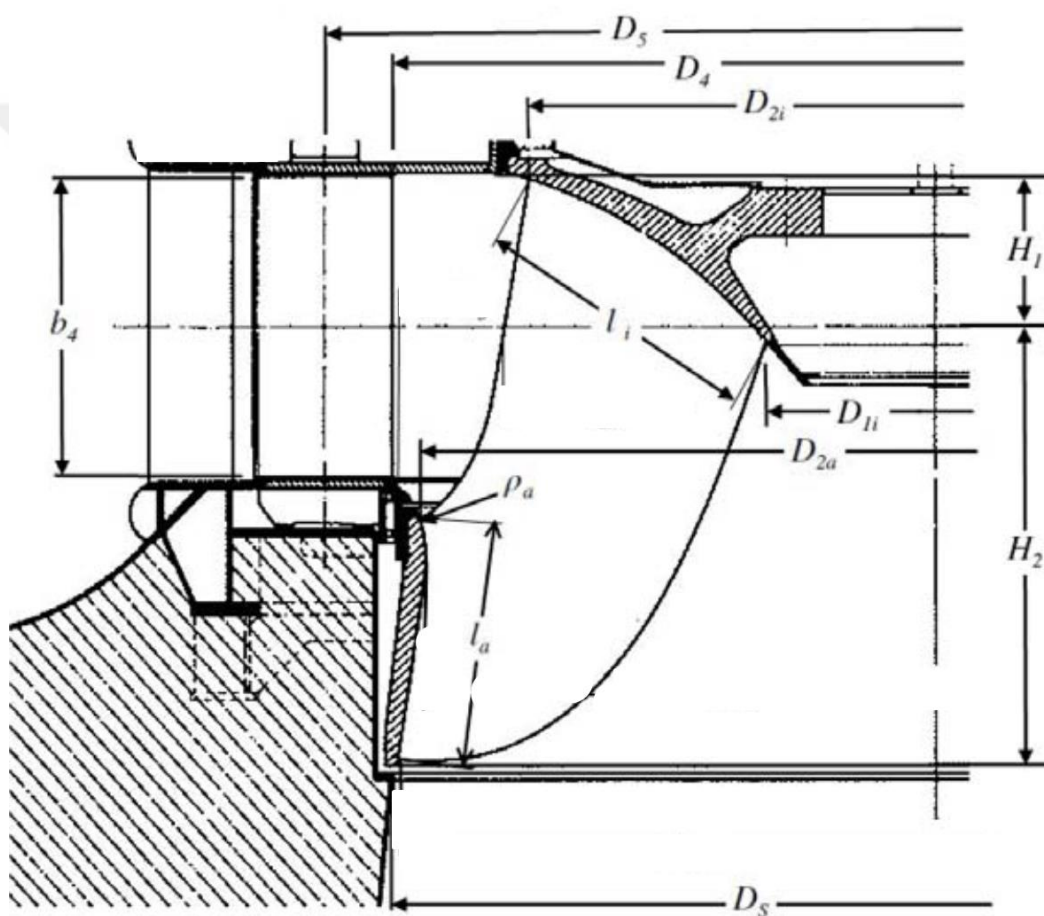


Figure 2.12 : Designation of main parameters of runner for Table 2.10, adapted from [63].

As it is seen in Table 2.10, hydraulic shape of the Kadincik I HPP runner is quite proper for its specific speed. Although recommendation of Raabe on maximum net head is so far away from the other design suggestions and therefore its reliability is low, Kadincik I HPP may still have problems in design head and flowrate. Furthermore, Table 2.10 gives a chance to conclude that there is no main

parametrization that provides all the information necessary for determination of the meridional shape of the runner. One can even get benefit from various methodologies on runner parametrization at the same time, but there will still exist unknown geometrical dimensions. Besides, all these parameters depend on the empirical correlations; therefore, it is hard to say the parameters listed in Table 2.10 are 100 % exact. Therefore, CFD can help to find out the optimum dimensions. In fact, preliminary design can start with the averages of the recommendations explained above and then parameters can be adjusted further with the help of the CFD analyses.

2.1.10 Determination of blade angles and profiles of runner

Before passing to the CFD modelling, blade angles and thickness distribution should be decided. Gjøsæter [64] states that outlet blade angle (β_2) usually varies between 15 and 22 degrees according to the experiences of Brekke [65]. Nonetheless, blade angles can be determined from velocity triangles more precisely. From Figure 2.13, the dependency of blade angles (β) on meridional velocity (c_m), peripheral velocity (u), circumferential velocity (c_u), relative velocity (w) and absolute velocity (c) can be seen. With the help of the predetermined geometrical dimensions in Table 2.10, these velocity values can be calculated (Equations (2.39) - (2.48)). Subsequently, Figure 2.13 gives us various alternatives to find out inlet and outlet blade angles. In these calculations, it is important to notice that no remaining swirl is assumed at the outlet of the runner; consequently, c_u at the outlet should be taken as zero. Another assumption is made during the calculation of inlet angular momentum. In Equation (2.43), circumference hydraulic efficiency (η_u) is assumed as 0.96 which is a commonly preferred value for the runner [64]. Moreover, in good designs, it is desired to have constant c_m distribution along to blade in streamwise direction. As a result, c_m at the outlet is chosen same as the one at the inlet (Equation (2.40)). For the designations used in Equations (2.39) - (2.50), 1 refers to runner inlet whereas 2 represents the runner outlet.

Table 2.10 : Main parameters of various scientists for runner of Kadincik I HPP.

Main Parameters (based on Figure 2.12)	De Siervo and De Leva	US Department of IBR	Giesecke and Leeb	Schweiger and Gregori	Thomann	Raabe	Chapallaz	Bovet	Average	Actual Values of Kadincik I HPP	Unit
H_{max}	-	-	-	-	185.000	362.000	-	-	273.500	194.000	m
Q_{opt}	-	-	-	-	21.000	-	-	-	21.000	21.000	m ³ /s
D_s	1.740	1.468	1.606	1.609	1.682	1.652	1.722	1.738	1.652	1.700	m
D_{2a}	1.725	1.908	1.934	2.003	1.979	2.107	2.075	2.108	1.980	1.975	m
D_{1i}	-	-	1.064	-	-	-	-	-	1.064	0.867	m
D_{2i}	1.979	1.835	1.934	-	1.919	2.077	2.104	2.107	1.994	1.840	m
D_4	-	-	-	-	2.572	2.219	-	-	2.396	2.000	m
D_5	2.658	2.202	-	2.383	-	-	-	-	2.414	2.300	m
b_4	0.319	0.264	0.339	0.301	0.356	0.312	0.353	0.314	0.320	0.360	m
H_1	0.219	-	-	-	-	-	-	-	0.219	0.220	m
H_2	0.581	-	-	-	-	-	-	0.592	0.586	0.565	m
l_i	-	-	-	-	0.495	0.611	-	-	0.553	0.609	m
l_a	-	-	-	-	0.317	0.379	-	-	0.348	0.377	m
ρ_a	-	-	-	-	0.247	-	-	-	0.247	0.158	degree

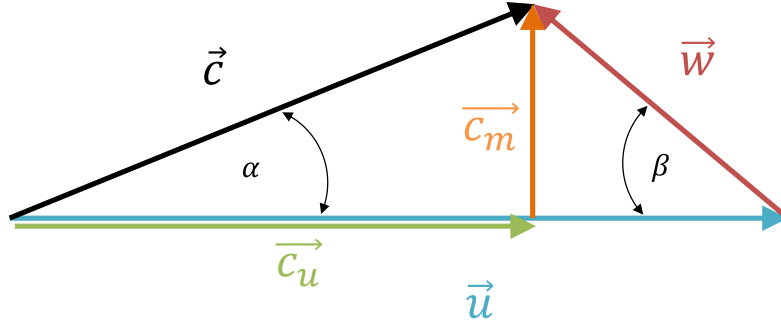


Figure 2.13 : Velocity angle in Francis turbine.

$$c_{m1} = \frac{Q_{opt}}{D_{LE} * \pi * b_4} \quad (2.39)$$

$$c_{m2} = c_{m1} \quad (2.40)$$

$$u_1 = \frac{D_{LE} * \omega}{2} \quad (2.41)$$

$$u_2 = \frac{D_{TE} * \omega}{2} \quad (2.42)$$

$$c_{u1} = \frac{H_{net} * \eta_u * g}{u_1} \quad (2.43)$$

$$c_{u2} = 0 \quad (2.44)$$

$$w_1 = \sqrt{c_{m1}^2 + (u_1 - c_{u1})^2} \quad (2.45)$$

$$w_2 = \sqrt{c_{m2}^2 + u_2^2} \quad (2.46)$$

$$c_1 = \sqrt{c_{m1}^2 + c_{u1}^2} \quad (2.47)$$

$$c_2 = \sqrt{c_{m2}^2 + c_{u2}^2} \quad (2.48)$$

$$\beta_1 = \tan^{-1} \left(\frac{c_{m1}}{u_1 - c_{u1}} \right) \quad (2.49)$$

$$\beta_2 = \tan^{-1} \left(\frac{c_{m2}}{u_2 - c_{u2}} \right) \quad (2.50)$$

As it is observed in Table 2.10, position of the leading and trailing edges according to the rotation axis is not same along the blade span. Therefore, blade should be divided into sections from zero span (hub) to 100 % span (shroud) and the formulas above should be applied to all sections. This study was conducted for Kadincik I HPP and results are shown in Table 2.11. The values recommended in Table 2.11 and the actual ones shown in Figure 2.14 are quite different than each other.

Although Table 2.11 does not reflect the exact blade angle definition which should be utilized in the blade, it can be stated that Kadincik I HPP has some problems with blade angles. Of course, final decision about this issue will be made according to results of the CFD analyses. However, at this point, it should be stated that outlet blade angle has a great effect on turbine performance and needs to be decided very carefully [54].

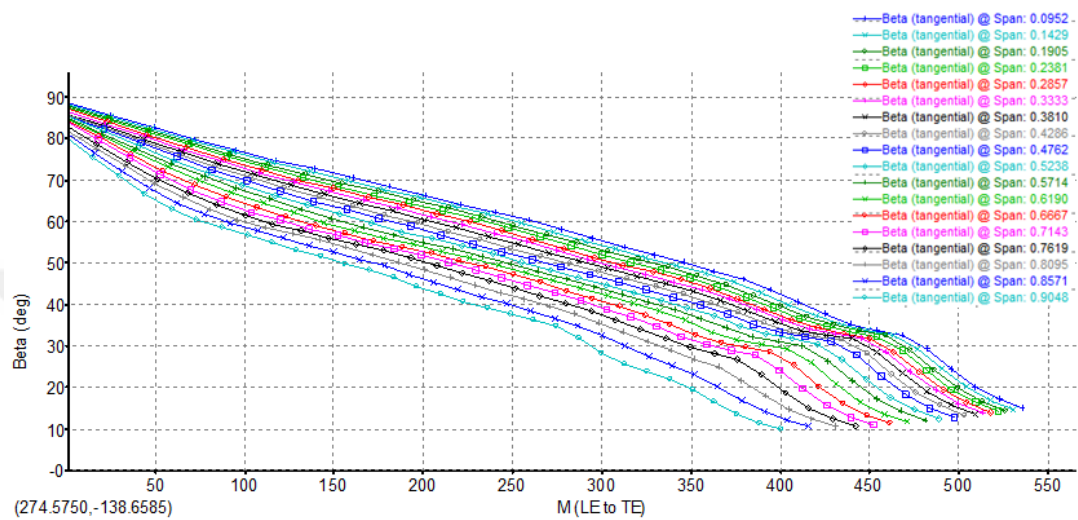


Figure 2.14 : Blade angle distribution of Kadincik I HPP.

After finding out the inlet and outlet blade angles, linear distribution of betas in between can be a good option for starting point of the runner design. Subsequently, blade angles are modified according to flow condition at best efficiency point with the help of the CFD. Nonetheless, blade thickness distribution is another issue needed to be discussed before starting CFD analyses. Although there are some recommended formulas for blade thickness distribution in old books, 4- or 6-digit NACA-profiles are preferred in today's designs [56] [63]. Number of the blades depends on both runner blade thickness distribution and number of the guide vanes. It is usually chosen as odd number, most frequently 13, 15 and 17. Moreover, division of number of the runner blades with the number of the guide vanes should be as far from an integer as possible to minimize the extent of the pressure pulsations which occur when the runner blades pass the guide vanes [64]. Final thickness distribution decision should be made after FSI analyses. Lastly, Norwegian University of Science and Technology suggests the shape of the leading and trailing edge shown in Figure 2.15, especially the trailing edge shape is chosen for minimizing the amplitude of von Karman vortices [64].

Table 2.11 : Calculated velocities and blade angles for Kadincik I HPP.

Span	D_{LE}	D_{TE}	c_{m1}	c_{m2}	u₁	u₂	c_{u1}	c_{u2}	w₁	w₂	c₁	c₂	β₁	β₂
[-]	[m]	[m]	[m/s]	[m/s]	[m/s]	[m/s]	[m/s]	[m/s]	[m/s]	[m/s]	[m/s]	[m/s]	[°]	[°]
0.00	1.84	0.87	10.81	10.81	41.29	19.46	41.28	0.00	10.81	22.26	42.67	10.81	89.94	29.06
0.17	1.86	1.01	10.69	10.69	41.80	22.57	40.78	0.00	10.74	24.98	42.16	10.69	84.58	25.34
0.33	1.89	1.14	10.57	10.57	42.30	25.69	40.30	0.00	10.75	27.78	41.66	10.57	79.25	22.36
0.50	1.91	1.28	10.44	10.44	42.81	28.80	39.82	0.00	10.86	30.64	41.17	10.44	74.04	19.93
0.67	1.93	1.42	10.32	10.32	43.31	31.92	39.36	0.00	11.05	33.55	40.69	10.32	69.03	17.92
0.83	1.95	1.56	10.20	10.20	43.82	35.03	38.90	0.00	11.32	36.49	40.22	10.20	64.27	16.23
1.00	1.98	1.70	10.07	10.07	44.32	38.15	38.46	0.00	11.65	39.46	39.76	10.07	59.80	14.79

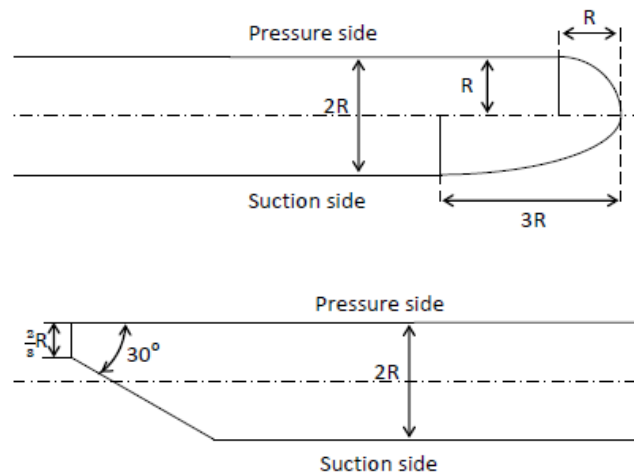


Figure 2.15 : Leading (top) and trailing (bottom) edge geometries, adapted from [64].

2.1.11 X – Blade technology

Apart from the outlet blade angle, blade leaning is also one of the most important parameters to homogenize the runner blade pressure [66]. Blade leaning angle is defined as the angle normal to the flow direction, i.e. leaning to a runner blade can be established by tilting the vertical inlet [67]. After many researches on the leaning angle, in the beginning of 1982, hydraulic shape of Francis turbine with reversed leading edge was introduced and patented (US 4479757) by GE Hydro (Figure 2.16 - left). For many years, this technology had been tried to be improved. And, in 1998, during the development of the Three Gorges Project in China, X-Blade Technology came up and has been patented (no. 19963261) [68].

X-Blade design and conventional design differ from each other in meridional view (Figure 2.16 – Right). X-Blade has larger angular extension at the outlet (6), at least 15° , than one at the inlet (5). Ratio between the diameter at the attachment point of the trailing edge at the hub (D_d) and at shroud (D_b) is generally between 0.3 - 0.4. Intersection of trailing edge with hub (D) is in a lower location than the middle point of leading edge (15). Furthermore, X-Blade design has negative inlet lean angle and skewed outlet whereas conventional blades have positive inlet blade lean. This special shape brings some advantages to X-Blade Technology. First of all, X-Blades have higher efficiencies at all operation points than conventional designs [69]. If the runner is operating under wide variety of head and flow rate, then this ability becomes much more significant. Second contribution of X-Blade to Francis turbine is more uniform flow distribution in the runner. One of the typical problems of

conventional design is high velocities in the flow near the hub, which cause low pressure areas and therefore cavitation, secondary flows and sand erosion. As a result of this fact, inlet cavitation erosion on the suction side close to hub is commonly encountered in conventional designs. With CFD and model test, it is proved that this is eliminated with X-Blade Design (Figure 2.17 and Figure 2.18). Thirdly, wider range of stability can be achieved in X-Blades, i.e. runner can operate in different operation conditions without undergoing critical inter blade vortices, inlet cavitation or draft tube pressure pulsation phenomena. In fact, X-Blade design lowers the draft tube pressure pulsation level because it has a skewed outlet and smaller outlet diameter at hub. Moreover, thanks to its less curved and less complicated hydraulic shape, X-Blades are easier to manufacture [68] [70]. Due to all these advantages of this new design methodology, X-Blade technology is commonly preferred in today's Francis turbine designs.

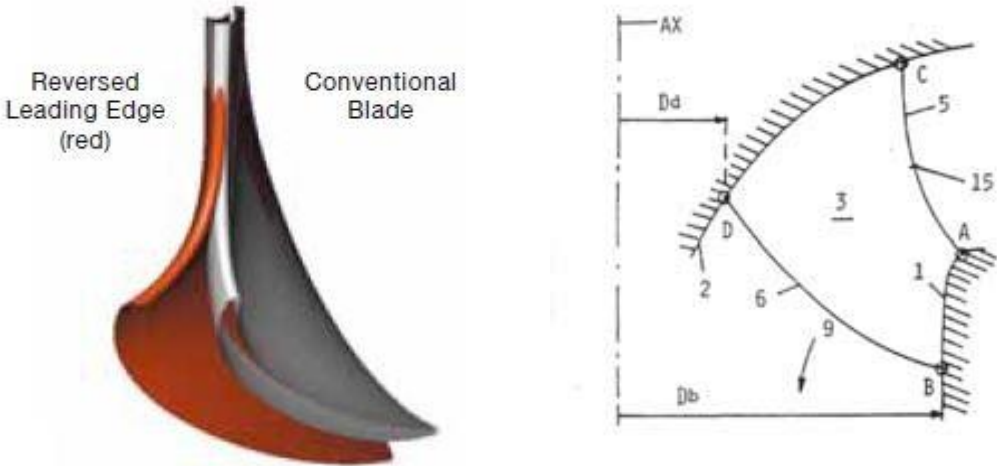


Figure 2.16 : Reversed leading edge geometry (Left) – meridional view of X-Blade (Right), adapted from [68].

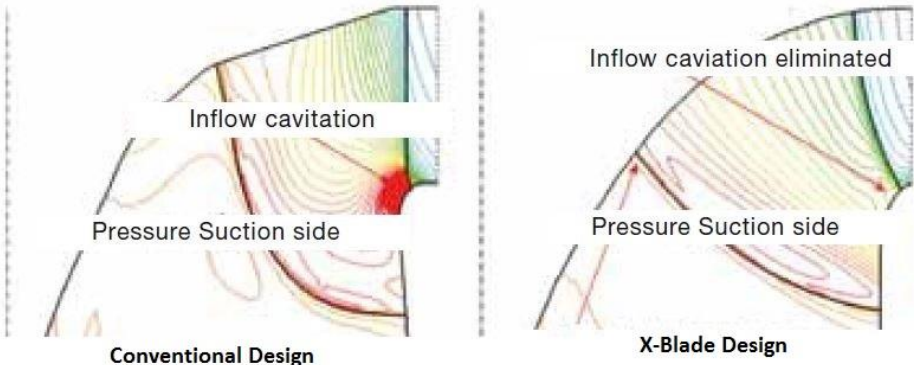


Figure 2.17 : Inlet cavitation erosion in conventional design, adapted from [70].

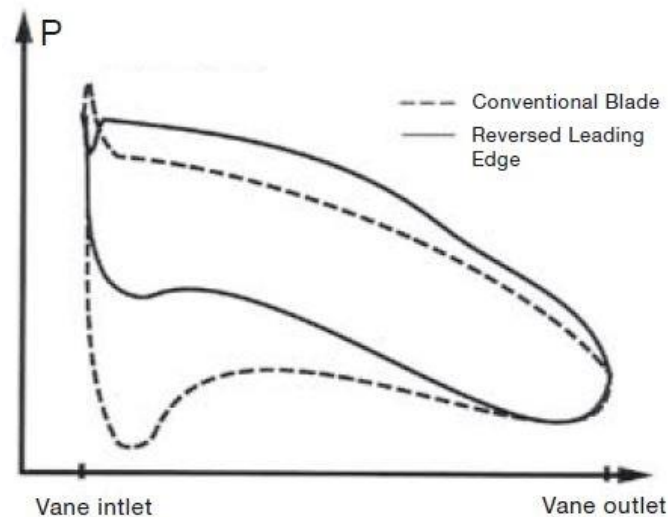


Figure 2.18 : Pressure distribution along the runner, adapted from [70].

2.2 Design of the Draft Tube

Draft tube is the mechanical component of a Francis turbine, whose responsibility is to detract water from runner. It is an essential feature because it has a great influence on the turbine peak efficiency, energy output and cavitation performance. Like runner, its design also starts with determination of main parameters. Most of the scientists correlate draft tube parameters with runner discharge diameter.

2.2.1 Main parametrization of De Siervo and De Leva

To begin with, recommendations of De Siervo and De Leva are still commonly benefitted by many designers. They made the draft tube dimensions dependent on runner discharge diameter, Equation (2.8), and specific speed, Equation (2.4). Designation of the parameters is shown in Figure 2.19. Corresponding formulas can be found in Equations (2.51) - (2.60).

Draft tube of Kadincik I HPP is not directly comparable with the recommended draft tube geometry of De Siervo and De Leva because they proposed a design which separated into two parts after the elbow (Figure 2.19). On the other hand, this kind of a separation is not seen in Kadincik I. In other words, U and V parameters do not exist in this hydropower plant. When the other parameters are compared (Table 2.12), it is seen that cross sectional parameters are conformable with real dimensions. Nevertheless, same sentences cannot be established for lengths. Whereas the vertical length of the actual design is considerably smaller than the De Siervo and De Leva's

recommendation, horizontal length is too high for the same main parametrization. It should be noted that longer draft tubes means higher friction losses.

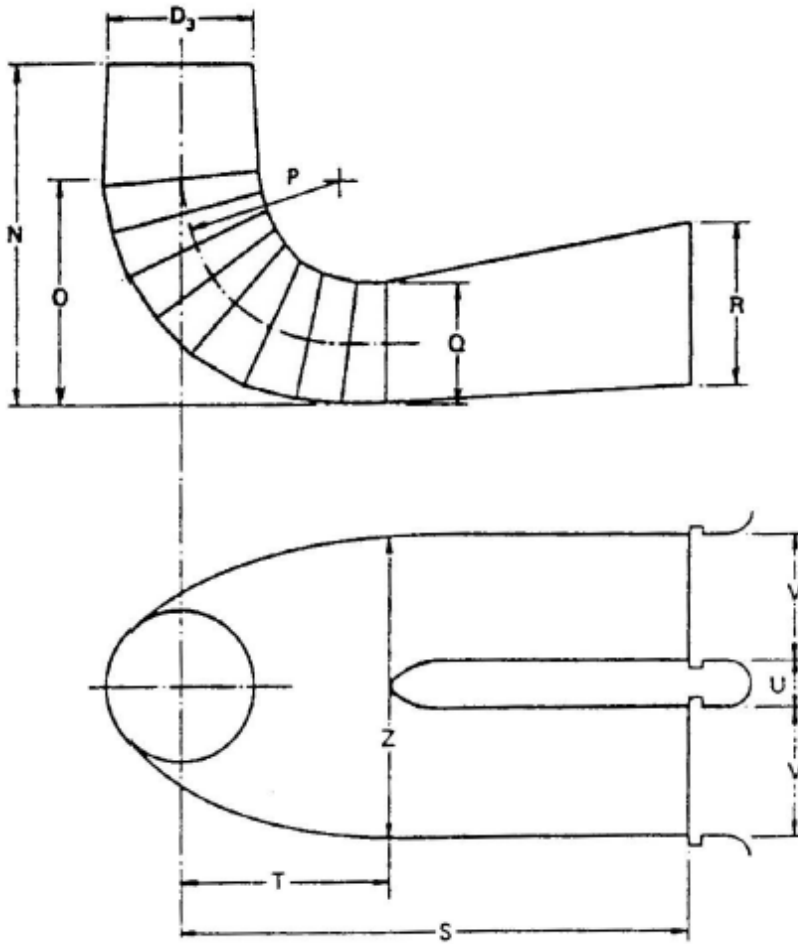


Figure 2.19 : Geometrical parameter definition of De Siervo and De Leva for draft tube, adapted from [59].

$$N = \left(1.54 + \frac{203.5}{n_s}\right) * D_3 \quad (2.51)$$

$$O = \left(0.83 + \frac{140.7}{n_s}\right) * D_3 \quad (2.52)$$

$$P = (1.37 - 0.00056 * n_s) * D_3 \quad (2.53)$$

$$Q = \left(0.58 + \frac{22.6}{n_s}\right) * D_3 \quad (2.54)$$

$$R = \left(1.6 - \frac{0.0013}{n_s}\right) * D_3 \quad (2.55)$$

$$S = \left(\frac{n_s}{-9.28 + 0.25 * n_s}\right) * D_3 \quad (2.56)$$

$$T = (1.50 + 0.00019 * n_s) * D_3 \quad (2.57)$$

$$U = (0.51 - 0.0007 * n_s) * D_3 \quad (2.58)$$

$$V = \left(1.10 + \frac{53.7}{n_s}\right) * D_3 \quad (2.59)$$

$$Z = \left(2.63 + \frac{33.8}{n_s}\right) * D_3 \quad (2.60)$$

Table 2.12 : Geometrical parameters of De Siervo and De Leva for draft tube.

Designation of Dimension (based on Figure 2.19)	De Siervo and De Leva Recommendation		Actual Situation in Kadincik I HPP	
	Value	Unit	Value	Unit
N	5.442	meter	3.605	meter
O	3.354	meter	2.028	meter
P	2.259	meter	2.062	meter
Q	1.316	meter	1.040	meter
R	2.784	meter	2.410	meter
S	9.798	meter	14.320	meter
T	2.652	meter	3.150	meter
U	0.731	meter	-	meter
V	2.643	meter	-	meter
Z	5.035	meter	4.450	meter

2.2.2 Main parametrization of United States Department of the Interior Bureau of Reclamation

United States Department of the Interior Bureau of Reclamation has made similar recommendations about draft tube together with runner. While it utilizes the runner discharge diameter to calculate runner parameters, another dimension called design diameter of draft tube (D_4) is introduced for the determination of draft tube parameters. In fact, draft tube design diameter is defined as the diameter where draft tube cone ends. United States Department of the Interior Bureau of Reclamation suggests three different draft tube shapes; without pier nose, with one pier nose (like the one in De Siervo and De Leva) and with two pier noses. The one interested for Kadincik I HPP is shown in Figure 2.20 where the ratios of all parameters with respect to the D_4 are also available.

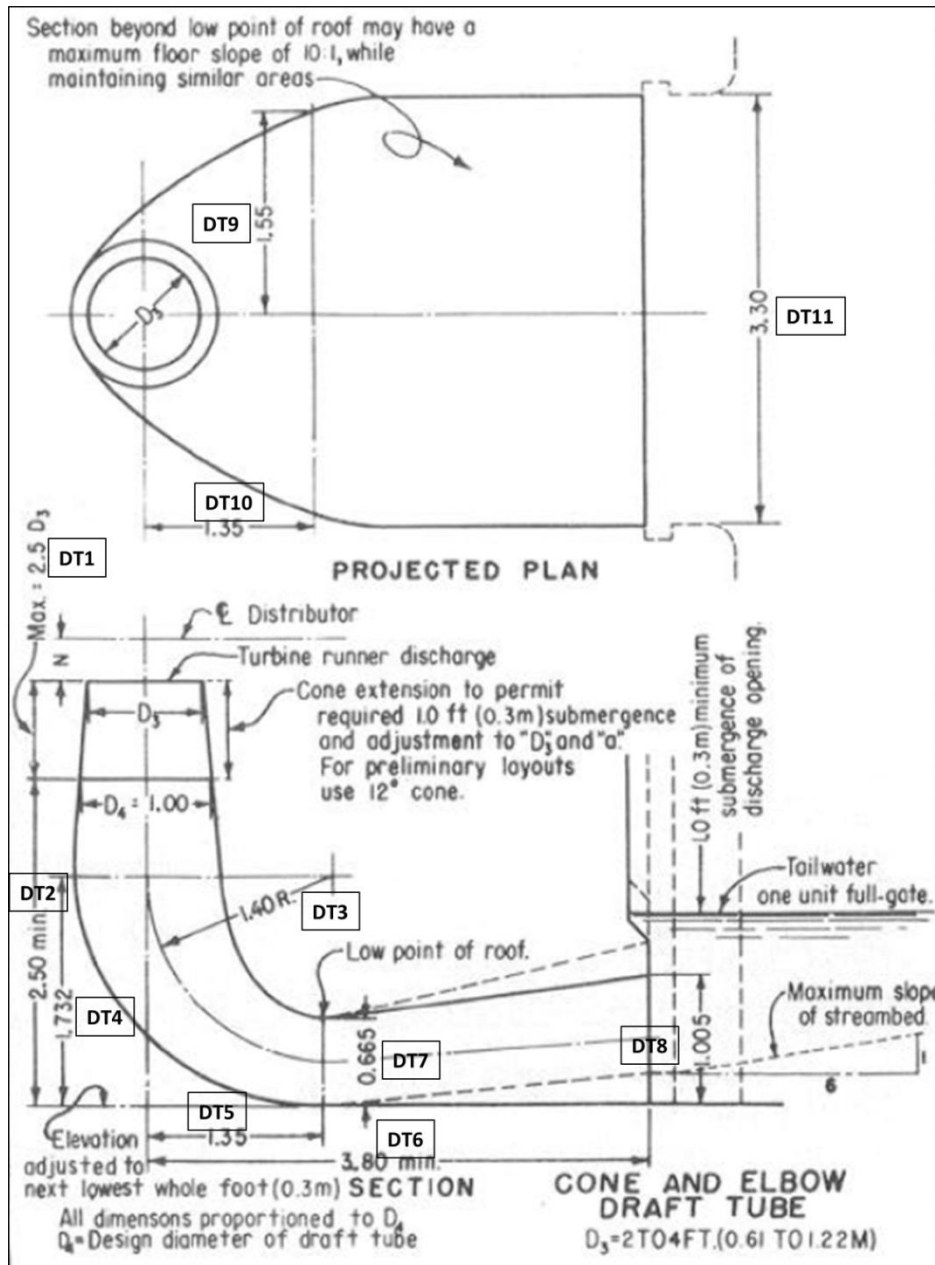


Figure 2.20 : Geometrical parameter definition of United States Department of the Interior Bureau of Reclamation for draft tube, adapted from [46].

Apart from the De Siervo and De Leva, United States Department of the Interior Bureau of Reclamation also gives the information about draft tube cone opening angle and draft tube exit opening angle. According to this parametrization method, draft tube cone opening angle should be chosen as 12 degree which is also supported by Prof. Ayder stating that this angle can be chosen up to 14 degree due to the swirling flow [71]. However, Hydraulic Fluid Machinery Institute of Graz Technical University suggests that 7 degree can be a proper choice for this angle. The determination of this angle is so significant because inception of vortex rope due to

swirling flow occurs in the cone region. Another angle recommended in this parametrization method is the draft tube exit opening angle. A triangle is used for visualization in Figure 2.20. Whereas United States Department of the Interior Bureau of Reclamation defines the maximum of this angle as 9.5 degree, Hydraulic Fluid Machinery Institute of Graz Technical University has experienced that good performances can be attained with a draft tube exit opening angle less than 6 degree. The importance of this angle is coming from the positive pressure gradient in the diffuser, i.e. if this angle is too high, separation is faced around the outlet of the draft tube.

Table 2.13 : Geometrical parameters of United States Department of the Interior Bureau of Reclamation for draft tube.

Designation of Dimension (based on Figure 2.20)	United States Department of the Interior Bureau of Reclamation Recommendation		Actual Situation in Kadincik I HPP	
	Value	Unit	Value	Unit
D ₃	1.468	meter	1.700	meter
DT1	3.670 (max)	meter	1.577	meter
D ₄	2.370	meter	1.950	meter
DT2 = DT4	3.377	meter	2.028	meter
DT3	2.730	meter	2.062	meter
DT5	2.633	meter	3.150	meter
DT6	7.410 (min)	meter	14.320	meter
DT7	1.297	meter	1.040	meter
DT8	1.960	meter	2.410	meter
DT9	3.023	meter	1.950	meter
DT10	2.633	meter	3.150	meter
DT11	6.435	meter	4.450	meter
Cone Opening Angle	12	degree	4.39	degree
Exit Opening Angle	9.5 (max)	degree	6.95	degree

Before examining the comparison between the geometrical parameter determined by this method and the actual dimensions of Kadincik I HPP (Table 2.13), it should be noted that elbow section of Kadincik I HPP starts immediately after the cone; therefore, DT2 and DT4 dimensions corresponds to same geometrical datum in Kadincik I HPP. Table 2.13 also indicates that draft tube of Kadincik I is too long to perform efficiently, but different than the De Siervo and De Leva, cross sectional parameters does not have any consistency, either. In brief, it is hard to say that

Kadincik I HPP obeys the recommendation of United States Department of the Interior Bureau of Reclamation for draft tube.

2.2.3 Main parametrization of Lugaresi and Massa

Lugaresi and Massa are the scientists that also made some researches to establish empirical correlations for runner outlet diameter and some draft tube parameters. They use their specific speed definition, which depends only on net head, Equation (2.6). In order to decide the runner outlet diameter, they follow the same calculation with Schweiger and Gregori [60] and the formula is shown in Equation (2.61). In the determination of the peripheral velocity coefficient (k_u), they get benefit from Equation (2.62). Subsequently, they proposed empirical correlations for P, Q and Z dimensions (shown in Figure 2.21) which are presented from Equation (2.63) to Equation (2.65).

$$D_3 = \frac{60 * k_u * \sqrt{2 * g * H_{net}}}{\pi * n} \quad (2.61)$$

$$k_u = 0.293 + 0.0081 * n_q \quad (2.62)$$

$$P = 0.4278 + 2.8124 * D_3 \quad (2.63)$$

$$Q = 0.2729 + 0.67 * D_3 \quad (2.64)$$

$$Z = -0.5679 + 2.7409 * D_3 \quad (2.65)$$

Although recommended runner discharge diameter by Lugaresi and Massa is very close to the runner outlet diameter of Kadincik I HPP, parameters for draft tube deviate from the actual values (Table 2.14). Only similarity can be attained in parameter Z, but in the same section width of the tube is predicted so different than the real one which suggests the consistency in Z is only a coincidence. Finally, Lugaresi and Massa gives only limited information about the draft tube that makes the further studies a must, but even these parameters are far away from the actual situation of draft tube.

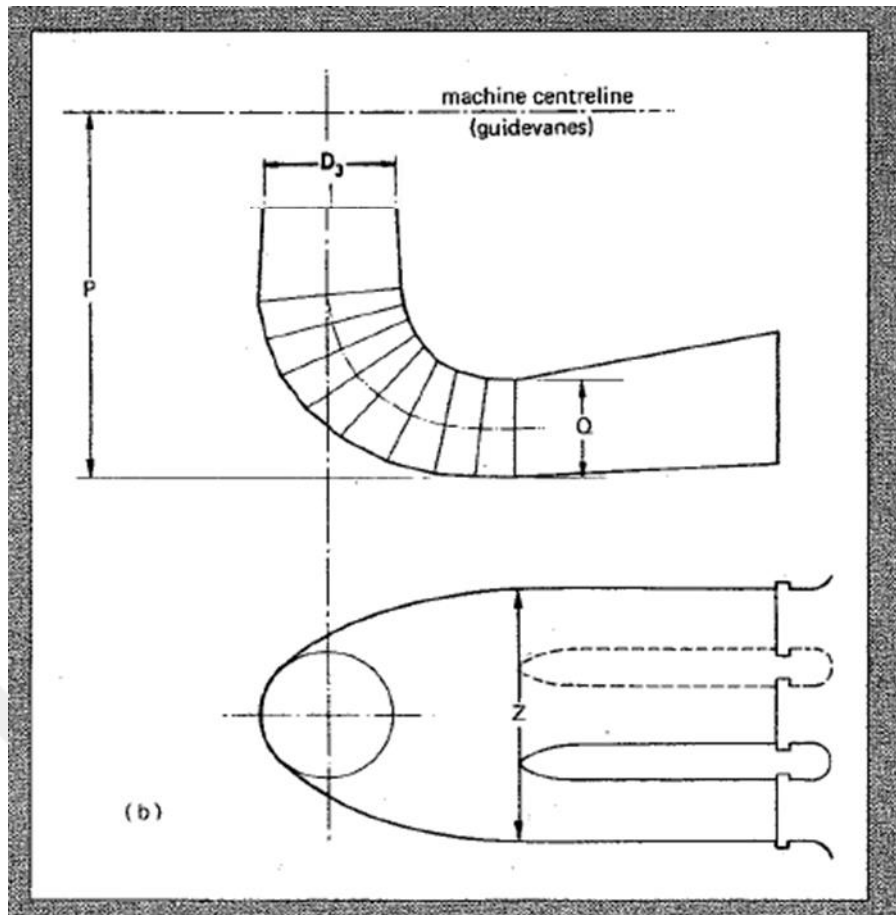


Figure 2.21 : Geometrical parameter definition of Lugaresi and Massa for draft tube, adapted from [61].

Table 2.14 : Geometrical and hydraulic parameters of Lugaresi and Massa for draft tube.

Designation of Dimension (based on Figure 2.21)	Lugaresi and Massa Recommendation		Actual Situation in Kadincik I HEP	
	Value	Unit	Value	Unit
k_u	0.639	-	-	-
D_3	1.767	meter	1.700	meter
P	5.398	meter	3.605	meter
Q	1.457	meter	1.040	meter
Z	4.276	meter	4.450	meter

2.2.4 Main parametrization of Gubin

Gubin published a book for the design of the draft tubes of hydroelectric power plants which contains a lot of beneficial information. His design recommendation for the draft tubes of Francis turbines includes one pier nose, as it is shown in Figure 2.22 together with parameter definition. Moreover, he proposed two curves to find

out guide vane height and runner inlet diameter, where blade touches to the hub (Figure 2.23). In the end, he summarized all the relations between parameters in Figure 2.24. Figure 2.24 is separated for different specific speed ranges. Gubin utilizes the definition of specific speed shown in Equation (2.1) in this classification.

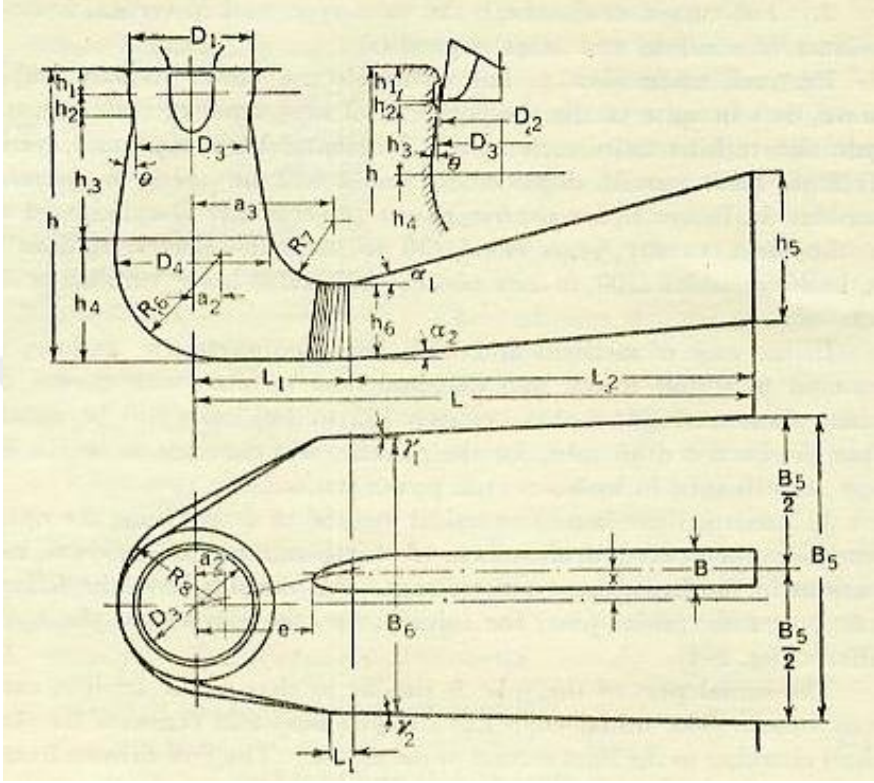


Figure 2.22 : Geometrical parameter definition of Gubin for draft tube, adapted from [47].

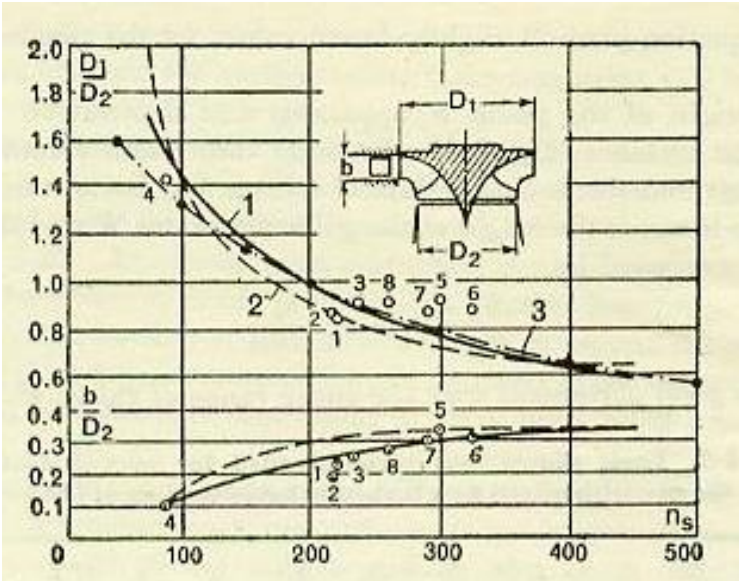


Figure 2.23 : Empirical Correlations between Runner Dimensions (Gubin), adapted from [47].

Type of tube	h/D_1	D_1	h	L	B_5	D_4	h_4	h_6	L_2	h_5	Where used
20	2.3	0.460	1.058	1.610	1.000	0.470	0.470	0.235	0.650	0.431	low specific speeds PO170, PO230, PO310 (runner type PO533, PO246)
		1.000	2.300	3.500	2.170	1.040	1.040	0.510	1.410	0.937	
4E	2.3	0.460	1.058	2.070	1.154	0.568	0.568	0.284	0.773	0.552	medium specific speeds PO115, PO170 (runner type PO82, PO638)
		1.000	2.300	4.500	2.500	1.230	1.230	0.617	1.590	1.200	
4H	2.5	0.460	1.154	2.070	1.260	0.622	0.622	0.311	0.807	0.604	medium and high specific speeds PO45, PO75, PO115, PO170 (runner type PO638, PO82, PO211, PO123)
		1.000	2.500	4.500	2.740	1.352	1.352	0.670	1.750	1.310	

Figure 2.24 : Correlation of parameters for draft tube (Gubin), adapted from [47].

Table 2.15 : Geometrical parameters of Gubin for draft tube.

Designation of Dimension (based on Figure 2.24)	Gubin Recommendation		Actual Situation in Kadincik I HPP	
	Value	Unit	Value	Unit
D_2	1.740	meter	1.700	meter
D_1	2.131	meter	1.840	meter
b	0.313	meter	0.360	meter
h	4.901	meter	3.605	meter
L	9.588	meter	14.320	meter
B_5	5.327	meter	4.450	meter
D_4	2.621	meter	1.950	meter
h_4	2.621	meter	2.028	meter
h_6	1.315	meter	1.040	meter
L_2	3.388	meter	11.258	meter
h_5	2.557	meter	2.410	meter
Cone Opening Angle	3.30 – 6.00	degree	4.39	degree

Specific speed of Kadincik I HPP is 126.615 which can be categorized as medium speed runner. Therefore, its draft tube can be compared with the 4E type of tubes (Figure 2.24). This comparison is presented in Table 2.15. As it is observed, runner

dimensions are close to the suggested values; however, there are considerable gaps between recommended and actual dimensions of draft tube. These differences are strongly felt especially in the parameters after the elbow, e.g. L and L₂. Furthermore, Gubin proposed that cone opening angle should be between 3.30 and 6.00 degrees contrary to United States Department of the Interior Bureau of Reclamation. In brief, he introduced smoother transition in the cone region.

2.2.5 General main parametrization

In order to summarize the previously discussed parametrization methods for draft tube, Figure 2.25 and Table 2.16 were created. By looking them, it can be concluded that draft tube design of Kadincik I HPP is not so proper to perform efficiently due to its too short vertical and too long horizontal lengths. Although it shows better quality in cross sectional dimensions, short vertical distance may not provide enough place for vortex to be stabilized. Therefore, flow may reach the elbow with considerable amount of disturbances. On the other hand, long vertical dimensions can cause dramatic friction losses. K, G and H parameters should be carefully adjusted to obtain maximum 2 m/s velocity at the outlet of the draft tube in best efficiency point and to minimize friction losses.

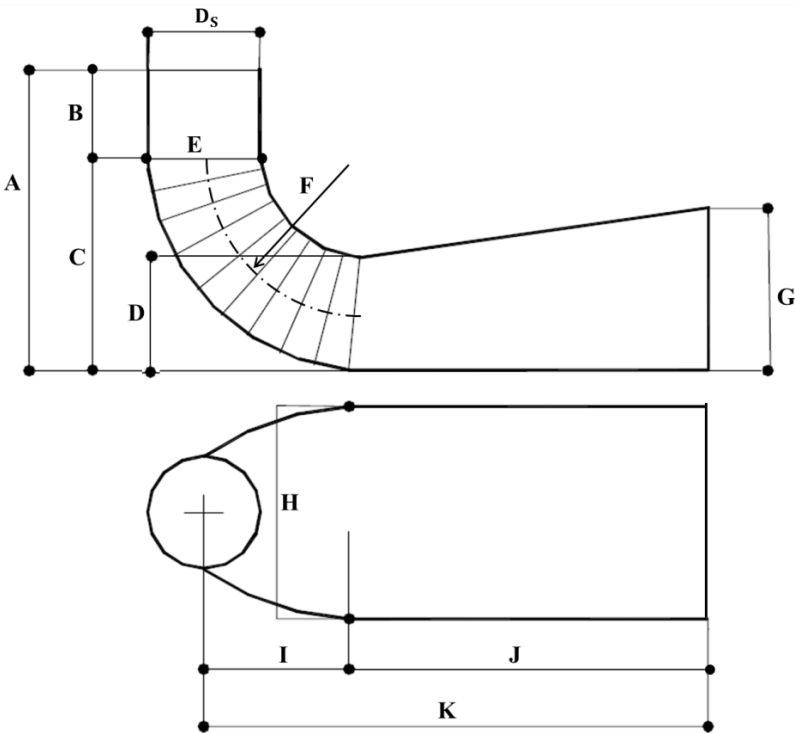


Figure 2.25 : Designation of the main parameters of draft tube for Table 2.16.

Table 2.16 : Main parameters of various scientists for draft tube of Kadincik I HPP.

Main Parameters (based on Figure 2.25)	De Siervo and De Leva	US Department of IBR	Lugaresi and Massa	Gubin	Average	Actual Values of Kadincik I HPP	Unit
D _s	1.740	1.468	1.767	1.740	1.679	1.700	m
A	5.442	7.047	-	4.901	5.797	3.605	m
B	2.088	3.670	-	2.280	2.679	1.577	m
C	3.354	3.377	-	2.621	3.118	2.028	m
D	1.316	1.297	1.457	1.315	1.346	1.040	m
E	-	2.370	-	2.621	2.496	1.950	m
F	2.259	2.730	-	-	2.494	2.062	m
G	2.784	1.960	-	2.557	2.433	2.410	m
H	5.035	6.435	4.276	5.327	5.268	4.450	m
I	2.652	2.633	-	6.200	3.828	3.150	m
J	7.146	4.778	-	3.388	5.104	11.258	m
K	9.798	7.410	-	9.588	8.932	14.320	m

In a paper by Hothersall [72], a historical comparison between different draft tubes was established. Draft tube of Kadincik I HPP was also checked with the designs in that paper in Figure 2.26. In the end, it is concluded that the extremely long draft tube of Kadincik I HPP is out of the range of the presented ones.

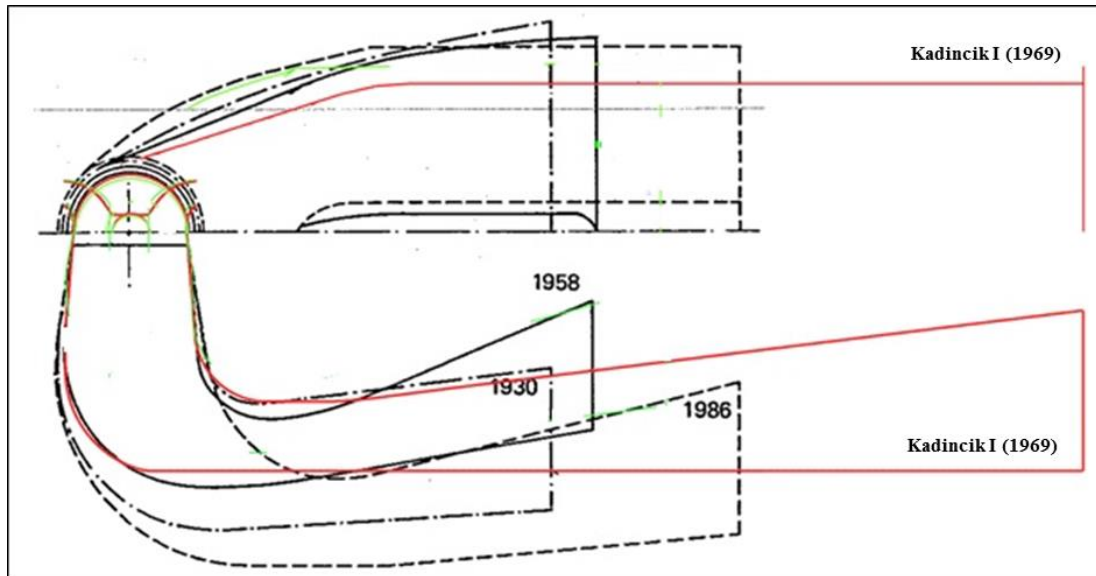


Figure 2.26 : Meridional view of Kadincik I HPP draft tube in comparison with literature, adapted from [72].

2.2.6 Cross sectional design of draft tube

After the determination of the main parameters, cone and exit opening angles, it should be decided whether the pier nose is introduced to the design or not. Although one pier nose is frequently preferred in draft tube design in order to strengthen the mechanical design, good performances can be attained also with other configurations. Subsequently, increase in the area should be distributed very carefully and transition between circular cross section to rectangular cross section should be as smooth as possible to prevent flow separation. In fact, there are some draft tube designs whose outlet cross sections are also circular, but this kind of draft tubes has to be longer than the rectangular one in order to lower outlet velocity in a desired level. These draft tubes are preferred mostly for turbines with low specific speed because the influence of draft tube design on turbine performance is not that significant in low specific speeds with respect to the higher ones and it is a lot easier to design and manufacture the draft tubes with circular cross section through the diffuser. After the preliminary 3D model is generated, all the parameters and cross section definitions should be adjusted according to the CFD results.

2.3 Design of the Spiral Case

The duty of spiral case is to distribute kinetic energy of water along the periphery of the guide vanes and runner. In theory, same amount of water should pass between stay vanes. Therefore, the cross sectional area of volute decreases along the circumference to keep the fluid velocity towards to the vanes. Although there are some volute types seen in Figure 2.27, single volute is frequently preferred for Francis turbines because it is the least expensive one with respect to the production costs [73]. On the other hand, considerable radial forces are acting on the single volute especially at off-design conditions and these forces are the source of bearing loads, bending stresses in the shaft and shaft deflection [73].

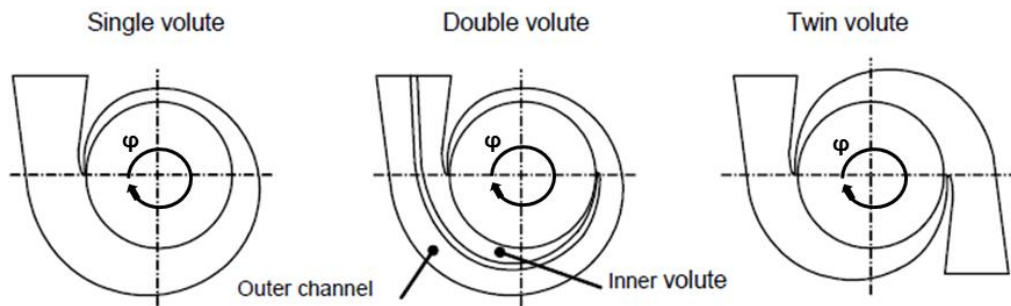


Figure 2.27 : Spiral casing types, adapted from [73].

Second issue needed to be settled before main parametrization is the determination of the cross sectional shape. Despite of the fact that there are various alternatives, some of which are even rarely used, Francis turbine designers choose mostly circular cross section seen in Figure 2.28.

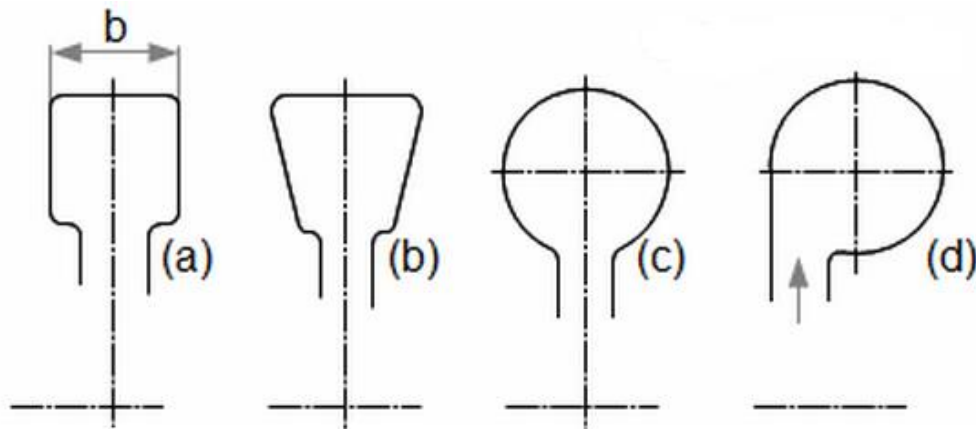


Figure 2.28 : Cross sectional shape of the spiral casing, adapted from [74].

2.3.1 Main parametrization of De Siervo and De Leva

De Siervo and De Leva made design recommendations for volute, also. As previously discussed, they correlated all turbine dimensions with runner discharge diameter. This point of view was not changed in spiral casing. They proposed empirical formulas, Equations (2.66) - (2.76), for the main parameters shown in Figure 2.29.

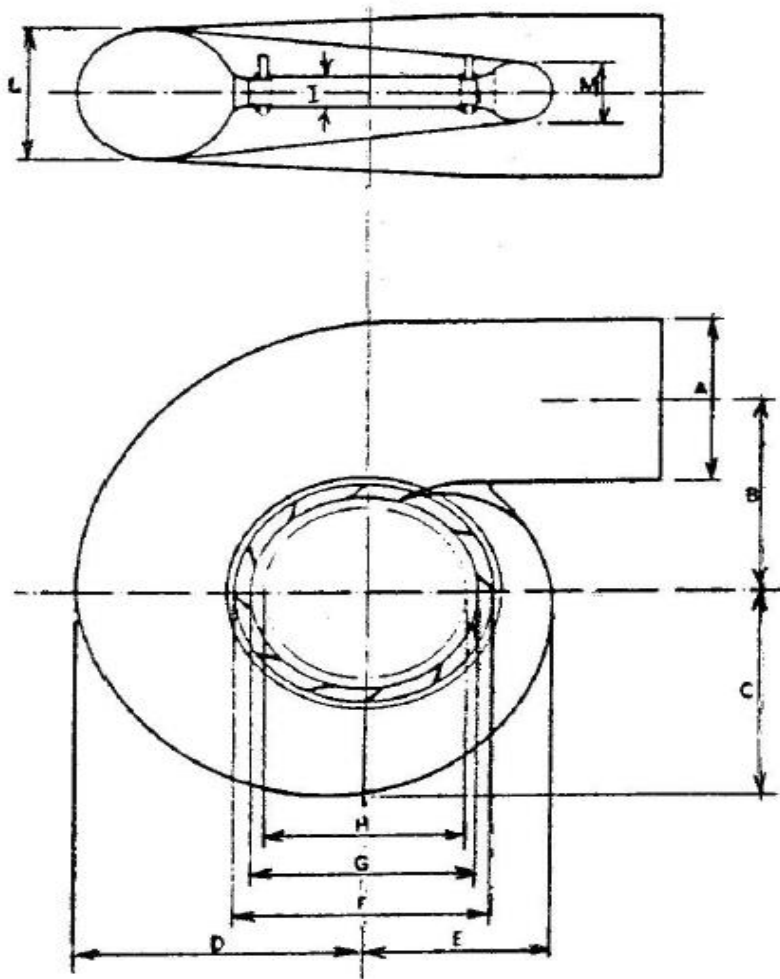


Figure 2.29 : Geometrical parameter definition of De Siervo and De Leva for spiral case, adapted from [59].

$$A = \left(1.20 - \frac{19.56}{n_s} \right) * D_3 \quad (2.66)$$

$$B = \left(1.10 + \frac{54.80}{n_s} \right) * D_3 \quad (2.67)$$

$$C = \left(1.32 + \frac{49.25}{n_s} \right) * D_3 \quad (2.68)$$

$$D = \left(1.50 + \frac{48.80}{n_s}\right) * D_3 \quad (2.69)$$

$$E = \left(0.98 + \frac{63.60}{n_s}\right) * D_3 \quad (2.70)$$

$$F = \left(1.00 + \frac{131.40}{n_s}\right) * D_3 \quad (2.71)$$

$$G = \left(0.89 + \frac{96.50}{n_s}\right) * D_3 \quad (2.72)$$

$$H = \left(0.79 + \frac{81.75}{n_s}\right) * D_3 \quad (2.73)$$

$$I = (0.1 + 0.00065 * n_s) * D_3 \quad (2.74)$$

$$L = (0.88 + 0.00049 * n_s) * D_3 \quad (2.75)$$

$$M = (0.60 + 0.000015 * n_s) * D_3 \quad (2.76)$$

Above parameters were calculated for Kadincik I HPP and compared with the actual dimensions (Table 2.17). Although there are differences up to 35 cm in some parameters, it can be concluded that existing dimensions show consistency with the recommended ones by keeping the difficulties during the production in mind.

Table 2.17 : Geometrical parameters of De Siervo and De Leva for spiral case.

Designation of Dimension (based on Figure 2.29)	De Siervo and De Leva Recommendation		Actual Situation in Kadincik I HPP	
	Value	Unit	Value	Unit
D ₃	1.740	meter	1.700	meter
A	1.822	meter	1.600	meter
B	2.658	meter	2.300	meter
C	2.965	meter	2.745	meter
D	3.272	meter	2.940	meter
E	2.569	meter	2.460	meter
F	3.524	meter	3.210	meter
G	2.859	meter	2.583	meter
H	2.484	meter	2.100	meter
I	0.319	meter	0.360	meter
L	1.640	meter	1.449	meter
M	1.047	meter	1.022	meter

2.3.2 Main parametrization of United States Department of the Interior Bureau of Reclamation

United States Department of the Interior Bureau of Reclamation [46] conducted studies on 60 turbines to propose a chart for preliminary design of spiral casing

(Figure 2.30). Main parameters were correlated with specific speed and runner discharge diameter which are visualized in Figure 2.31.

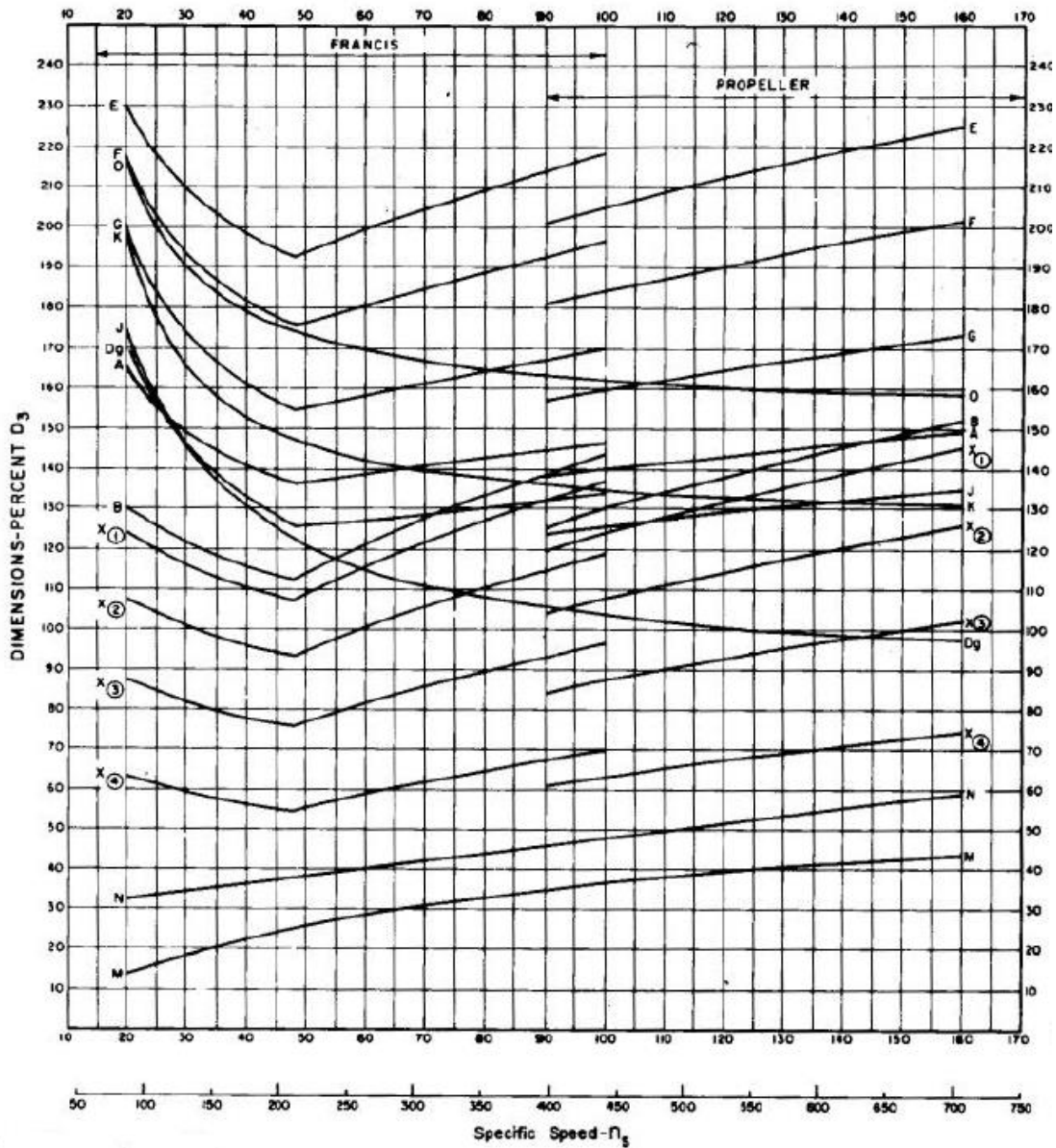


Figure 2.30 : Correlation of parameters for spiral case (United States Department of the Interior Bureau of Reclamation), adapted from [46].

Although recommended runner discharge diameter is approximately 25 cm lower than the actual one, United States Department of the Interior Bureau of Reclamation suggests main spiral case parameters which are quite similar to the real dimensions (Table 2.18). Nevertheless, C and O can be counted as exceptions in this consistency. The difference between O parameter and corresponding dimension may bring some doubts about the position of the stay vanes, but when this dimension is checked with De Siervo and De Leva it is seen that 3.210 meter is not that high for the farthest

point of stay vanes from rotation axis. Furthermore, it should be kept in mind that C parameter is defined as minimum 1.468 meter for Kadincik I HPP; consequently, it is hard to make any conclusion for this dimension before examining other main parametrization methods for the volute.

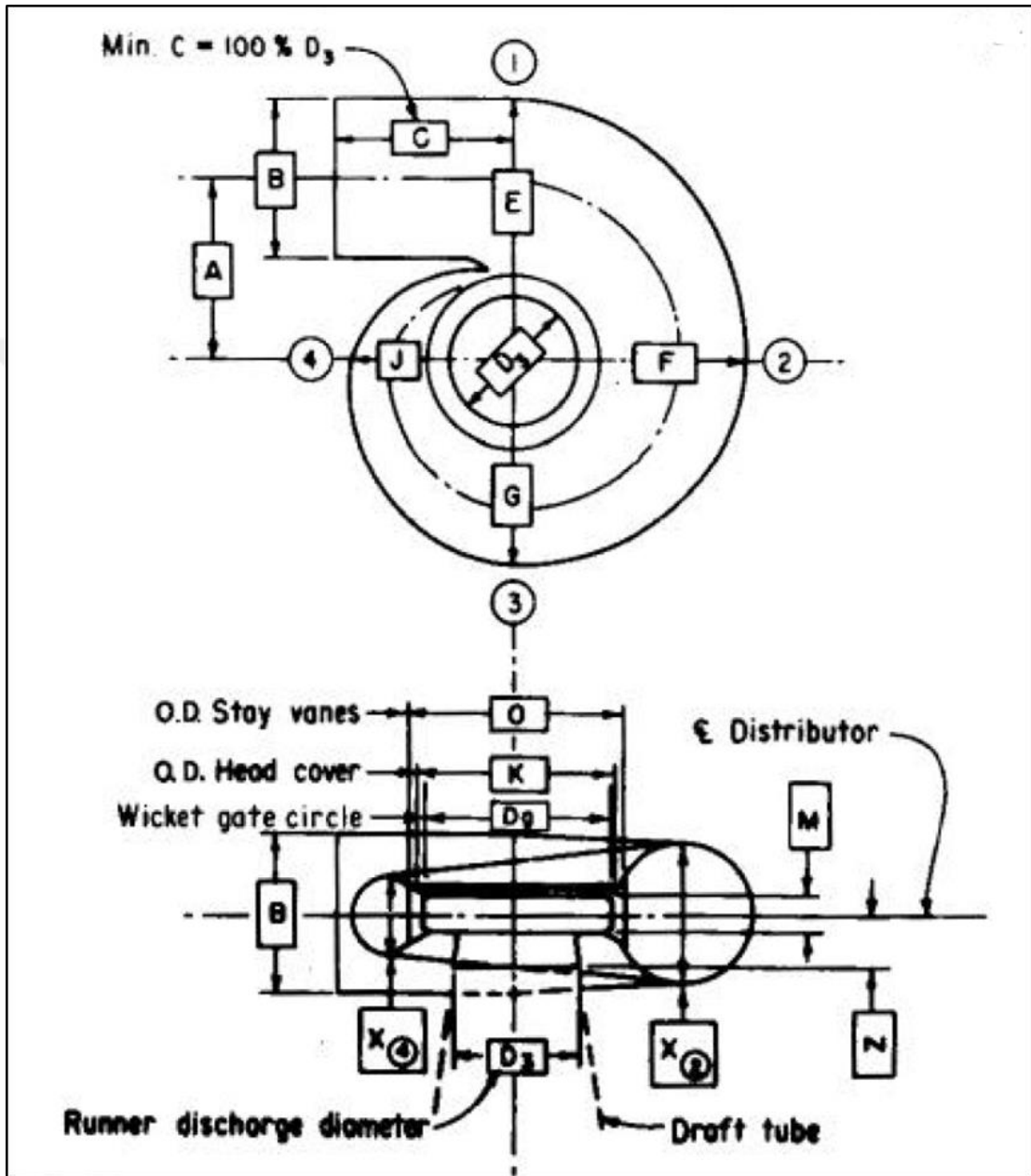


Figure 2.31 : Geometrical parameter definition of United States Department of the Interior Bureau of Reclamation for spiral case, adapted from [46].

Table 2.18 : Geometrical parameters of United States Department of the Interior Bureau of Reclamation for spiral case.

Designation of Dimension (based on Figure 2.31)	United States Department of the Interior Bureau of Reclamation Recommendation		Actual Situation in Kadincik I HPP	
	Value	Unit	Value	Unit
D ₃	1.468	meter	1.700	meter
A	2.202	meter	2.300	meter
B	1.806	meter	1.600	meter
C	1.468 (min)	meter	2.300	meter
D _g	2.202	meter	2.300	meter
E	3.112	meter	3.100	meter
F	2.877	meter	2.940	meter
G	2.584	meter	2.740	meter
J	2.173	meter	2.460	meter
M	0.264	meter	0.360	meter
N	0.514	meter	0.565	meter
O	2.833	meter	3.210	meter

2.3.3 General main parametrization

Two parametrization methodologies explained above combined in Table 2.19 for the dimensions shown in Figure 2.32. In Table 2.19, averages of the parameters are calculated and compared with Kadincik I HPP dimensions. It can be concluded that design of Kadincik I HPP spiral case does not have dramatic problems with respect to the main parametrization. Nonetheless, whether the flow arrives the runner uniformly in radial direction is determined after the CFD analyses.

Volute design is always conducted for optimum flow rate of turbine; therefore, it is quite important to find out the best efficiency. Please note that there are some doubts about the optimum net head and discharge of the Kadincik I HPP, which was already stated. Cover angle (wrap angle) shown in Figure 2.27 as ϕ is chosen generally between 340 and 350 degrees for Francis turbines. After the limiting cover angle, last part of the spiral case is faced with the volute inlet and this region is called cutwater. The design of the cutwater is very crucial topic. There is almost no published recommendation for the design of this region. Indeed, the cutwater geometry is determined in the light of the experiences and manufacturing restrictions.

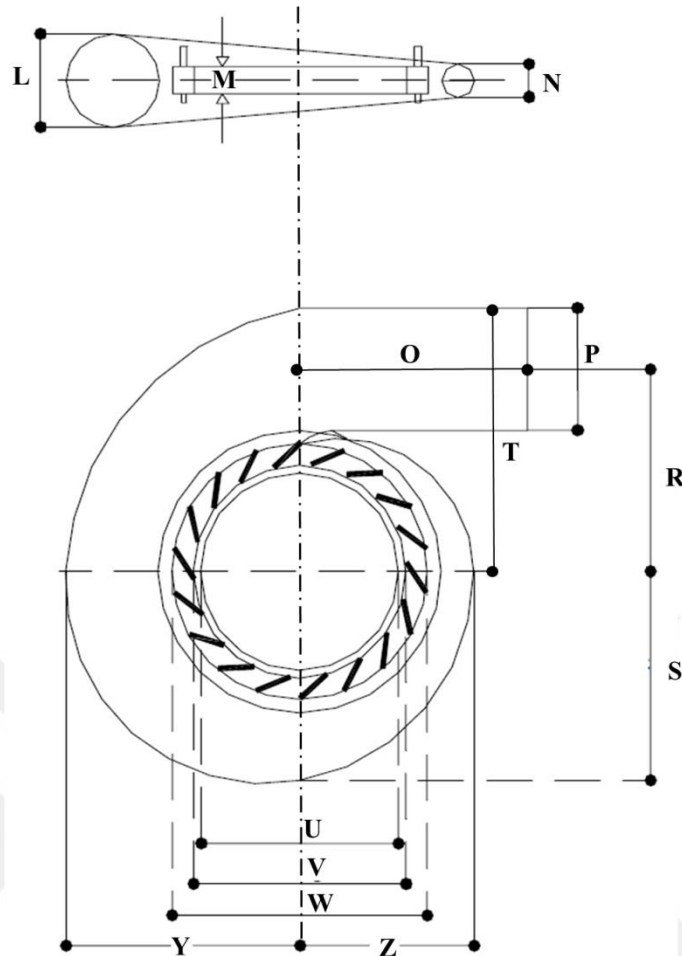


Figure 2.32 : Designation of the main parameters of spiral case for Table 2.19.

Table 2.19 : Main parameters of various scientists for spiral case of Kadincik I HPP.

Main Parameters (based on Figure 2.32)	De Siervo and De Leva	US Department of IBR	Average	Actual Values of Kadincik I HEP	Unit
D_s	1.740	1.468	1.604	1.700	m
L	1.640	-	1.640	1.449	m
M	0.319	0.264	0.292	0.360	m
N	1.047	-	1.047	1.022	m
O	-	1.468 (min)	1.468 (min)	2.300	m
P	1.822	1.806	1.814	1.600	m
R	2.658	2.202	2.430	2.300	m
S	2.965	2.584	2.774	2.745	m
T	-	3.112	3.112	3.100	m
U	2.484	-	2.484	2.100	m
V	2.859	-	2.859	2.583	m
W	3.524	2.833	3.179	3.210	m
Y	3.272	2.877	3.075	2.940	m
Z	2.569	2.173	2.371	2.460	m

2.3.4 Cross sectional design of spiral case

After these considerations on the volute geometry, the turn comes to the calculation of the cross sections. There are mainly three approaches for this calculation. First of all, constant swirl (free vortex) method is explained because it is widely preferred in today's designs. This method based on the potential axis symmetric flow assumption and got benefit from conservation of the angular momentum [75]. Multiplication of the circumferential velocity and radius (velocity moment) is proved as constant with the help of the Newton second law and Bernoulli Equation. The resulting formula is shown in Equation (2.77). By knowing this multiplication in front of the stay vanes, circumferential velocities can be decided at different distances from rotation axis (Equation (2.78)). Cross sectional area can be determined by benefiting from flow rate (Equation (2.79)). These calculations should be repeated at different cover angles along the spiral case to establish cross sectional area through the whole volute.

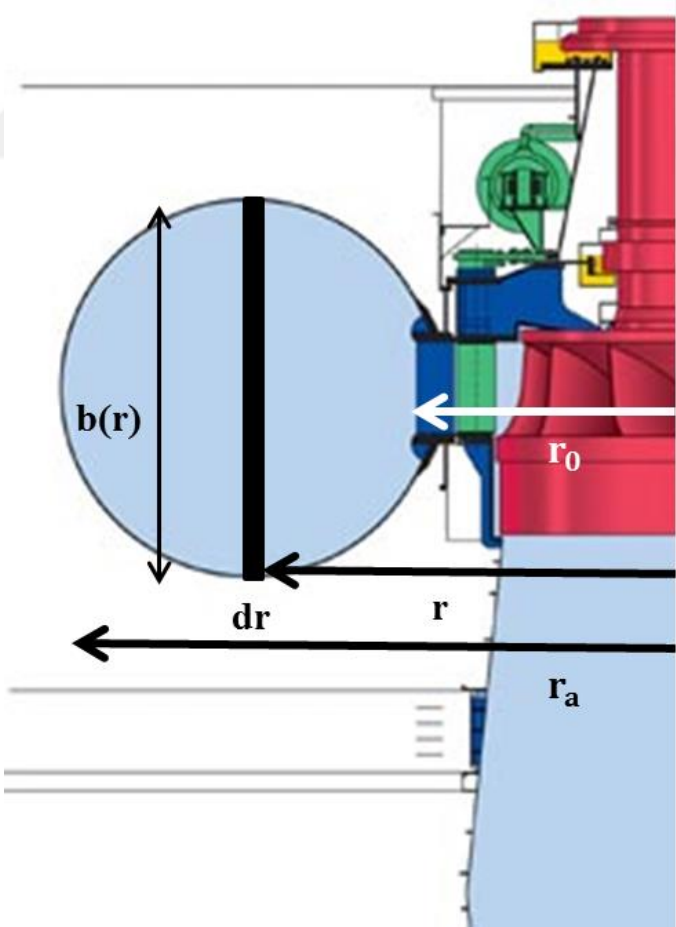


Figure 2.33 : Meridional view of spiral case.

$$c_u * r = \text{constant} \quad (2.77)$$

$$c_{u0} * r_0 = c_u(r) * r \quad (2.78)$$

$$Q = \int_{r_0}^{r_a} c_{u0} * \frac{r_0}{r} * b(r) * dr = c_{u0} * r_0 \int_{r_0}^{r_a} \frac{b(r)}{r} * dr \quad (2.79)$$

Alternatively, volute can be designed with the assumption of constant velocity through whole cross sections over the circumference [73]. In this method, calculations start with the throat area (designated as P in Figure 2.32). Areas of different sections are found out with Equation (2.80). Although this method can be an option for the Francis turbines with a specific speed less than 25 ($n_q < 25$), Gülich [73] strongly recommends to use conservation of angular momentum approach for the turbines with higher specific speeds.

$$A(\varphi) = \frac{Q(\varphi)}{c_{u,th}} = \frac{Q}{c_{u,th}} * \frac{\varphi}{\varphi_{max}} = A_{th} \frac{\varphi}{\varphi_{max}} \quad (2.80)$$

It is not surprising to face with spiral cases which have the linear area decrease principle because they are easier to design and manufacture. In fact, this method is also preferred by many designers nowadays. However, regardless of which method is applied to a volute, it should supply the water uniformly over the entire perimeter of the wicket gates by causing minimum hydraulic losses. Furthermore, easy manufacturing, transportation and assembling bring advantages. In structural point of view, spiral case should be strong enough to resist maximum internal water pressure and water hammer.

Flow inside the volute is almost two-dimensional. However, this situation changes at the inlet of the stay vane channel. The flow is accelerated into the stay vanes. Meanwhile sectional velocity profiles and pressure distributions are considerably distorted. As a result, flow becomes largely three dimensional near the inlet of stay vane channel. Moreover, a good spiral case design should lower the tangential velocity in the volute to suppress secondary flows and adjust the flow angle to the stay vane inlet angle in order to lower the collision loss at the front end of the stay vanes and swirl brought by flow separation [76] [77]. In order to prevent secondary flow patterns, stay vanes are overlapped with the spiral casing as shown in Figure 2.34.

Whether spiral case of Kadincik I HPP obeys one of the methods explained above is determined after the CFD analyses. There is also a possibility that the volute can violate these three approaches, but it can still deliver the flow to the runner in a desired manner. Therefore, uniformity of the flow around the guide vane inlet and outlet is checked in CFD. Nevertheless, it is possible to investigate the area distribution of spiral case at this point. This study reveals if the spiral case of Kadincik I HPP obeys the linear area decrease law or not. By looking to Figure 2.35, it can be stated that spiral case of Kadincik I HPP violates the design law of linear area distribution because deviation between linear area and corrected area lines is not minor. Furthermore, the radius is an area-averaged radius of the whole plane (including stay vanes) and decreases dramatically for large angles. This radius has its minimum at the end of the cutwater at about 1.34 m.

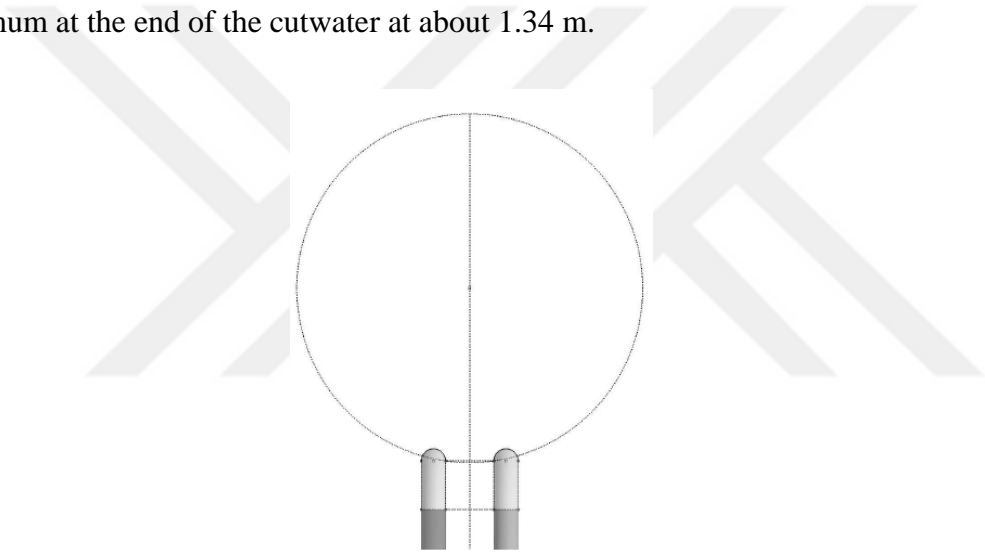


Figure 2.34 : Overlap of stay vanes over spiral case, adapted from [78].

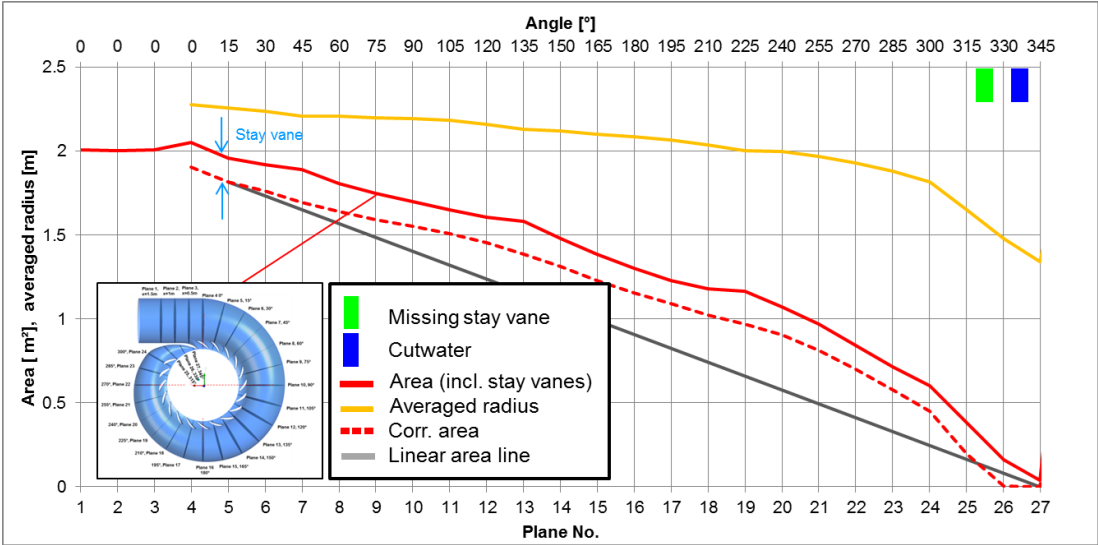


Figure 2.35 : Area distribution of spiral case of Kadincik I HPP.

2.4 Design of the Stay Vanes and Guide Vanes

Guide vanes are the apparatus utilized for the adjustment of the turbine load. They not only increase or decrease the flow rate but also change the direction of the fluid flowing through the runner. Therefore, they have a direct influence on the turbine performance. In the design procedure of the guide vanes, first step is the selection of the number of the vanes. The important thing in this selection is that division of the number of the wicket gates to the number of the runner blades should be as far away from an integer as possible in order to minimize the extent of the pressure pulsations occur when runner blades pass the guide vanes [64].

In the design point where the peak efficiency is attained, guide vane outlet diameter ($D_{gv,o}$) is adjusted as approximately five percent larger than the runner inlet diameter to have adequate distance between wicket gates and runner [64]. On the other hand, rotation axis of the guide vane (D_{gv}) is calculated with the help of the speed number (Ω) which is defined in Equation (2.81). In fact, diameter for wicket gate rotation axis is a function of runner inlet diameter (D_1) and speed number (Ω), Equation (2.82) [78].

$$\Omega = \frac{\omega}{\sqrt{2 * g * H_{net}}} * \sqrt{\frac{Q_{opt}}{\sqrt{2 * g * H_{net}}}} \quad (2.81)$$

$$D_{gv} = D_1 * (0.29 * \Omega + 1.07) \quad (2.82)$$

In the fully closed position, guide vanes are expected to prevent water from flowing through the runner and they should not be able to rotate in full circle under the water pressure that causes a considerable moment on guide vane shaft. Therefore, vanes are designed in such a way that in fully closed position they blocked the circular area passing through the wicket gate rotation axis and they overlap in a certain level to resist against further rotation. The mathematical representation of this idea is shown in Equation (2.83) which gives also the guide vane length. Note that 15 % overlapping is chosen in order to be on the safe side and N_{gv} refers to the number of the vanes. Subsequently, inlet diameter of the wicket gates ($D_{gv,i}$) can be calculated with the help of the cosine theorem, Equation (2.84) [78].

$$L_{gv} = 1.15 * \frac{D_{gv} * \pi}{N_{gv}} \quad (2.83)$$

$$D_{gv,i} = 2 * \sqrt{L_{gv}^2 + \frac{D_{gv,o}^2}{4} - 2 * L_{gv} * \frac{D_{gv,o}}{2} * \cos\left(\frac{\pi}{2} + \alpha_{gv,o}\right)} \quad (2.84)$$

As it is seen in Equation (2.84), velocity triangles and guide vane blade angles should be found out in order to obtain guide vane inlet diameter. With this aim, free vortex (conservation of the angular momentum) approach is extended from spiral case to the inlet of the runner. This region includes also stay vanes and wicket gates. In the design procedure of the runner, circumferential velocity (c_{u1}) just in front of the runner blade (designated as D_1 in Figure 2.36) is already calculated. By using Equations (2.85) and (2.86), meridional and circumferential velocities at the end of the guide vanes ($c_{m-gv,o}$ and $c_{u-gv,o}$) can be easily obtained. Velocity triangle configuration and angle definitions presented in Figure 2.13 are also valid for wicket gates. Therefore, $\alpha_{gv,o}$ is calculated with Equation (2.87).

$$c_{m-gv,o} = \frac{Q_{opt}}{\pi * D_{gv,o} * b_0} \quad (2.85)$$

$$c_{u-gv,o} = \frac{c_{u1} * D_1}{D_{gv,o}} \quad (2.86)$$

$$\alpha_{gv,o} = \tan^{-1}\left(\frac{c_{m-gv,o}}{c_{u-gv,o}}\right) \quad (2.87)$$

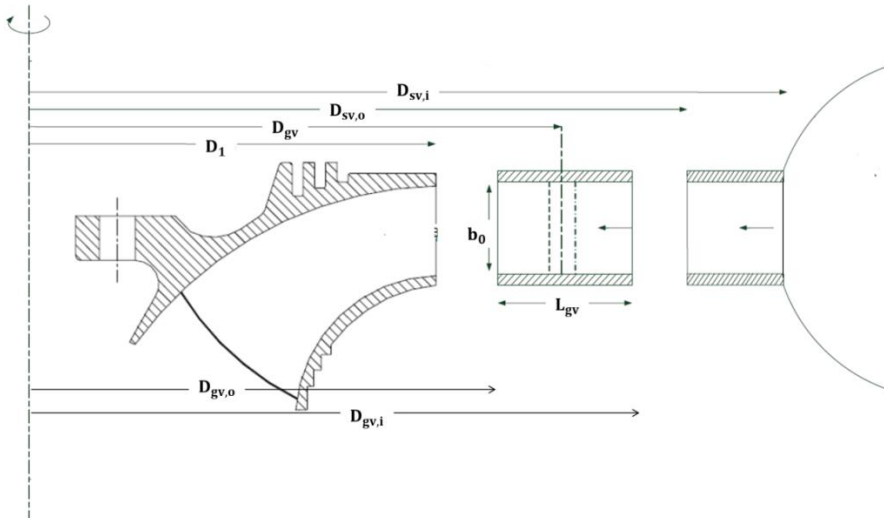


Figure 2.36 : Meridional view of a radial machine.

Blade angles should also be determined at the inlet of the wicket gates. Consequently, velocities are calculated with the same principle and velocity triangles are utilized for getting blade angles. Details of the procedure are presented in Equations (2.88) - (2.90).

$$c_{m-gv,i} = \frac{Q_{opt}}{\pi * D_{gv,i} * b_0} \quad (2.88)$$

$$c_{u-gv,i} = \frac{c_{u1} * D_1}{D_{gv,i}} \quad (2.89)$$

$$\alpha_{gv,i} = \tan^{-1} \left(\frac{c_{m-gv,i}}{c_{u-gv,i}} \right) \quad (2.90)$$

In general, guide vane rotation axis is located somewhere between the midpoint and three quarters of the vane length upstream from the trailing edge [64]. Smooth and symmetrical 4- and 5- digit NACA profiles are often utilized for blade thickness distribution in order to lower the losses. NACA 0006, NACA 0014, NACA 0018 and NACA 65 series are the most frequently preferred ones.

Although the main purpose of the stay vanes is to keep the volute together, it also helps flow to go towards the guide vanes. In order not to disturb flow before reaching the runner, stay vanes should be designed properly. This necessity brings significance to the calculation of the inlet and outlet blade angles of stay vanes. However, before passing to the velocity and angle calculation, number of the stay vanes should be determined. The number of the stay vanes is chosen as either the number of the wicket gates or the half of it.

Stay vane outlet diameter is generally defined as 2 % percent larger than the wicket gate inlet diameter and the stay vane inlet diameter can be determined from the main parametrization presented in spiral case design [78]. By knowing the diameters and the circumferential velocity at the inlet of the runner, velocities and blade angles can be calculated by using Equations (2.91) - (2.96).

$$c_{m-sv,o} = \frac{Q_{opt}}{\pi * D_{sv,o} * b_0} \quad (2.91)$$

$$c_{u-sv,o} = \frac{c_{u1} * D_1}{D_{sv,o}} \quad (2.92)$$

$$\alpha_{sv,0} = \tan^{-1} \left(\frac{c_{m-sv,0}}{c_{u-sv,0}} \right) \quad (2.93)$$

$$c_{m-sv,i} = \frac{Q_{opt}}{\pi * D_{sv,i} * b_0} \quad (2.94)$$

$$c_{u-sv,i} = \frac{c_{u1} * D_1}{D_{sv,i}} \quad (2.95)$$

$$\alpha_{sv,i} = \tan^{-1} \left(\frac{c_{m-sv,i}}{c_{u-sv,i}} \right) \quad (2.96)$$

The length and thickness of the stay vane should be decided according to the maximum force acting on the vanes. Determination of these parameters can be conducted iteratively by evaluating every alternative with mechanical analyses. Finally, curvature of the stay vanes from inlet to outlet can be calculated with free vortex assumption and the conservation of mass law [78].

3. CAVITATION PHENOMENON IN FRANCIS TURBINE

3.1 Definition of Cavitation

When the water is flowing throughout the turbine, it encounters with the low pressure regions. This causes the generation of water vapor bubbles, i.e. vapor cavities. They grow because dynamic pressure decreases up to vapor pressure of the liquid at constant temperature. This growth is stopped by the high pressure regions. And, if the pressure is high enough, it can even make the bubbles to collapse. This phenomenon is called cavitation. Collisions of the bubbles create pressure pulses and if these pressure pulses occur near to the surface and are greater than the limit of the material mechanical stress, then a few micrometers of the material are separated from the surface in each pulse. This lack of material on the surface is called cavitation erosion or cavitation damages [79].

Cavitation is an undesired phenomenon during the operation because it causes flow instabilities, excessive vibrations, damage to material surfaces and deterioration of the machine performance. For the prevention of these effects, machine setting level and operation at off-design conditions play significant roles in addition to turbine design. Initially, machine-setting level (Figure 3.1) determines the NPSE (Net Positive Suction Specific Energy) and therefore Thoma number of the plant (Equations (3.1) and (3.2)). In order not to have cavitation, Thoma number of the turbine should be lower than the Thoma number of the plant (plant cavitation number). With keeping this in mind, it is a pretty good idea to make z_2 in Figure 3.1 as big as possible. Furthermore, when turbine runs in part load or overload, cavitation risk appears. For instance, if the operation head is bigger than the design one, cavitation can occur on the suction site of the runner blade. Another example is part load vortex rope which is generated due to the remaining swirl given in draft tube in part load. Similar situation is seen in overload also. More energy is taken from the water by turbine in overload and that cause negative circumferential

velocity in draft tube entrance. This velocity is the reason of the overload vortex rope generation [79] [80].

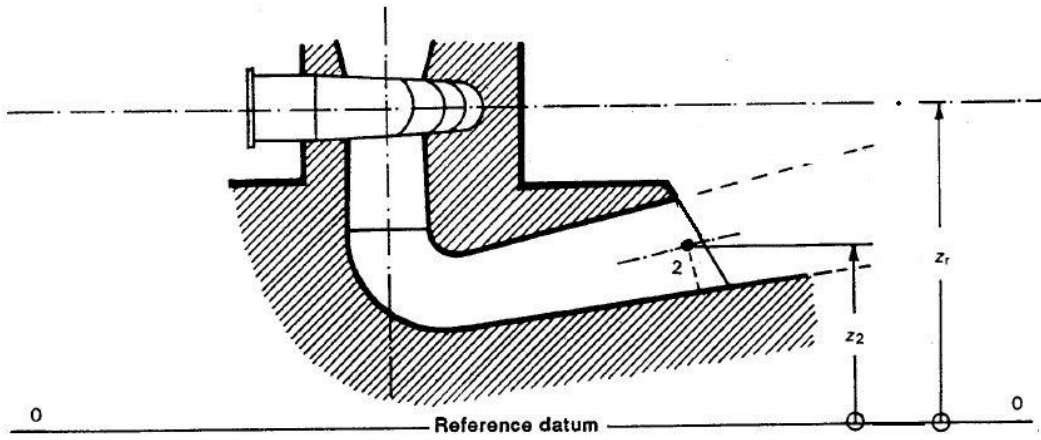


Figure 3.1 : Machine levels of Francis turbine, adapted from [80].

$$NPSE = g_2 * NPSH = \frac{(P_{abs2} - P_{va})}{\rho_2} + \frac{v_2^2}{2} - g_2 * (z_r - z_2) \quad (3.1)$$

$$\sigma_P = \frac{NPSE}{E} \quad (3.2)$$

$$E = g * Z_g * \left[1 - \frac{\rho_{air}}{\rho_{water}} \right] \quad (3.3)$$

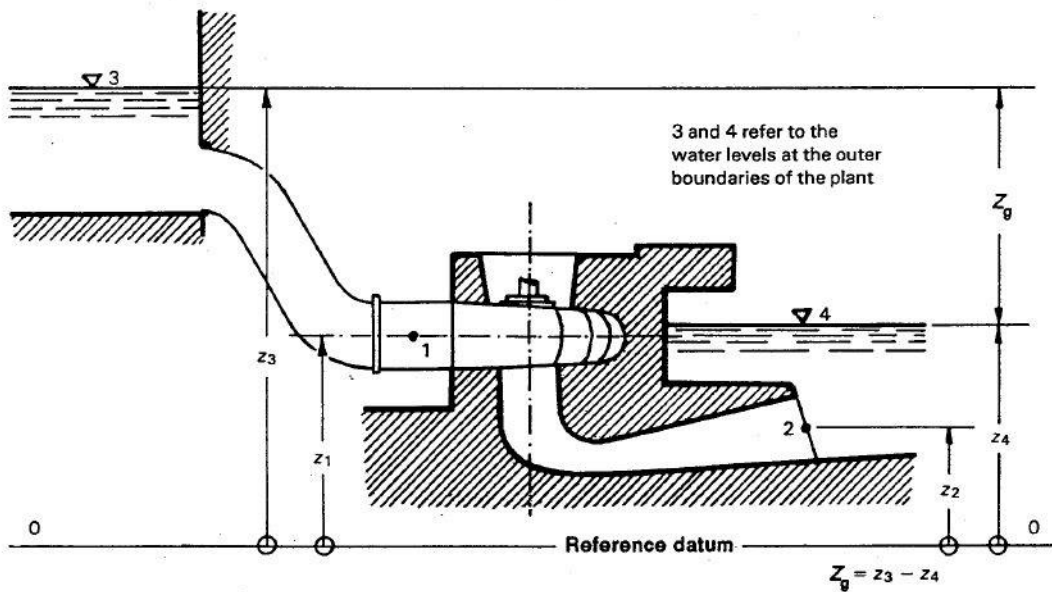


Figure 3.2 : Reservoir levels of Francis turbine, adapted from [80].

3.2 Types of Cavitation in Francis Turbine

3.2.1 Leading edge cavitation

This type of cavitation takes place on the suction side of the runner blade when turbine operates at higher head than the design head. On the other hand, if the operation head is less than the design head, cavitation damages may be seen on the pressure side of the blade. Leading edge cavitation is a very serious problem due to its considerable erosive power. Furthermore, it causes pressure fluctuations [79][81].

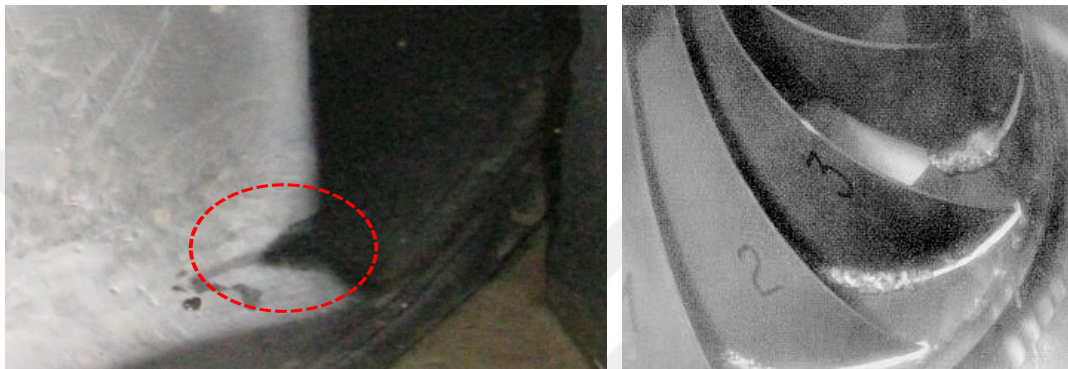


Figure 3.3 : Leading edge cavitation – on pressure side (left) - on suction side (right).

3.2.2 Travelling bubble cavitation

The water vapor bubbles, initiating in low pressure regions, grow in overload; i.e. when Thoma number of the operated turbine exceeds plant Thoma number. These bubbles have a risk of collision on the blade, especially around the mid-chord near the trailing edge at suction side. This collision causes hazardous erosion, noise and therefore a fall in turbine efficiency [79].



Figure 3.4 : Travelling bubble cavitation, adapted from [81].

3.2.3 Vortex rope

The flow leaves the runner with an absolute circumferential velocity if the turbine is not operated at the best efficiency point. This velocity originates a vortex rope which starts below the runner cone in the center of the draft tube. The vortex rope has a helical shape, rotates in the same direction with the runner and presents a precession rotation at 0.25 – 0.35 times the runner rotation speed when operation is at part load. If precession frequency of part load vortex rope coincides with one of the natural frequencies of the draft tube and penstock, strong fluctuation and therefore strong vibrations can be faced. Even, vortex rope can touch the draft tube walls. On the other hand, at overload, vortex rope is axially centered in the draft tube and rotates in the opposite direction with runner. In brief, vortex rope generation should always be considered and tried to control because it is the reason behind the stability problems of machine operations due to its pressure fluctuations in the hydraulic installation [81][82].

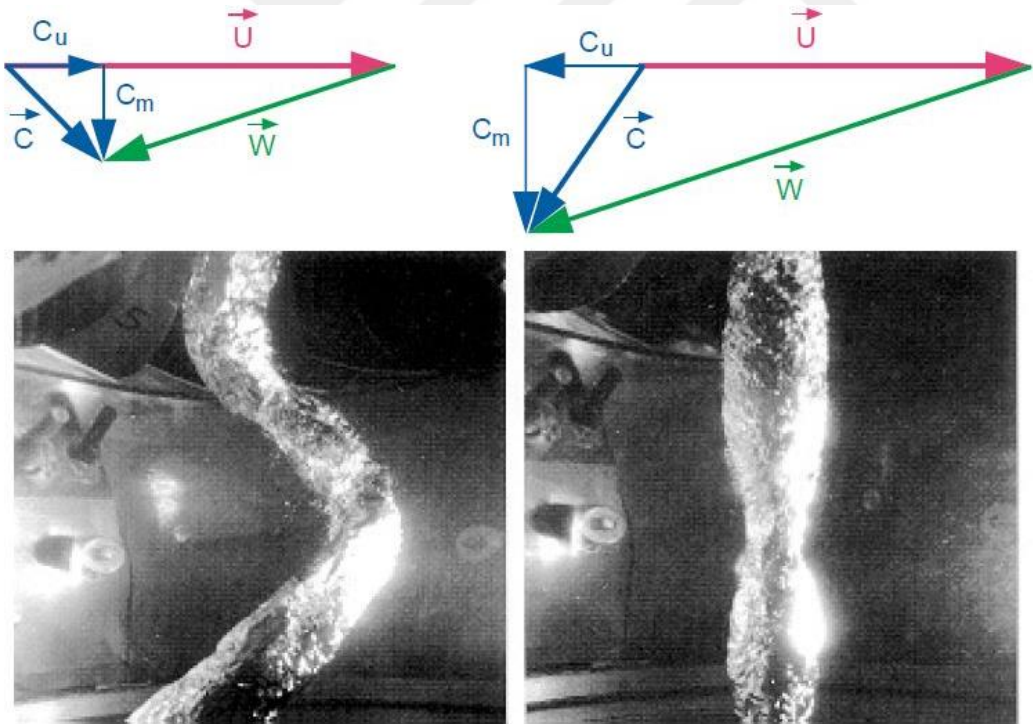


Figure 3.5 : Vortex rope and velocity triangles in the entrance of draft tube – part load (left) – overload (right), adapted from [79].

3.2.4 Inter – blade vortex cavitation

This kind of cavitation occurs due to the secondary vortices between blades which is the result of the flow separation. Unless these vortices touch the runner surface, there

can be no cavitation erosion because of inter – blade vortex. This type of cavitation damages can be seen at the leading edge around hub or mid-way of the hub between blades close to the suction side. The secondary vortices, causes inter – blade vortex cavitation, reveal at partial load or extremely high head operations. This cavitation should be avoided because high noise level, instability and strong vibration are some of its drawbacks [79].

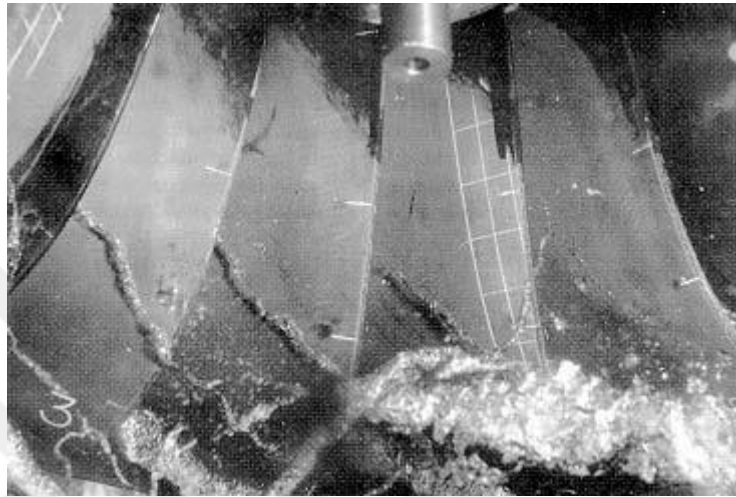


Figure 3.6 : Inter – blade vortex cavitation, adapted from [81].

3.2.5 Von Karman vortex cavitation

Periodic vortex shedding from trailing edge of the runner blades, stay vanes and guide vanes can cause dramatic pressure pulsations and noise if the lock-in phenomenon happens. This type of cavitation mostly affects trailing edge geometry [79].



Figure 3.7 : Von Karman vortex cavitation, adapted from [81].

Leading edge cavitation due to its high erosion capability, travelling bubble cavitation due to its detrimental effect in the performance of the turbine and vortex rope due to its limitation in the operation stability are the most significant cavitation types for Francis turbine. In fact, these cavitations limit the operation range of the turbine. This limitation is visualized in Figure 3.8. In this Figure, A shows the suction side leading edge cavitation limit, B shows the pressure side leading edge cavitation limit, C stands for the inter-blade vortex cavitation limit and D represents the vortex rope limit. Furthermore, Figure 3.9 visualizes the cavitation regions by defining them with respect to the types listed above. In this Figure, 1 corresponds to leading edge cavitation, 2 – travelling bubble cavitation, 3 – vortex rope, 4 – inter blade vortex cavitation and 5 – Von Karman vortex cavitation.

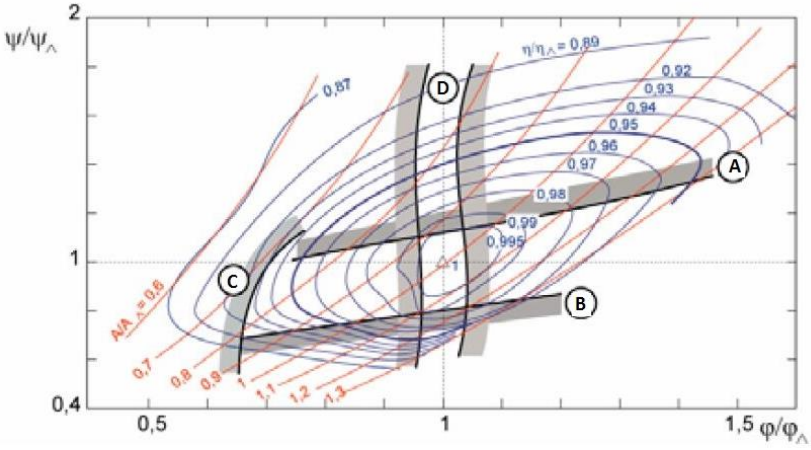


Figure 3.8 : Cavitation limits, adapted from [79].

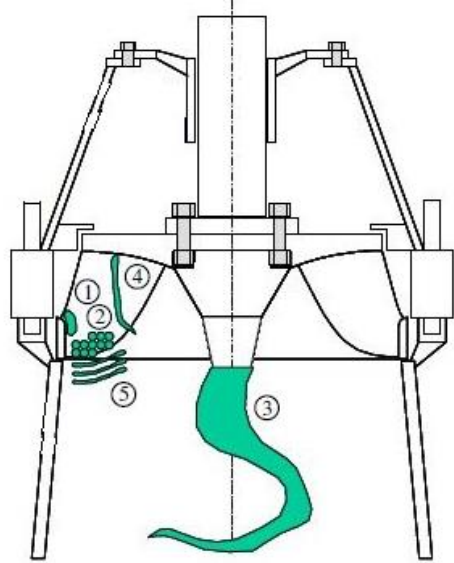


Figure 3.9 : Cavitation regions, adapted from [81].

3.3 Evaluation of Cavitation Behavior – Histogram Method

Cavitation phenomenon has been a substantial topic in the hydraulic machinery for many years. Before CFD was commonly used in the evaluation of the performance for the fluid machinery, model testing was the best way for cavitation investigations. However, with the improved technology, people started to search numerical ways to find out cavitation inception in order to reduce cost and time of the projects. Nonetheless, this does not mean that there is no need for model test. In fact, model test is a must for the turbines, whose power is more than 10 MW, whereas test procedure may be skipped for smaller turbines.

There are mainly four types of cavitation models that can be utilized in numerical investigation of cavitation. First one is called the bubble dynamics model where rate of cavitation is predicted with phase averaged distributions of pressure and bubbles [83]. It is based on the famous Rayleigh-Plesset equation, which provides the basis for the rate equation controlling vapor generation and condensation. Rayleigh-Plesset describes the growth and collapse of a gas bubble in a flow. Second type is named as interface tracking method. In this model, only the liquid flow is investigated with the assumption of the cavities surrounded by liquids; however, simulation of the interface shape and the cavity changes from author to author [83]. Thirdly, single-phase (phase change) model presents the mass transfer between the phases by establishing a mixture condition between liquid and vapor. For the phase definition, barotropic or equilibrium models are utilized. In barotropic model, pressure of the system is checked for whether it is greater than the vapor pressure or not. If it is greater than vapor pressure, then the fluid is assumed as liquid and density of the liquid is got as density of the fluid. If the pressure is less than vapor pressure, vice versa. Equilibrium model uses the equations for water, but it needs the solution of the energy equation, also. Finally, two-phase model includes the non-equilibrium effects during vaporization and condensation contrary to single-phase model [83]. Although it gives quite accurate results with respect to the cavitation, the cost of the CFD analyses exponentially increases.

Although cavitation can be investigated in CFD with transient analysis and multi-phase flow simulations, which depend on the cavitation models explained above [84] - [87], these calculations need so much computational power and time; consequently,

advantages of CFD disappear. On the other hand, it is proved that cavitation performance can be evaluated properly with steady state, single phase simulations [89] [90]. Evaluation of cavitation phenomenon in steady state analysis starts with the same procedure with the one in multiphase flows. First, turbine and plant Thoma number are derived. These numbers depends on the NPSE, Equation (3.1). When Equations (3.1), (3.2) and (3.3) are combined, plant Thoma cavitation coefficient takes the form of Equation (3.4). On the other hand, turbine Thoma number can be calculated with the help of the reserve cavitation coefficient, whose formulation is provided in Equation (3.5) [88]. Subsequently, turbine cavitation number can be derived as Equation (3.6) which depends on the minimum pressure on the runner blade, changes with the operation mode and if it is less than plant Thoma number, operation is cavitation free. However, minimum pressure on the blade found in steady state CFD analysis is misleading. Here, minimum pressure that has the reasonable area should be found. For this purpose, statistical histogram method was developed and the formula for the turbine Thoma number is modified to get Equation (3.7).

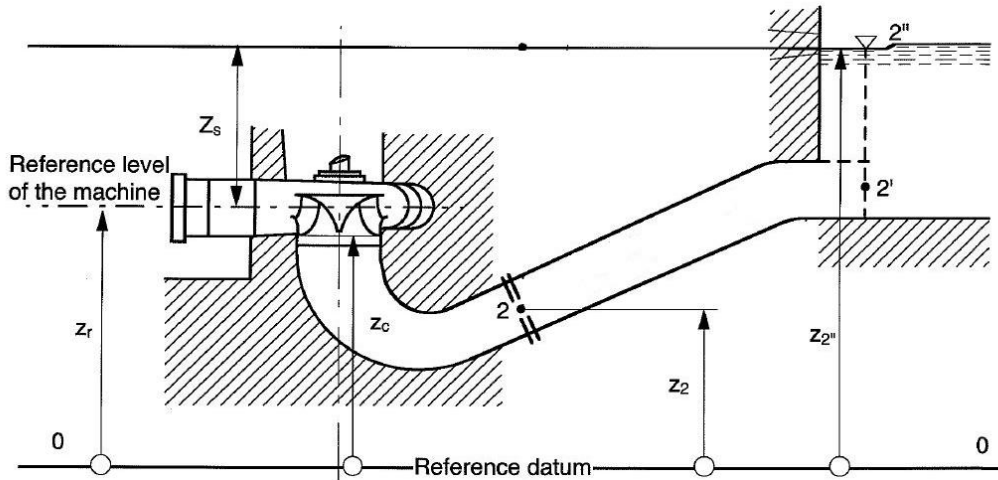


Figure 3.10 : Francis turbine machine and tail water level definitions for Thoma number calculations, adapted from [91].

$$\sigma_P = \frac{\frac{(P_{amb} - P_{va})}{\rho * g} - Z_S}{H_{net}} \quad (3.4)$$

$$\sigma_{rez} = \frac{(P_{min} - P_{va})}{\rho * g} = \sigma_P - \sigma_T \quad (3.5)$$

$$\sigma_T = \frac{P_{t,o} - P_{\min}}{\rho * g H_{\text{net}}} \quad (3.6)$$

$$\sigma_{T,\text{his}} = \frac{P_{t,o} - P_{\text{his}}}{\rho * g H_{\text{net}}} \quad (3.7)$$

Histogram method is utilized in order to find a certain pressure on the runner blade under which pressure values are remaining on a defined fraction of the blade surface. In other words, it calculates the “histogram pressure” from the blade pressure distribution and a determined percentage of the blade surface is loaded with pressures lower than this P_{his} . Here, the crucial part is the designation of blade surface fraction. Graz Technical University conducted a study with Alstom Hydro in order to find what the most suitable percentage is for the histogram pressure and therefore histogram Thoma number calculation. They compared CFD and model test results of several Francis and bulb turbines and pumps. This study shows that P_{his} decided with 1 % of blade surface in CFD gives consistent results with model test outcomes (Figure 3.11) [89][90].

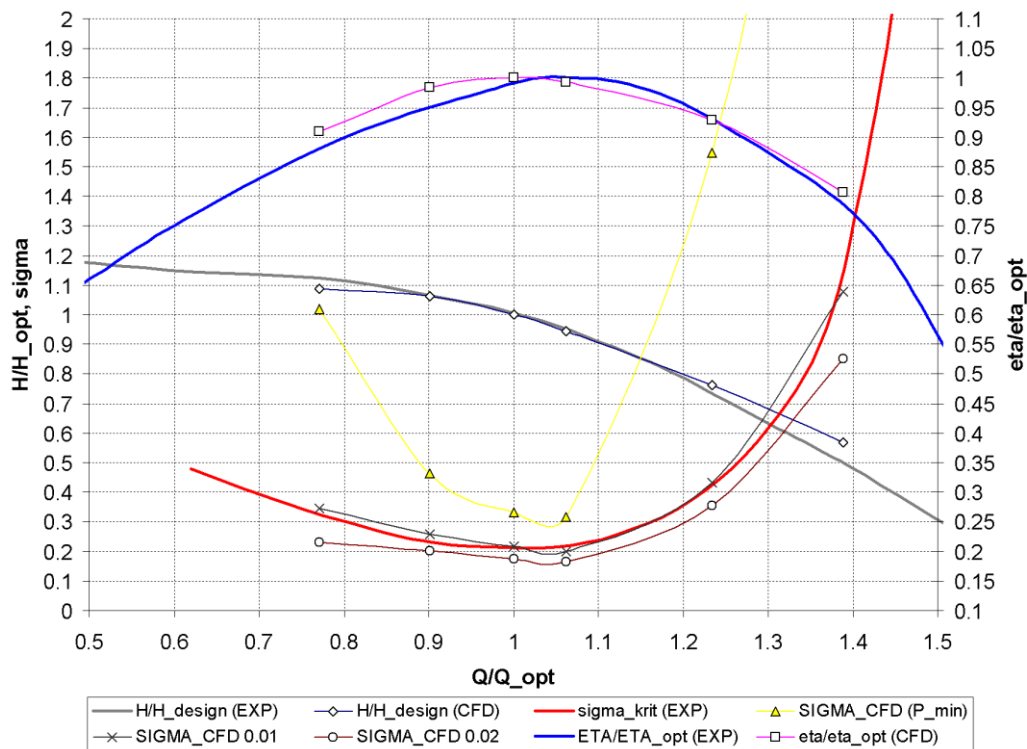


Figure 3.11 : Comparison of numerical simulation with model test results, adapted from [90].

The workflow of the histogram method in the evaluation of cavitation behavior can be summarized like that:

- Export of the pressure and the area of each node on the blade, hub and shroud from CFD by using a macro
- Arrangement of these pairs of values according to the pressure by starting with the lowest pressure
- Normalization of the area of the runner blade, hub and shroud – End of this step, pressure histogram is obtained
- Search of the histogram pressure which is lower than 1% of the area
- Calculation of $\sigma_{T, his}$ with the help of P_{his}
- Comparison of $\sigma_{T, his}$ with σ_p
 - $\sigma_p > \sigma_{T, his}$ – Cavitation free operation
 - $\sigma_p = \sigma_{T, his}$ – Cavitation inception
 - $\sigma_p < \sigma_{T, his}$ – Cavitation

4. CFD ANALYSIS OF EXISTING UNIT

Comprehensive CFD analyses of Kadincik I HPP were conducted in order to find out the performance of existing unit in the power plant. Studies were initiated with 3D CAD modelling of mechanical parts of the turbine with the help of the technical drawings, laser scanning and observations inside the unit. While the geometries of guide vanes and runner were generated from the point clouds coming from the laser scan arm, 3D models of spiral case, stay vanes and draft tube were created according to the technical drawings. After the inspection of the mechanical parts inside the unit, 3D geometry of the wetted area meaningful for CFD analysis got ready.

Geometry generation was followed by meshing process. A mesh independency study was realized for each component by establishing meshes with different densities for verification of mesh quality and calculation of convergence. Then, adequately dense meshes of all components got involved in CFD analyses. RANS (Reynolds Averaged Navier Stokes) calculations revealed the performance of the existing unit and the losses of each component separately. Subsequently, all mechanical components were further examined in detail and compared with the ones in literature.

At the end of the CFD analyses of Kadincik I HPP, the hill chart of the turbine was obtained and checked whether the machine is operating around best efficiency point or not. The doubts, which cause this study, arise from the fact that tail water level of the Kadincik I HPP increased 8.9 meter after its commissioning due to construction of another power plant at the downstream of Kadincik I HPP. In other words, net head of turbine decreased 8.9 meter after the 3-year-operation. The results of the CFD demonstrate that high efficiency values occur far away from the operation range of existing unit.

4.1 Description of Power Plant

The powerhouse is located at Tarsus, Mersin, Turkey and went into operation in 1971. The nominal power of 70 MW is generated by means of two units consisting

of Francis turbines with a runner discharge diameter of $D_s = 1.975$ m for a maximum flow rate of $Q = 25$ m³/s (per unit) and a gross head of $H_{gross}=199$ m. Although the net head of the power plant differs depending on the mode of operation, one unit or two unit operations, the nominal net head of turbine is 194 m. The manufacturer of the turbine with a rotational speed of 428.6 rpm is Neyrpic (now Alstom). There is a 7085 meter long horizontal energy tunnel which is connected to 371 meter long steel penstock with a surge tank whose function is to prevent water hammer phenomenon. Looking from the downstream, Kadincik I HPP discharges its water to upper reservoir of Kadincik II HPP; i.e. the tail water of Kadincik I is directly the headwater of Kadincik II (Figure 4.1).

Table 4.1 : Characteristics of Kadincik I HPP.

Description	Value	Unit
Location	Tarsus	-
Date of Operation	1971	-
Manufacturer of Turbine	Neyrpic	-
Number of the Unit	2	-
Nominal Power	35	MW/machine
Maximum Discharge	25	m ³ /s
Gross Head	199	m
Design Net Head	194	m
Rotational Speed	428.6	rpm
D_s	1.975	m

There is no on-site efficiency measurement available for Kadincik I HPP. Data from commissioning of the machine is the only reliable information about the power plant. Commissioning test results are presented in Table 4.2 and Table 4.3 (original figures in Appendix A). While Table 4.2 stands for single unit operation, Table 4.3 shows the results of parallel operation. As it is seen from these tables, discharge measurement was not conducted and net head was calculated with the head losses defined in the specifications of turbine. Because of the fact that there was no available flowrate information, turbine efficiency could not be determined. On the other hand, generator efficiency can be derived from Table 4.2 with the ratio of generator output power to the turbine shaft power. Then, average generator efficiency is found out as 96.44 %. This value was utilized to calculate shaft power for two-unit operation (Table 4.4).

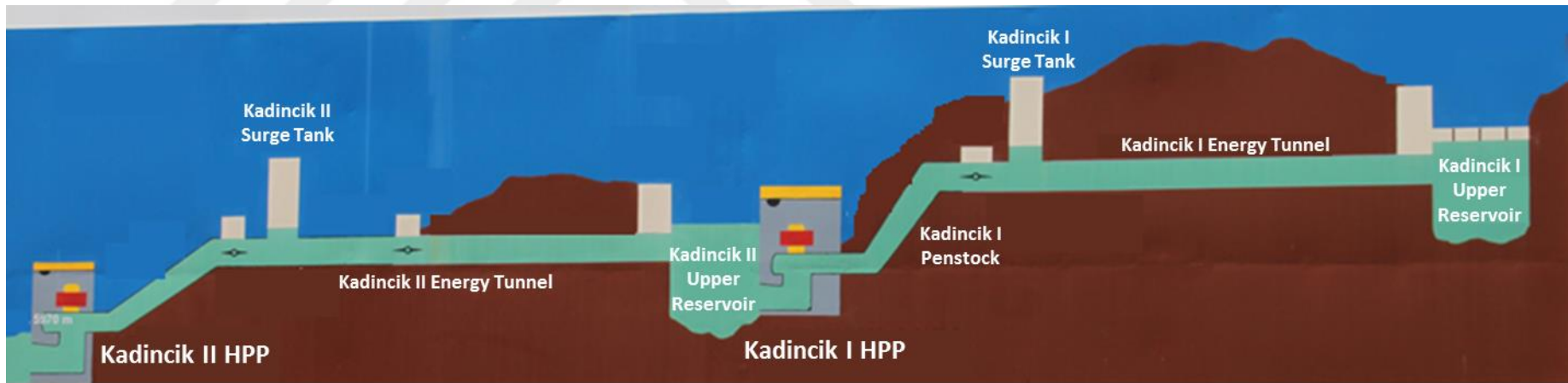


Figure 4.1 : Schematic view of Kadincik I and II power plant

Table 4.2 : Commissioning test results of Kadincik I HPP (single unit).

Generator Output [MW]	Shaft Power [HP]	Servo Piston Position		Upper Reservoir Level [m]	Tail Water Level [m]	Gross Head [m]	Head Losses [m]	Net Head [m]
		[%]	[mm]					
12.0	16700	30	72	406.5	206.7	199.8	1.0	198.8
18.0	25100	40	99	406.3	206.8	199.5	1.5	198.0
26.0	36200	50	131	406.3	206.9	199.4	2.6	196.8
31.0	43200	60	152	406.3	207.0	199.3	3.7	195.6
35.5	49300	70	178	406.2	207.0	199.2	4.8	194.4
40.0	53000	80	201	406.2	207.0	199.2	5.5	193.7
41.0	56500	85						
43.0	60000	90						

Table 4.3 : Commissioning test results of Kadincik I HPP (two units).

Total Generator Output [MW]	Generator 1 Output [MW]	Generator 2 Output [MW]	Servo Piston Position		Upper Reservoir Level [m]	Tail Water Level [m]	Gross Head [m]	Head Losses [m]	Net Head [m]
			[%]	[mm]					
40.0	30.0	10.0	30	75	405.9	206.1	199.8	6.2	193.6
45.0	30.0	15.0	40	97	405.9	206.1	199.8	8.0	191.8
55.0	30.0	25.0	50	127	405.8	206.1	199.7	12.0	187.7
60.0	30.0	30.0	60	149	405.7	206.2	199.5	14.3	185.2
62.0	30.0	32.0	70	175	405.6	206.3	199.3	16.6	182.7
65.5	30.0	35.5	80	199	405.6	206.3	199.3	17.5	181.8
66.0	30.0	36.0	85	211	405.6	206.3	199.3	18.0	181.3
68.5	30.0	38.5	90	223	405.4	206.3	199.1	19.5	179.6
70.0	30.0	40.0	98	-	405.4	206.3	199.1	21.0	178.1

Table 4.2 suggests that the turbine struggled with cavitation problems in overload. However, similar situation was not faced in parallel operation. In Figure 4.2, the net head is shown for one and two machine operation for the measurements in 1971. The actual tail water level is much higher today because of the operation of Kadincik II, started in 1974. Therefore, the gross head is 8.9 m lower and thus also the net head (see blue line in Figure 4.2).

Table 4.4 : Calculated shaft power for Kadincik I HPP.

Total Shaft Power [MW]	Shaft Power of Unit 1 [MW]	Shaft Power of Unit 2 [MW]	Servo Piston Position [%]	Servo Piston Position [mm]	Net Head [m]	Net Head with Actual TWL [m]
ONE UNIT OPERATION						
12.45	12.45	-	30.00	72.00	198.80	189.90
18.72	18.72	-	40.00	99.00	198.00	189.10
26.99	26.99	-	50.00	131.00	196.80	187.90
32.21	32.21	-	60.00	152.00	195.60	186.70
36.76	36.76	-	70.00	178.00	194.40	185.50
39.52	39.52	-	80.00	201.00	193.70	184.80
42.13	42.13	-	85.00	-	-	-
44.74	44.74	-	90.00	-	-	-
TWO UNIT OPERATION						
41.48	31.11	10.37	30.00	75.00	193.60	184.70
46.66	31.11	15.55	40.00	97.00	191.80	182.90
57.03	31.11	25.92	50.00	127.00	187.70	178.80
62.22	31.11	31.11	60.00	149.00	185.20	176.30
64.29	31.11	33.18	70.00	175.00	182.70	173.80
67.92	31.11	36.81	80.00	199.00	181.80	172.90
68.44	31.11	37.33	85.00	211.00	181.30	172.40
71.03	31.11	39.92	90.00	223.00	179.60	170.70
72.59	31.11	41.48	98.00	-	178.10	169.20

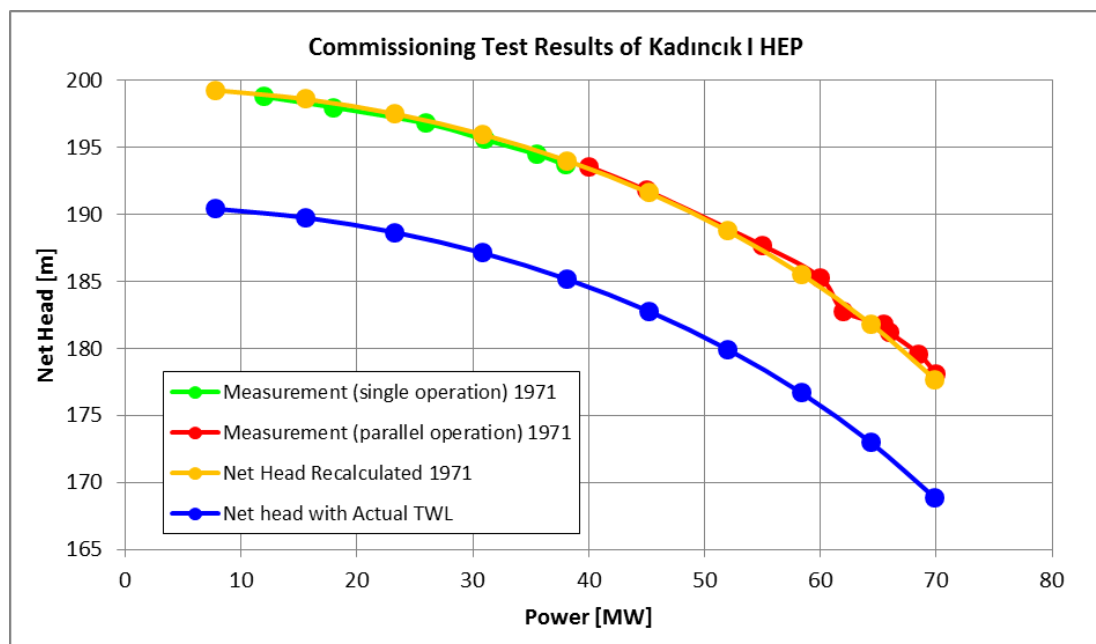


Figure 4.2 : Net head vs shaft power.

4.2 Geometry of Main Components

4.2.1 Laser scanning

There are one spare runner and two spare guide vanes in the power plant which are identical with the ones installed in the machine. Their point clouds were generated with FARO – Edge Laser Scan Arm in Polyworks 2014 software (Figure 4.3). In ideal case, tolerance level of the scan arm is around 0.064 mm; however, in the scanning of mechanical parts of Kadincik I HPP, maximum error was estimated approximately 1 mm due to considerable vibration in the power plant, repositioning of the scan arm (3 times) and the inevitable errors from calibration.



Figure 4.3 : Laser scanning studies in Kadincik I HPP.

Two different spare guide vanes were scanned. With the help of the horizontal planes created in Polyworks 2014, cross sections of these two guide vanes were extracted and compared with the technical drawings. It is concluded that two cross sections coming from laser scanning and the one in technical drawings do not differ from each other significantly. Therefore, one of the guide vane geometry scanned with laser scan arm was considered as real geometry of guide vanes. This one guide vane geometry was positioned according to the information in technical drawings and multiplied by 20 in order to reach the number of the guide vanes in existing unit. Fully open and fully closed guide vane positions were again adjusted in the light of technical drawings.

The 0° -position of the guide vane is at the closed guide vane position, where guide vanes are touching to each other. On the other hand, fully open position were determined with the help of the wicket gate opening a_0 . This term is defined as the diameter of the largest fictive cylinder that fits between two guide vanes (Figure 4.4). In the specification of the power plant, maximum wicket gate opening is designated as 0.125 meter, which corresponds to 22.5° maximum guide vane angle.

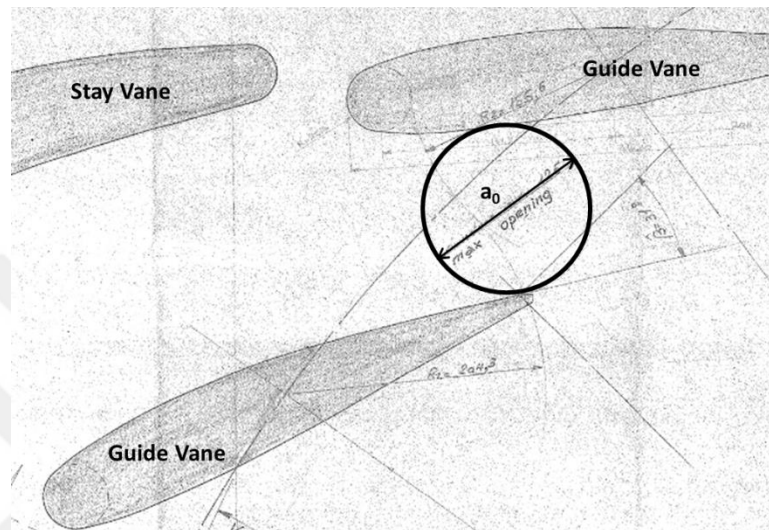


Figure 4.4 : Wicket gate opening.

The offset between the guide vane angle and the inflow angle was estimated as 1.9° in the CAD system as the direction of the chamber line at the leading edge against the profile (Figure 4.5). The relation between guide vane angle, inflow angle and wicket gate opening is revealed in Table 4.5.

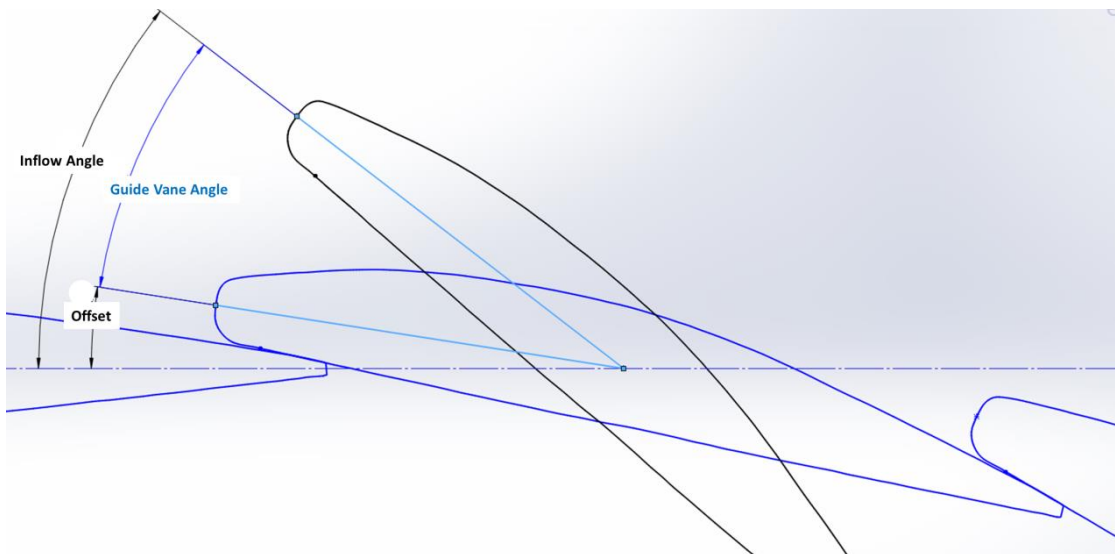


Figure 4.5 : Guide vane angle and inflow angle definition.

Table 4.5 : Guide vane flow angles for Kadincik I HPP.

Guide vane position [°]	Inflow angle [°]	a_0 [m]
0.00	6.60	0.000
7.50	14.10	0.044
10.00	16.60	0.058
12.50	19.10	0.072
15.00	21.60	0.086
17.50	24.10	0.099
20.00	26.60	0.112
22.50	29.10	0.125
25.00	31.60	0.138
27.50	34.10	0.150

Due to the fact that there was no technical drawing that gives a chance to get 3-D geometry of runner, three runner blades were scanned and compared with each other. Maximum deviation between the blades is around 5 mm. When the diameter of the runner (1975 mm) and the manufacturing technologies of 1970s are considered, 5 mm is negligibly small. Similar to the process conducted for guide vanes, one of the scanned runner blades was chosen, smoothed in Polyworks, positioned and multiplied. Afterwards, polygon model was generated from the point clouds and imported to Catia – Digitized Shape Editor Module in order to create turbo surfaces (Figure 4.6).

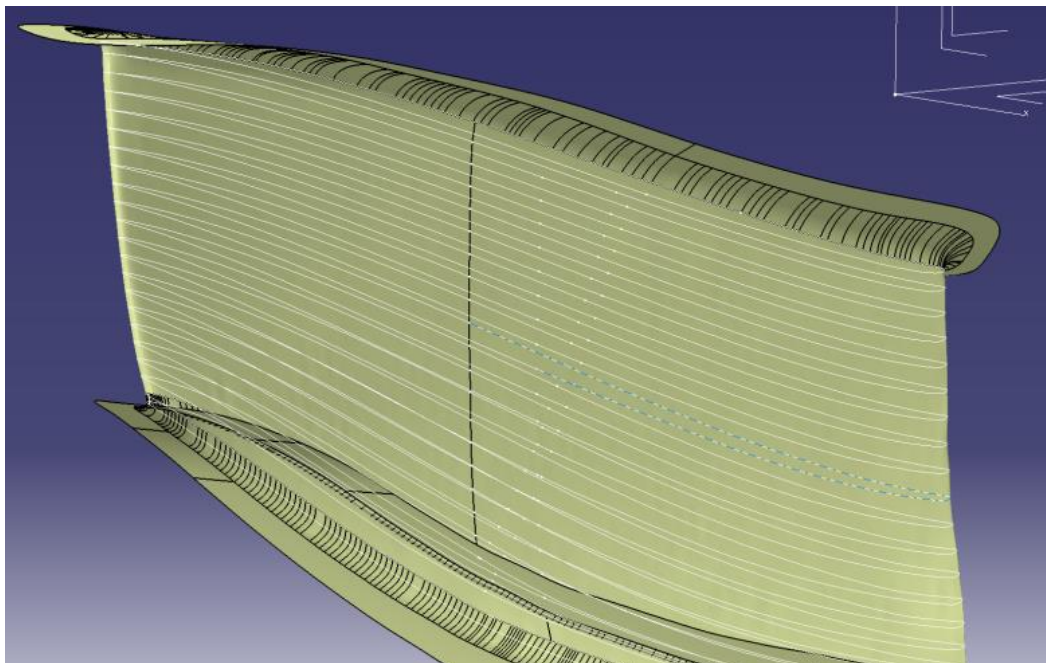


Figure 4.6 : Scanned geometry of runner blade.

4.2.2 CAD modelling

Spiral case, stay vanes and draft tube geometries were modelled under the guidance of technical drawings. Some unclear parts, such as cutwater region of the spiral case and concrete part of the draft tube, were clarified with an inspection inside the unit (Figure 4.7).



Figure 4.7 : Cutwater region of spiral case (left – reality, right – CAD model).

The origin of the coordinate system is determined as the intersection of the machine axis with a mid-plane, which is exactly the symmetry plane of the spiral case and the guide vanes. The positive z-axis was located in direction of the flow into the draft tube. Therefore, the machine rotates clockwise around the z-axis. The mass flow enters the spiral casing and leaves the draft tube in the negative x-direction.

An outblock was added after the draft tube in order to prevent the disturbances at the outlet region which occur when the outlet boundary condition is defined at the end of the draft tube [92]. This kind of outblock structure or draft tube extensions are frequently utilized in the literature to improve the quality of analysis and eliminate the back flows [93] - [96]. Another method to avoid these perturbations is to establish radial equilibrium to outlet boundary condition. Although outblock approach is used in the CFD analysis of Kadincik I HPP, CFD results of both methods are compared in the following sub-chapters.

Outblock behaves like an extension of the draft tube; however, its dimensions are a lot greater than this component. With this characteristic, outblock resembles to lower reservoir of power plant; however, its mission should not be confused with tail water.

4.3 Meshing

In general, for CFD calculation purposes, the free volume between the blades and the volumes of spiral case and draft tube have to be meshed and a fine mesh density is needed in the regions with high gradients of variables (e.g. velocity and pressure). As a result, fine grid density, so called inflation layers, is required close to the walls and the blade itself. Meshing of each domain was conducted separately and every domain had inflation layers in order to catch the boundary layer development.

Unstructured mesh, which was generated in ICEM CFD, was utilized for spiral casing because of its complex and unsuitable geometry for structured mesh (Figure 4.8). On the other side, draft tube and out block geometries were appropriate for a structured grid. Hence, they were meshed structurally in the same program with spiral case. Draft tube grid showed double butterfly (O-grid) blocking structure in cross section. It was segmented around elbow section in streamwise direction (Figure 4.10).

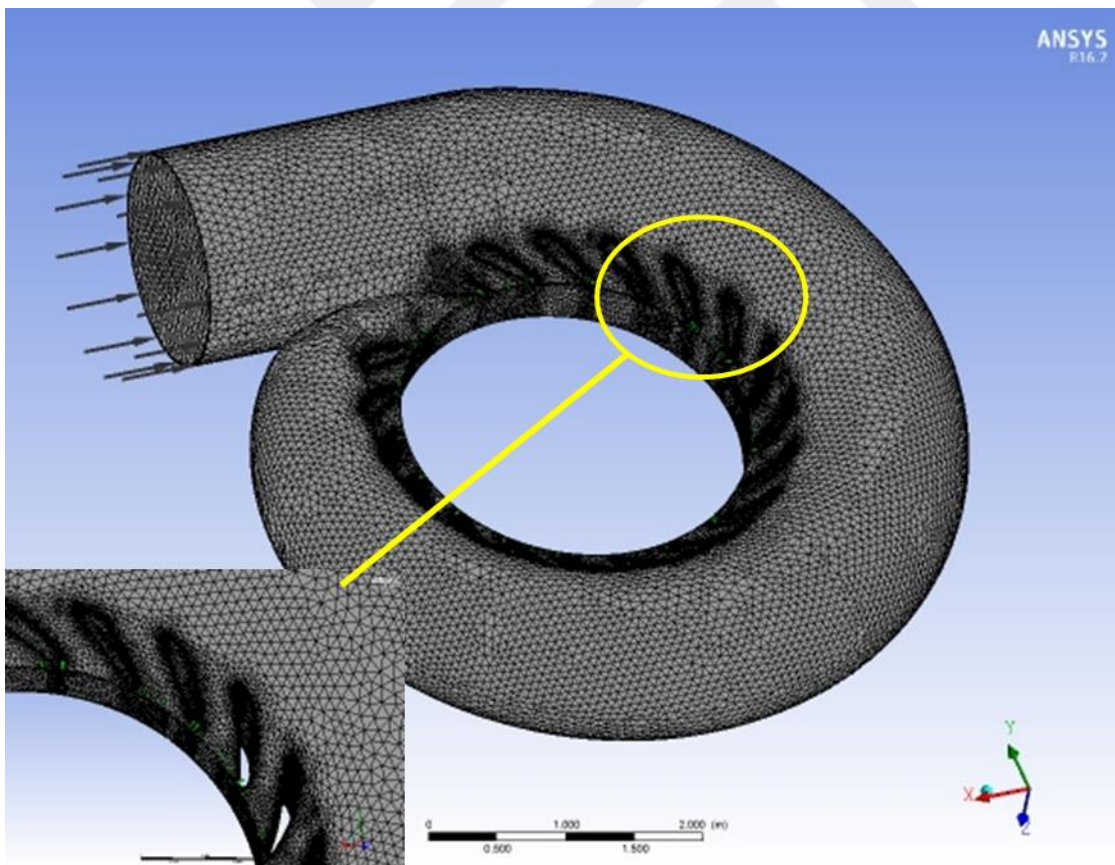


Figure 4.8 : Unstructured mesh of spiral case.

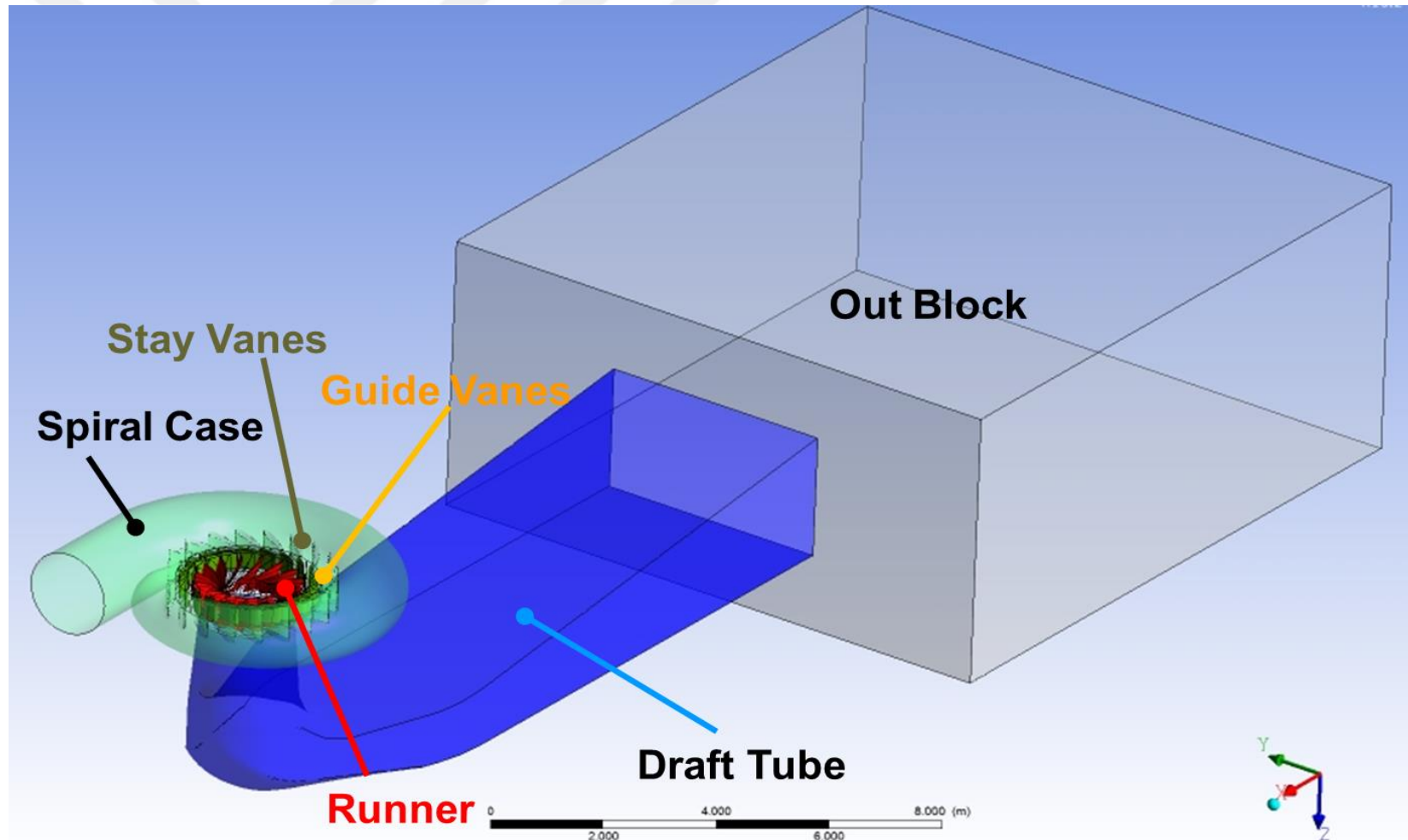


Figure 4.9 : CAD model of Kadincik I HPP.

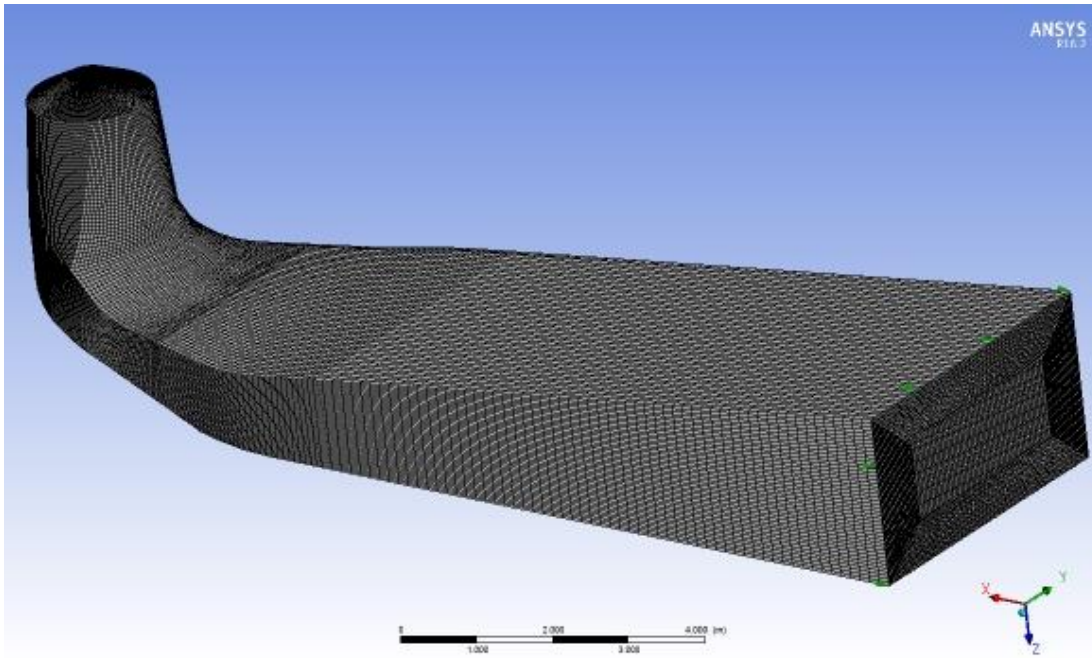


Figure 4.10 : Structural mesh of draft tube.

Formation of the structured guide vane and runner meshes was carried out in TurboGrid. HJCL topology (Figure 4.11) was preferred to prevent highly skewed elements at the leading edge of the blade. According to blade angle, HJCL topology configures surface blocking in some layers automatically. By taking full periodicity into account, mesh is generated with the help of these blocking layers. In this study, meshing was performed only for one guide vane and one runner blade, but then they were copied around machine axis.

y^+ determination is a significant step in meshing if the good quality mesh is desired because it is directly related with the boundary layer flow. Although it is impossible to observe y^+ values before CFD analysis, TurboGrid software needs target y^+ . The physical meaning and importance of this value are discussed in the following sub-chapters.

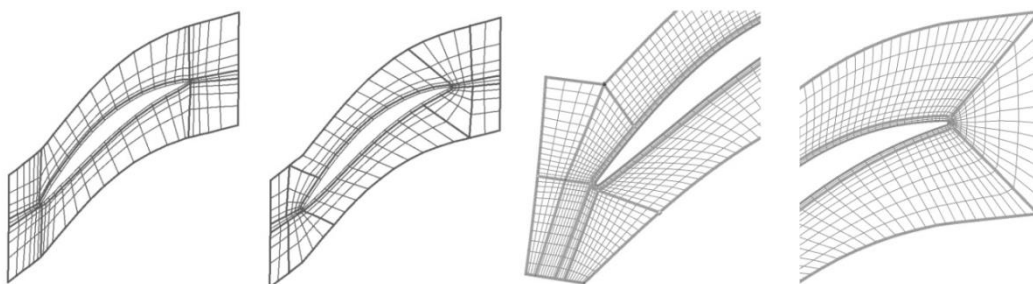


Figure 4.11 : H -, J-, L-, C- Topologies (from left to right).

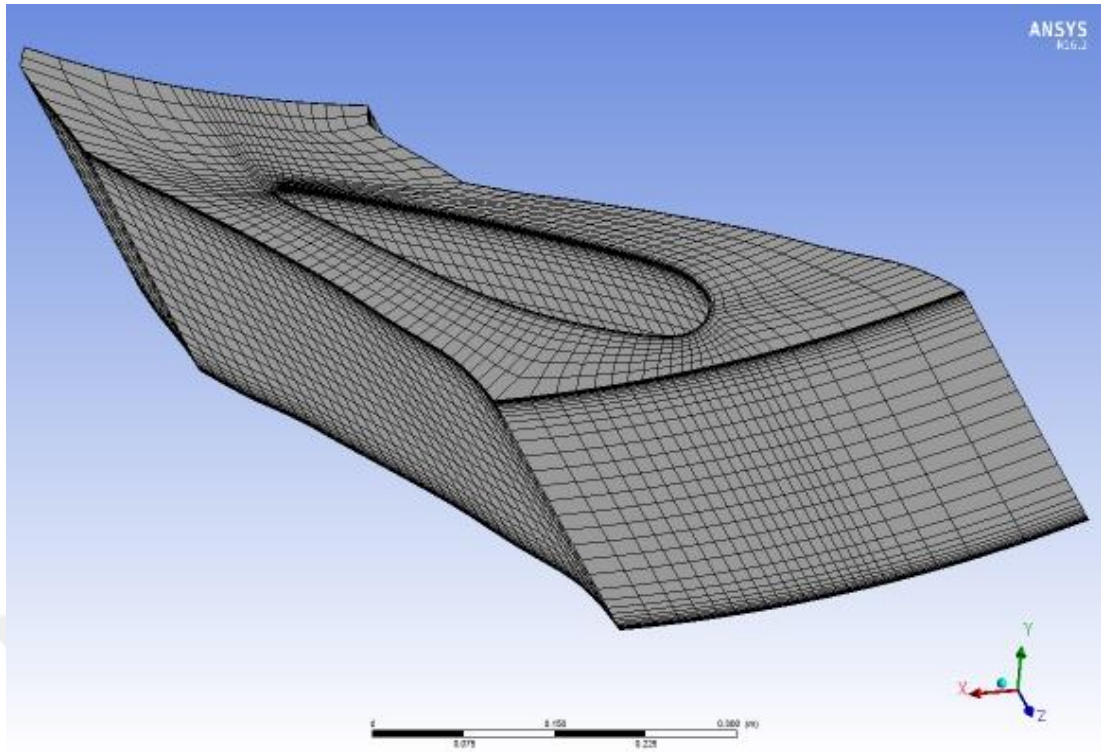


Figure 4.12 : Guide vane mesh.

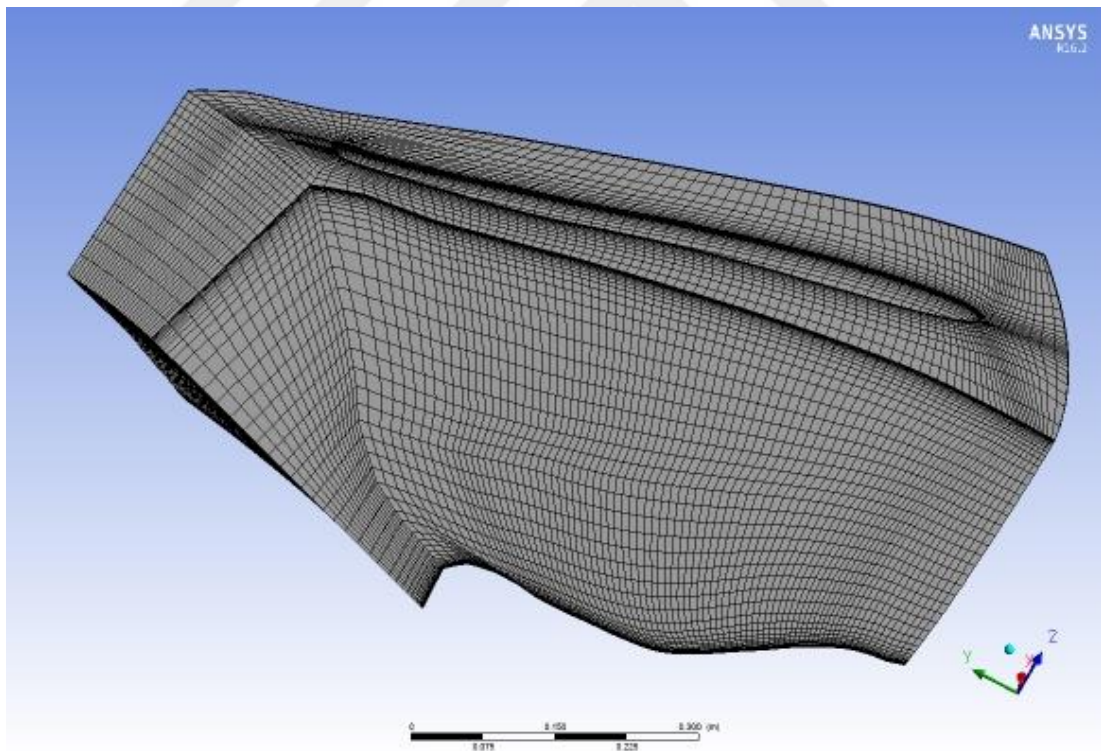


Figure 4.13 : Runner mesh.

A mesh independency study is realized for each component by establishing meshes with different densities for verification of mesh quality and calculation of convergence. Details of meshes for all components are given in Appendix B. The

changes in the mesh generation settings concerning y^+ and the numbers of layers are also included there. Finally, total number of the elements and the nodes for four different mesh configurations are summarized in Table 4.6 and Table 4.7. Mesh independency study, whose details can be followed from Appendix C, shows that the results are not changing considerably by any further improvement in mesh quality after the medium mesh density. Therefore, CFD analyses are conducted with medium meshes.

Table 4.6 : Number of the mesh nodes for Kadincik I HPP.

Domain	Coarse Million Nodes	Medium Million Nodes	Fine Million Nodes	Very Fine Million Nodes
Spiral Case	0.99	1.45	3.68	4.96
Guide Vanes	1.59	2.34	4.80	8.38
Runner	1.53	4.04	7.05	11.89
Draft Tube	1.36	2.25	3.47	5.42
TOTAL	5.47	10.08	19.00	30.65

Table 4.7 : Number of the mesh elements for Kadincik I HPP.

Domain	Coarse Million Elements	Medium Million Elements	Fine Million Elements	Very Fine Million Elements
Spiral Case	2.77	3.72	9.78	12.95
Guide Vanes	1.45	2.16	4.52	7.92
Runner	1.38	3.75	6.61	11.24
Draft Tube	1.33	2.20	3.41	5.35
TOTAL	6.93	11.83	24.32	37.46

4.4 CFD Model

4.4.1 Governing equations and turbulence modelling

Among three conservation laws (conservation of mass, momentum and energy), it is reasonable to apply only conservation of mass and momentum formulas for incompressible fluids, such as water. This simplification reduces the computation time in CFD analyses. The implementation of these laws results in well-known Navier-Stokes equations, which describes the fluid motion in space. Navier – Stokes’s equations for incompressible fluids in x-, y- and z-directions are presented in Equations (4.1) - (4.3). These three formulas can also be combined to one equation

in Equation (4.4) in which left hand side stands for total acceleration whereas first term of the right hand side corresponds to body forces, second term refers to pressure gradient and last term represents the viscous forces.

$$\rho \frac{Du}{Dt} = \rho g_x - \frac{\partial P}{\partial x} + \mu \left(\frac{\partial^2 u}{\partial x^2} + \frac{\partial^2 u}{\partial y^2} + \frac{\partial^2 u}{\partial z^2} \right) \quad (4.1)$$

$$\rho \frac{Dv}{Dt} = \rho g_y - \frac{\partial P}{\partial y} + \mu \left(\frac{\partial^2 v}{\partial x^2} + \frac{\partial^2 v}{\partial y^2} + \frac{\partial^2 v}{\partial z^2} \right) \quad (4.2)$$

$$\rho \frac{Dw}{Dt} = \rho g_z - \frac{\partial P}{\partial z} + \mu \left(\frac{\partial^2 w}{\partial x^2} + \frac{\partial^2 w}{\partial y^2} + \frac{\partial^2 w}{\partial z^2} \right) \quad (4.3)$$

$$\rho \frac{D\vec{V}}{Dt} = \rho \vec{g} - \nabla P + \mu \nabla^2 \vec{V} \quad (4.4)$$

While solving the Equation (4.4), turbulence model choice has considerable significance. Especially, its importance appears in flows dominated by boundary layer behavior.

Although flow itself shows a rather steady behavior in mean flow sense, turbulence eddies move unsteadily in three dimensions. However, steady state simulations are frequently preferred for engineering applications because they need less computational power, simulation time and most of the time only the time averaged expressions are under consideration [97].

Turbulence models can be classified into three main groups; no time averaging models, models directly solving the Reynolds stresses and eddy viscosity models. First model can be exemplified as Direct Numerical Simulation (DNS) and Large-Eddy Simulation (LES) [98]. Whereas DNS solves unsteady Navier-Stokes equations without any requirement of modelling, LES resolves the motion of the largest eddies and skips the smaller ones than the mesh density. Therefore, these two unsteady simulation methods need enormous computational power and time. Furthermore, in order to capture details, grid resolution should be high [97]. Similarly, models directly solving the Reynolds stresses are complex and very expensive with respect to the computational power and time because they establish extra terms, which means extra modelling. Finally, eddy viscosity models assume the exchange of turbulent energy to the molecular viscosity [98]. They are utilized to predict fluctuating components of Navier-Stokes equations which are divided into mean and fluctuating parts, whereas Reynolds Average Navier Stokes (RANS) equations

govern the mean flow. Steady state solutions are possible with RANS equations because they are time-averaged, but these models are not able to solve large eddies. Eddy viscosity models (RANS turbulence models) are the only way to simulate turbulent flows in steady state condition. Consequently, they are frequently preferred in engineering applications [97].

Eddy viscosity concept was first introduced by Joseph Boussinesq who related turbulence stresses with mean flow. Later, Ludwig Prandtl established the mixing length concept together with boundary layer. He stated that eddy viscosity must change from wall to the inside of the fluid. Today, RANS turbulence models based on Prandtl’s Mixing Length Concept are called algebraic models, such as Cebecci-Smith and Baldwin-Lomax [98]. These models give accurate responses to wall-bounded, attached flow fields with small pressure gradient. Subsequently, one equation models, such as Baldwin-Barth and Spalart-Almaras, became popular to solve turbulence kinetics. The advantage of these models on algebraic models is they can handle with the separation of the boundary layers. This is quite important because capturing separation means the designation of pressure losses and performance characteristics of turbomachinery components. With the improvements in technology and computational power, two equation turbulence models were introduced. They consist of two partial differential equations and can be listed as $k - \epsilon$, $k - \omega$ and Shear Stress Transport (SST) models.

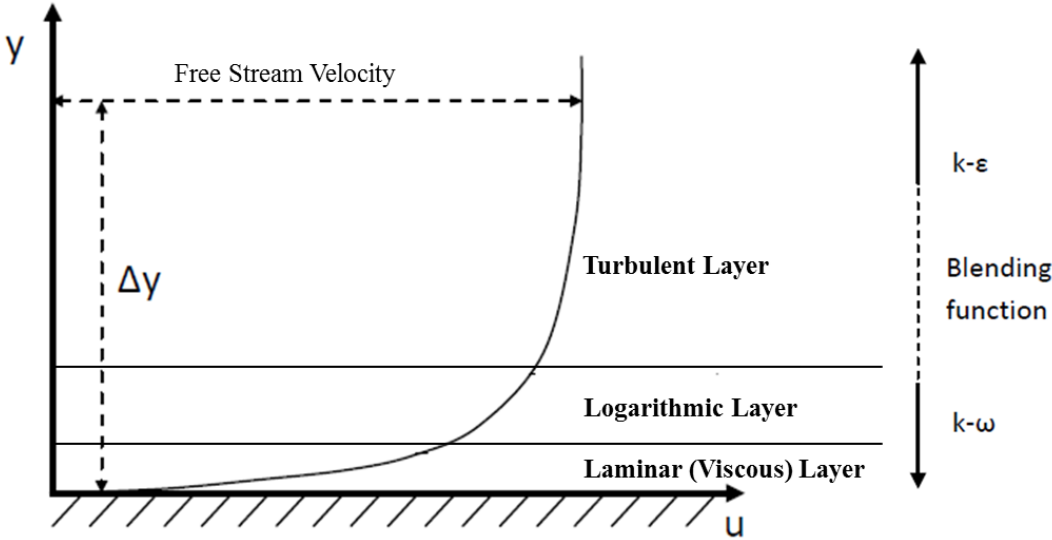


Figure 4.14 : Boundary layer illustration, adapted from [67].

The $k - \varepsilon$ turbulence model is regarded as an industry standard with respect to the stability and numerical robustness. The model proposed a correlation between turbulence viscosity and turbulence kinetic energy and energy dissipation [99]. It is applicable in the free stream area, but it has some limitations to cover boundary layer separation and swirling flows which occurs in the rotating flows through a curved surface [67]. However, the model is still widely preferred because it is the simplest turbulence model which provides good performance for many engineering application and it has been validated by many researchers [100].

To solve the problems occurs in $k - \varepsilon$ model within the viscous sublayer, $k - \omega$ turbulence model can be utilized because it provides accurate results in this sublayer with its near wall treatment for low Reynolds number calculations. It does not contain complex non-linear damping functions; therefore, it is more robust than $k - \varepsilon$. The $k - \omega$ turbulence model depends on the two transport equations proposed by Wilcox in 1986. While one stands for turbulence kinetic energy, the other one is used to find out turbulent frequency [99]. These two formulas bring new empirical terms and this causes more computational expense than $k - \varepsilon$. Furthermore, the $k - \omega$ model is valid only for y^+ values less than 2, where y^+ is a dimensionless number corresponds to the distance from wall to the first node, i.e. it is an indicator of mesh resolution. It is hard to sustain mesh resolution necessary for $k - \omega$ in every application; as a result, this brings some limitation to the method. For flow simulations with high Reynolds numbers, the viscous boundary layer is extremely thin. So, the amount of nodes in that region is very high and the cells in the same region become very flat (high aspect ratios) and thus convergence is poor. Finally, although $k - \omega$ shows better performance in the viscous sublayer, it is too sensitive in free stream region.

After deep looking into $k - \varepsilon$ and $k - \omega$ turbulence models, it can be stated that whereas $k - \varepsilon$ performs better in free stream region calculations, $k - \omega$ handles with separations in viscous sublayer more conveniently. Moreover, it can be easily seen that low Reynolds number approach brings severe restrictions on the grid generation and sometimes it is even impossible to create such meshes. Menter [101] saw this problem and came up with a new turbulence model called Shear Stress Transport (SST) model. SST uses an automatic smooth switching mechanism from $k - \omega$ to $k -$

ε through the boundary layer. In other words, $k - \omega$ turbulence model is utilized near to the wall, while $k - \varepsilon$ turbulence model is preferred in the free stream area (Figure 4.14). The transition between the turbulence models are provided gradually with the help of a blend factor. Moreover, Menter [102] proposed an automatic wall treatment instead of purely low Reynolds number approach. This treatment benefits from the known solutions of ω in viscous and logarithmic sublayers. By using the blending approach between these solutions, Menter made the results insensitive to the wall mesh refinement. In fact, SST turbulence model does not need low y^+ . The y^+ values less than 300 are adequate for the validity of the automatic wall function.

4.4.2 Chosen methodology

The Navier-Stokes equations were solved with Reynolds Averaged Navier Stokes (RANS) formulation in the commercial CFD software ANSYS CFX. The instantaneous time averaged variables are decomposed into mean and fluctuating values with the help of a Reynolds decomposition.

Menter's SST turbulence model with automatic wall functions was applied. For the regions where the mesh resolves the viscous sub-layer the Low Reynolds model is utilized and for the other regions the logarithmic wall functions are benefited by ANSYS CFX solver. Thus, the y^+ value of the meshes is of minor importance.

Three governing equations coming from Navier-Stokes and two additional equations derived from turbulence model have been analytically solved. The solver uses a control volume based technique during the conversion of the governing equations to algebraic equations and solves the governing equations sequentially [103].

The CFD code (ANSYS CFX) utilizes a cell-centered control volume with identical nodes for velocity and pressure (collocated grid approach). For advection scheme high resolution was chosen rather than upwind in order to get better accuracy. In High Resolution Scheme, blend factor changes between one and zero. If there is a dramatic change between values at cell centers, blend factor becomes around zero. Contrary, blend factor is about one at the regions where values at the cell centers are relatively small. This feature makes High Resolution Advection Scheme second order accurate whereas Upwind Advection Scheme is first order.

All CFD analyses were conducted for steady state conditions in order to decrease computation time dramatically. If the proper timescale is chosen, it is possible to get

convergence in 1000 iterations for steady state analysis. In most cases, automatic timescale factor is enough for convergence. However, unless the convergence can be achieved by automatic way, timescale factor should be defined as a function and after 100 iterations it can be increased. Observing RMS values for convergence may be misleading sometimes. Therefore, stability of efficiency, flowrate and head values is assumed as an indicator of convergence.

For the runner, an additional approach called MFR (Multiple Frame of References) with the assumption of steady state incompressible fluid was utilized. This approach is simply a steady state approximation for individual cell zones moving in different rotational speeds [104]. At the interfaces between cell zones, flow variables in one zone are taken in the calculation of fluxes at the boundary of the neighboring zone by applying a local reference frame transformation [105]. MFR does not consider the grid as fixed for computation. Instead of that, it freezes the motion of the moving part in a specific position and observes the instantaneous flowfield with the rotor in that position [105]. It is reasonable to apply this approach to the interfaces heavily depend on the velocity formulation because the vector quantities, such as velocity and velocity gradients, vary with the change in reference frame. On the other hand, scalar variables (pressure, density etc.) need no special treatment across the interface between moving and stationary domains.

MFR approach changes the formula for conservation of momentum. While the velocity related terms take a different form from the absolute velocity formulation for steadily rotating frame, other terms remain same also in the relative velocity formulation for steadily rotating frame. The appearances of the equations in these two methods are presented in Equations (4.5) and (4.6).

$$\frac{\partial}{\partial t}(\rho\vec{V}) + \nabla \cdot (\rho\vec{V}_r\vec{V}) + \rho(\vec{\omega} \times \vec{V}) = -\nabla P + \nabla\bar{c} + \vec{F} \quad (4.5)$$

$$\frac{\partial}{\partial t}(\rho\vec{V}) + \nabla \cdot (\rho\vec{V}_r\vec{V}_r) + \rho(2\vec{\omega} \times \vec{V}_r + \vec{\omega} \times \vec{\omega} \times \vec{r}) = -\nabla P + \nabla\bar{c} + \vec{F} \quad (4.6)$$

With these settings listed above, CFD model of the Kadincik I HPP (Figure 4.15) is prepared. CFD model consists of spiral case, stay vanes, 24 guide vanes, 15 runner blades, draft tube and out block. Water enters to the turbine from the inlet of the spiral case. Spiral case mesh is followed by guide vane meshes, which are rotationally copied 23 times (in total 24 guide vanes), and the interface in between

these domains is defined as a general grid interface (GGI). On the other hand, each guide vane mesh is connected to each other with 1:1 grid interface, which is also used between runner blade meshes multiplied 14 times in rotation axis. The mesh of runner domain consists of main block and out block which are linked also with 1:1 grid interface. Guide vane and runner domains, as well as runner and draft tube domains, are connected with frozen rotor interface in order to introduce MFR approach to the rotating elements. Frozen rotor interface is especially beneficial when the circumferential flow variation that every blade passage experiences is large during a full revolution. With the assumption of quasi-steady flow around the rotating component at each rotation angle, computations are performed in steady state mode by including the rotational effects, such as Coriolis and centrifugal terms, in rotating domains. Out block domain was connected to downstream of draft tube with GGI.

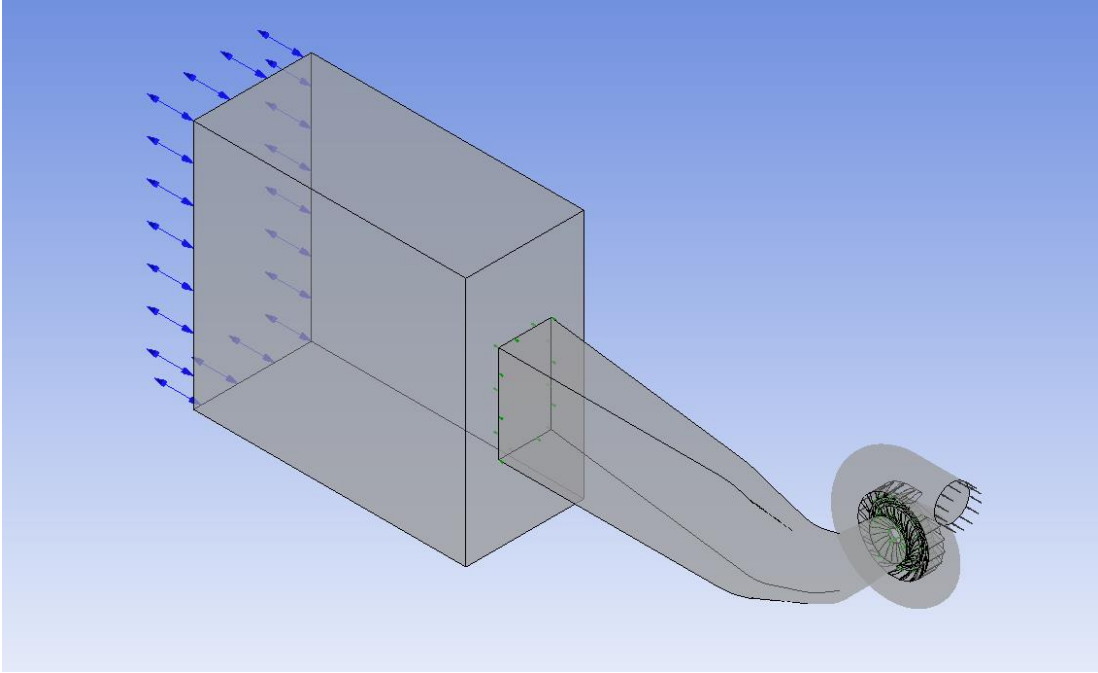


Figure 4.15 : Kadincik I HPP CFD flow domain.

4.4.3 Boundary conditions

Water enters to the turbine from the inlet of the spiral case; hence, inlet boundary condition, which is total pressure, is defined at this surface. Inlet total pressure is adjusted according to outlet boundary condition, which is introduced as one bar static pressure. The aim is to get the desired net head in the CFD analysis, where net head is defined as total pressure difference between inlet and outlet. The result of this

analysis gives the discharge value; therefore, it is possible to check the achieved net head at that configuration and necessary modifications should be done at inlet boundary condition until desired net head value is obtained.

Although definition of inlet boundary condition at the entrance of the spiral case is not a controversial topic, there is no generally accepted method for establishment of outlet boundary condition. However, widely preferred idea is to define outlet boundary condition directly at the end of the draft tube. While some of the advocates of this idea adopt the constant static pressure over the outlet approach, others utilize radial equilibrium for pressure distribution. Despite of the fact that constant static pressure at the outlet is not realistic in hydropower applications, its impact on the flow is damped before the elbow section of the draft tube [106]. Therefore, this approach can be proper provided that flow upstream of the elbow section of draft tube is under investigation. On the other hand, radial pressure equilibrium boundary condition assigns the specified static pressure only to the position of minimum radius with respect to the axis of the rotation. The static pressure at the rest of the boundary is distributed with the assumption of negligible radial velocity. Therefore, pressure distribution at the outlet is governed by circumferential velocity, Equation (4.7).

$$\frac{dP}{dr} = \rho \frac{c_u^2}{r} \quad (4.7)$$

When a large swirling component is present in the flow, it is proper to define radial static pressure distribution at the outlet. Consequently, this approach is commonly used in turbomachinery applications where a swirling flow is created by a rotor and is not recovered with a mechanical component, such as a stator [107]. If the hydropower applications are considered, this approach is faced with some obstacles. First of all, in optimum operation conditions, swirling component of the flow is damped in the draft tube. Even if the turbine operates at extreme part load, large swirls cannot reach to the draft tube outlet. Moreover, draft tube outlet is placed in a fix position from the machine axis. In other words, every point at the outlet surface has the same radial distance from the rotation axis. As a result, minimum radius determination can be misleading. Finally, even radial equilibrium approach is not adequate for the elimination of back flows.

Another idea regarding outlet boundary condition of a Francis turbine is to add an out block, which has a greater volume than the draft tube, at the end of the draft tube and establish the average static pressure boundary condition to the outlet of the out block in order to eliminate the disturbances and the back flows occur in the draft tube domain [92] - [96]. This approach enables the fluid to flow freely from the draft tube outlet, which is the actual situation in a hydropower plant. Although there exists some back flows and perturbations in the flow due to the average static pressure definition at the end of the out block, these undesired phenomena are damped inside the out block and cannot reach the draft tube outlet thanks to huge geometry of out block; therefore, turbine performance is not affected from outlet boundary condition.

For the CFD analysis of Kadincik I HPP, both radial equilibrium and out block approaches were tested for design net head. With the same inlet boundary conditions, same static pressure was imposed at the end of the draft tube with radial equilibrium and at the end of the out block with average static pressure option. Different operation conditions were realized with the help of the different guide vane openings. Numerical results for both approaches are displayed in Table 4.8. From this table, it can be concluded that turbine performance parameters are quite close to each other for all operation conditions, which suggests that there is no need to increase computational time with a massive out block structure. However, when static pressure distribution at the outlet of the draft tube and the streamlines inside the domain are observed (Figure 4.16 - Figure 4.18), it reveals that flow shows more realistic behavior with out block than the one in radial equilibrium. In Figure 4.16, which stands for optimum operation condition, it is hard to see any difference between two approaches because the flow shows a favorable trend at best efficiency point. Nevertheless, in extreme part load (Figure 4.17) and overload (Figure 4.18), fluid flow is expected to be concentrated on one side of the draft tube wall because in these conditions either remaining energy is delivered from the runner or excessive energy is taken from the fluid. These situations can be observed in the models with out block geometry and corresponding static pressure distributions take the form according to these phenomena. On the other hand, radial static pressure distribution forces the flow to be stable at the end of the draft tube. The flow becomes quite uniform after a certain distance from elbow section unrealistically. Resulting static

pressure distributions at the end of the draft tube prove these extra ordinary situations.

Table 4.8 : Numerical results for different outlet boundary conditions.

Operation Condition	Outlet Boundary Condition	Net Head [m]	Discharge [m ³ /s]	Numerical Hydraulic Efficiency [%]
Part Load (7.5 degree guide vane angle)	Radial Equilibrium	194.0	11.1	85.3
	Out Block	194.1	11.1	85.1
Best Efficiency Point (15 degree guide vane angle)	Radial Equilibrium	193.8	20.7	92.8
	Out Block	194.1	20.8	92.8
Over Load (22.5 degree guide vane angle)	Radial Equilibrium	193.7	27.2	88.8
	Out Block	194.1	27.1	88.7

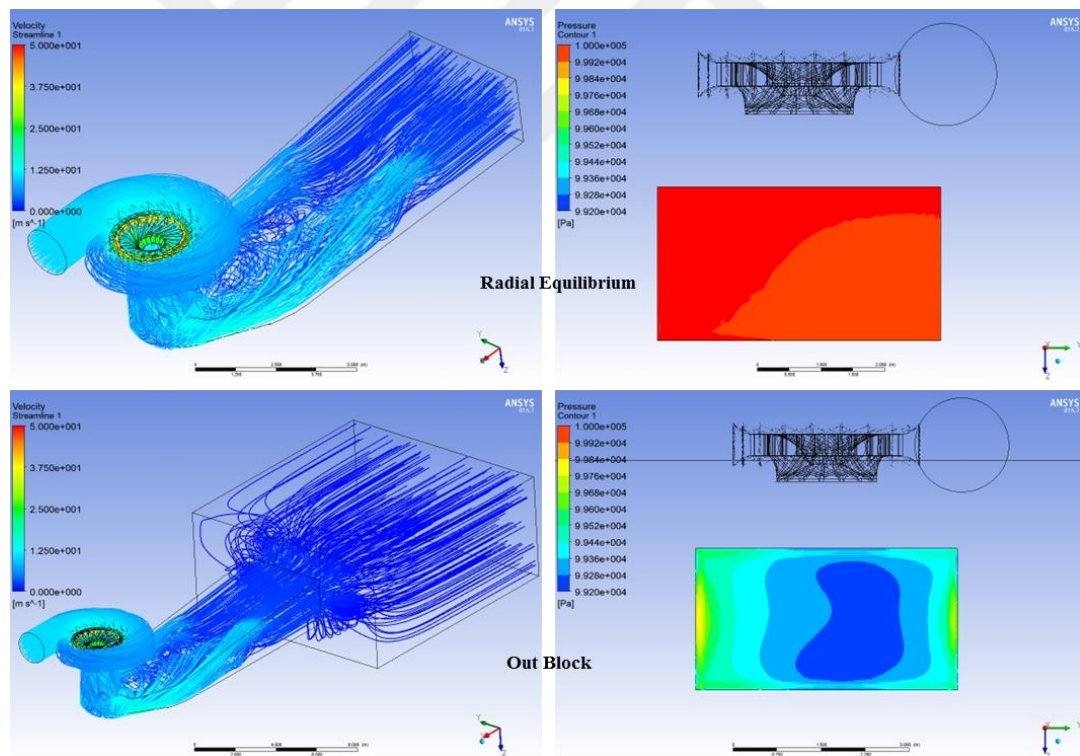


Figure 4.16 : Streamlines and static pressure distribution at the draft tube outlet for different outlet boundary conditions at best efficiency point (15° guide vane angle).

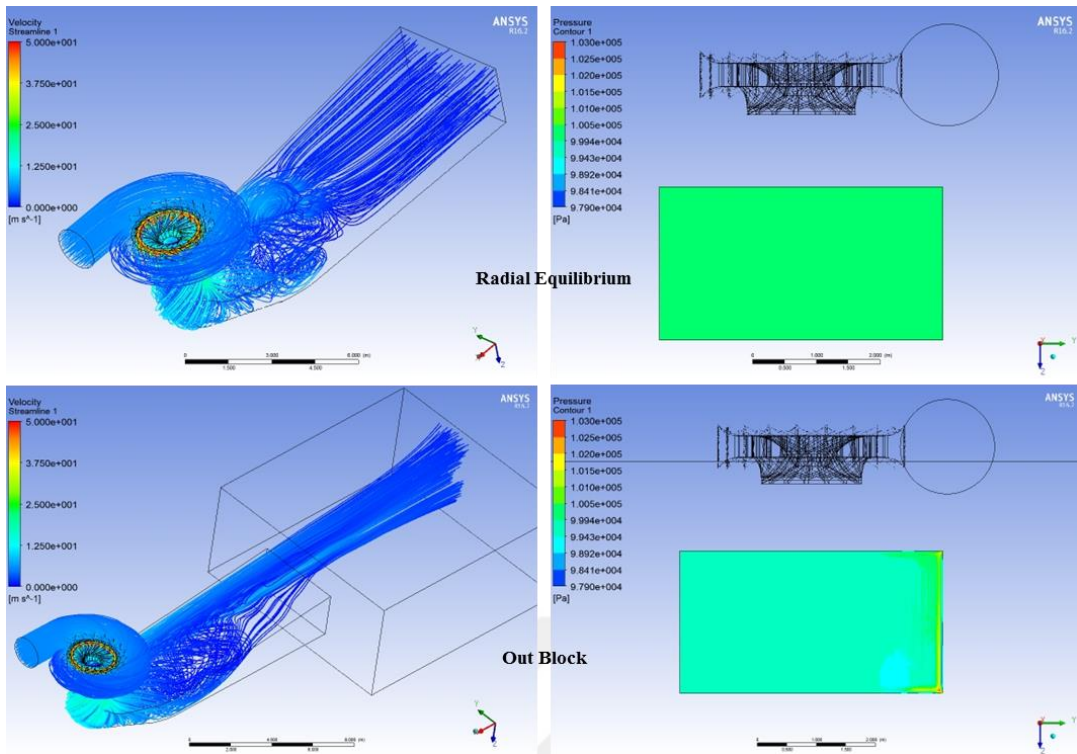


Figure 4.17 : Streamlines and static pressure distribution at the draft tube outlet for different outlet boundary conditions at extreme part load (7.5° guide vane angle).

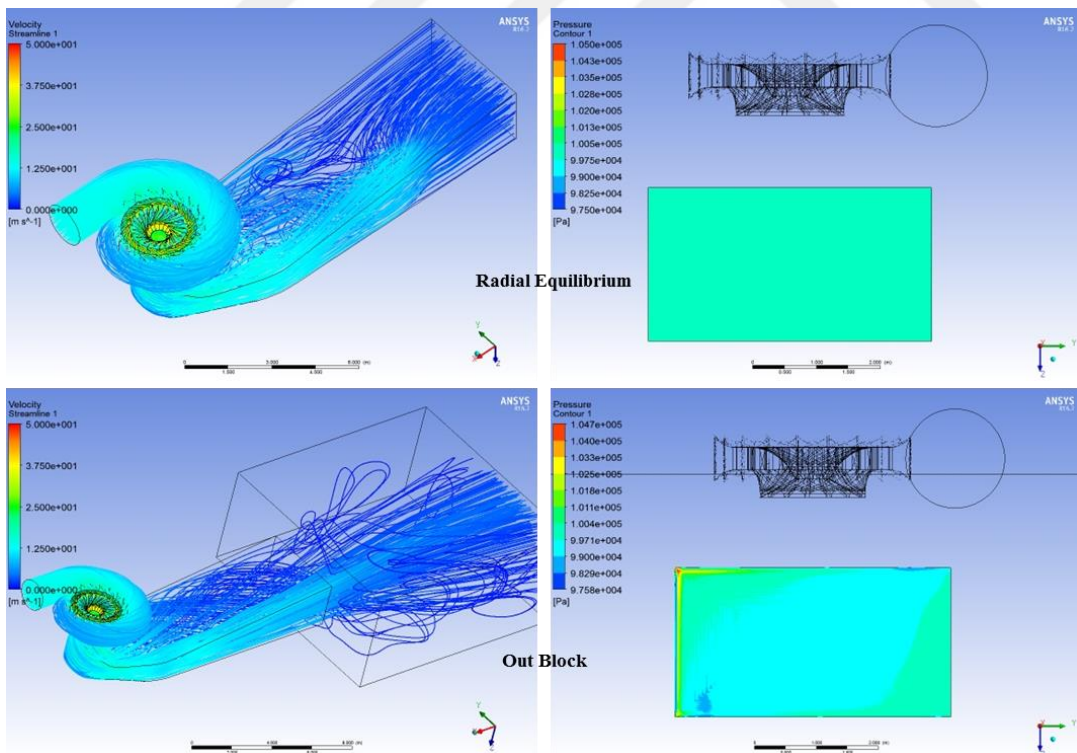


Figure 4.18 : Streamlines and static pressure distribution at the draft tube outlet for different outlet boundary conditions at over load (22.5° guide vane angle).

To sum up, out block approach was applied for CFD analysis of Kadincik I HPP. Instead of defining outlet boundary condition at the end of draft tube, one bar static pressure was introduced at the outlet of the out block as opening pressure. Inlet boundary condition was defined to the entrance of spiral case as total pressure.

4.5 Evaluation of the CFD Results

4.5.1 Overall performance definitions

In the evaluation of the performance of existing unit, following terms, which are mass flow averaged, and formulations were frequently used. Initially, IEC 60041 standard defines the net head as the difference between total pressure at the inlet of the spiral case and the total pressure at the draft tube outlet, which is the summation of static pressure and velocity head at that region, Equation (4.8). Turbine hydraulic efficiency is taken from the same standard as the ratio of the shaft power and the available hydraulic power, Equation (4.9). To see the performance of each component separately, a head loss analysis, i.e. efficiency splitting, is conducted. In this process, total pressure difference between the inlet and the outlet of each domain corresponds to head loss of this component, Equation (4.10). To divide this value by the inlet total pressure results in percentage losses (Equation (4.11)), which can be considered as the reverse of the component efficiency, Equation (4.12). Nevertheless, this approach is not valid for the runner because the runner takes energy from the water. Therefore, this issue should also be considered in the runner head loss, Equation (4.13), and the runner hydraulic efficiency, Equation (4.14). In the end, cumulative performance of the existing unit was obtained, which is nothing but the same thing with turbine efficiency, Equation (4.15).

$$H_{\text{net}} = \frac{P_{t,i} - P_{t,o}}{\rho g} = \frac{P_{t,i} - \left(P_{s,o} + \frac{\rho}{2} \left(Q/A_o \right)^2 \right)}{\rho g} \quad (4.8)$$

$$\eta_h = \frac{T * \omega}{\rho g Q H_{\text{net}}} \quad (4.9)$$

$$H_{\text{loss},i} = \frac{(P_{t,i} - P_{t,o})_i}{\rho g} \quad (4.10)$$

$$H_{\text{loss},i,\%} = \frac{(P_{t,i} - P_{t,o})_i}{P_{t,i}} \quad (4.11)$$

$$\eta_i = 1 - H_{\text{loss},i,\%} \quad (4.12)$$

$$H_{\text{loss},r} = \frac{(P_{t,i} - P_{t,o})_r}{\rho g} - \frac{T * \omega}{\rho g Q} \quad (4.13)$$

$$\eta_r = \frac{\frac{T * \omega}{Q}}{(P_{t,i} - P_{t,o})_r} \quad (4.14)$$

$$\eta_h = 1 - \frac{\sum H_{\text{loss}}}{H_{\text{net}}} = 1 - \frac{H_{\text{loss},s} + H_{\text{loss},g} + H_{\text{loss},r} + H_{\text{loss},d}}{H_{\text{net}}} \quad (4.15)$$

In the cavitation performance investigation, a static histogram analysis is utilized to find out minimum blade pressure. With the help of this minimum pressure value and Equation (4.16), turbine Thoma number is calculated for that operation point. On the other hand, Equation (4.17) establishes plant Thoma number, whose formulation assumes the vapor pressure as minimum runner blade pressure and also takes the altitude of the machine axis against the tail water level into account.

$$\sigma_{T,\text{his}} = \frac{P_{t,o} - P_{\text{his}}}{\rho * g} \quad (4.16)$$

$$\sigma_p = \frac{\frac{(P_{t,o} - P_{va})}{\rho * g} - (Z_{\text{TWL}} - Z_M)}{H_{\text{net}}} \quad (4.17)$$

4.5.2 Evaluation of CFD results at design head

First, CFD simulations were conducted for a net head of 194.1 meter, which is the design net head of the machine. Variation of the flowrate is provided with the variation of the wicket gate angles. The overall performance is displayed in Figure 4.19 for hydraulic efficiency, power production and cavitation performance. Furthermore, head losses of all components are visualized in Figure 4.20 to see the performance of each component separately. Finally, these losses are converted into hydraulic efficiencies with the help of the (4.12) and (4.14). This gives a chance to

observe where the mechanical parts of the turbine reach their peak efficiencies (Figure 4.21).

Figure 4.19 concludes that best efficiency point of the turbine is around 21 m³/s flowrate for 194.1 meter net head, which corresponds to 15° guide vane opening. Therefore, 21 m³/s should be accepted as design flowrate of the turbine. Power production increases almost linearly up to 27.5 m³/s discharge; however, after this point, no considerable elevation is observed in power. The cavitation performance is also presented in Figure 4.19. Cavitation risk was observed after the flowrate of Q = 25 m³/s because in this region the cavitation coefficient σ_T is greater than the σ_P . Nevertheless, it is very rare to see discharge values greater than 26 m³/s at the power plant and the maximum flowrate of the turbine is designated as 25 m³/s. Consequently, it can be stated that turbine already shows a good performance regarding to cavitation. This good cavitation characteristic is most probably a result of the elevation of the tail water level due to the construction of Kadincik II HPP because the increase in the tail water level means the increase in the plant Thoma number which provides wider cavitation free operation range.

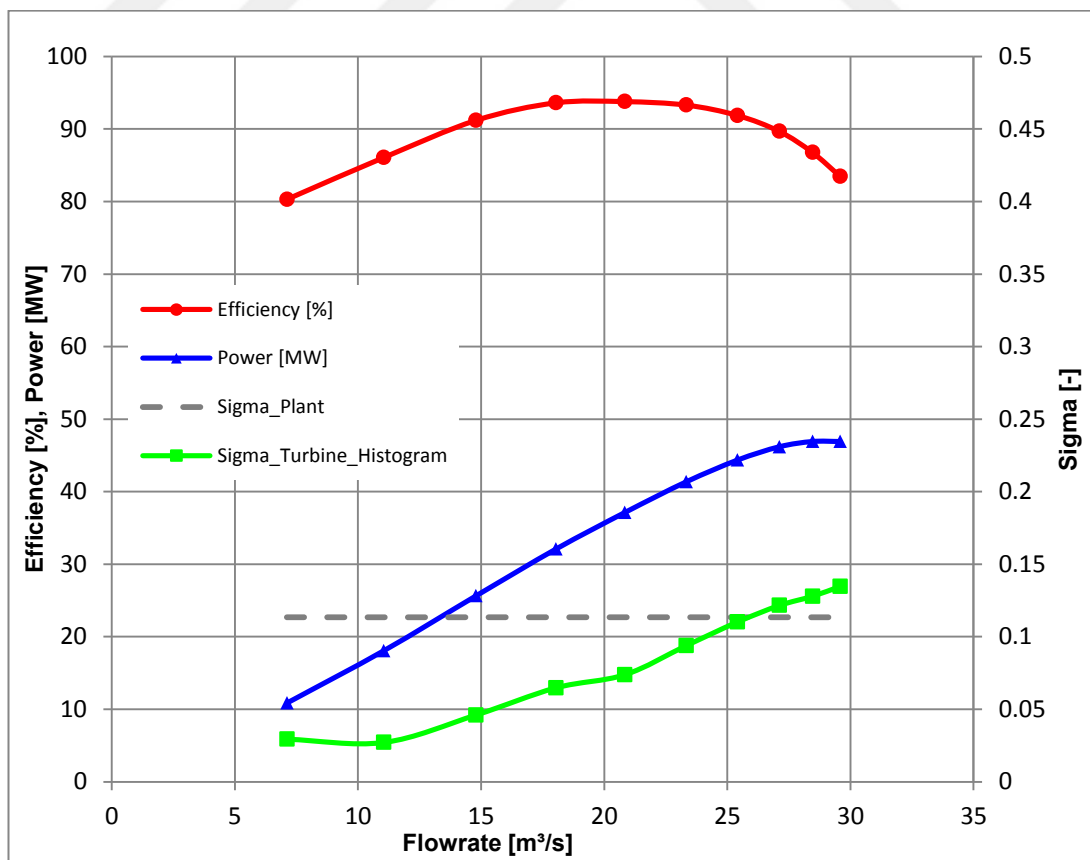


Figure 4.19 : The overall CFD performance of Kadincik I HPP at design head.

In Figure 4.20 and Figure 4.21, the hydraulic efficiency and percentage head loss for each component is shown separately. Efficiencies of spiral case and stay vanes were decreasing with an increase in flowrate. On the contrary, the increase in the efficiency of the guide vane continues until the full load. In general, best efficiency points of guide vane, runner and draft tube should coincide and be around 80 % of the full load. Efficiencies of the runner and the draft tube show a different pattern than the other mechanical parts. While runner efficiency gets its top value around 22.5 m³/s flowrate, this peak is seen at a flow rate of about Q = 18 m³/s in draft tube. After then, both efficiencies start to lower. In brief, every mechanical component attains its best efficiency at different operation conditions, which is against the characteristics of a proper Francis turbine design.

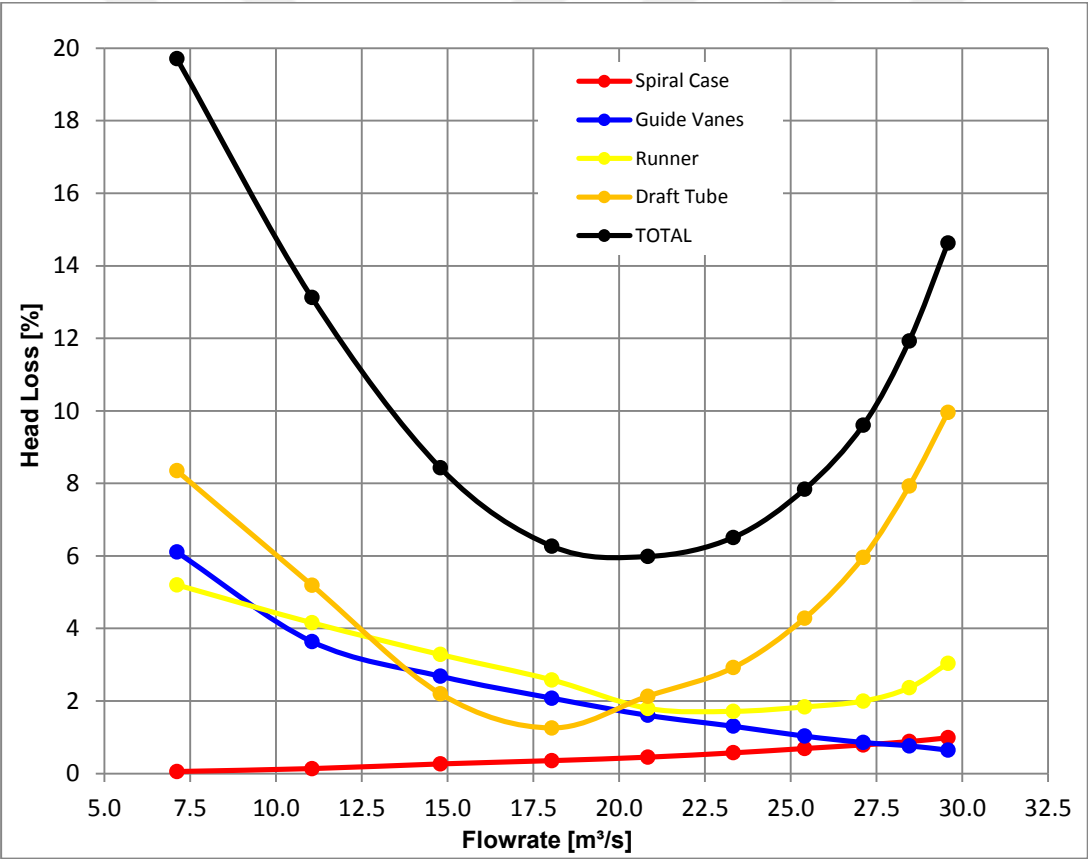


Figure 4.20 : CFD percentage head losses of mechanical components.

All the results presented in Figure 4.19, Figure 4.20 and Figure 4.21 are coming from the CFD analysis with medium mesh density. As it is already stated, SST turbulence model is preferred and this model provides automatic wall functions to resolve boundary layer flow. In order the automatic wall functions to be activated, maximum y^+ should be less than 300. Therefore, y^+ values are investigated at the end of the

CFD analysis and it was observed that y^+ greater than 55.7 is not faced in the model. Contour plots of the y^+ can be reached from Appendix D.

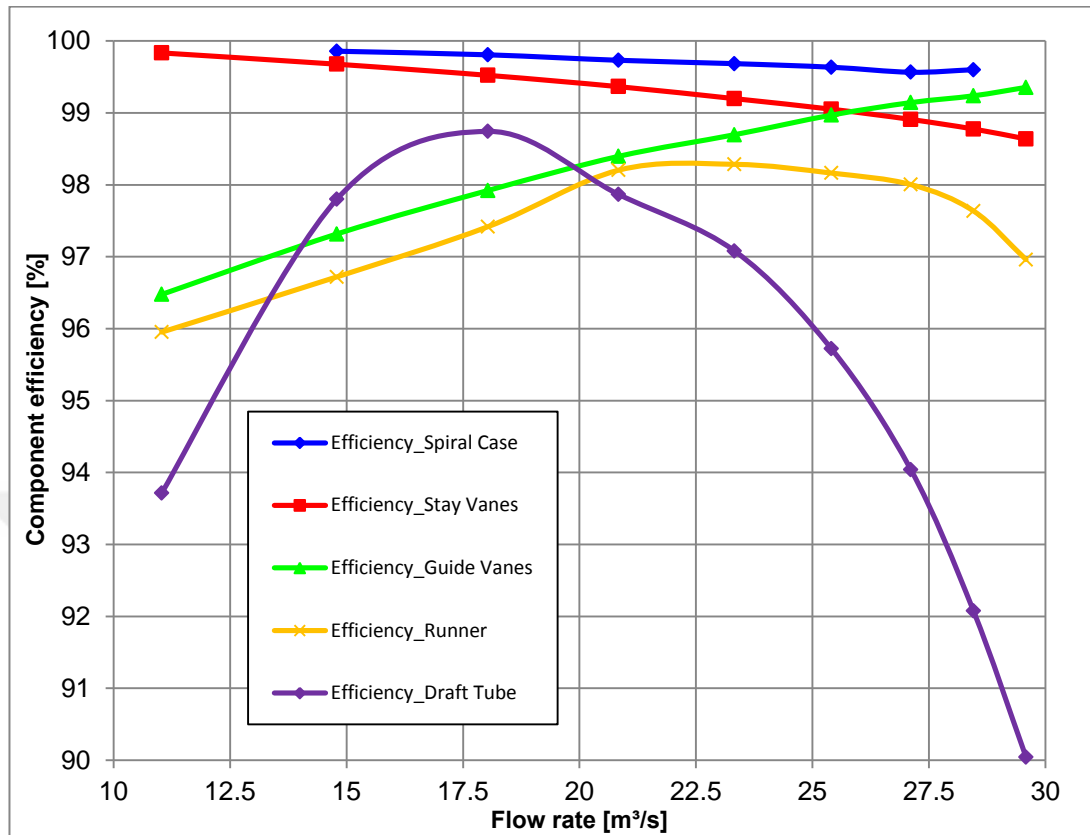


Figure 4.21 : CFD single component efficiencies for Kadincik I HPP.

Although peak efficiencies of components are reached at different flowrates, turbine attains its overall best efficiency is around $21 \text{ m}^3/\text{s}$. This value is also consistent with the literature, which suggests that turbine maximum efficiency should lie between the 80 % and 90 % of the maximum discharge. As a result, each mechanical component is further investigated at 194.1 meter net head and $21 \text{ m}^3/\text{s}$ flowrate in detail.

4.5.3 Spiral case

To evaluate the design of the spiral case, several uniformly distributed planes are generated rotationally around the machine axis (Figure 4.22). Up to 345° , a plane is placed at every 15° angle. Then, three additional parallel planes are constructed to cover inlet portion of the spiral casing. Rotationally created planes include the stay vane region in the middle.

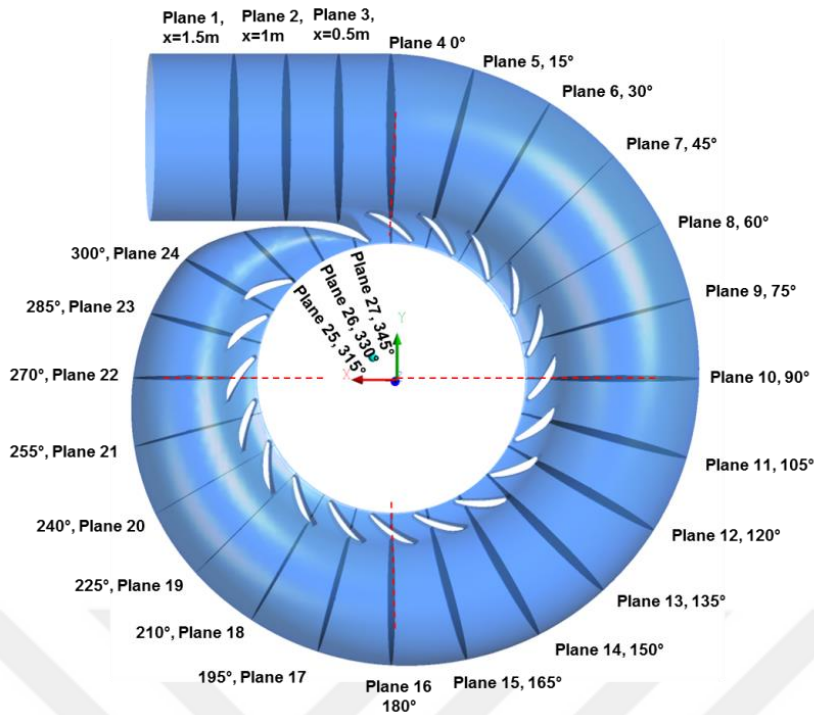


Figure 4.22 : Post processing planes of spiral case.

It is already shown with the help of the planes in Figure 4.22 that spiral case of the Kadincik I HPP violates the linear area decrease design law. Subsequently, another well-known design approach called constant swirl is considered. Swirls are plotted as contours at the planes 4, 10, 16 and 22 (Figure 4.23). These figures suggest that in the design of the volute constant swirl approach is followed, although swirl varies a little bit at plane 4 and 22. Note that plane 4 is just after the throat region and it is expected not to have fully developed constant swirl contour. On the other hand, plane 22 is not as uniform as planes 10 and 16. This can be the reason of the unsuitable cutwater design but the conclusion should be made up after further investigations.

Figure 4.25 presents the static pressure distribution in front of the stay vanes. As it is observed from this figure, static pressure increases throughout the spiral case. This dispersion is due to the dramatic decrease in c_u velocity, which is perpendicular to the radial distance from rotation axis (Figure 4.24), when the fluid flows through the cutwater (Figure 4.26). However, total pressure is not changing considerably on this contour (Figure 4.27). This suggests that other velocity component (c_r), which is the velocity component towards to machine axis (Figure 4.24), should increase in streamwise direction. Figure 4.28 verifies this statement by showing higher c_r in cutwater region than the one in the area after the throat.

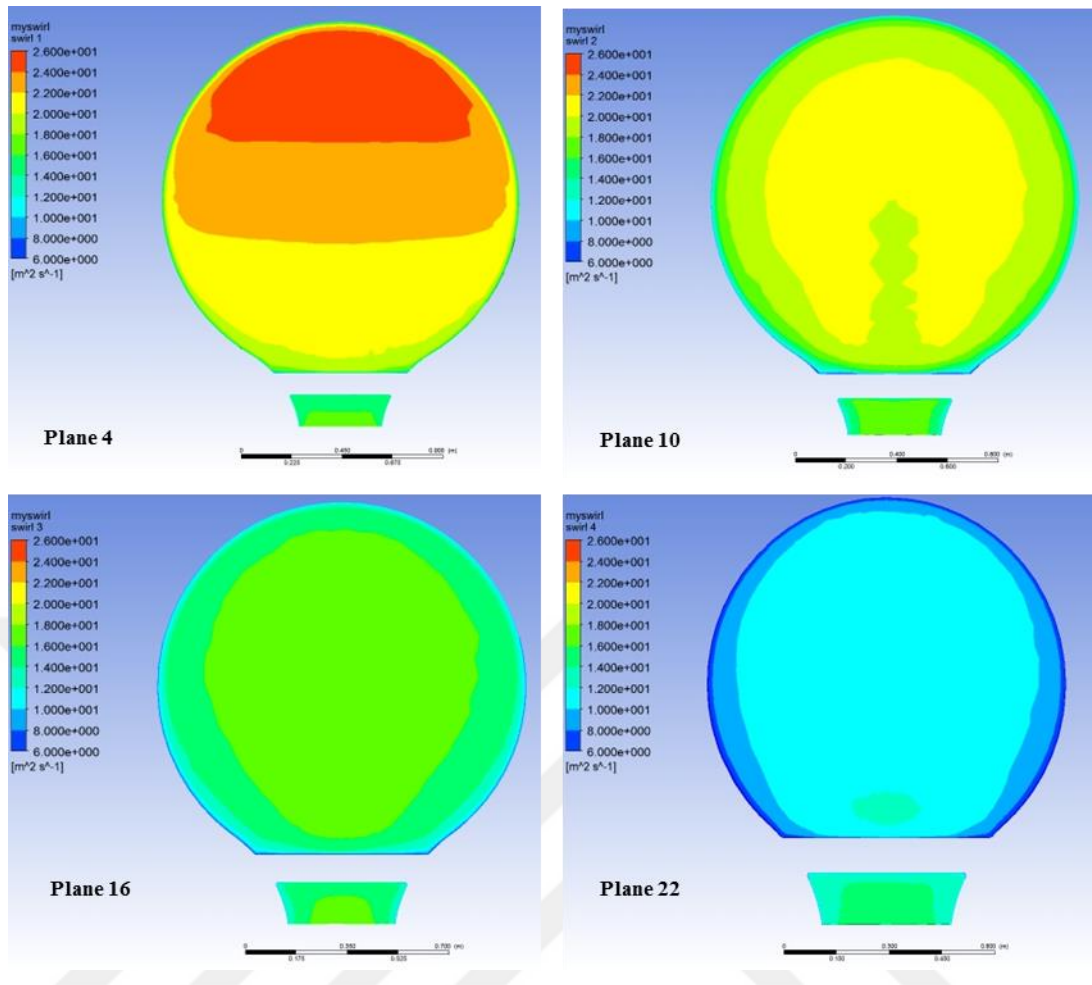


Figure 4.23 : Swirl contours at different spiral case planes.

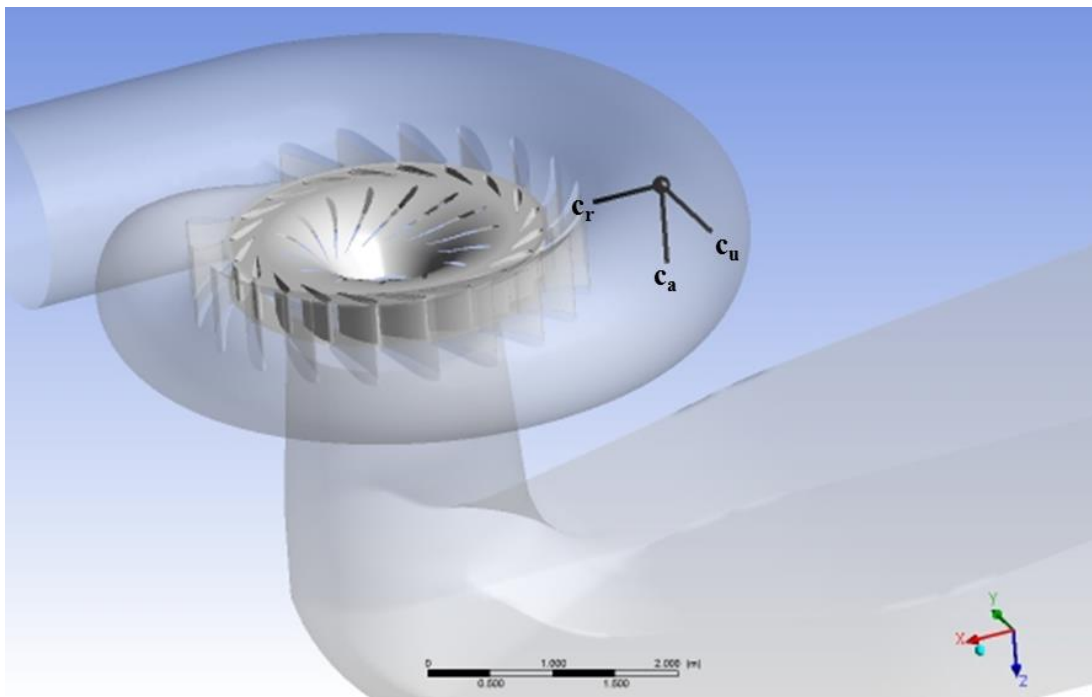


Figure 4.24 : Velocity components in a radial machine.

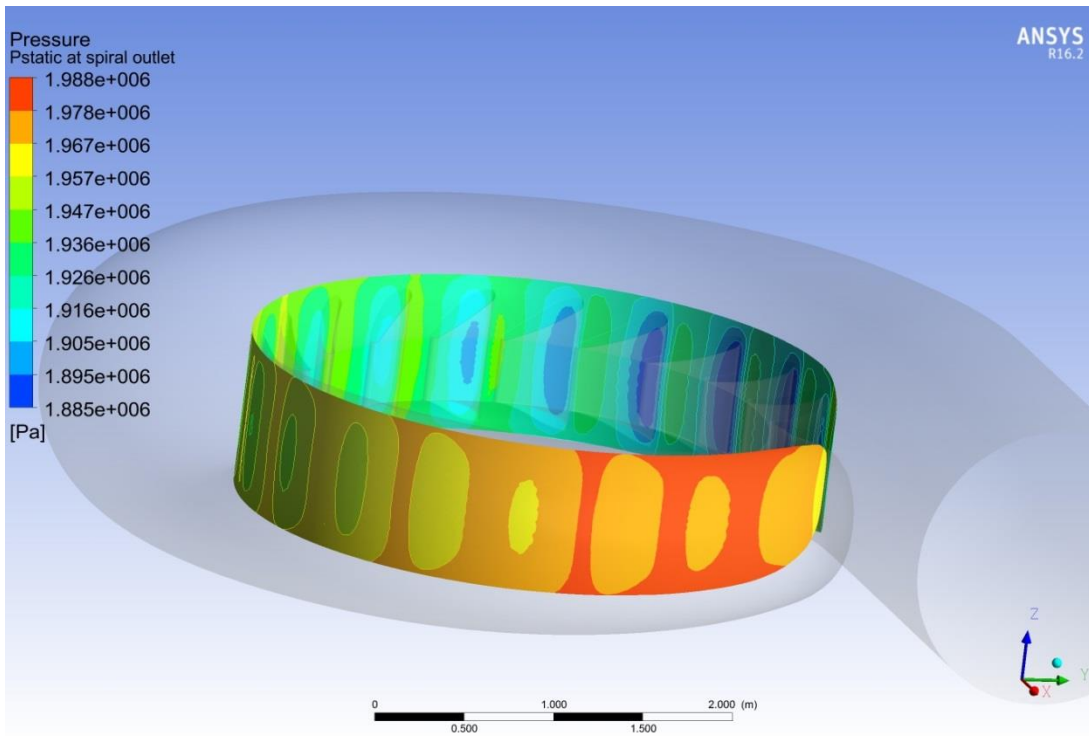


Figure 4.25 : Static pressure distribution in front of the stay vanes.

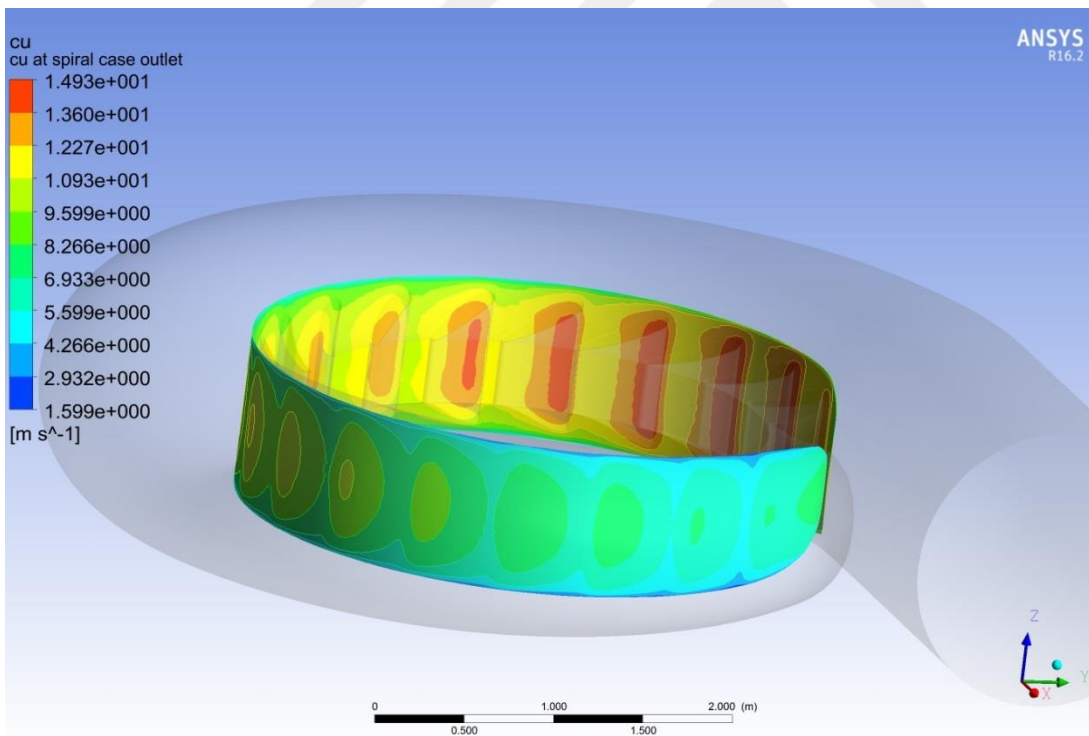


Figure 4.26 : c_u velocity distribution in front of the stay vanes.

The radial velocity is the variable responsible for the amount of water passing between stay vanes. Its distribution reveals that excessive amount of water reaches the cutwater region and is forced to pass stay vane domain, which causes high radial

velocities at that region, although favorable radial velocity dissipation is observed at the rest of the contour.

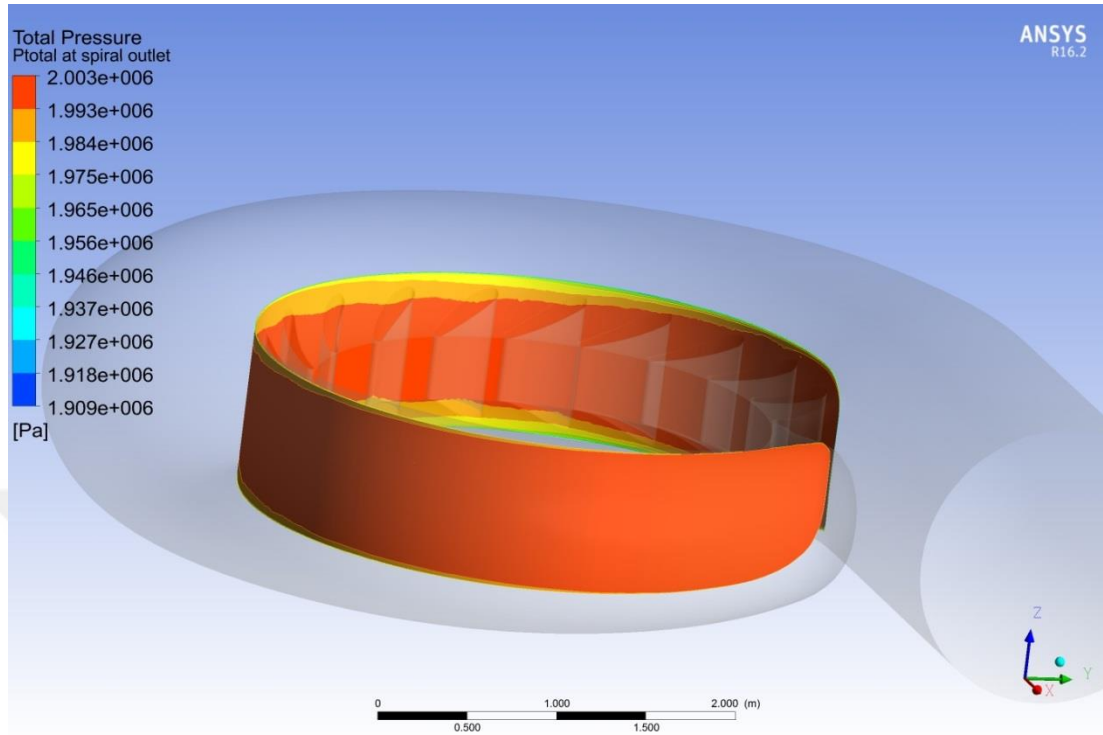


Figure 4.27 : Total pressure distribution in front of the stay vanes.

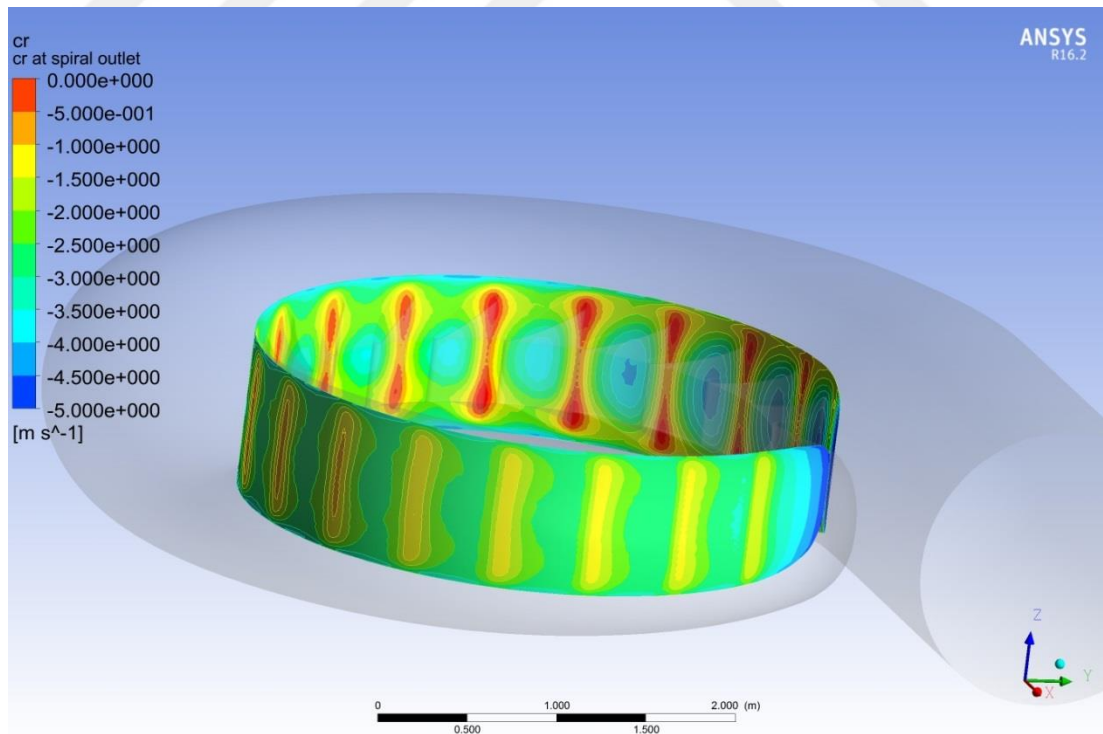


Figure 4.28 : c_r velocity distribution in front of the stay vanes.

4.5.4 Stay vanes

Static pressure distribution at the outlet of the stay vanes shows a similar behavior with the one in front of them (Figure 4.29). It is hard to say any improvement is achieved across this domain with respect to the static pressure. In fact, the static pressure difference between the first stay vane and the last one increases.

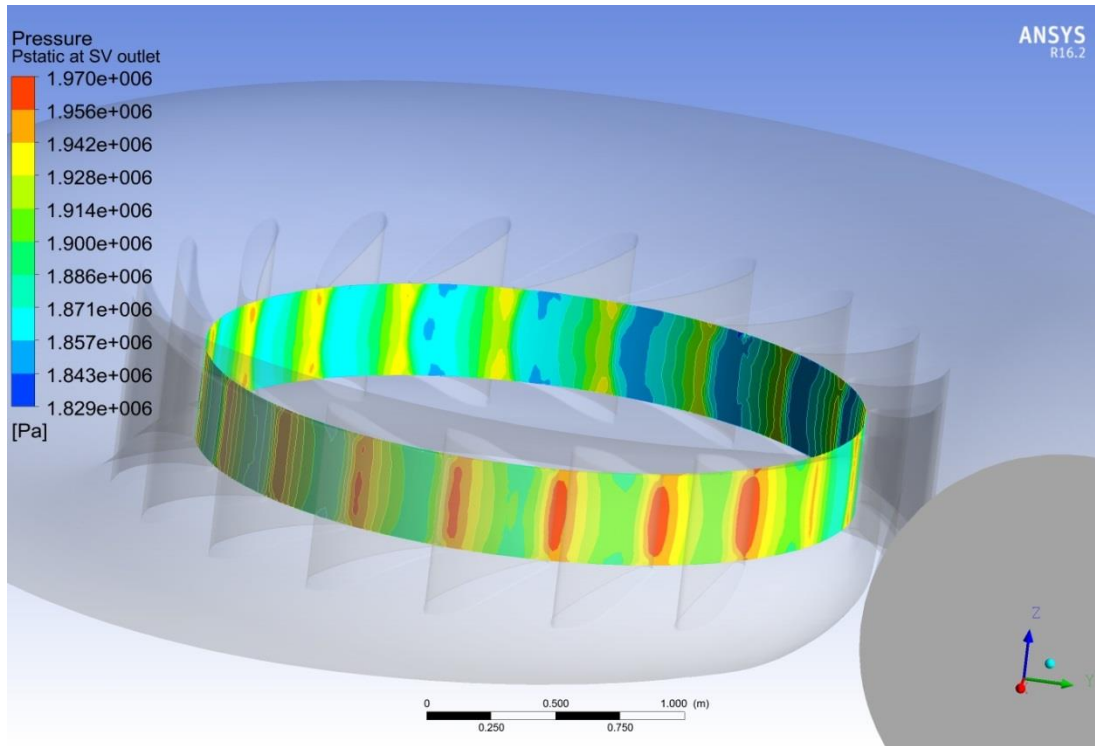


Figure 4.29 : Static pressure distribution at the outlet of the stay vanes.

By looking Figure 4.30, it can be concluded that c_r velocity increases across this domain. Furthermore, more homogenous c_r distribution is found out on the circumferential contour. This finding suggests that almost the uniform flow enters the guide vanes. However, the effect of the excessive amount water passing through the cutwater region is still felt.

On the contrary to c_r velocity, c_u does not undergo this kind of a severe change in magnitude. The only noteworthy difference in c_u distribution between inlet and outlet contours of stay vanes is the improvement of circumferential velocity around cutwater region (Figure 4.31).

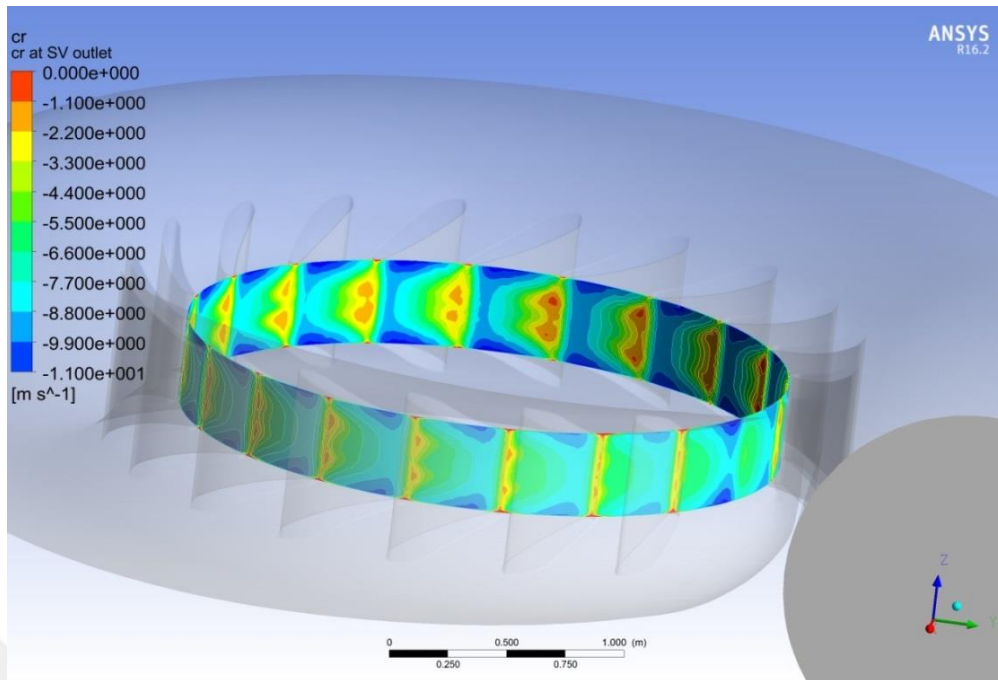


Figure 4.30 : c_r velocity distribution at the outlet of the stay vanes.

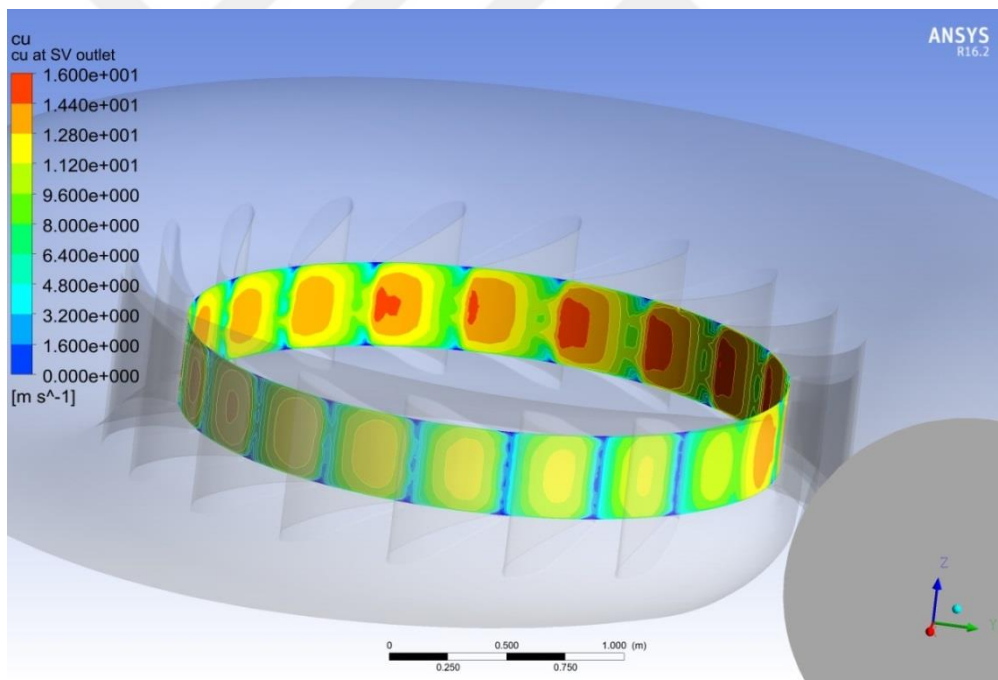


Figure 4.31 : c_u velocity distribution at the outlet of the stay vanes.

In total pressure contour at the end of the stay vanes (Figure 4.32), the effect of the vanes is clearly observed. The vanes resist to the flow; therefore, they cause loss of energy, which is seen in this figure as a decrease in total pressure. However, this contour does not show a uniform behavior. While higher pressure losses are faced in larger areas around the first stay vanes, pressure losses lower after passing half of

them. The reason behind this situation can be observed in Figure 4.34 and Figure 4.33. As it is seen from these figures, the stagnation point of the flow is at the pressure side of the stay vanes for the first half of the vanes. This causes low pressure zones at the suction side around the leading edge and at the pressure side around the trailing edge. Moreover, the low pressure values near the trailing edge affect the flow downstream. On the other hand, rest of the stay vanes do not suffer from this problem. In other words, the stagnation point of the flow is exactly at the leading edge. Therefore, inlet and outlet flow angles are the same with the ones of stay vanes and the flow separation is not faced at these vanes contrary to the first stay vanes.

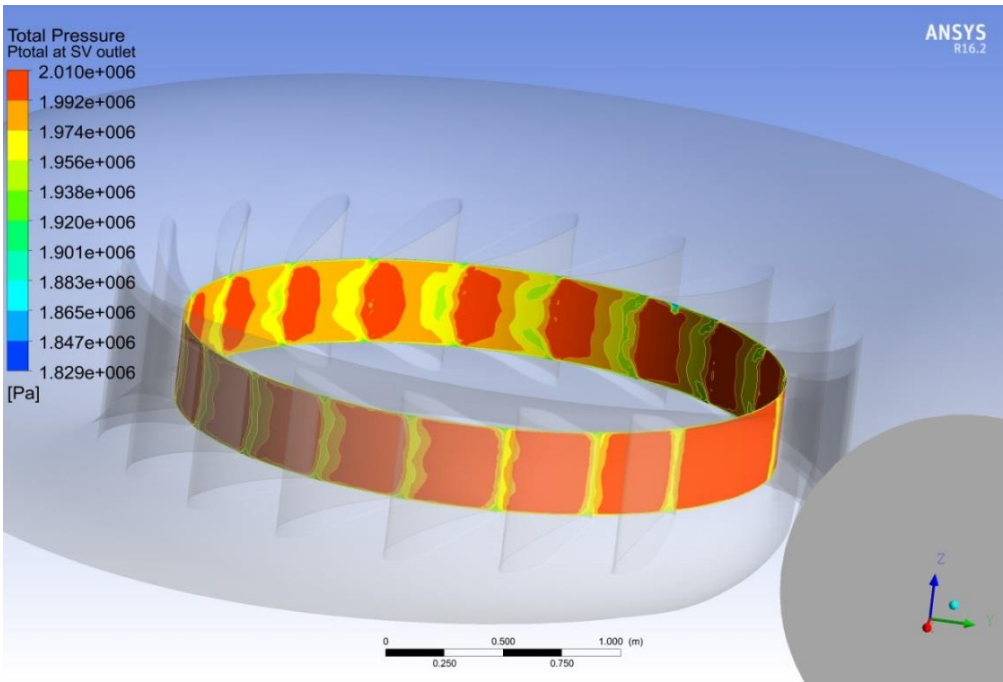


Figure 4.32 : Total pressure distribution at the outlet of the stay vanes.

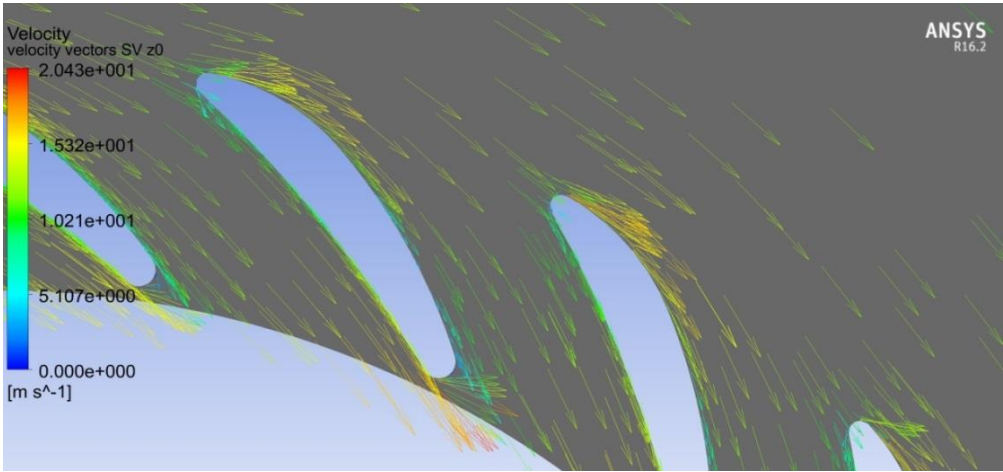


Figure 4.33 : Velocity vectors for first stay vanes.

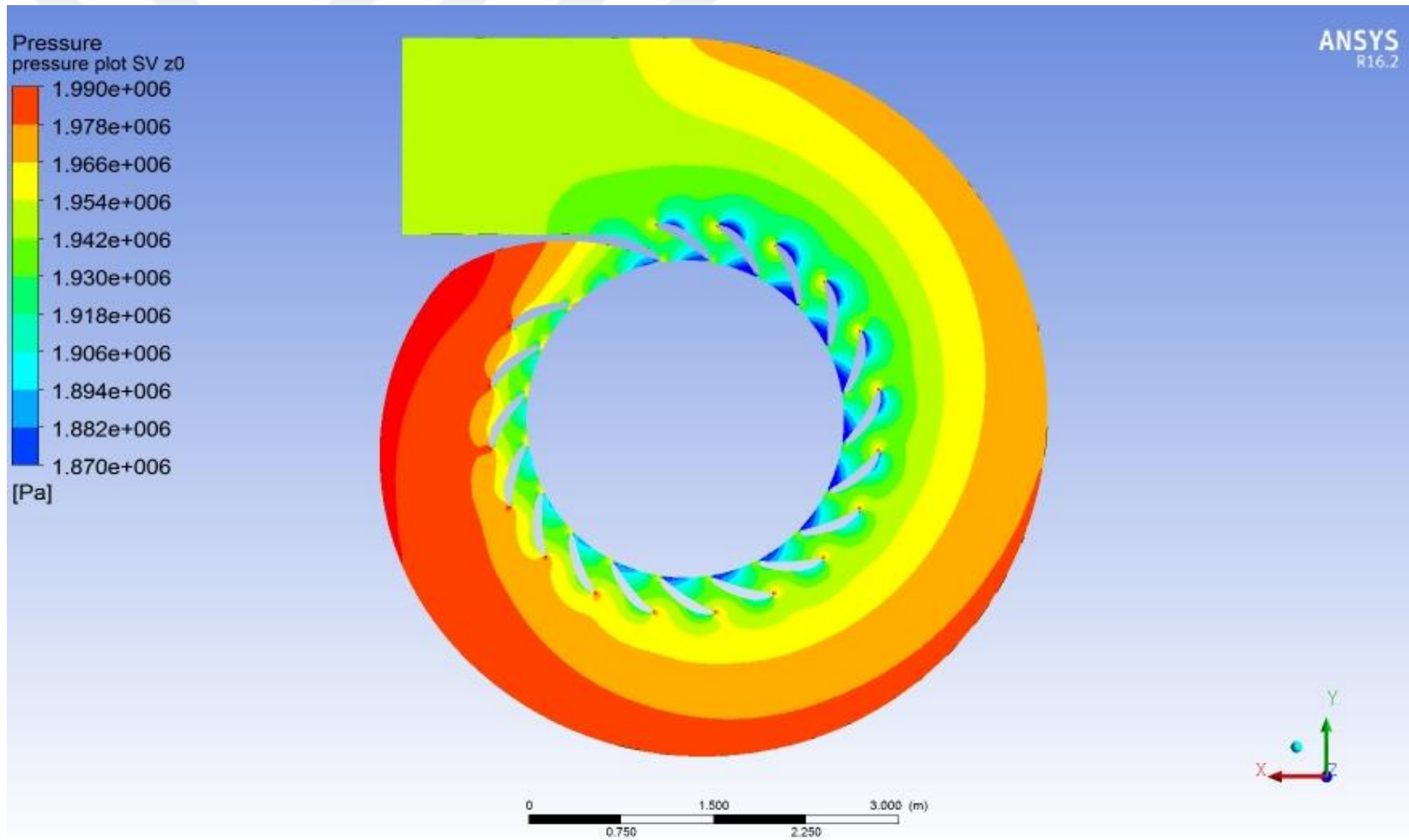


Figure 4.34 : Static pressure contour of stay vanes at z=0 meter

4.5.5 Guide vanes

By comparing the total pressure contours at upstream (Figure 4.32) and downstream (Figure 4.35) of guide vanes, it can be concluded that guide vanes create more resistance to the flow than the stay vanes because wider low pressure regions are encountered at the end of this domain. This is due to the fact that flow hits to the pressure side of the wicket gates (Figure 4.36). In fact, by considering guide vanes do not attain their best efficiency point at highest flowrate (Figure 4.21), it is expected to see the stagnation point is not directly on the leading edge of the guide vane for 15° guide vane angle. Because of this situation, the leading edge is circulated by the water and high velocities occur, which is shown in Figure 4.36. This yields a low pressure zone at the location opposite side of the stagnation point of unsymmetrical profile of the guide vane.

Static pressure (Figure 4.37), c_u (Figure 4.38) and c_r (Figure 4.39) velocity distributions at the end of the guide vanes suggest that fluid flow does not show a homogenous behavior along spanwise direction. Especially close to shroud, static pressure lowers and around the same regions circumferential and radial velocity components increases. This can cause the low pressure areas on the leading edge of the runner near to shroud.

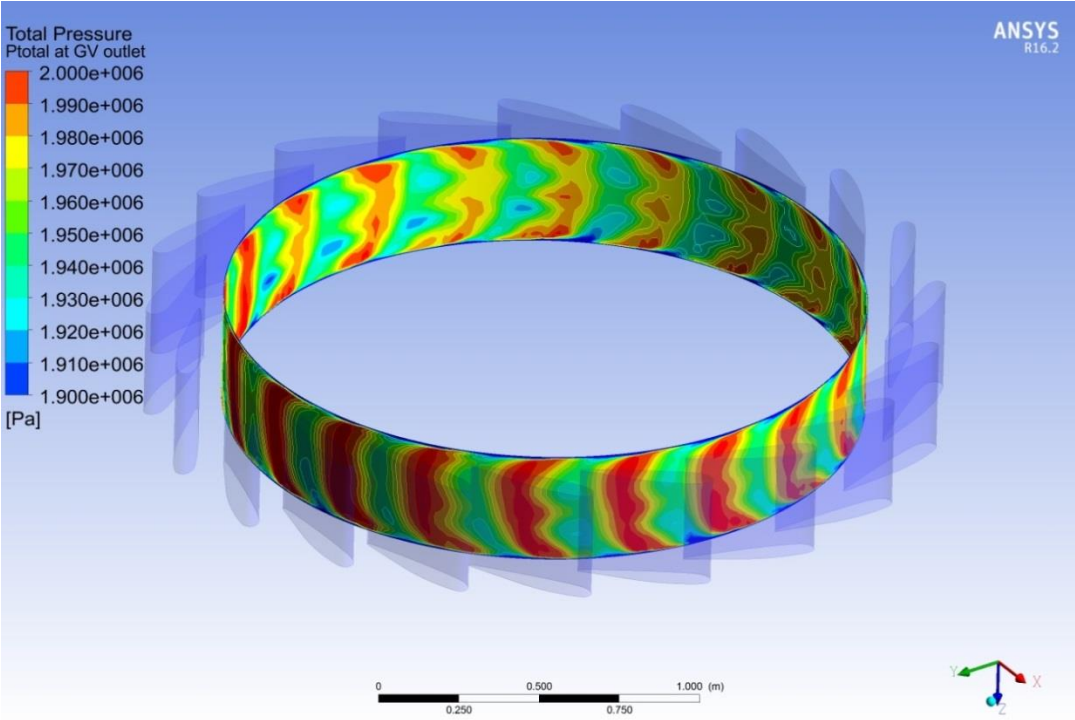


Figure 4.35 : Total pressure distribution at the outlet of the guide vanes.

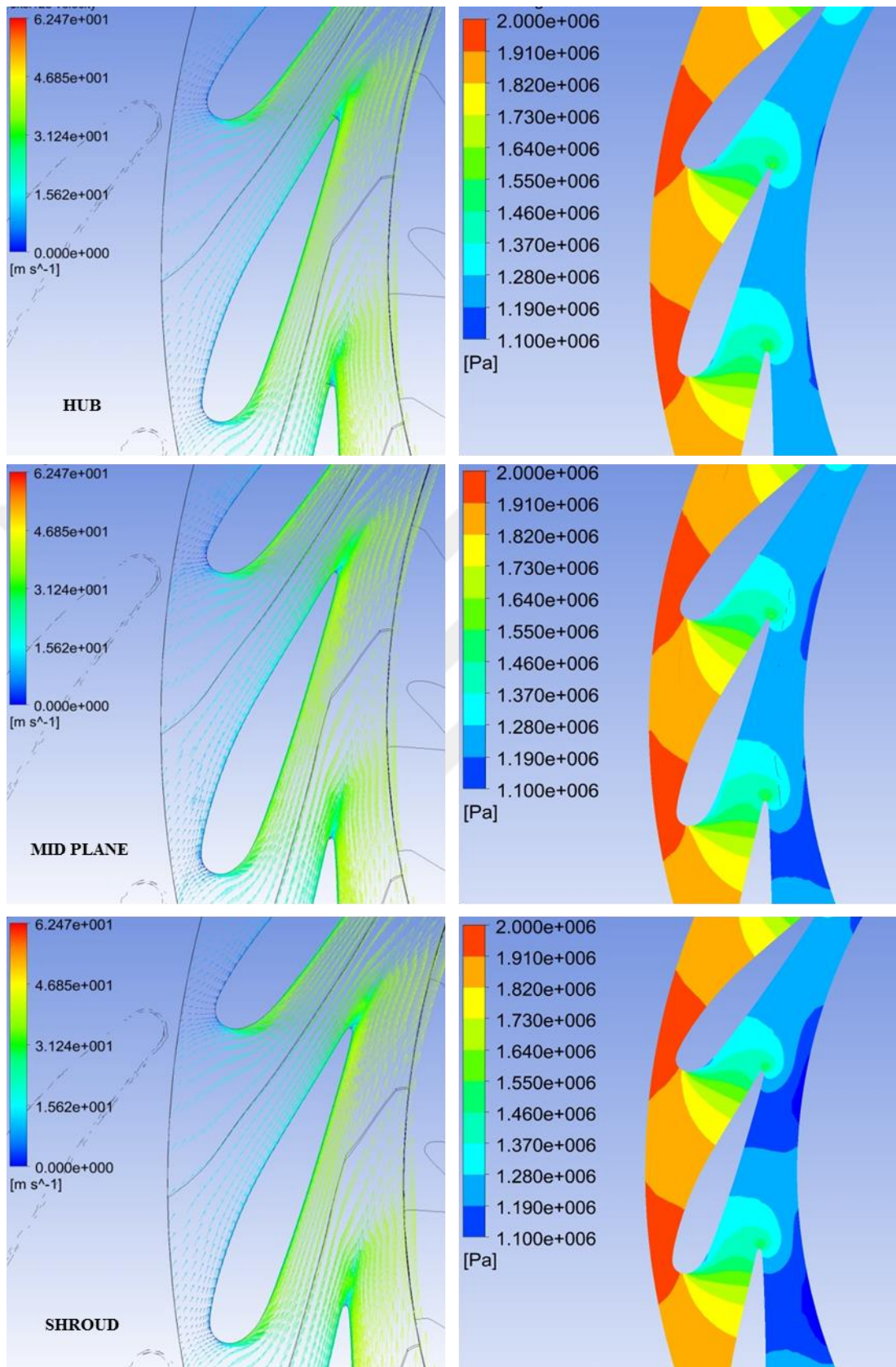


Figure 4.36 : Velocity vectors and pressure contours of guide vanes.

Furthermore, Figure 4.39 shows that c_r velocity component is not distributed uniformly in circumferential direction. However, it seems like following a periodic pattern. This idea is also supported by Figure 4.40 where amount of mass flow passing between guide vanes are presented. For each guide vane passage, the mass flow is evaluated at the inlet and at the outlet of the passage. Then, the results are normalized with the mass flow per passage, averaged over the full circumference. In Figure 4.40, this is depicted for the design point of the turbine. The negative influence of the cutwater can clearly be seen but except from this it is possible to say that flow reaches to the guide vanes homogenously. Nevertheless, same statement is not valid for the flow at the outlet of the guide vanes. Although they reduce the effect of the cutwater considerably, amount of water passing through each guide vane varies up to 9 % of the normalized mass flow. Moreover, peak and bottom points of mass flow in circumferential direction occur just the opposite side of the machine. Therefore, turbine shaft suffers from the high radial forces, which are the sources of the vibration.

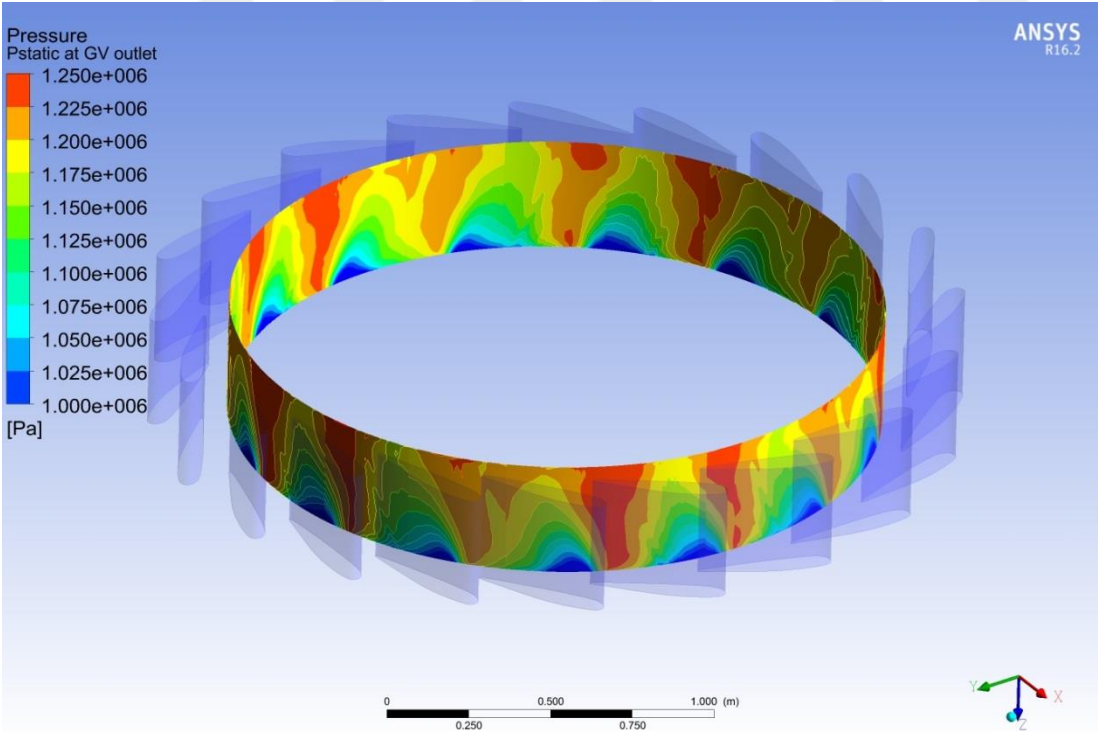


Figure 4.37 : Static pressure distribution at the outlet of the guide vanes.

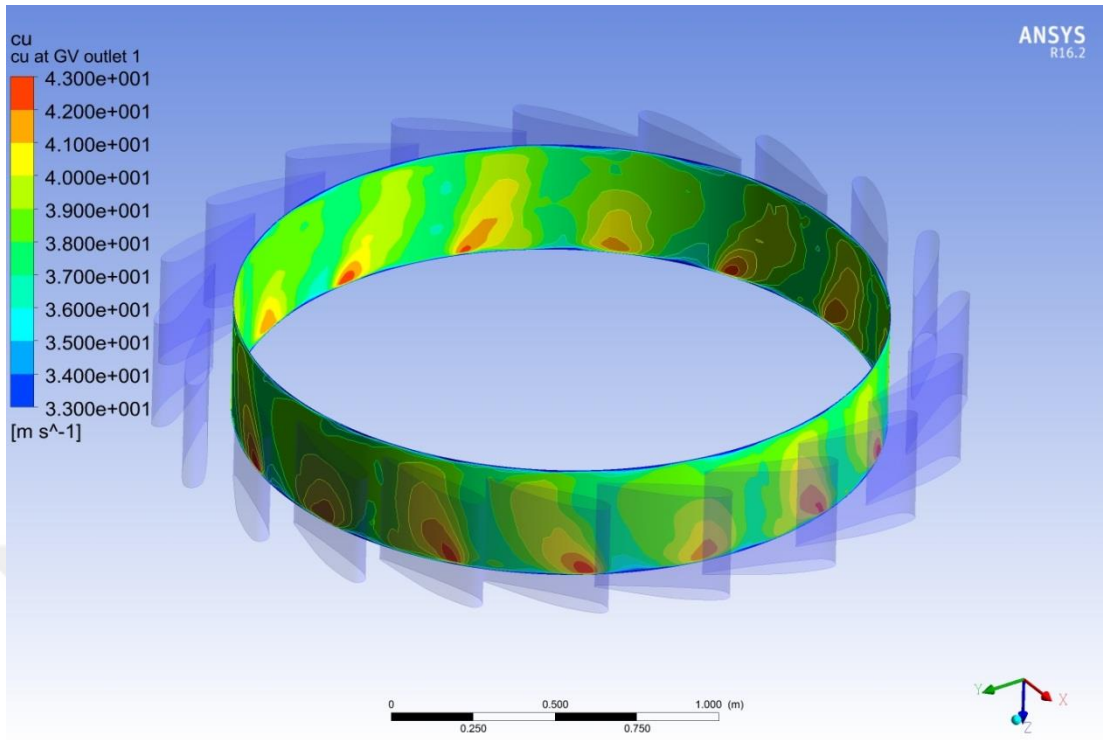


Figure 4.38 : c_u velocity distribution at the outlet of the guide vanes.

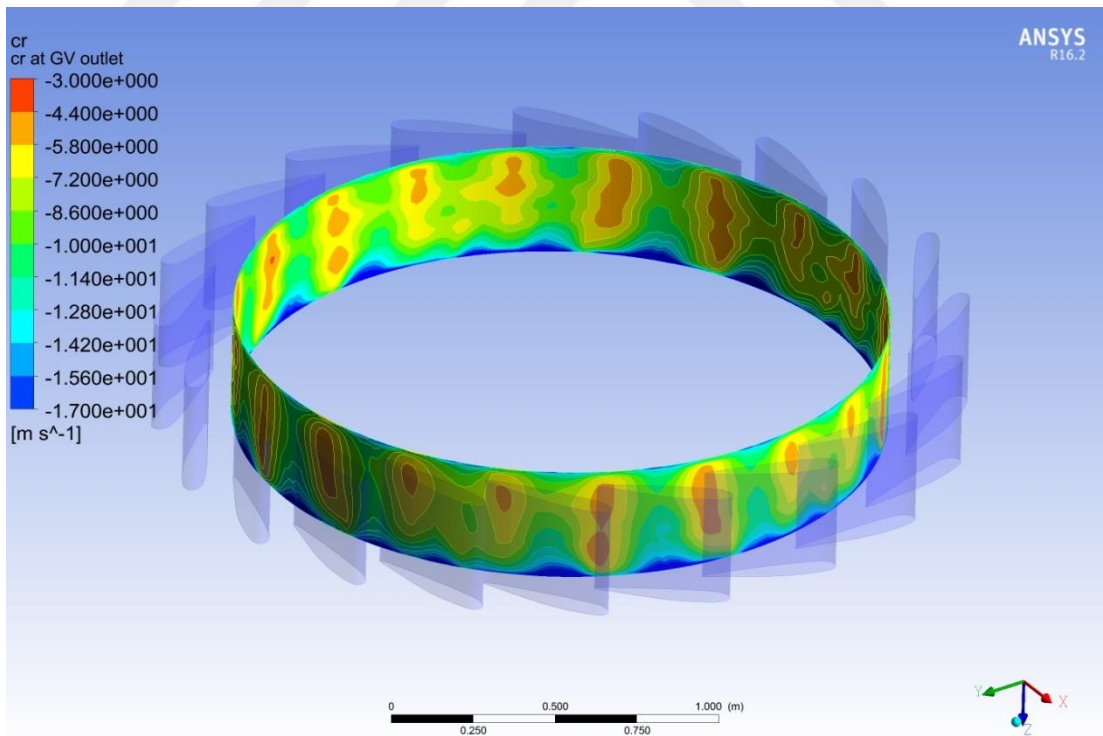


Figure 4.39 : c_r velocity distribution at the outlet of the guide vanes.

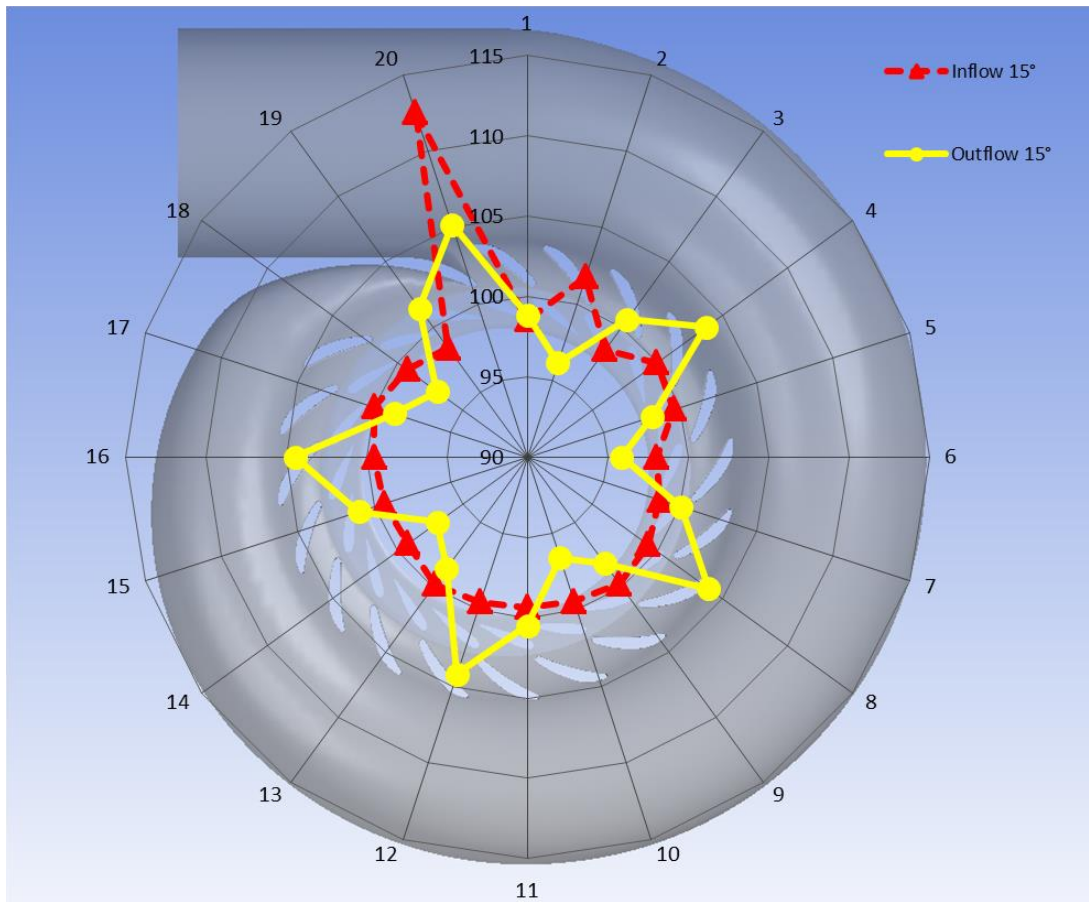


Figure 4.40 : Normalize mass flow through the guide vanes.

4.5.6 Runner

Area averaged velocity profiles for the inlet and the outlet of the runner are presented in Figure 4.41 and Figure 4.42. As this is a clockwise rotating machine against the chosen coordinate system orientation, the c_u -value is positive. This c_u -value is expected to be converted into torque by the runner in order to generate energy. Consequently, c_u component of the velocity should be around zero at the outlet of the runner in BEP. In Kadincik I HPP, the c_u -value at the runner outlet is almost zero.

Taking the design point of the runner as a basis, it is also desired to gain an almost constant c_m -distribution at the runner inlet and outlet. Although it is hard to say this design requirement is satisfied with Kadincik I HPP runner, it should be admitted that velocity distribution shows a favorable trend at both the inlet and outlet; however, this topic is still open to improvements.

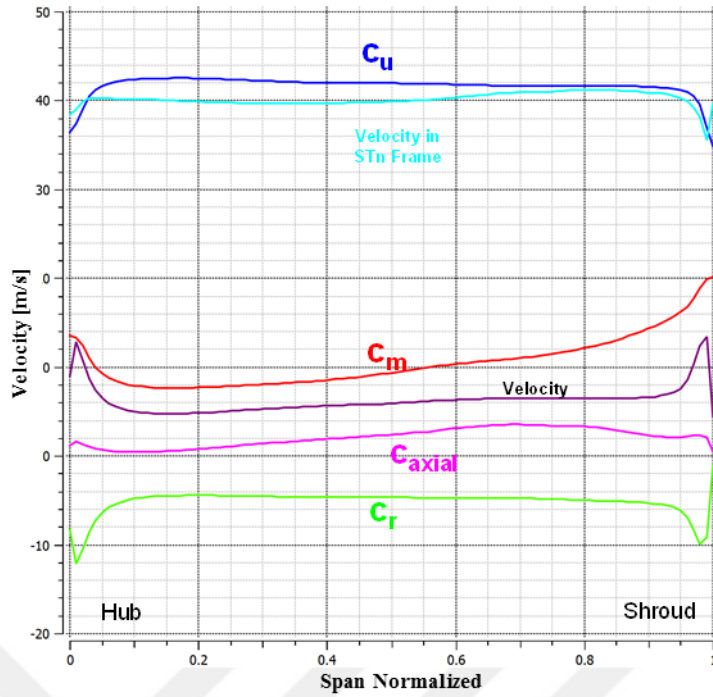


Figure 4.41 : Velocity distributions at the inlet of the runner.

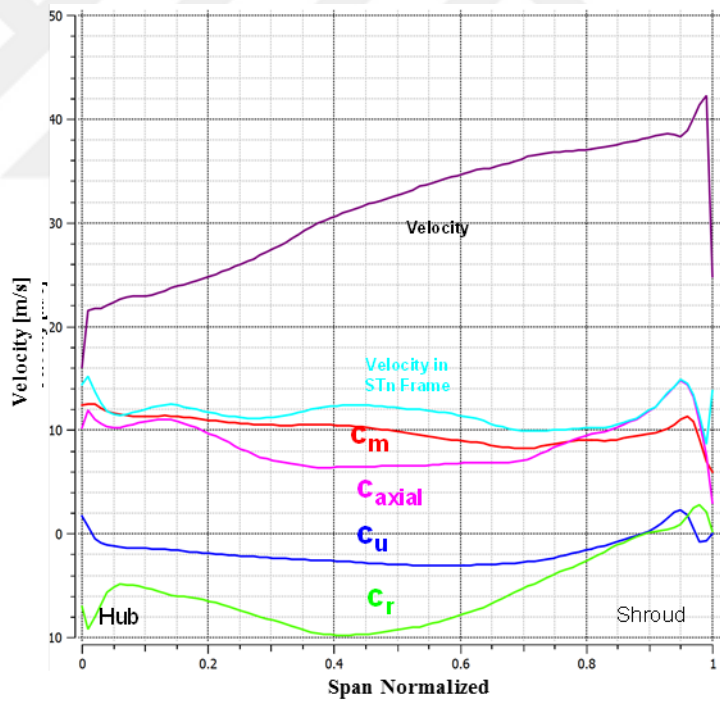


Figure 4.42 : Velocity distributions at the outlet of the runner.

Although it is favorable to see high pressure regions at the leading edge and low pressure regions at the trailing edge in runner blades, low pressure zones are detected around the leading edge of the runner (at the suction side) and also around the trailing edge due to the hydraulic design of the runner. This situation is visualized in Figure 4.43 and Figure 4.46. Especially at the shroud region, there is a small zone

with low pressure around the leading edge. This is due to the flow with high velocity coming from the guide vanes and the stagnation point occurring at the pressure side of the blade. Consequently, the flow circulates around the leading edge from pressure to suction side with high velocities in this region.

According to Figure 4.46, in higher streamwise locations the pressure increases again, but for locations near to the shroud after 40 % streamwise location at the suction side, the pressure is decreasing once more. For a span of 50 % and less, the hydraulic shape works correctly. Finally, in the low pressure zones shown in Figure 4.43, cavitation damages are detected during the inspection inside the unit (Figure 4.47).

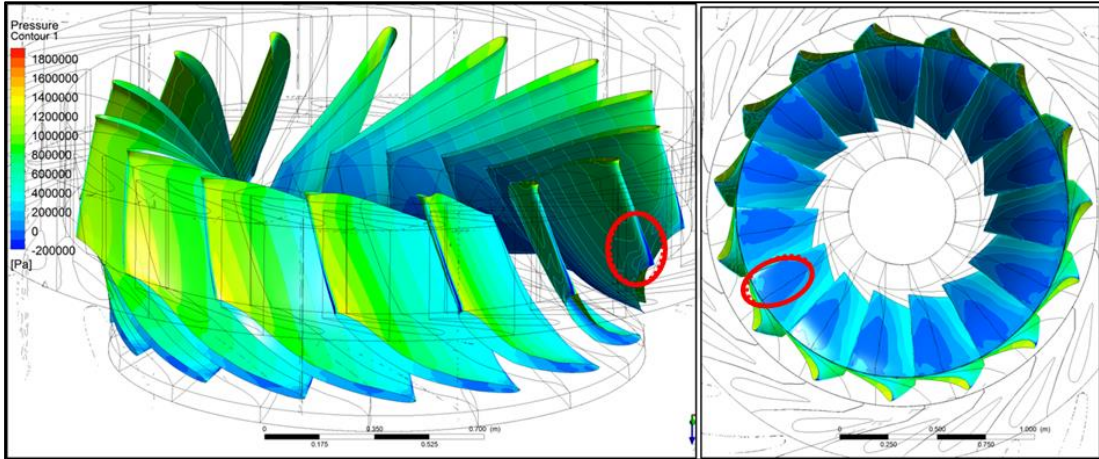


Figure 4.43 : Static pressure distribution on the runner blades.

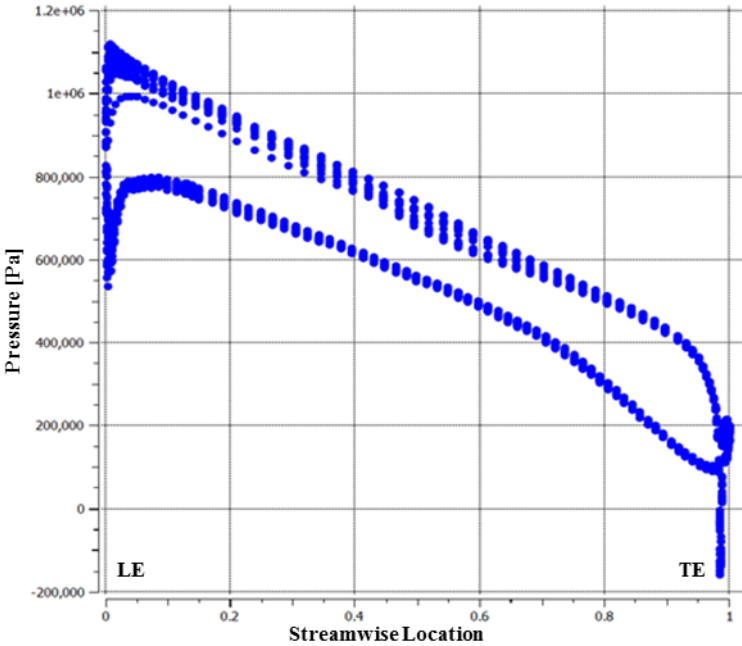


Figure 4.44 : Blade Loading at Span 5 % (close to hub).

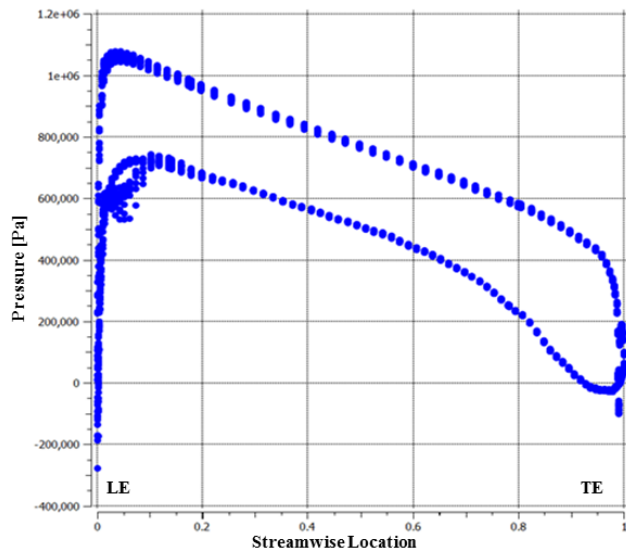


Figure 4.45 : Blade Loading at Span 50 % (mid plane).

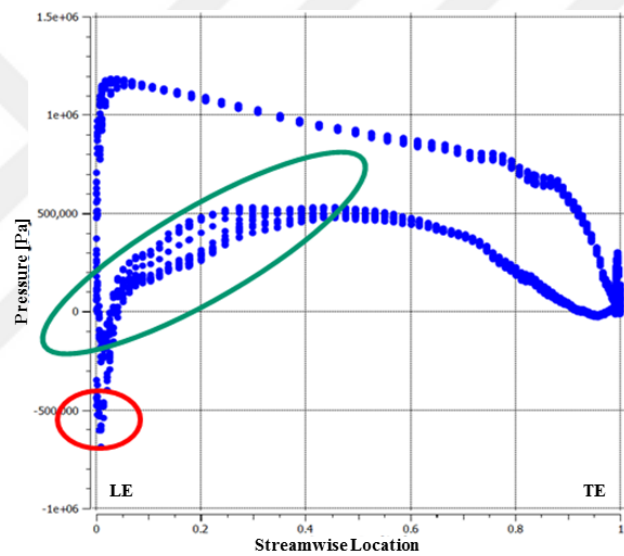


Figure 4.46 : Blade Loading at Span 95 % (close to shroud).



Figure 4.47 : Cavitation damages at the runner, leading edge (left), trailing edge (right).

4.5.7 Draft tube

In the evaluation of the draft tube, 5 cross sectional planes are generated in order to investigate the flow behavior inside the draft tube in addition to the evaluations in meridional cross section (Figure 4.48). First plane is placed in the beginning of the draft tube domain whereas second one is at the end of the cone geometry where the elbow section starts. Plane 3 stands at the end of the elbow section; however, in this plane cross sectional geometry does not become rectangular. Plane 4 and 5 are placed through the outlet of the draft tube. In fact, plane 5 is directly at the outlet boundary.

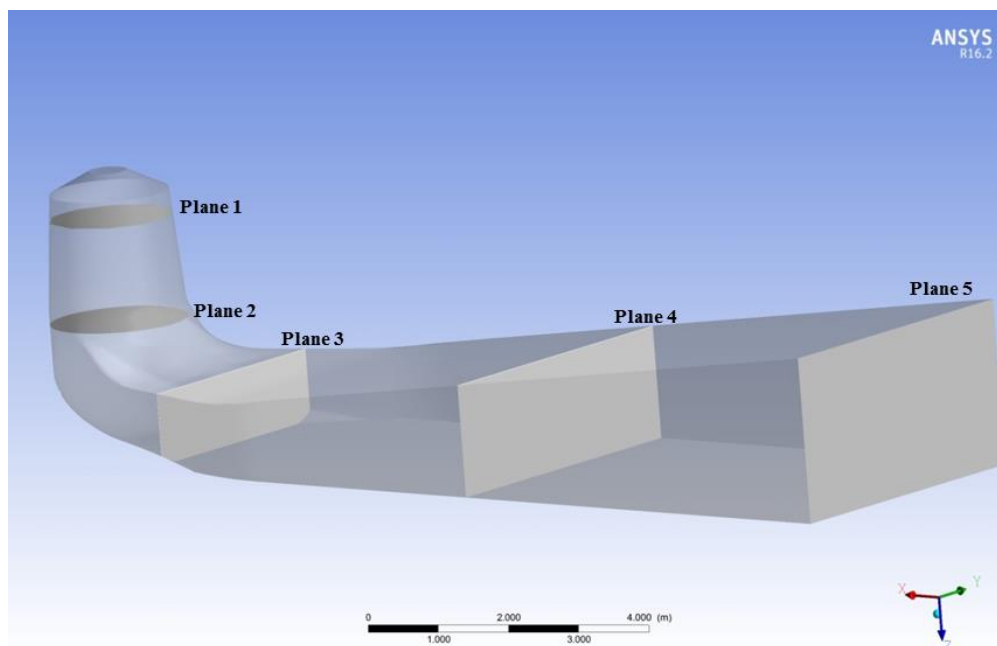


Figure 4.48 : Draft tube post processing planes.

It is already shown that slightly negative c_u is delivered to the draft tube from the runner, which reveals that excessive amount of energy is taken from the water. Influence of this situation is seen as vortex rope generation at the cone region of draft tube. As it is seen in Figure 4.49, flow can be divided into three zones at the cone. The zone close to wall of the draft tube and the one in the core have the positive c_u velocities whereas the area in between circulates in opposite direction. Although this vortex does not get in contact with the draft tube wall at plane 1 (Figure 4.50 - left), the situation becomes critical at plane 2 because vortex starts to touch the surface (Figure 4.50 - right). This can cause vibration problems during the operation.

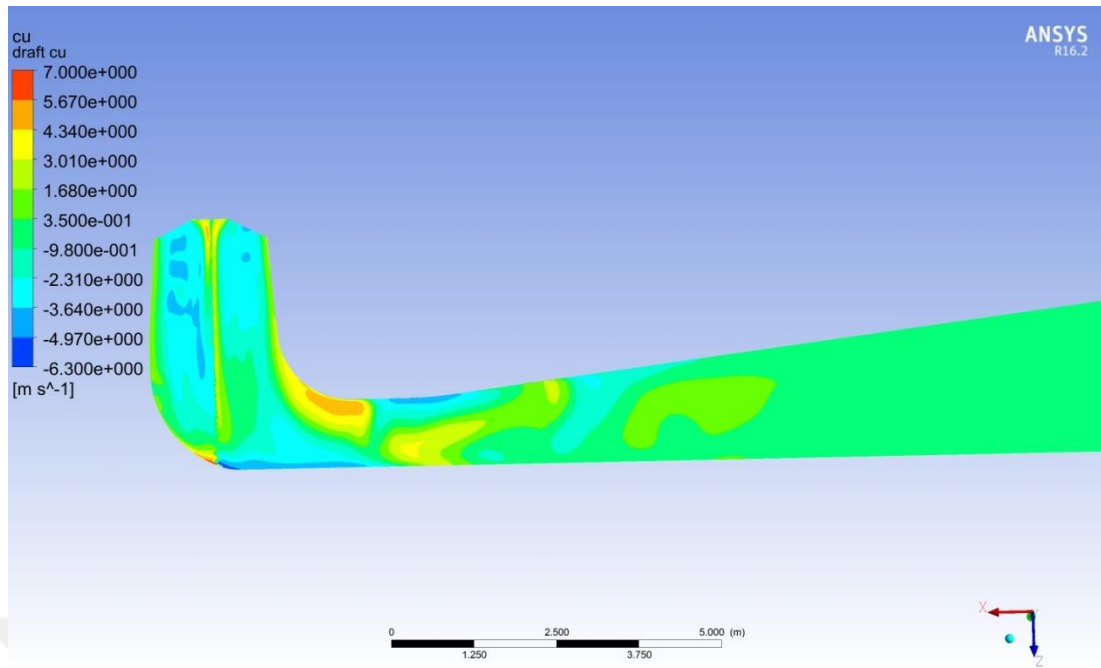


Figure 4.49 : c_u velocity contour at meridional cross section of draft tube.

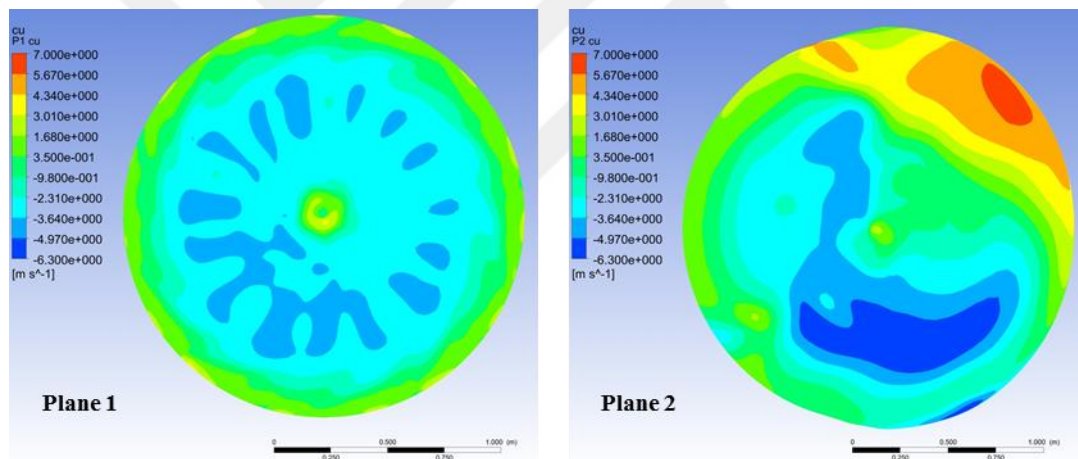


Figure 4.50 : c_u velocity contours at plane 1 and 2.

On the contrary to c_u , absolute velocity (c) decreases from the machine axis to draft tube wall (Figure 4.51). This distribution is also reflected in static and total pressure distributions (Figure 4.52 and Figure 4.53). It is seen that neither of these values can be stabilized and homogenized in cross section until the plane 4 (Figure 4.54, Figure 4.55 and Figure 4.56). This can be one of the reasons for the preference of very long draft tube geometry. At the end of the draft tube, it could be stated that homogenized static and total pressure distributions are attained (Figure 4.57). Furthermore, absolute velocity at the end of the draft tube almost does not exceed 2 m/s which is highly suggested in literature [108] (Figure 4.58).

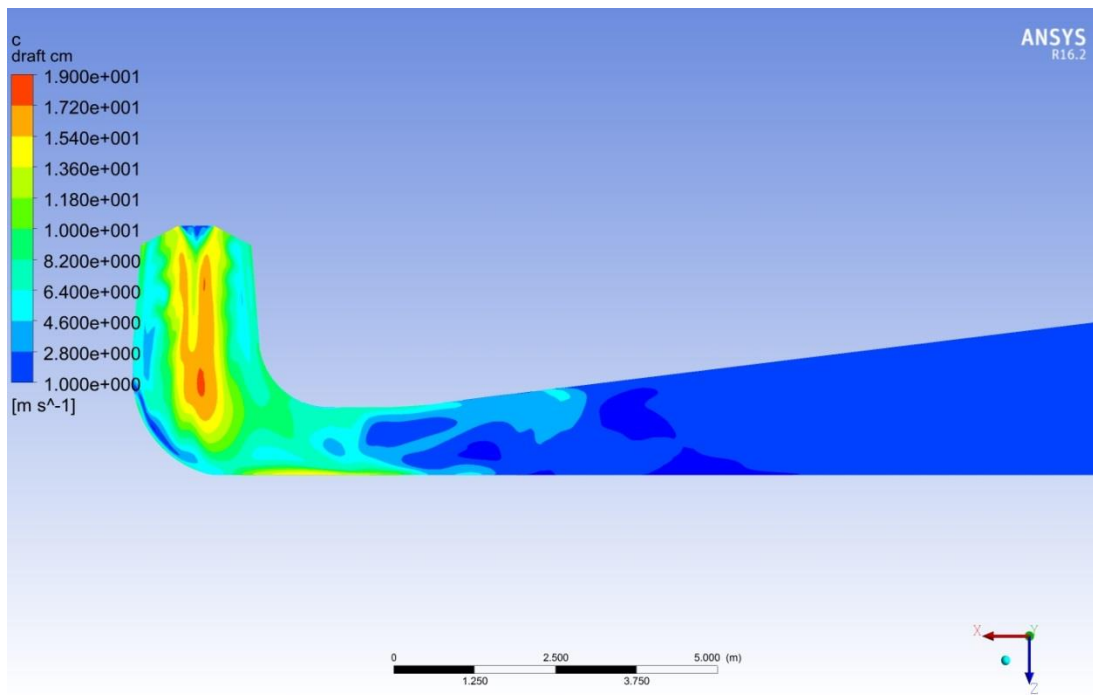


Figure 4.51 : Absolute velocity contour at meridional cross section of draft tube.

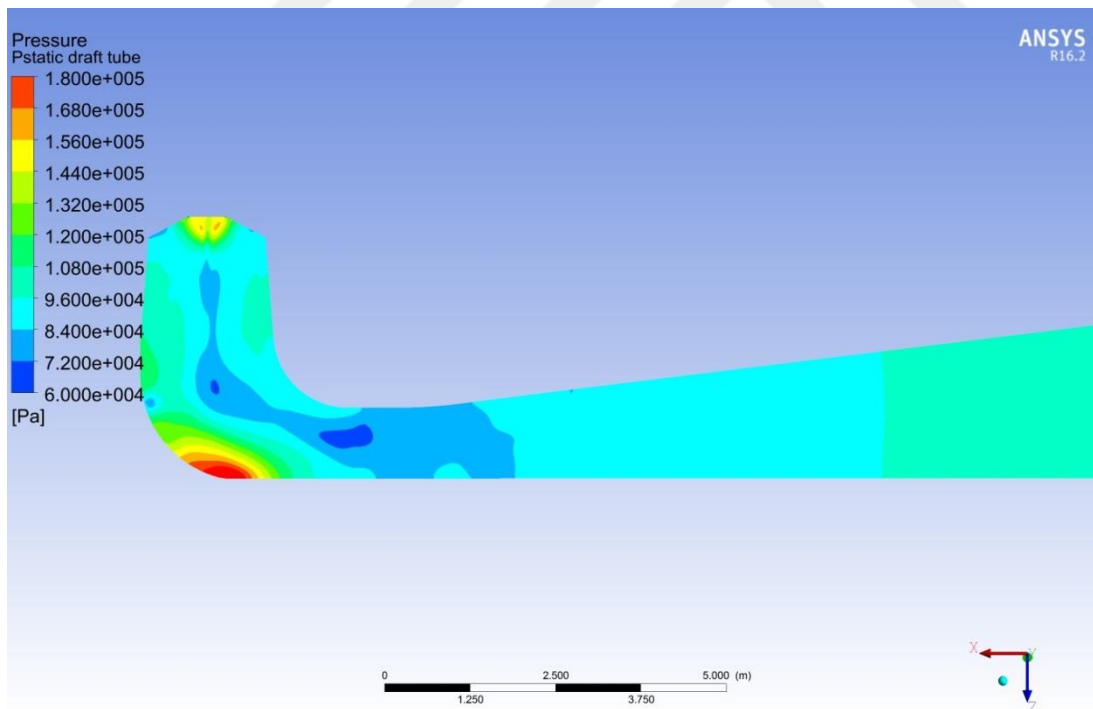


Figure 4.52 : Static pressure distribution at meridional cross section of draft tube.

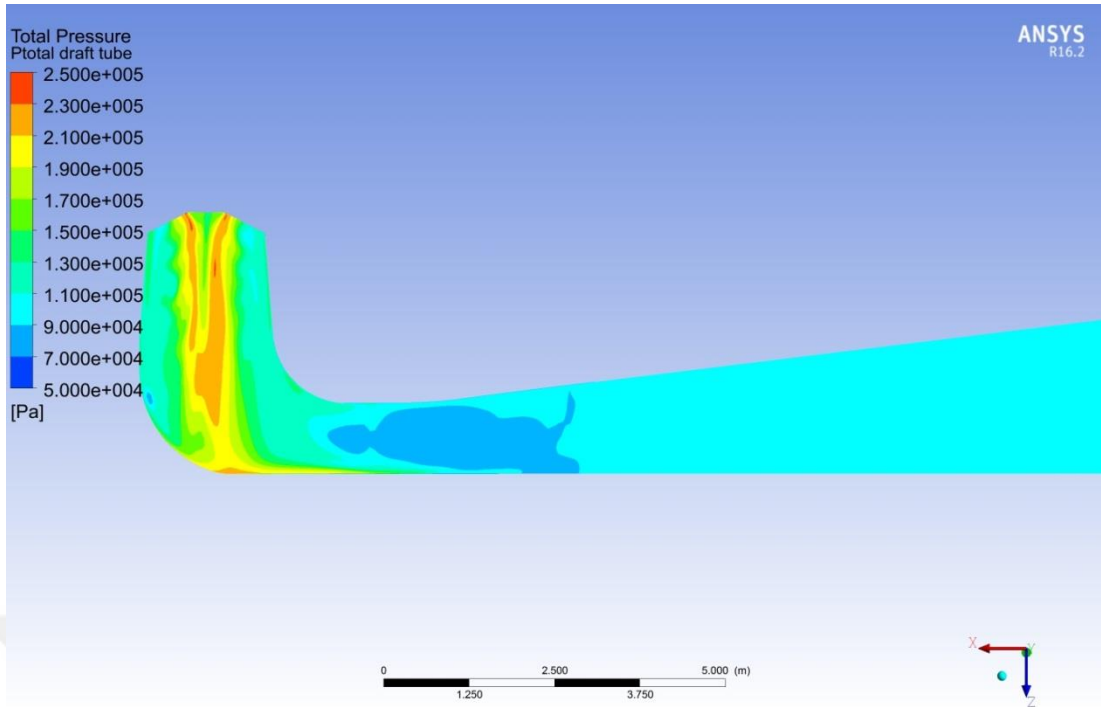


Figure 4.53 : Total pressure distribution at meridional cross section of draft tube.

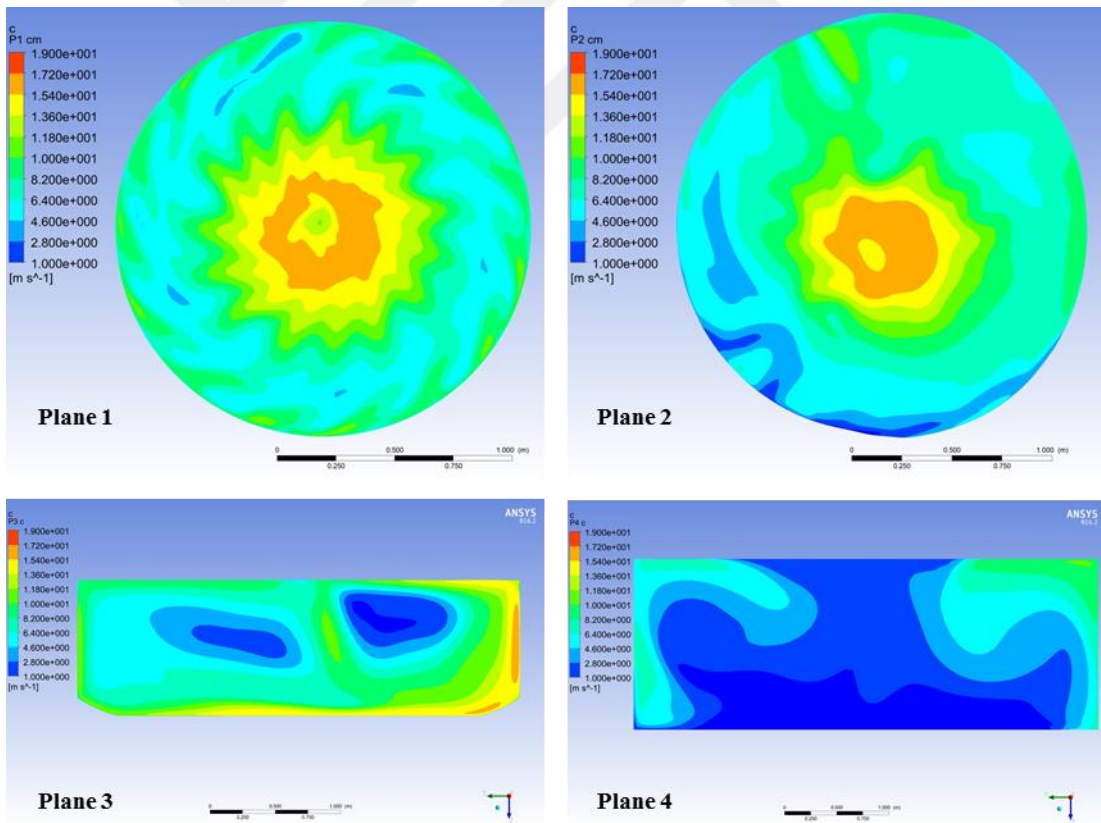


Figure 4.54 : Absolute velocity contours at plane 1, 2, 3 and 4.

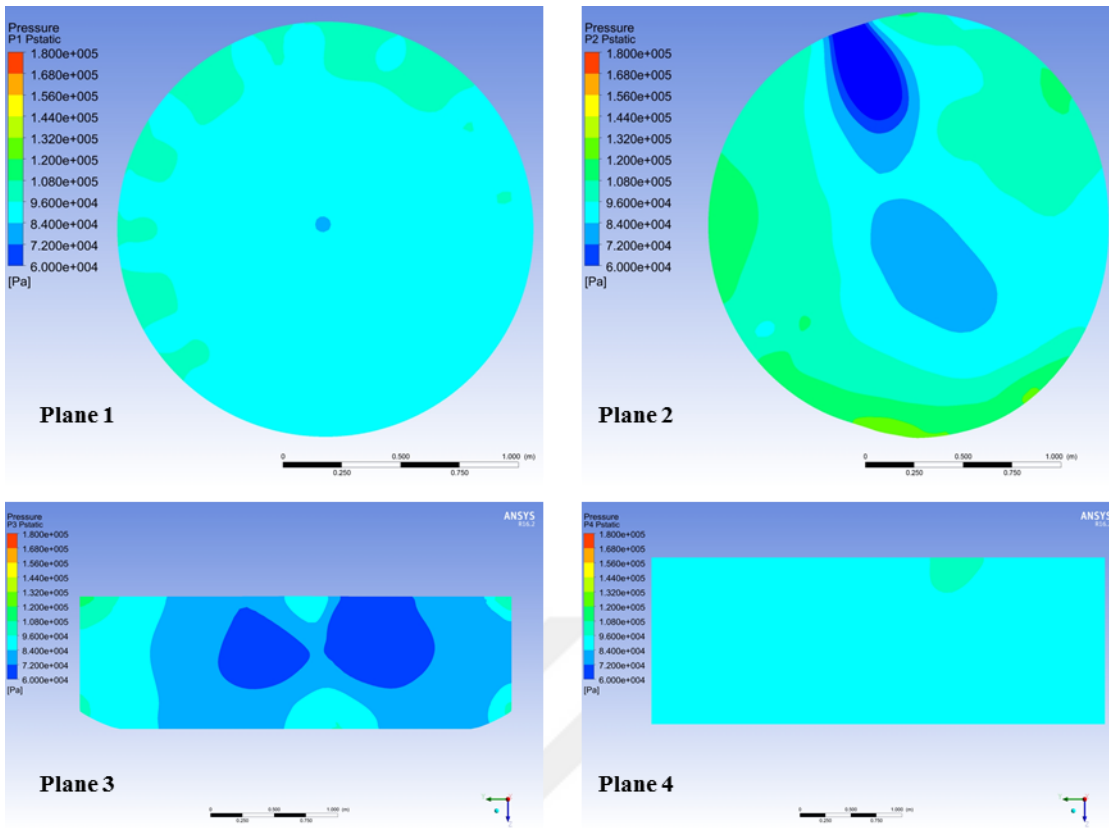


Figure 4.55 : Static pressure contours at plane 1, 2, 3 and 4.

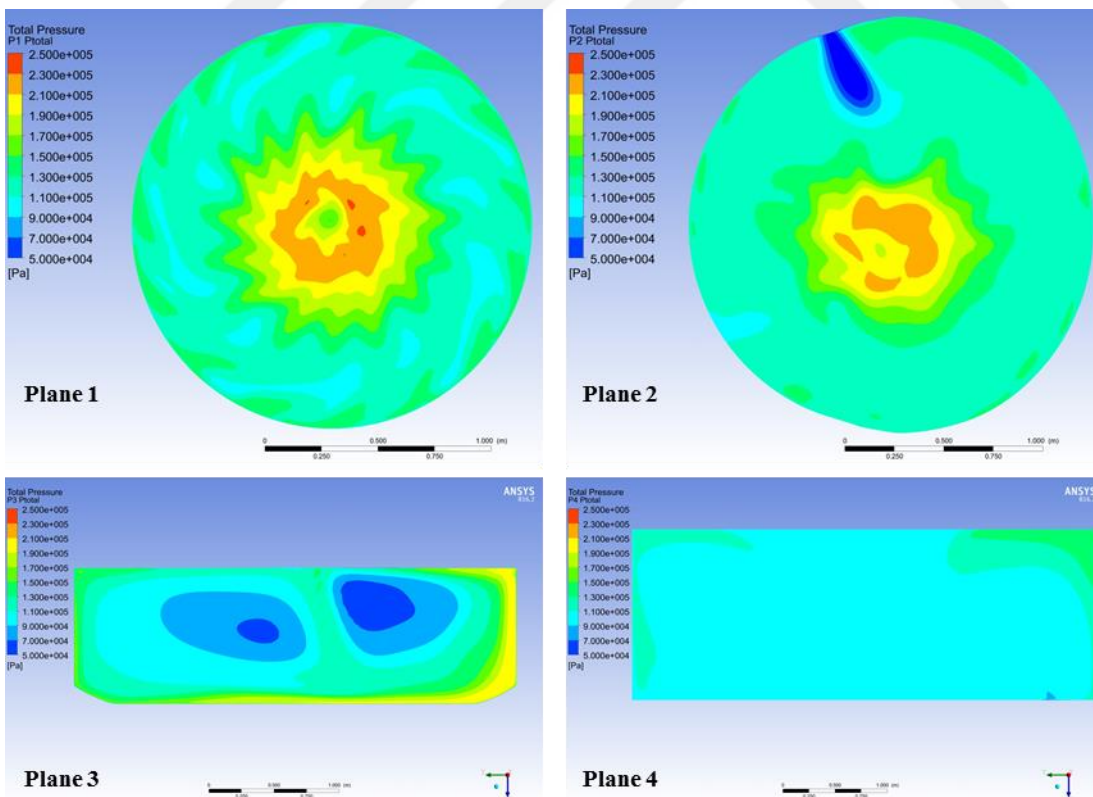


Figure 4.56 : Total pressure contours at plane 1, 2, 3 and 4.

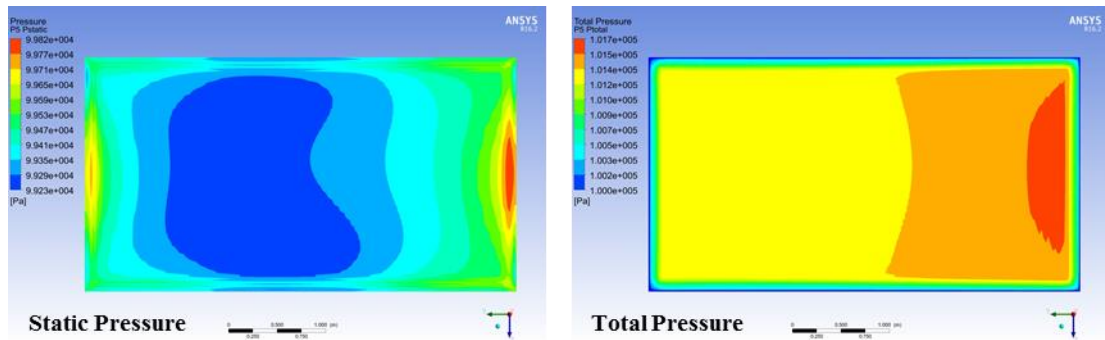


Figure 4.57 : Static and total pressure distributions at the outlet of draft tube.

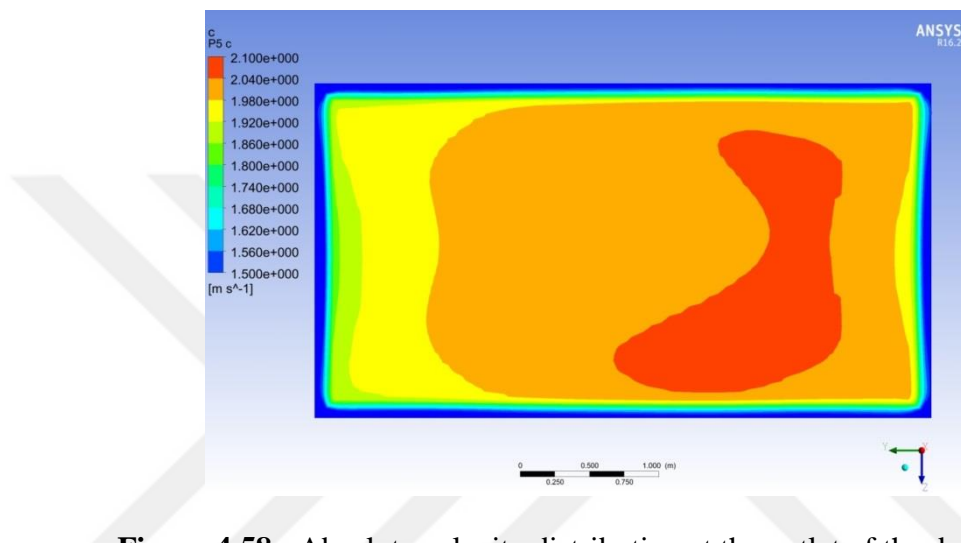


Figure 4.58 : Absolute velocity distribution at the outlet of the draft tube.

4.5.8 Numerical hill chart

In order to understand the whole performance of the existing unit, CFD analyses were conducted in different flow rates and different net heads, which covers the operation conditions of power plant. As a result, hill chart of the turbine was obtained and compared with the operation conditions. However, CFD does not have any ability to cover disk frictions and leakage losses. In order to take these losses into account, the chart in Figure 4.59 was proposed by Prof. Schilling who established a relation between specific speed and Francis turbine losses [109]. As this figure is about 30 years old, it is a good basis for the situation at Kadincik I HPP. Nonetheless, figure is standardized for Reynolds number of 10^7 , whereas for Kadincik I, the Reynolds number is about 8.7×10^7 , Equation (4.18), and specific speed is around 39.

By looking Figure 4.59, leakage and disk friction losses can be estimated as 1.5 %, but once more this is only for Reynolds number of 10^7 . The conversion of this value

to different Reynolds numbers (for example to 8.7×10^7) is explained in IEC 60193 [91]. With the help of the Equations (4.19) and (4.20) from the standard, leakage and disk friction losses for Kadincik I HPP was determined approximately as 1.2 % and this value was subtracted from the CFD results. Note that in these equations, IEC60193 suggests v_{ref} and Re_{ref} values as 0.7 and 7×10^6 for Francis turbine.

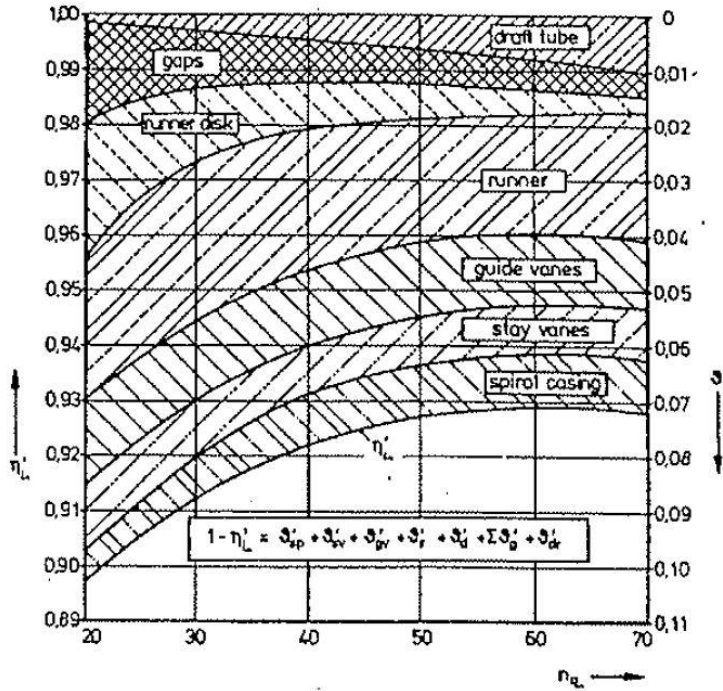


Figure 4.59 : Francis turbine losses as a function of the specific speed, adapted from [109].

$$Re_{Kadincik\ I} = \frac{n * \frac{\pi}{30} * \frac{D_s^2}{2}}{v} = \frac{428.6 * \frac{\pi}{30} * \frac{1.975^2}{2}}{1.004 * 10^{-6}} \cong 8.7 * 10^7 \quad (4.18)$$

$$(\Delta\eta)_{model\ TO\ prototype} = \delta_{ref} \left[\left(\frac{Re_{ref}}{Re_{model}} \right)^{0.16} - \left(\frac{Re_{ref}}{Re_{prototype}} \right)^{0.16} \right] \quad (4.19)$$

$$\delta_{ref} = \frac{1 - \eta_{model}}{\left(\frac{Re_{ref}}{Re_{model}} \right)^{0.16} + \frac{1 - v_{ref}}{v_{ref}}} \quad (4.20)$$

To sum up, the efficiency results represented in Table E.1 are 1.2 % less than the CFD results. Moreover, these results were utilized in the generation of numerical hill chart. In Figure 4.60, hill chart of the turbine and operation points are presented. Although it should be admitted that turbine shows a good performance regarding the peak efficiency and the velocity field, it is obviously seen that high efficiencies are

so away from the machine operation. Furthermore, despite the fact that manufacturer designated the nominal net head of the turbine as 194 meter, CFD results reveals turbine shows even worse performance in higher heads than 160 meter. In fact, nominal operation condition of the turbine is around 155 meter net head and $17 \text{ m}^3/\text{s}$ discharge.

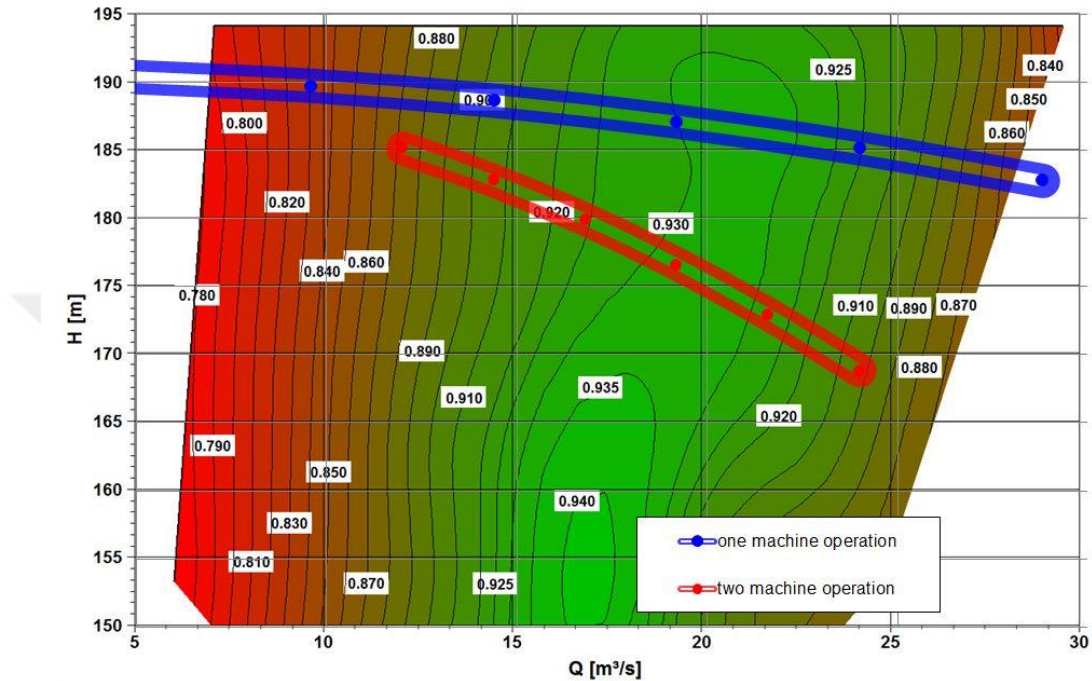


Figure 4.60 : Numerical hill chart of Kadincik I HPP.

4.6 Validation of CFD

There is no available efficiency measurement result conducted in Kadincik I HPP. Moreover, the number of measurement data from commissioning test is limited. As it is seen in Table 4.2 and Table 4.3, discharge and therefore efficiency measurement was not realized. However, it is possible to calculate shaft power for two-unit operation measurement with the help of the average generator efficiency calculated by the ratio of generator output and shaft power of single unit operation. Calculated shaft powers are already presented in Table 4.4 together with the percentage servo piston position. On the other hand, shaft power for CFD results can be obtained with the multiplication of hydraulic power and turbine efficiency presented in Table E.1. However, for the comparison, results should be represented at the same net head value. Therefore, shaft powers in Table 4.4 and the ones coming from CFD are

recalculated to the reference net head of 180 meters with the help of the Equation (4.21) [80].

$$\frac{P_{\text{recalculated}}}{P_{\text{measured}}} = \left(\frac{H_{\text{recalculated}}}{H_{\text{measured}}} \right)^{1.5} \tag{4.21}$$

The information provided in Table 4.4 as servo piston position in percentage corresponds to the guide vane opening. It is documented that maximum wicket gate opening (a_0) is 125 mm, which is nothing but the 100 % servo piston position. If a linear interpolation is conducted for the percentage values in Table 4.4, corresponding wicket gate opening for each servo piston position can be found easily (Table 4.9). Moreover, in Table 4.9, recalculated shaft powers for 180 meter net head are presented for both one and two-unit operation measurements. For the two-unit operation, turbine two is under consideration. On the other hand, last part of the Table 4.9 shows the recalculated shaft powers and wicket gate openings for CFD results, which are already found while the construction of guide vane profiles. Note that CFD results at 194.1 meter net head are taken as base in the recalculation of the shaft power. Finally, Figure 4.61 compares the shaft power results of commissioning test and CFD. As it is seen, the results of the measurement and CFD show a good agreement.

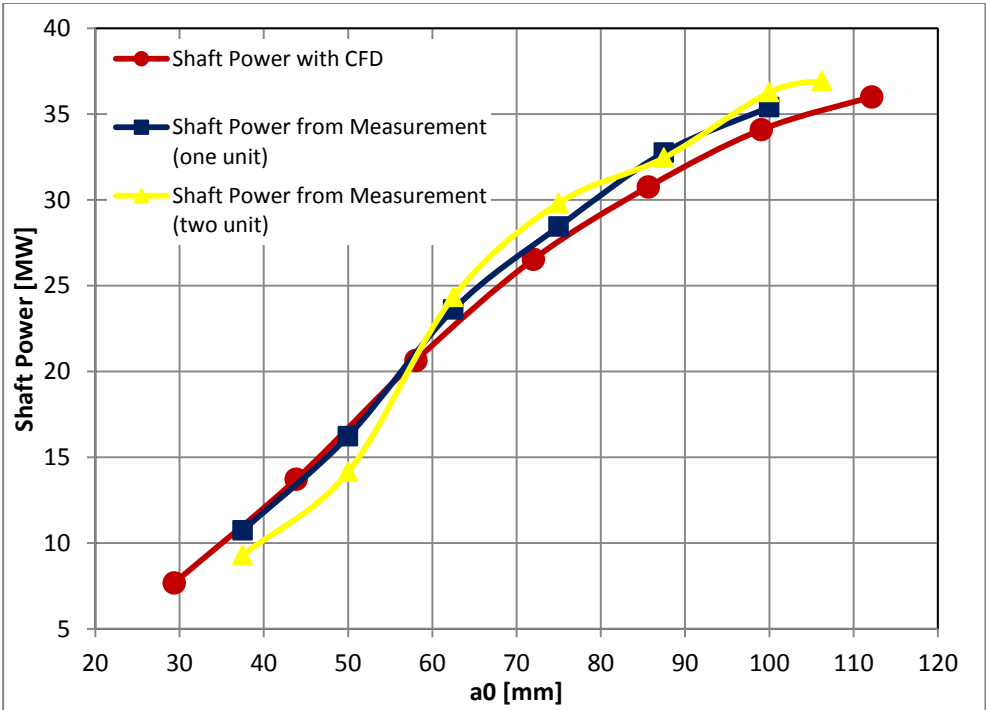


Figure 4.61 : Comparison of CFD results with measurements.

Table 4.9 : Recalculated shaft power for commissioning test and CFD results.

Shaft Power[MW]	Net Head [m]	Wicket Gate Opening		Recalculated Head [m]	Recalculated Shaft Power [MW]
		[%]	a_0 [mm]		
ONE UNIT OPERATION					
12.45	198.80	30.00	37.50	180.00	10.73
18.72	198.00	40.00	50.00	180.00	16.22
26.99	196.80	50.00	62.50	180.00	23.61
32.21	195.60	60.00	75.00	180.00	28.44
36.76	194.40	70.00	87.50	180.00	32.75
39.52	193.70	80.00	100.00	180.00	35.40
TWO UNIT OPERATION					
10.37	193.60	30.00	37.50	180.00	9.30
15.55	191.80	40.00	50.00	180.00	14.14
25.92	187.70	50.00	62.50	180.00	24.34
31.11	185.20	60.00	75.00	180.00	29.81
33.18	182.70	70.00	87.50	180.00	32.45
36.81	181.80	80.00	100.00	180.00	36.27
37.33	181.30	85.00	106.25	180.00	36.93
CFD RESULTS					
8.60	194.07	22.22	29.38	180.00	7.68
15.36	194.07	33.33	43.86	180.00	13.72
23.11	194.07	44.44	58.06	180.00	20.64
29.70	194.06	55.56	71.99	180.00	26.53
34.44	194.06	66.67	85.65	180.00	30.76
38.16	194.06	77.78	99.04	180.00	34.09
40.30	194.06	88.89	112.16	180.00	36.00



5. OPTIMIZATION OF RUNNER

Daily energy production data of Kadincik I HPP for ten years is analyzed in order to determine the new best efficiency point of the turbine with optimized runner. Subsequently, runner blade angles and blade length are modified according to flow conditions coming from CFD analyses to reach the peak efficiency around that point. Several optimization versions are created by hand-made optimization. While some of the new designs follow the traditional design method, in others X-Blade technology is introduced. Among these designs, most promising optimization versions for each design methodology (traditional and X-Blade) are chosen and their performances are compared with original turbine and each other.

5.1 Existing Situation

Based on the information given in annual production report for the last 10 years, an average yearly production is investigated more in detail. For visualization, power production is split into 5 MW steps and days of a year in operation are presented in percentages (Figure 5.1). It can be seen that for more than 60% of the year the power production is higher than 25 MW per unit per day. This includes one and two unit operation. During the last 10 years, 50.7 % of a year's time one unit operation has taken place.

The net head as a function of the power production is shown in Figure 4.2. Together with the CFD results for the power it is now possible to verify the flow rate for a given power production of one and two machine operation. Whereas Figure 5.2 and Figure 5.3 split the production into one and two machine operation, the averaged production per year (for the last 10 years) is shown versus the flow rate in Figure 5.4.

The average annual production of the power plant is 244 million kWh per year. The highest annual production is reached when the flow rate is in the range between 15 to 20 m³/s and – additionally – with lower percentage of yearly energy production ranges from 10 to 15 m³/s and 20 to 25 m³/s. The maximum flow rate is about 26

m³/s; consequently, cavitation-free operation at least up to this discharge value is one of the design targets.

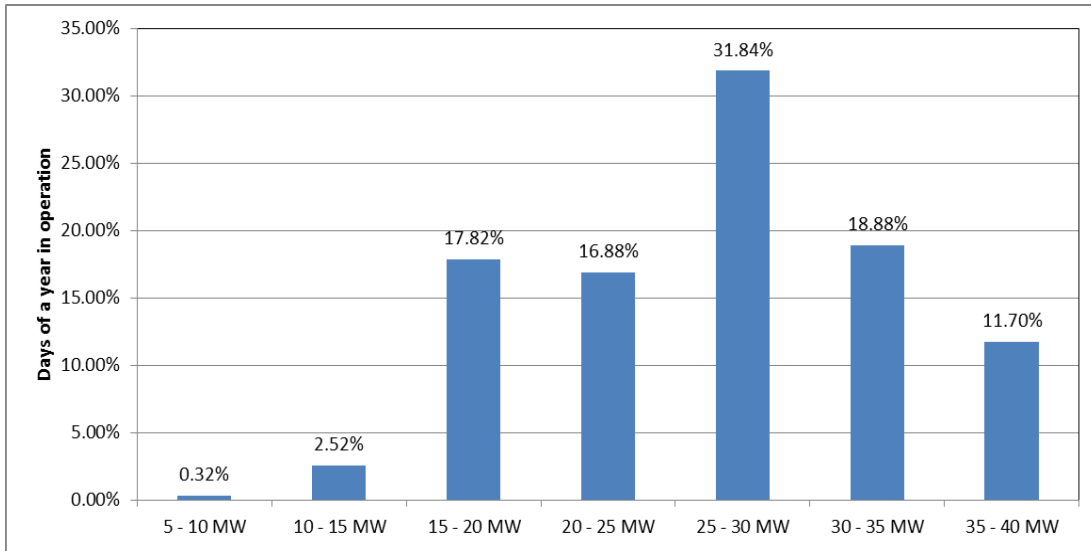


Figure 5.1 : Averaged yearly power production of Kadincik I HPP.

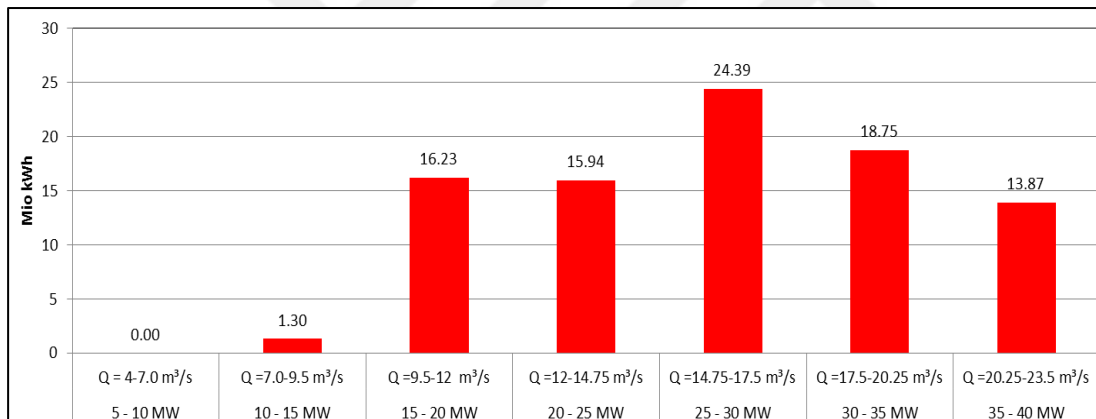


Figure 5.2 : Segmented annual production for one unit operation.

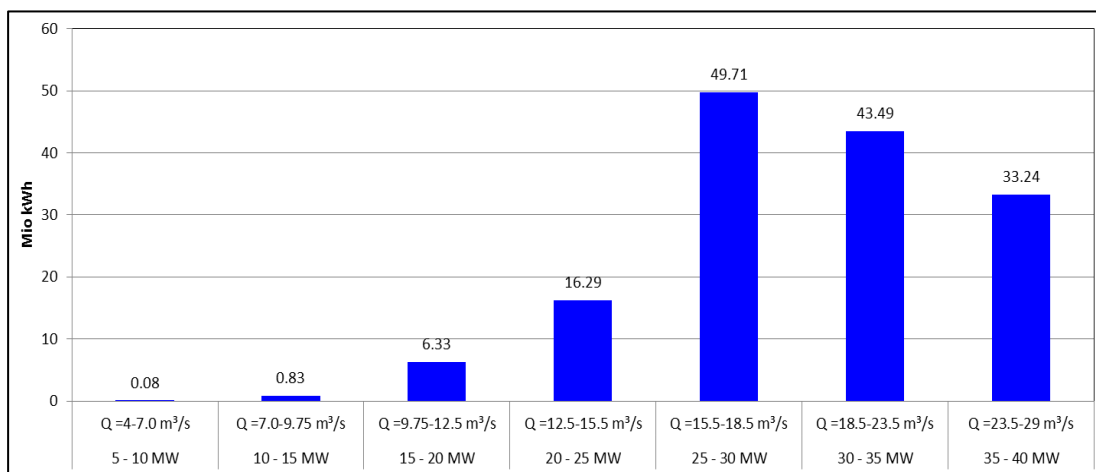


Figure 5.3 : Segmented annual production for two unit operation.

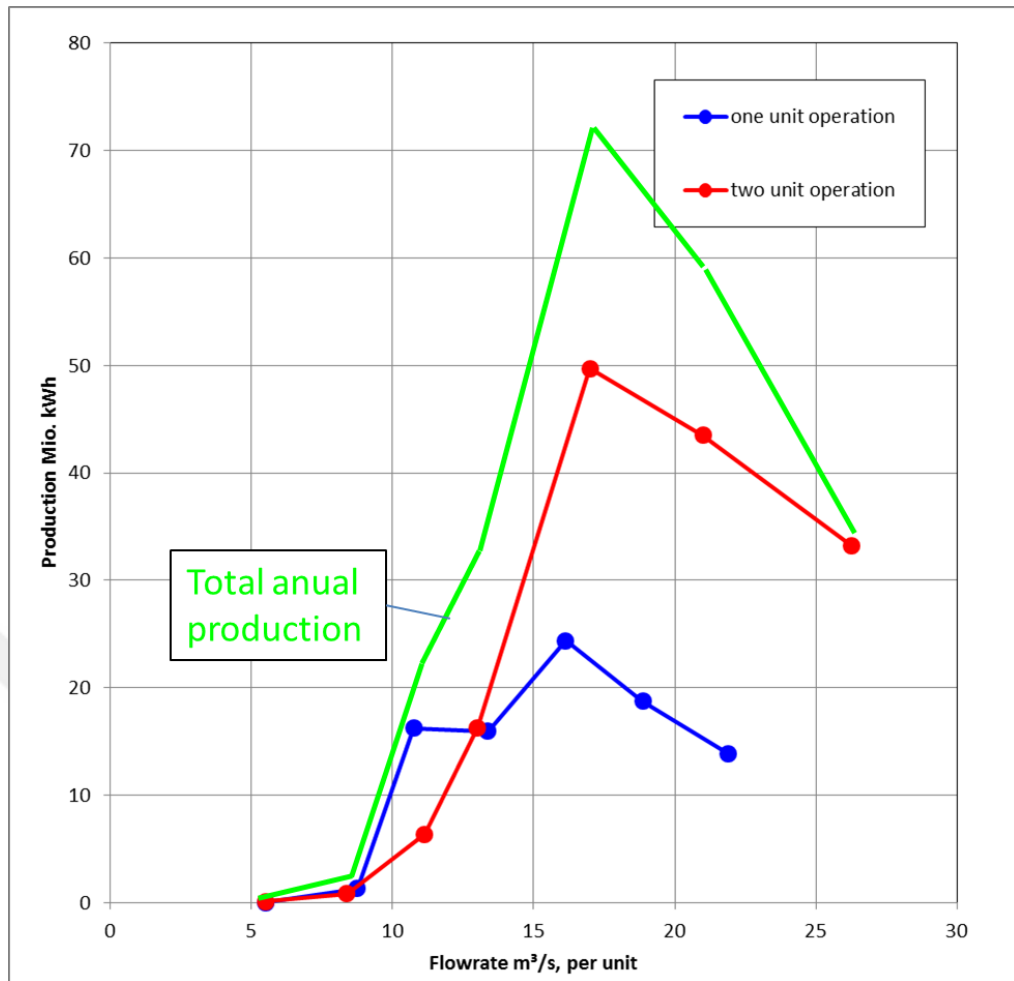


Figure 5.4 : 10 year-averaged power production per year.

5.2 Method of Optimization

Optimization studies starts with reconstruction of original runner in BladeGen® because this software allows the user to modify blade angles, blade length, hub and shroud contours and runner main parameters. Then, the geometry generation of the optimization versions is conducted engineer-based by hand – this means that no automated optimization routine is used.

Two different design approaches are followed in this study. First, original runner is modified according to CFD results with traditional methods. Although various optimization versions are created, the one with the best performance is chosen as the new runner geometry, which is optimized with traditional methods. Subsequently, X-Blade technology is introduced to original runner and further modifications are conducted according to the flow situation. Similar to the traditional optimization, runner design with best performance is determined among the X-Blade optimization

versions. In the end, numerical hill chart is generated for most promising optimization version for each design method with the help of the CFD results at different net heads and flow rates.

The method of optimization is well summarized in Figure 5.5.

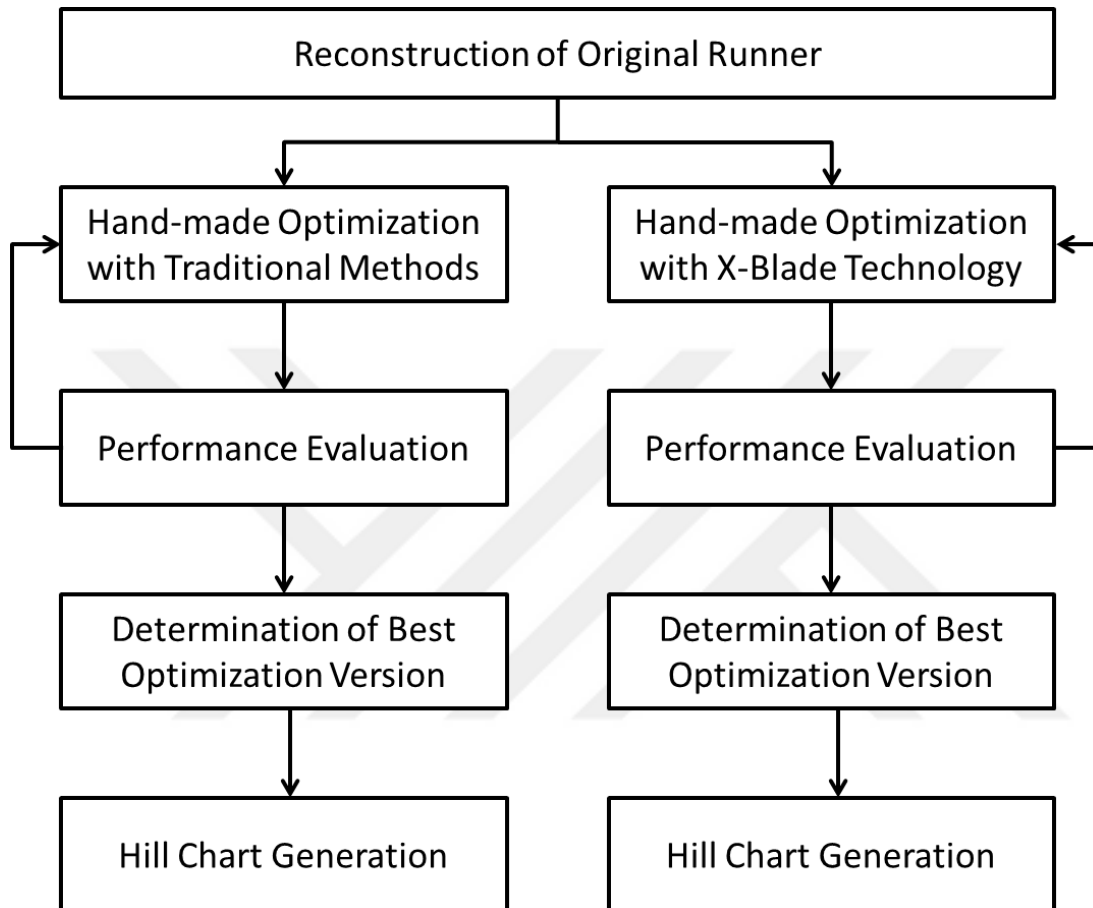


Figure 5.5 : Workflow of optimization process.

5.3 Reconstruction of Original Runner

A reconstruction of the original runner blade is carried out in a first step of the optimization. The commercial software package ANSYS-Bladegen® is used for the geometrical reconstruction which provides the basis for the optimization of the blade geometry.

The basis for a new Bladegen® design is always the definition of the meridional section, which is given in Figure 5.6 based on the original design. With the selection of a user-defined number of layers it is then possible to define the geometry data of the blade profiles.

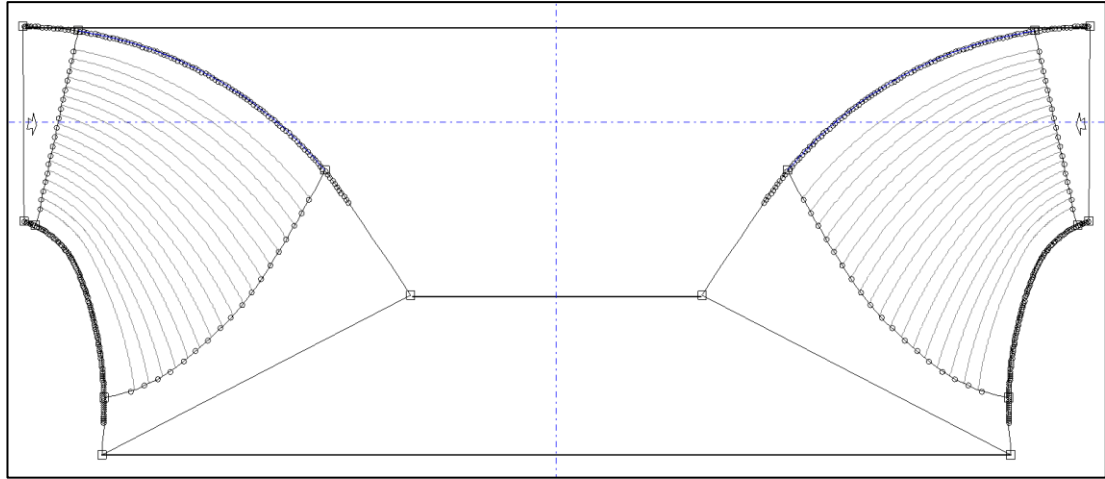


Figure 5.6 : Meridional view of the original runner of Kadincik I HPP with the layers for the geometry definition.

In order to define the profile data in Bladegen®, it is necessary to process information referring to the wrap angle “Theta” and thickness distribution as a function of the meridional length “M” for every single layer previously defined in Bladegen®.

To create the “Theta vs. M”-curves and thickness distribution for every blade section, meridional curves are exported from Bladegen® and rotated 360 degree around the rotation axis for surface creation. These surfaces are intersected with laser-scanned blade geometry and resulting splines are utilized as runner sections. With the help of the CAD software package CATIA, the splines defining all the blade sections are divided into one spline for the suction side and one spline for the pressure side of the blade. Furthermore, 100 equidistant points are distributed on the new curves. These points are exported into a neutral data file and imported into MS-Excel where a calculation sheet for the “Theta vs. M”-curves is prepared.

The connection of the corresponding data points on the suction and the pressure side allows for the calculation of mean values which finally serve as definition of the camber line for different blade sections. By the utilization of x and y coordinates of chamber line, wrap angle is calculated with Equation (5.1).

$$\theta = -\tan^{-1}\left(\frac{x}{y}\right) \quad (5.1)$$

Figure 5.7 shows the blade sections imported into MS-Excel with their calculated camber lines being marked with dashed lines. Furthermore, Figure 5.8 shows the

“Theta vs. M”-curves which are calculated based on the blade sections defined in Figure 5.7. Finally, also the thickness distribution extracted by the calculation of the absolute thickness (which equals to the absolute distance of the corresponding data points on the suction and the pressure side) as a function of the meridional length M is presented in Figure 5.9. It is obvious that the curves representing the thickness distribution show a rather bumpy trend especially close to the trailing edge. For the final optimization versions, the thickness distribution is certainly smoothed using regression curves.

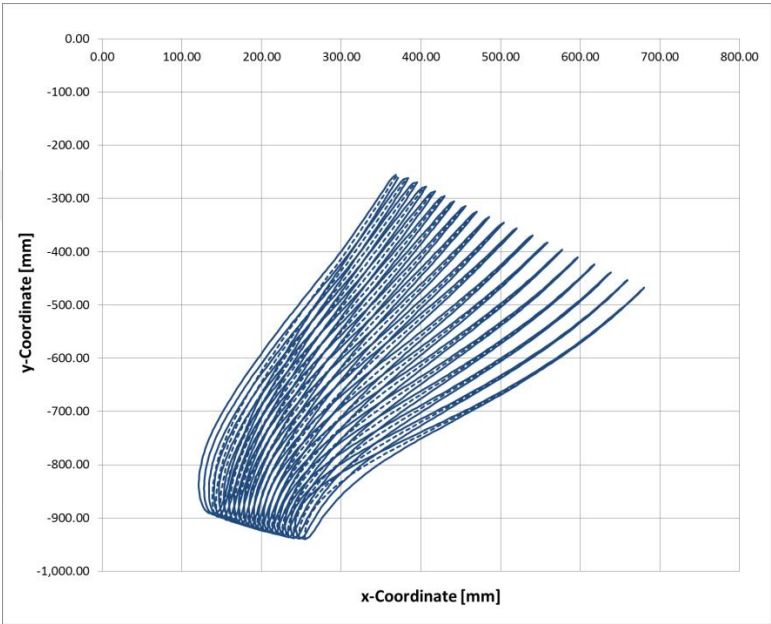


Figure 5.7 : Blade sections of the original runner of Kadincik I HPP.

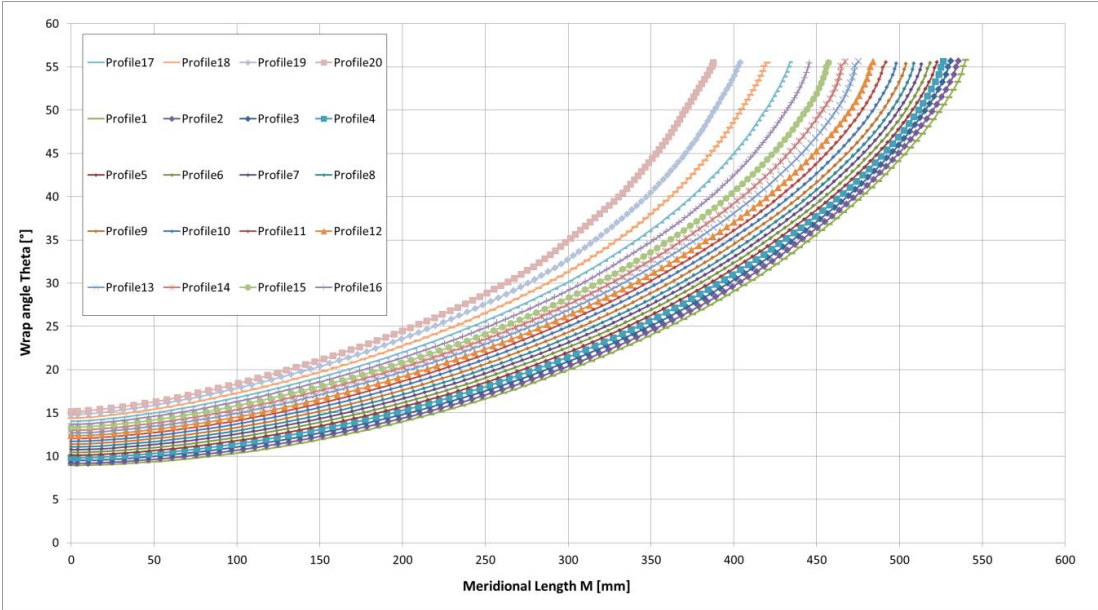


Figure 5.8 : “Theta vs M” curves of the original runner of Kadincik I HPP.

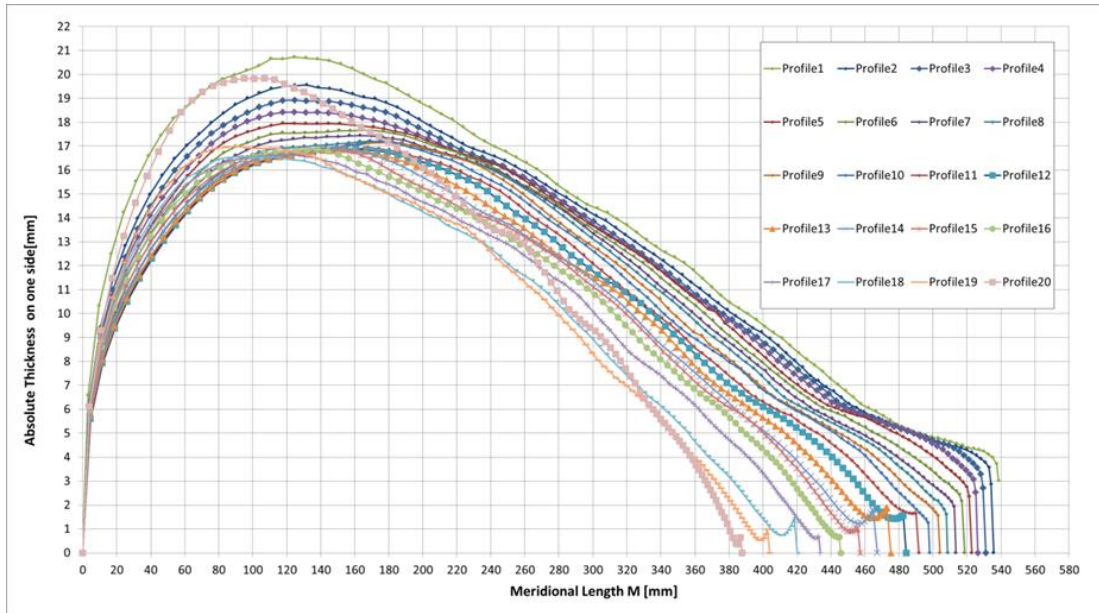


Figure 5.9 : Thickness distribution of the original runner of Kadincik I HPP.

After importing the “Theta vs. M”-curves as well as the “Thickness vs. M”-curves into ANSYS-Bladegen®, the blade geometry is finally fully-defined and Bladegen® is able to create a 3D-CAD-model of the runner (Figure 5.10).

Due to the fact that the “Theta vs. M”-curves are imported into the ANSYS-Bladegen® model, the blade angle distribution “Beta vs. M” is automatically calculated with Equation (5.2). The results for all blade layers are shown in Figure 5.12.

$$\tan(\beta(r)) = \frac{dr}{r * d\theta} \quad (5.2)$$

For the original runner blade of Kadincik I HPP, it can be summarized that the inlet angle of the original blade accounts for 88° close to the hub and for 80° close to the shroud. On the other hand, the beta angle at the outlet accounts for 15° close to the hub and 10° close to the shroud.

Once the reconstruction is finished, it is rather easy to change the shape of the leading and trailing edge in the meridional section, to adapt the blade angle distribution or to vary the thickness distribution of the blade.

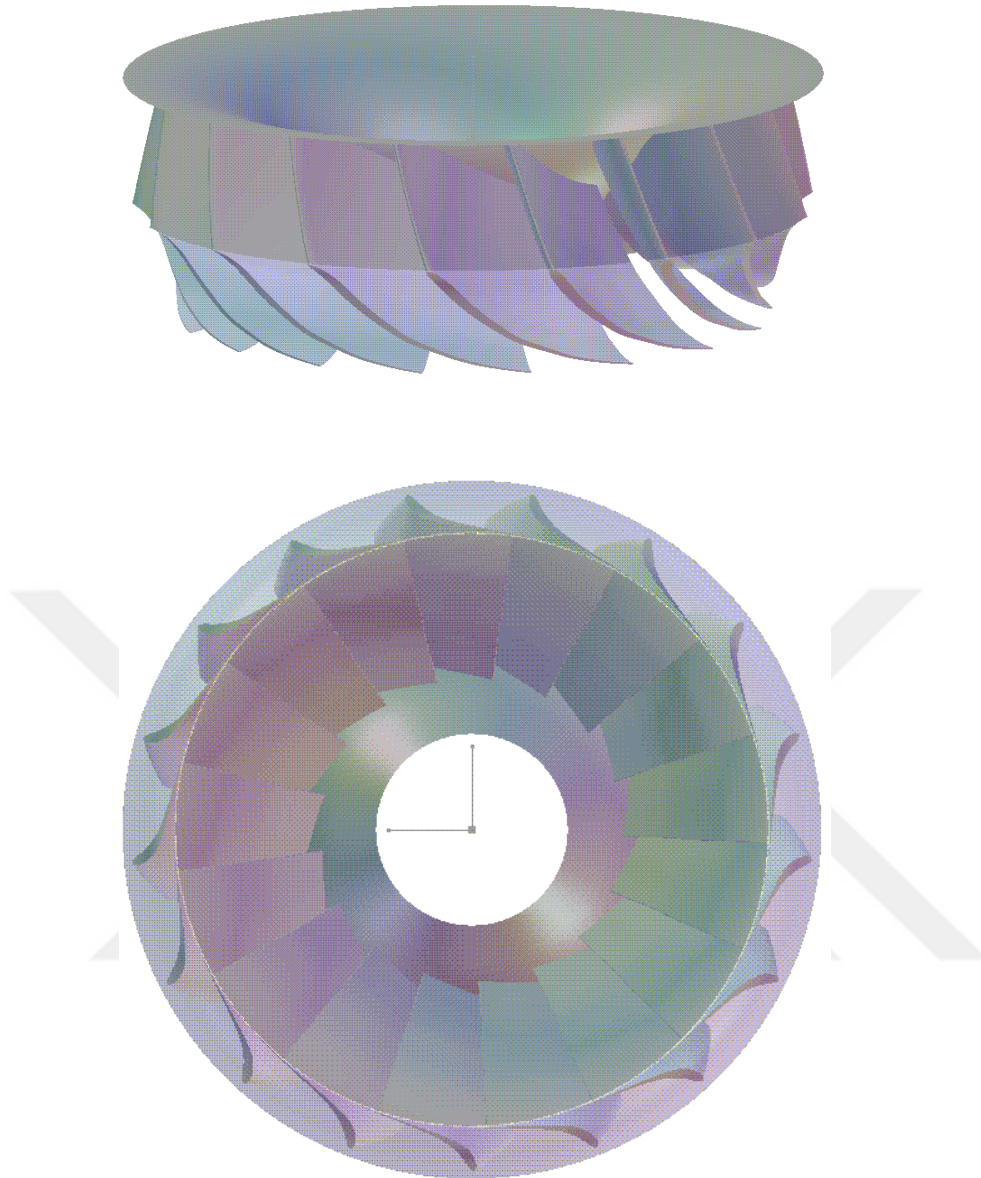


Figure 5.10 : CAD model of reconstructed original runner of Kadincik I HPP.

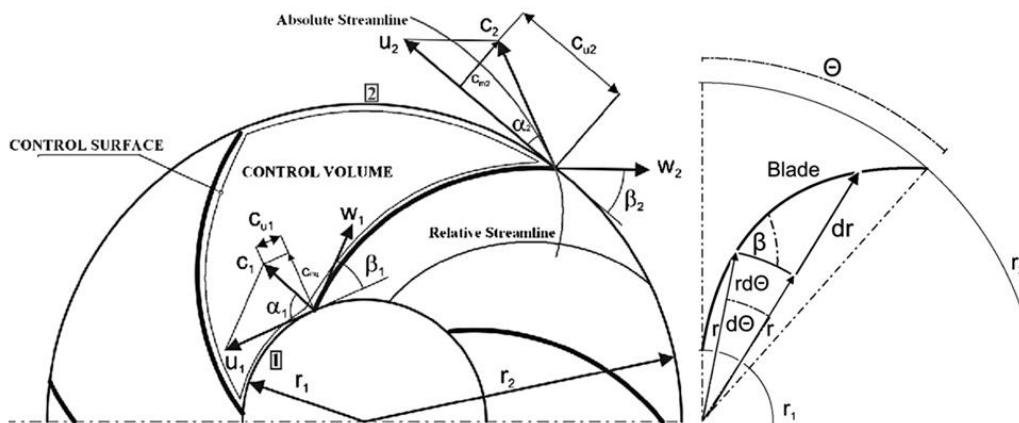


Figure 5.11 : Angle definition of radial turbomachines, adapted from [110].

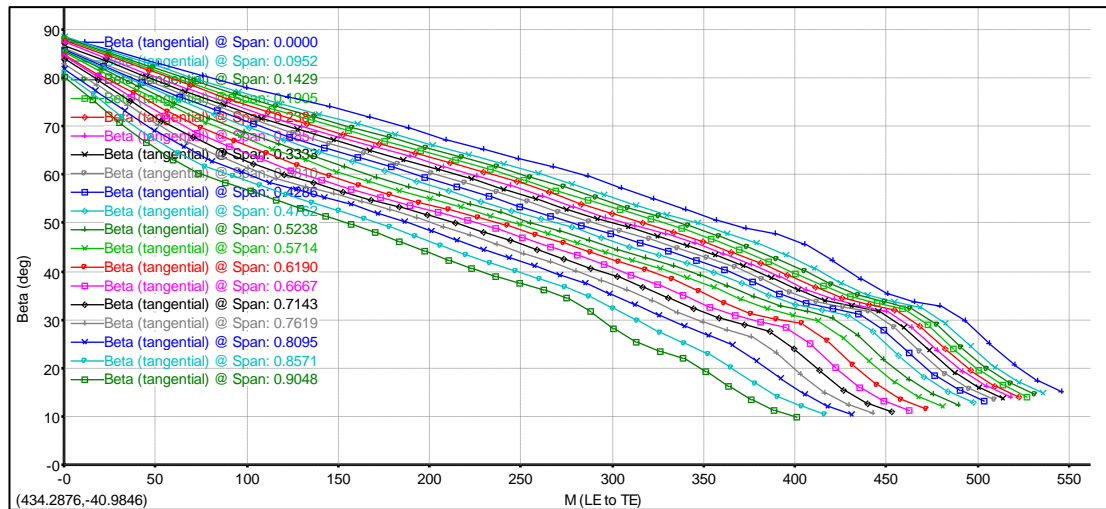


Figure 5.12 : “Beta vs M” curves of the original runner of Kadincik I HPP.

5.4 Optimization of Runner

The optimization targets can be listed as:

- Higher peak efficiency
- Improvement of the turbine efficiency over the whole range of operation
- Shift the best efficiency point of the turbine to operation points
- Improvement in cavitation performance
- More homogenous pressure distribution along the runner blade
- Constant c_m distribution at the outlet of the runner
- Zero c_u at the outlet of the runner

Before generating optimization versions, new desired best efficiency point of the turbine should be determined and modifications should be done in order to achieve this goal. By looking Figure 4.2, it can be concluded that turbine is operating in a net head range between 170 meter and 190 meter. Therefore, it is reasonable to choose the net head value of new peak efficiency point in this range, for instance around 180 meter. Furthermore, Figure 5.4 clearly shows that maximum annual production occurs around $17.5 \text{ m}^3/\text{s}$. However, the production decreases very sharply when flowrate lowers, whereas decrease in production is not that dramatic at overload. Consequently, nominal discharge of new runner is decided as $20 \text{ m}^3/\text{s}$. In brief, based on the findings gained in the course of the segmentation of the annual energy

production, the best efficiency point should be reached around a flow rate of $Q= 20 \text{ m}^3/\text{s}$ at a head level of around 180 m.

As it is already indicated with Figure 4.60, although the original turbine of Kadincik I HPP was designed for a nominal net head 194 meter, turbine achieves its best efficiency point around 155 meter net head and $17 \text{ m}^3/\text{s}$ discharge with a 94 % peak efficiency. This point is so far away from the operation conditions.

Although original turbine shows a good performance with respect to the peak efficiency and cavitation, these issues are still open to improvements. Cavitation initiation should be prevented at least up to $26 \text{ m}^3/\text{s}$ discharge which is observed very rarely in the power plant.

At best efficiency point of the original turbine, an inhomogeneous pressure distribution around the leading edge is found. While the inflow conditions between 0 % span (hub) and 75 % span appear appropriate, a low pressure region close to the shroud is detected on the suction side of the blade. This finding is visualized in Figure 5.13 (left) – showing the pressure distribution on the runner blades – whereas Figure 5.14 presents the blade loading at the best efficiency point. Additionally, there is a low pressure region on the suction side of the blades close to the trailing edge which is shown with the right picture of Figure 5.13 (a view of runner from draft tube). The regions with a dark blue color may cause serious cavitation problems – especially at full load operation. Nevertheless, apart from these problems, blade loading on the original runner is not bad because there is a smooth redirection of the flow from radial to axial direction (Figure 5.6).

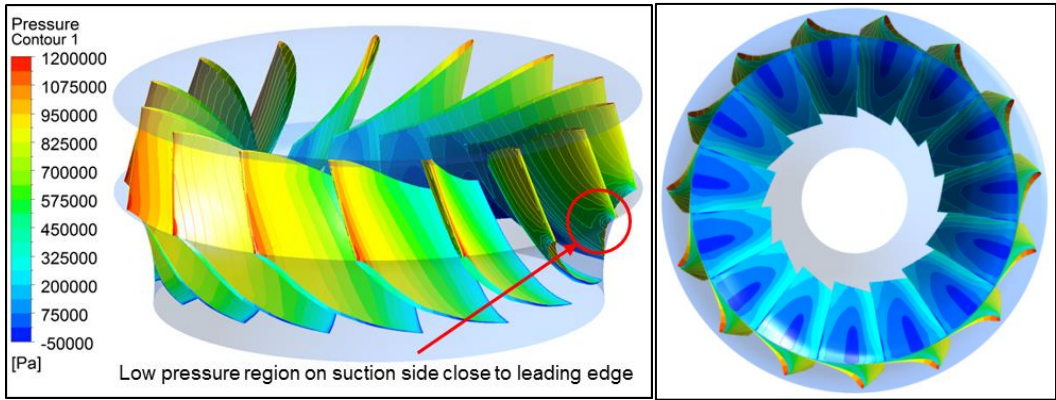


Figure 5.13 : Static pressure distribution on the original runner blades at best efficiency point ($H_{\text{net}}=155 \text{ m}$ and $Q=17 \text{ m}^3/\text{s}$).

It turns out that the c_m and c_u distributions at the runner outlet are both widely constant at best efficiency point for the original turbine of Kadincik I HPP – the c_u value being close to zero at the outlet of the runner as it should be (Figure 5.15). The range between the minimum and maximum c_m values basically accounts for just 2.0 m/s. Only close to the shroud, the deviation from the mean value of c_m is slightly higher. Furthermore, an analysis of the c_u distribution shows that the requirement of constant c_u is fulfilled over a wide range. There is no excessive amount of swirl remaining in the flow. Based on the fact that the peak efficiency of Kadincik I is already comparably high, this finding is not surprising.

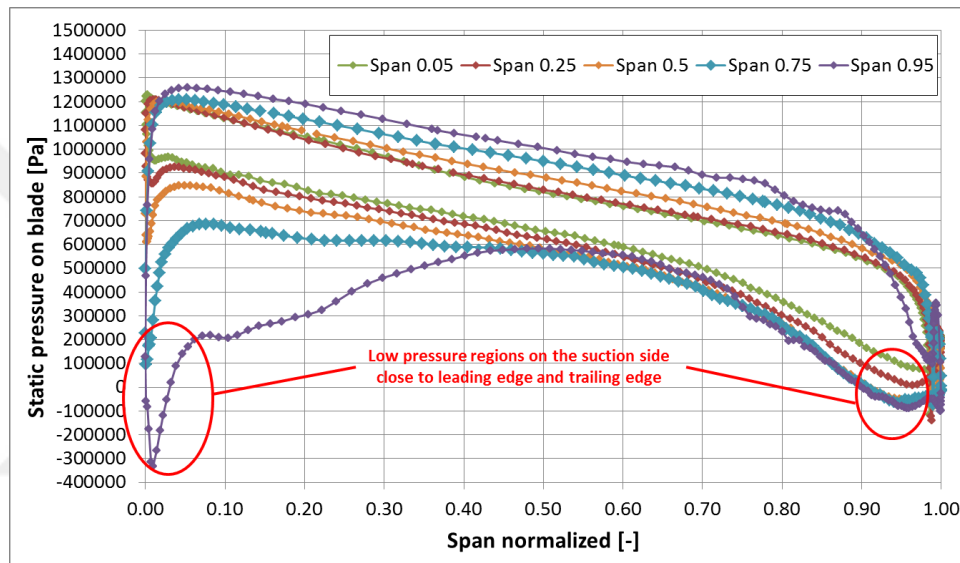


Figure 5.14 : Blade loadings of the original runner for various span values at best efficiency point ($H_{\text{net}}=155$ m and $Q=17$ m³/s).

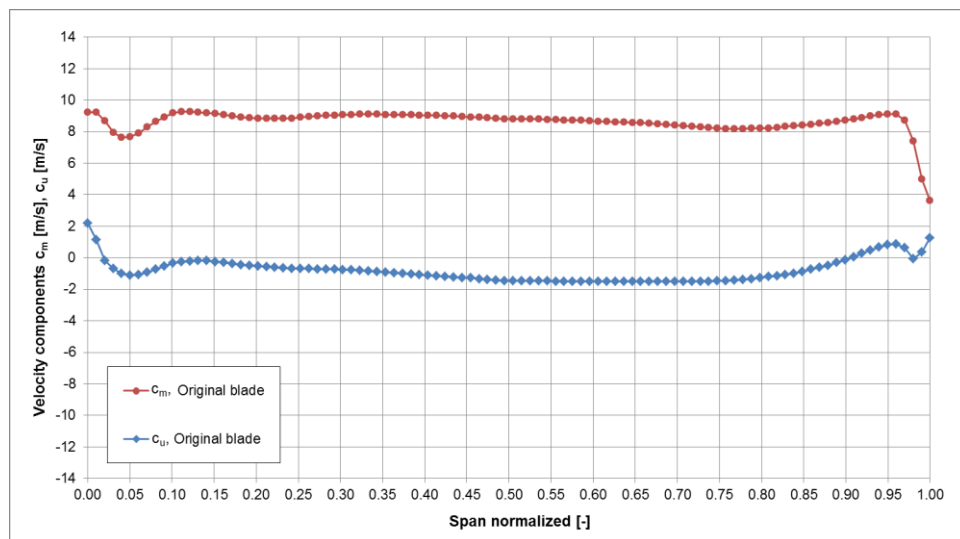


Figure 5.15 : c_m and c_u distribution at the outlet of the original runner of Kadincik I HPP at best efficiency point ($H_{\text{net}}=155$ m and $Q=17$ m³/s).

5.4.1 Optimization with traditional methods

The main modifications on the original runner blade are carried out for the slope of the leading and trailing edge in the meridional section and for the beta-angle-distribution.

First of all, modifications start with the smoothing of the beta curves and thickness distribution in order to eliminate local disturbances of flow. This is followed by changing the slope of the leading edge from strong inclination to almost vertical one, which is highly recommended by Prof. Raabe [111]. These changes result in an improvement of cavitation performance due to the longer blade profiles and better inflow conditions. Nonetheless, peak efficiency slightly decreases because flow is faced with more resistance in the runner and excessive energy is taken from the water. This problem is solved with the increase of outlet blade angles, from $\sim 3.5^\circ$ at shroud to $\sim 2^\circ$ at hub. With this modification, less c_u reduction in the runner is achieved; thus, much better cavitation performance is provided. Moreover, efficiency curve, and therefore best efficiency point, shifts to the higher flowrates which is desired to get maximum efficiency around $20 \text{ m}^3/\text{s}$. After all these changes in the hydraulic shape of the original design, most promising optimization version for traditional design is obtained.

Meridional shape of the optimized runner is shown in Figure 5.16. When leading edge geometry is compared with the one in original runner, it is seen that new design has much more straight leading edge.

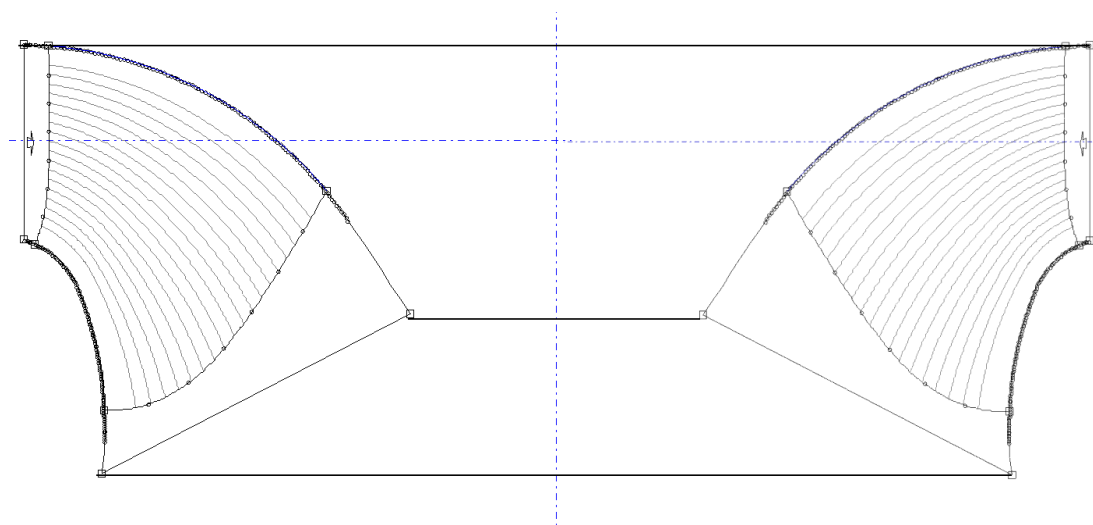


Figure 5.16 : Meridional view of optimized runner with traditional design methods.

The changes in beta angles (Figure 5.19) also affect the meridional shape and theta angle distribution (Figure 5.17). Finally, smoothed half thickness distribution is presented in Figure 5.18 and new runner design got the 3D shape visualized in Figure 5.20.

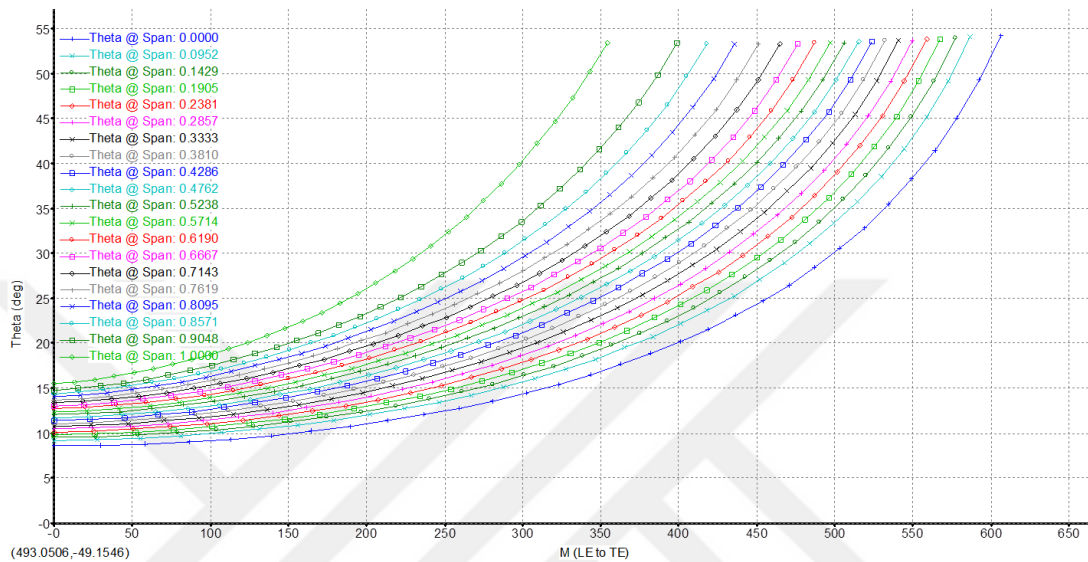


Figure 5.17 : “Theta vs M” curves of optimized runner with traditional design methods.

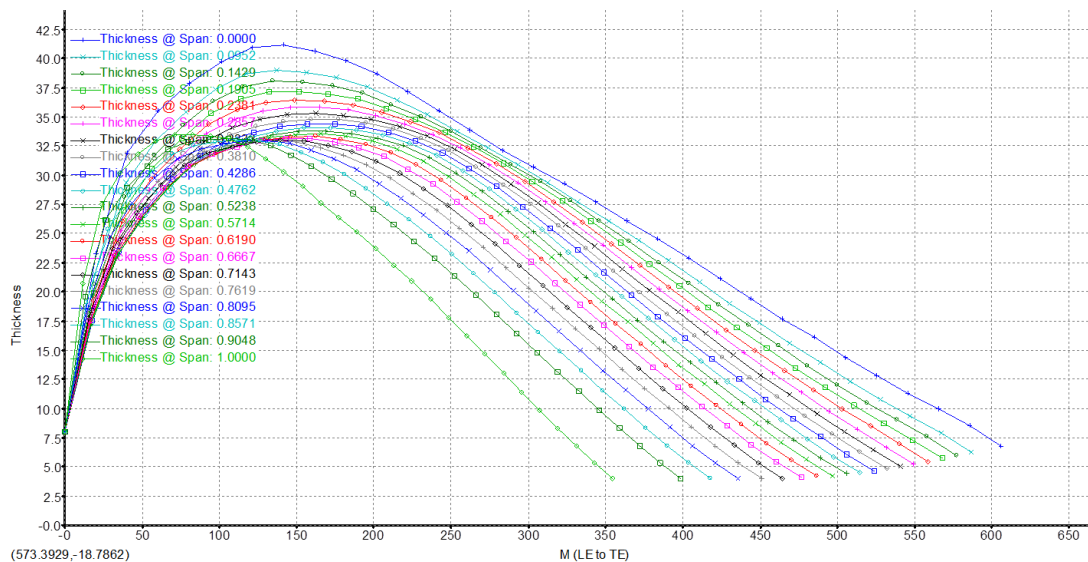


Figure 5.18 : Thickness distribution of optimized runner with traditional design methods.

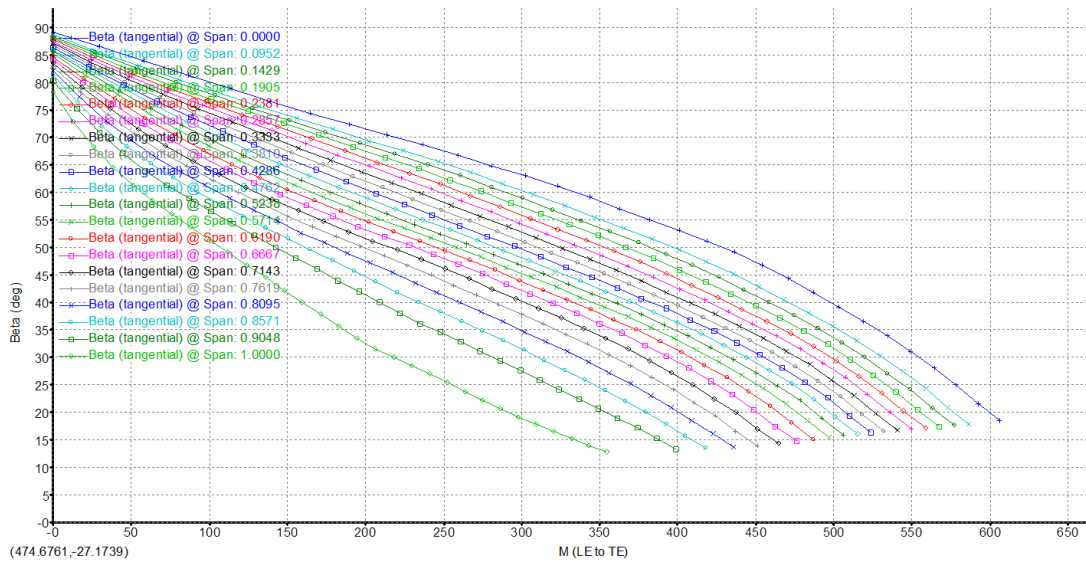


Figure 5.19 : “Beta vs M” curves of optimized runner with traditional design methods.

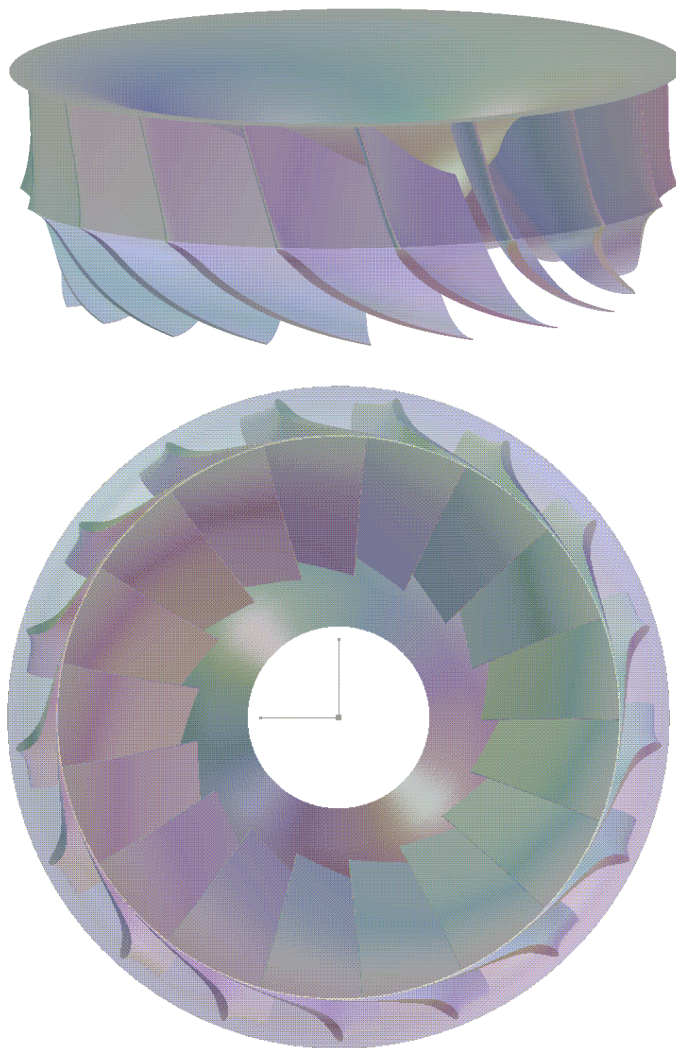


Figure 5.20 : CAD model of optimized runner with traditional design methods.

5.4.2 Optimization with X – Blade technology

The main modifications on the original runner blade are carried out for the position of the leading and trailing edge in the meridional section, for the beta-angle-distribution, for the wrap angle definition at the inlet of the runner, for the hydraulic shape of shroud and for the thickness distribution.

Changes in the geometry of original runner start with the introduction of X-Blade design. For this purpose, inlet wrap angles of the sections close to hub are increased whereas inlet wrap angles of the sections close to shroud are decreased. In fact, wrap angle definition at the inlet of the runner for X-Blade is vice versa of the one in traditional design.

Stronger X-Blade design is established around shroud than the hub in order to have more homogeneous pressure distribution at the leading edge. This step results in considerable amount of improvement in peak efficiency and cavitation performance; however, c_u at the runner outlet close to shroud is higher than zero which means remaining swirl is delivered to the draft tube.

The problem in the c_u distribution is tried to be solved with the extension of the trailing edge close to shroud in the meridional view towards the runner outlet and contraction of the trailing edge close to hub towards the inlet. At the same time, leading edge is shifted towards the runner inlet to have further improvement in the pressure distribution. After these steps, while more homogenous pressure and c_u distribution are achieved, c_m at the outlet close to the shroud is slightly too high.

c_m at the outlet close to shroud is lowered with the increased outlet beta angles and longer blade around the shroud. This modifications provides homogeneous velocity distribution; as a result, cavitation performance slightly improved. At the end of these modifications, it is seen that peak efficiency occurs in higher flow rates than desired. In order to shift efficiency curve to lower discharges, number of the runner blades is increased to 17 and shroud contour is contracted. Finally, original thickness distribution is changed with 4-digit-NACA profile by taking the maximum thickness values and position of original runner blade as base. After all these changes in the hydraulic shape of the original design, most promising optimization version for X-Blade design is obtained.

Meridional shape of the optimized runner is shown in Figure 5.21. Straighter leading edge can also be seen in this optimization version, but this time leading edge is closer to the inlet. Moreover, expanded trailing edge through the outlet close to shroud and shifted trailing edge towards to inlet near to hub is observed in this meridional shape.

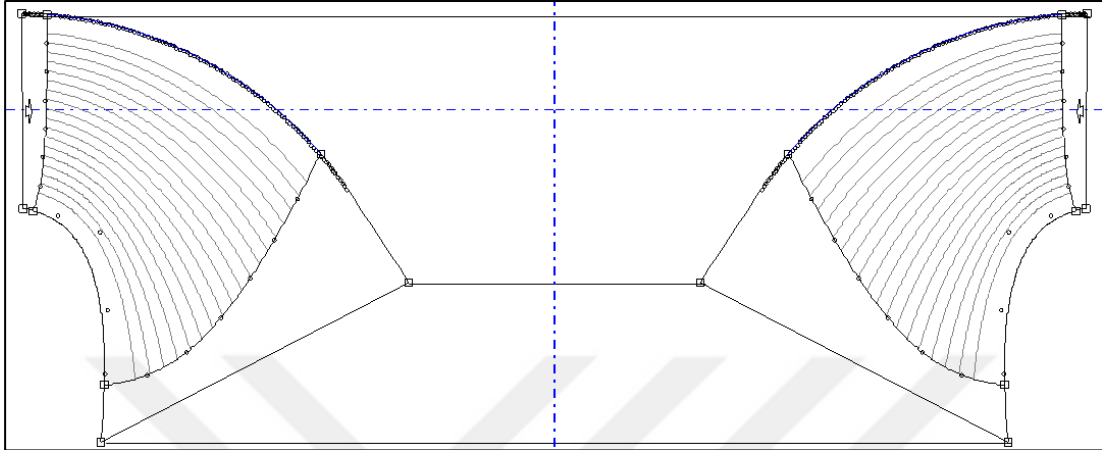


Figure 5.21 : Meridional view of optimized runner with X-Blade design method.

Wrap angle definition was completely changed at the inlet of the runner (Figure 5.22). This causes some small changes in beta distribution, but beta angles are further modified to obtain homogenous velocity distribution (Figure 5.24). Finally, half thickness distribution for 4-Digit NACA profile is presented in Figure 5.23 and new runner design gets the 3D shape visualized in Figure 5.25.

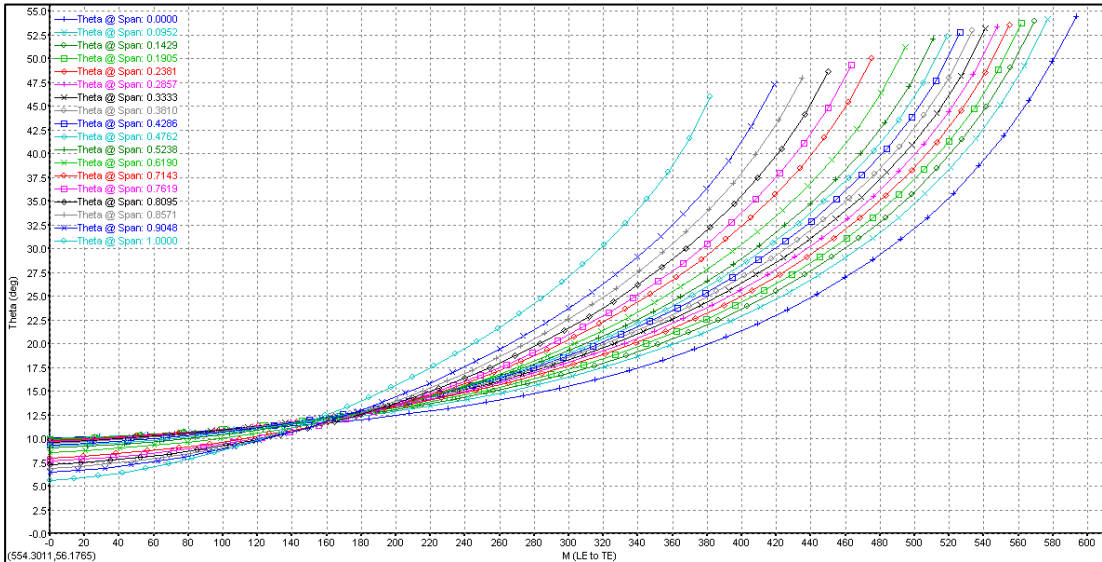


Figure 5.22 : “Theta vs M” curves of optimized runner with X-Blade design method.

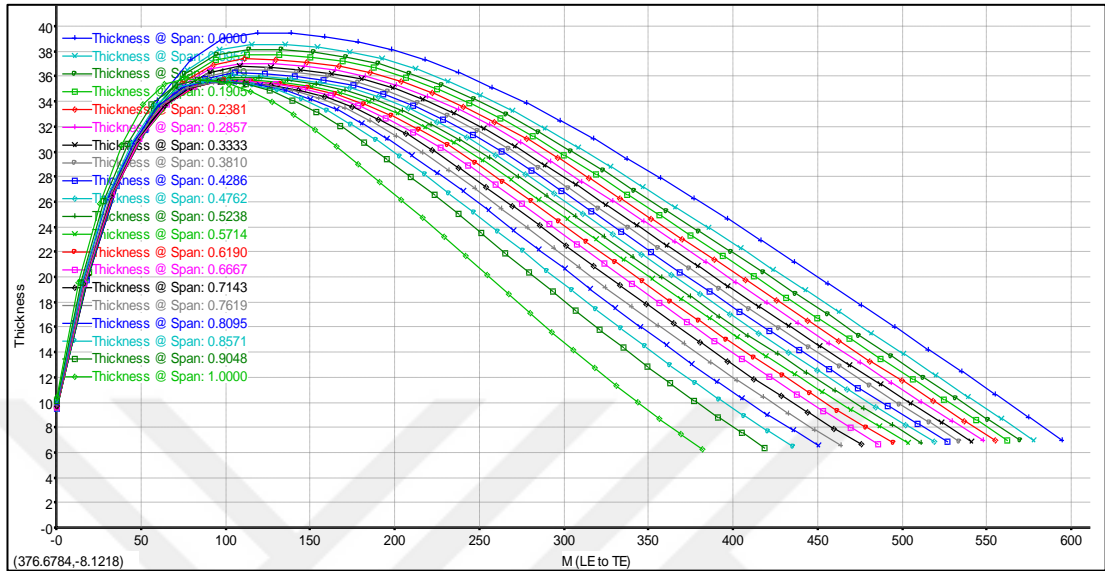


Figure 5.23 : Thickness distribution of optimized runner with X-Blade design method.

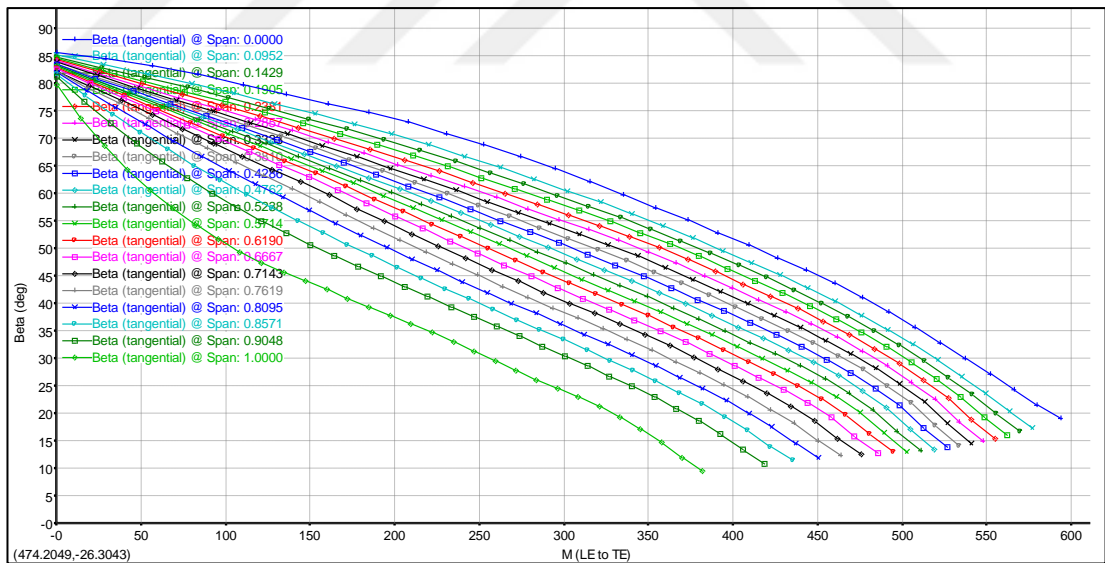


Figure 5.24 : "Beta vs M" curves of optimized runner with X-Blade design method.

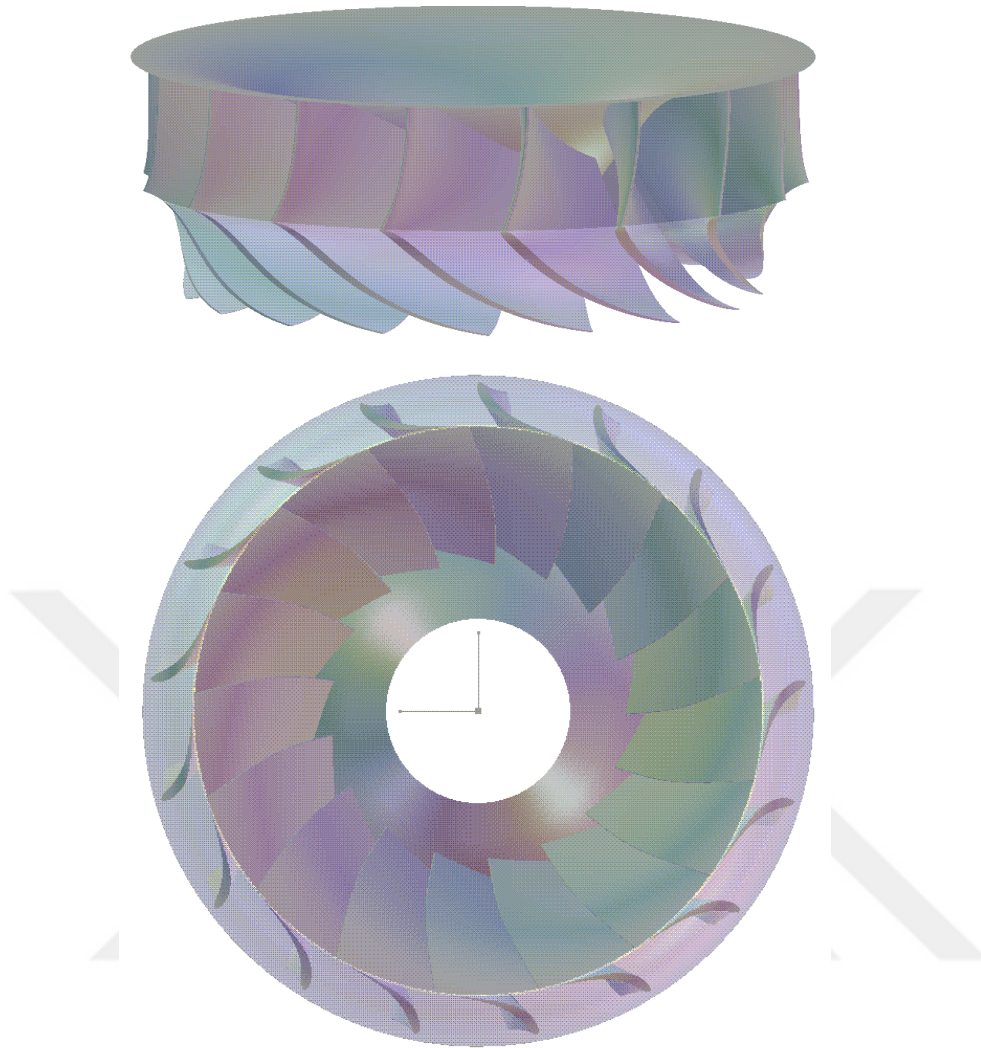


Figure 5.25 : CAD model of optimized runner with X-Blade design method.

5.5 Results of Proposed Designs

5.5.1 Results of traditional design

As it was done for the original turbine, CFD analyses in different net head and discharge levels are conducted for the turbine with traditionally optimized runner. The results achieved in the course of this study is presented in Appendix F. As it is already stated, CFD is not able to cover disk friction and leakage losses; hence, 1.2 percentage point was subtracted from the hydraulic efficiency based on CFD in order to obtain the resulting turbine efficiency (detail explanation is in 4.5.8. Numerical hill chart sub-chapter). Although lower runner disk frictions and leakage losses can be attained with today's-technology, these losses are considered as 1.2 % like in the

original turbine evaluation in order to make the relative comparison between the performances of the turbines.

Figure 5.26 shows the numerical hill chart of the Kadincik I HPP turbine with traditionally optimized runner geometry. Compared to the original turbine, the best efficiency point is shifted from $Q = 17 \text{ m}^3/\text{s}$ and $H_{\text{net}} = 155 \text{ m}$ to around $Q = 21 \text{ m}^3/\text{s}$ and $H_{\text{net}} = 174 \text{ m}$. The new best efficiency point of the optimized turbine fits much better to the operation range of the power plant than the original turbine configuration, although the peak efficiency still cannot be maintained through the wide range of operation. Furthermore, maximum efficiency is increased from 94 % to 94.3 %. New design establishes an efficiency increase at overload, whereas turbine performance deteriorates at part load operation conditions.

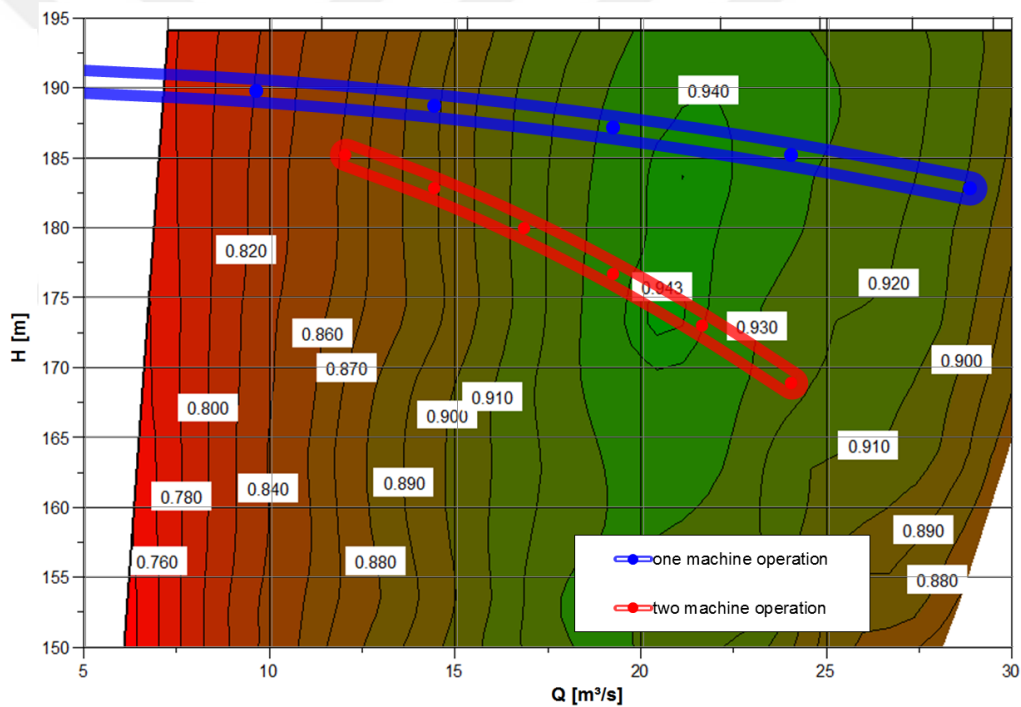


Figure 5.26 : Numerical hill chart for traditional optimization of Kadincik I HPP.

Head loss analysis is conducted for the optimized turbine with conventional methods at the design net head (174 meter) in order to investigate the performances of the mechanical components of the turbine separately. Figure 5.26 suggests that design flow rate is around $21 \text{ m}^3/\text{s}$. This is also supported by Figure 5.27 which reveals that minimum percentage head loss occurs at $21 \text{ m}^3/\text{s}$ for 174 meter net head. Furthermore, runner and draft tube components show their best performances at this

discharge level, whereas spiral case and guide vanes are so away from their minimum head loss points.

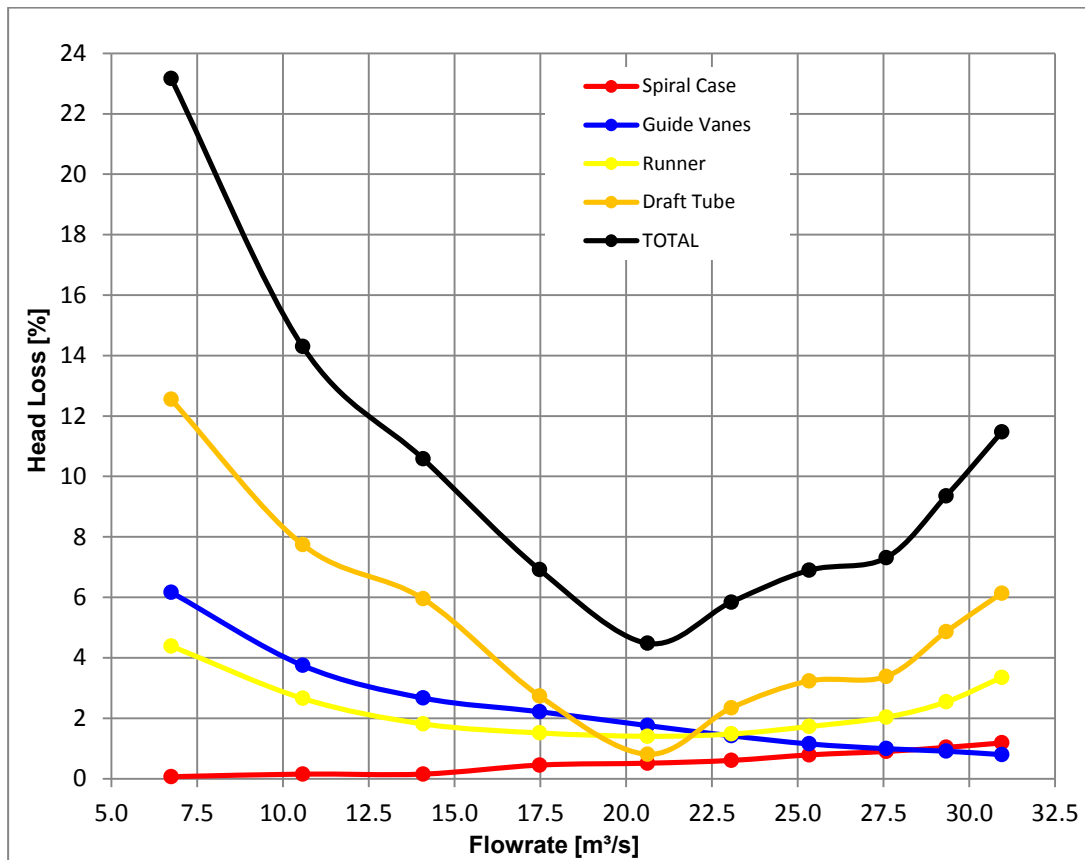


Figure 5.27 : CFD percentage head losses for mechanical components of conventionally optimized turbine.

Another improvement was achieved regarding the cavitation performance. The change in the slope of the leading edge and the smoothing operation of the beta curves and thickness distribution lead to longer blade profiles and better inflow conditions. These modifications numerously improve the cavitation performance of the turbine. The discharge value where the cavitation initiates is shifted from $Q = 25.0 \text{ m}^3/\text{s}$ to $Q = 29.0 \text{ m}^3/\text{s}$

In Figure 5.28, the cavitation performance is shown together with the power output plotted versus the flowrate. In optimization targets, it is stated that cavitation inception should be prevented at least up to $26 \text{ m}^3/\text{s}$ discharge which is observed very rarely in the power plant. In fact, it is very unlikely that the guide vane apparatus is capable of realizing an opening enables higher flowrates than $26 \text{ m}^3/\text{s}$. Therefore, it can be said that traditionally optimized version of Kadincik I HPP is over-safe for cavitation.

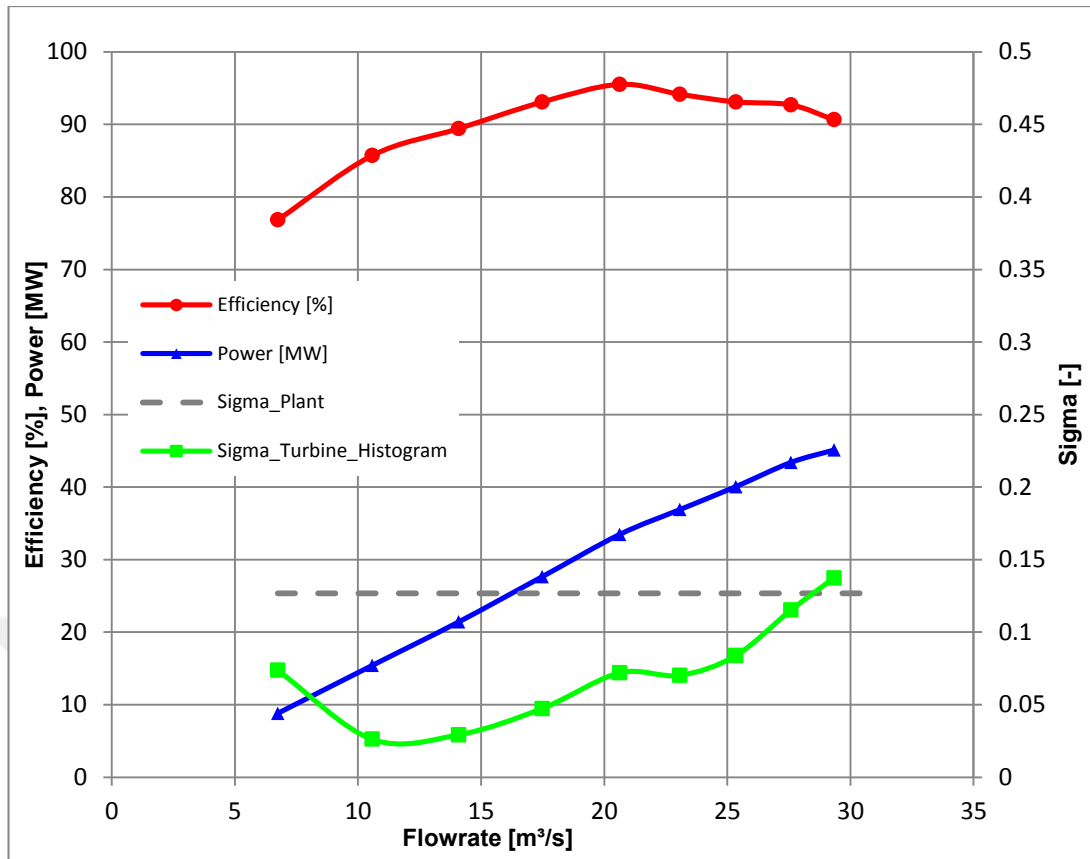


Figure 5.28 : The overall CFD performance of conventionally optimized turbine at design head.

Figure 5.29 presents the blade loadings of the original blade and the traditional optimization version evaluated for span values of 0.95, 0.75, 0.50, 0.25 and 0.05 at the best efficiency point of each turbine. Although it is hard to say pressure distribution of the proposed optimization version completely satisfies the optimization targets, it is clear that blade loading around the leading edge is considerably improved especially close to the shroud (Figure 5.30 and Figure 5.31). This is achieved by more vertical leading edge geometry and smoother beta curves.

Figure 5.32 presents a comparison of the spanwise distribution of the c_m - and c_u -velocity components at runner outlet between original and conventionally optimized blades, evaluated based on the numerical results at best efficiency point of each turbine. While the light orange and dark orange curves drawn refer to the c_m - and c_u -distributions of the original blade, the light blue and dark blue curves are related to the velocity distributions achieved with the conventional optimization. Except from the regions close to shroud, optimized runner shows more homogenous velocity distribution. After the 80 % span, c_m and c_u velocities start to fluctuate from the mean

value and velocity distribution in that region becomes slightly worse than the original one. This is a result of the increased outlet blade angles close to shroud which is applied in order to shift the efficiency curve to higher flowrates.

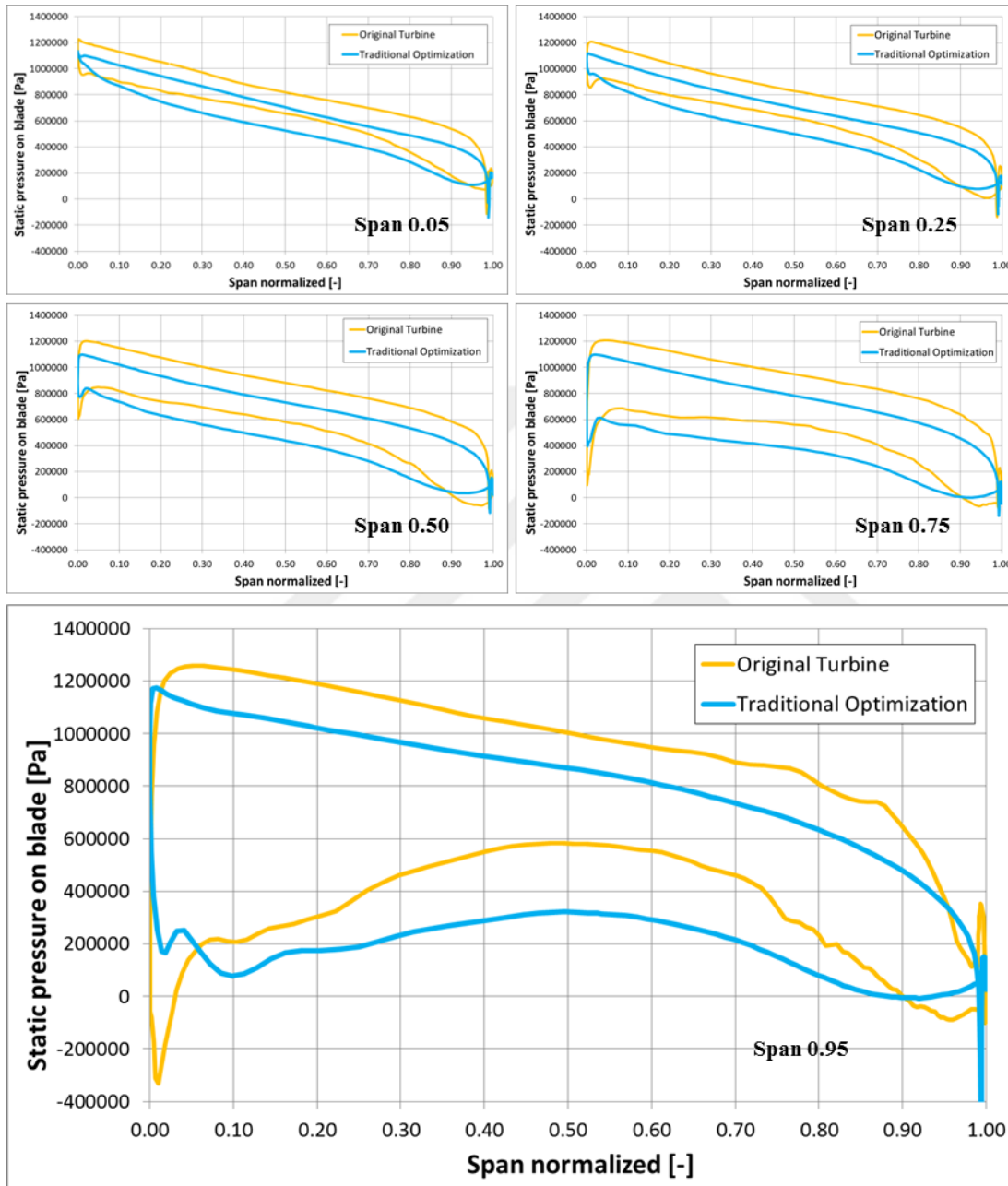


Figure 5.29 : Blade loading comparison of the original runner and traditional optimization version at their best efficiency points.

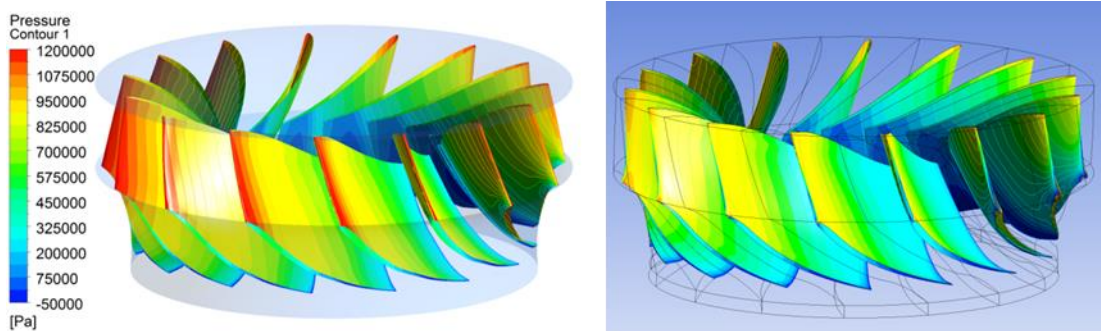


Figure 5.30 : Pressure contours of the original runner (left) and traditional optimization version (right) at their best efficiency points (view from upstream).

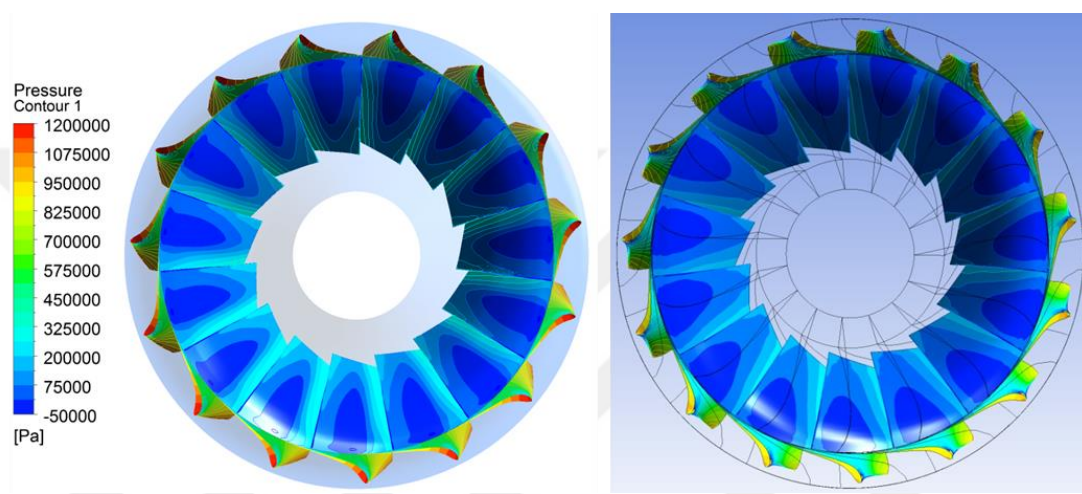


Figure 5.31 : Pressure contours of the original runner (left) and traditional optimization version (right) at their best efficiency points (view from downstream).

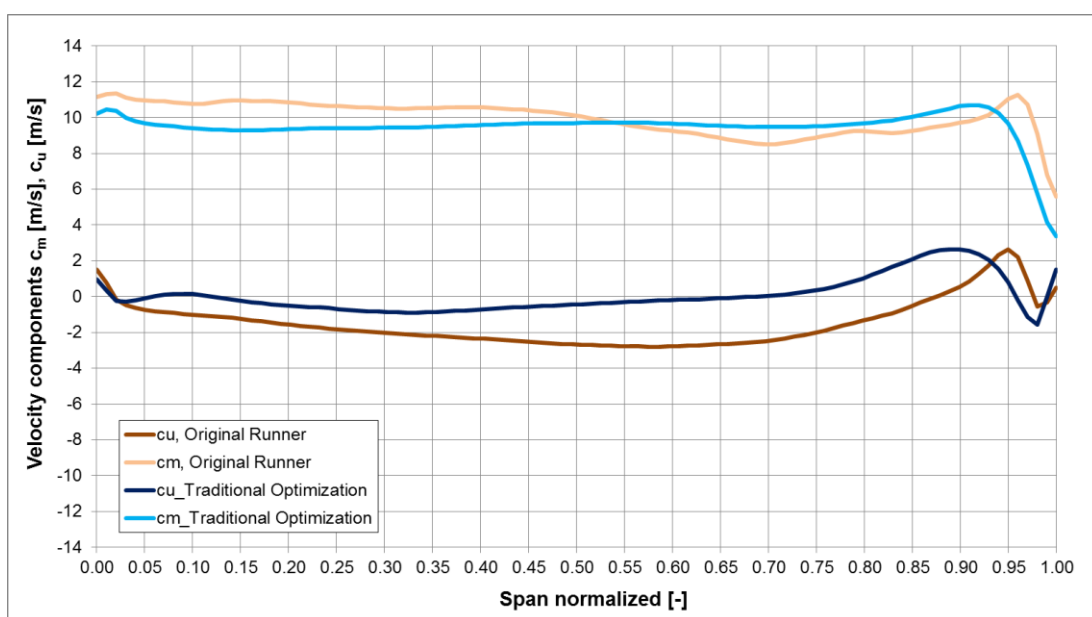


Figure 5.32 : Velocity distributions at the outlet of the runner for the original blade and traditional optimization version at their best efficiency points.

5.5.2 Results of X-Blade design

CFD analyses in different net heads and flow rates are conducted for the turbine whose runner is optimized with X-Blade technology in order to observe whether best efficiency point of the new turbine lies in the desired net head range and is around the desired discharge. The results of this study are presented in Appendix G. Once more, CFD is not able to cover disk friction and leakage losses; hence, 1.2 percentage is subtracted from the hydraulic efficiency based on CFD in order to obtain the resulting turbine efficiency (detail explanation is in 4.5.8. Numerical hill chart sub-chapter). In fact, it is possible to get lower disk frictions and leakage losses with potential of today's manufacturing technology. Nevertheless, these losses are considered as 1.2 % like in original turbine evaluation in order to make the relative comparison between original turbine and optimization versions.

Figure 5.33 shows the numerical hill chart of the Kadincik I HPP turbine whose runner is optimized with X-Blade technology. Compared to the original turbine, the best efficiency point is shifted from $Q = 17 \text{ m}^3/\text{s}$ and $H_{\text{net}} = 155 \text{ m}$ to around $Q = 20 \text{ m}^3/\text{s}$ and $H_{\text{net}} = 183 \text{ m}$, which fits better to the operation range of the power plant than the original turbine configuration. With the introduction of X-Blade design, not only the peak efficiency is increased from 94 % to 94.8 % but also high efficiency values are attained in wider range of operation. In fact, turbine can achieve high efficiencies for almost all operation points, which is the main difference between X-Blade and conventional optimization versions.

Head loss analysis is conducted for the optimized turbine with X-Blade technology at design net head (183 meter) in order to investigate the performances of the mechanical components of the turbine separately. First conclusion from Figure 5.34 is the runner and the draft tube show better performances at the design net head of the X-Blade optimization version than the ones at the net heads where maximum efficiencies were achieved for both original and conventionally optimized turbines. Moreover, X-Blade runner and draft tube attain their minimum head losses around $20 \text{ m}^3/\text{s}$, where turbine has its peak efficiency. On the other hand, spiral case and guide vane apparatus still show unfavorable behavior as they do for the original turbine and the traditional optimization version.

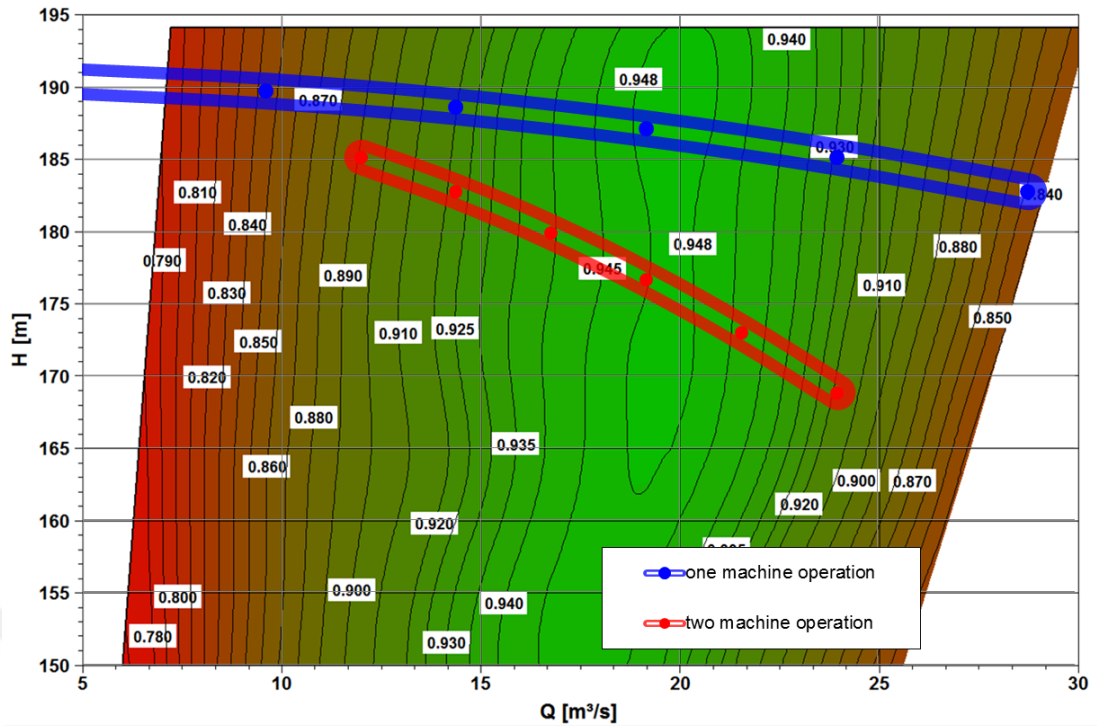


Figure 5.33 : Numerical hill chart for X-Blade optimization of Kadincik I HPP.

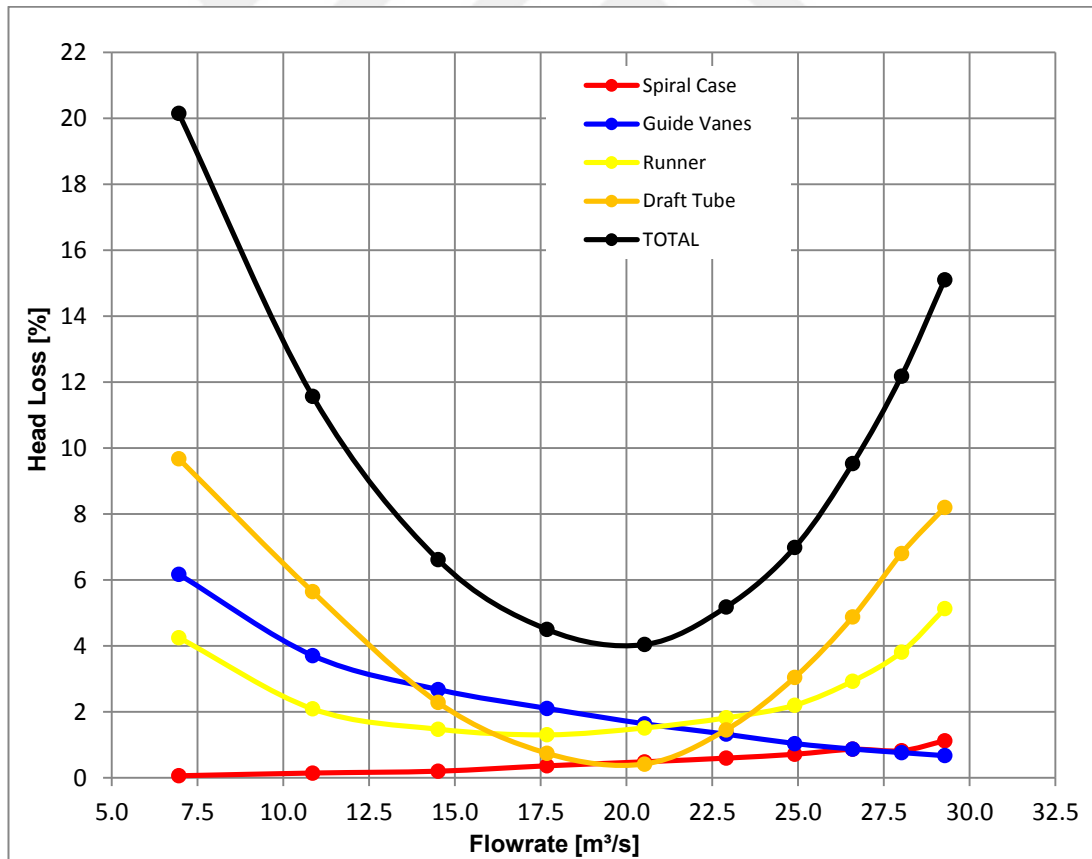


Figure 5.34 : CFD percentage head losses for mechanical components of X-Blade optimization.

The previously discussed increase in the blade angle at the outlet and the extension of the length of the blade profiles let to a lower pressure level around the runner outlet compared to the original runner design. Consequently, cavitation inception is shifted from $Q = 25.0 \text{ m}^3/\text{s}$ to $Q = 28.0 \text{ m}^3/\text{s}$ (Figure 5.35). This provides a cavitation free operation for Kadincik I HPP at all operation points. Although it seems traditionally optimized runner shows better performance with respect to the cavitation by introducing cavitation free operation up to $29.0 \text{ m}^3/\text{s}$, X-Blade design also satisfies the optimization target related with cavitation because the one unit of Kadincik I HPP does not operate above $26 \text{ m}^3/\text{s}$. Therefore, it can be concluded that while both optimization versions provide cavitation free operation for whole range of operation, traditional optimization version brings over-safe condition with respect to the cavitation.

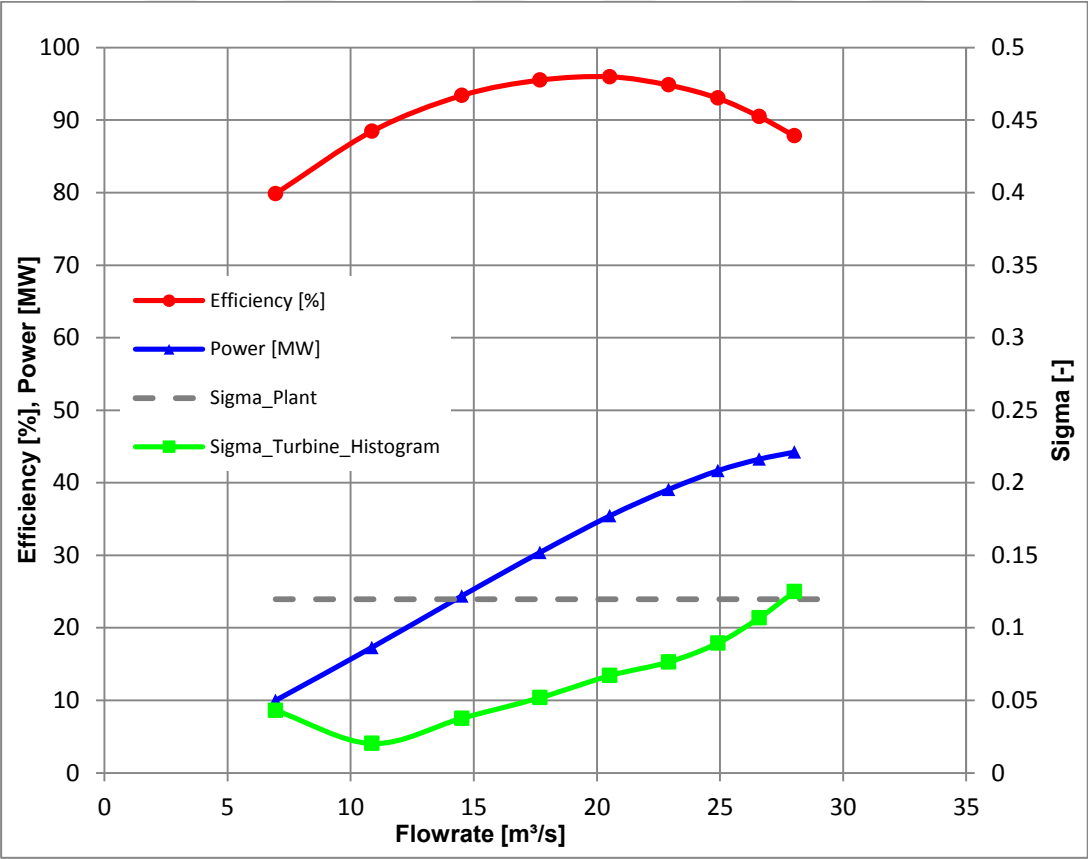


Figure 5.35 : The overall CFD performance of X-Blade optimization at design head. X-Blade design is well-known with its uniform flow distribution which results in homogenous pressure dispersion along the blade. On the other hand, conventional designs suffer from low pressure zones especially close to shroud. Figure 5.36 is a typical example of this situation which shows the blade loadings of the original blade

and optimization versions evaluated for the span values of 0.95, 0.75, 0.50, 0.25 and 0.05 at best efficiency point of each turbine. It turns out that X-Blade design brings a solution for the low pressure zones around the leading edge, which cannot be achieved with the traditional optimization. Furthermore, X-Blade design considerably homogenizes the pressure distribution, especially on the suction side of the blades (Figure 5.37 and Figure 5.38). This is reached by a smoother slope of the “Beta vs. M ”-curves and more importantly with the implementation of X-Blade design.

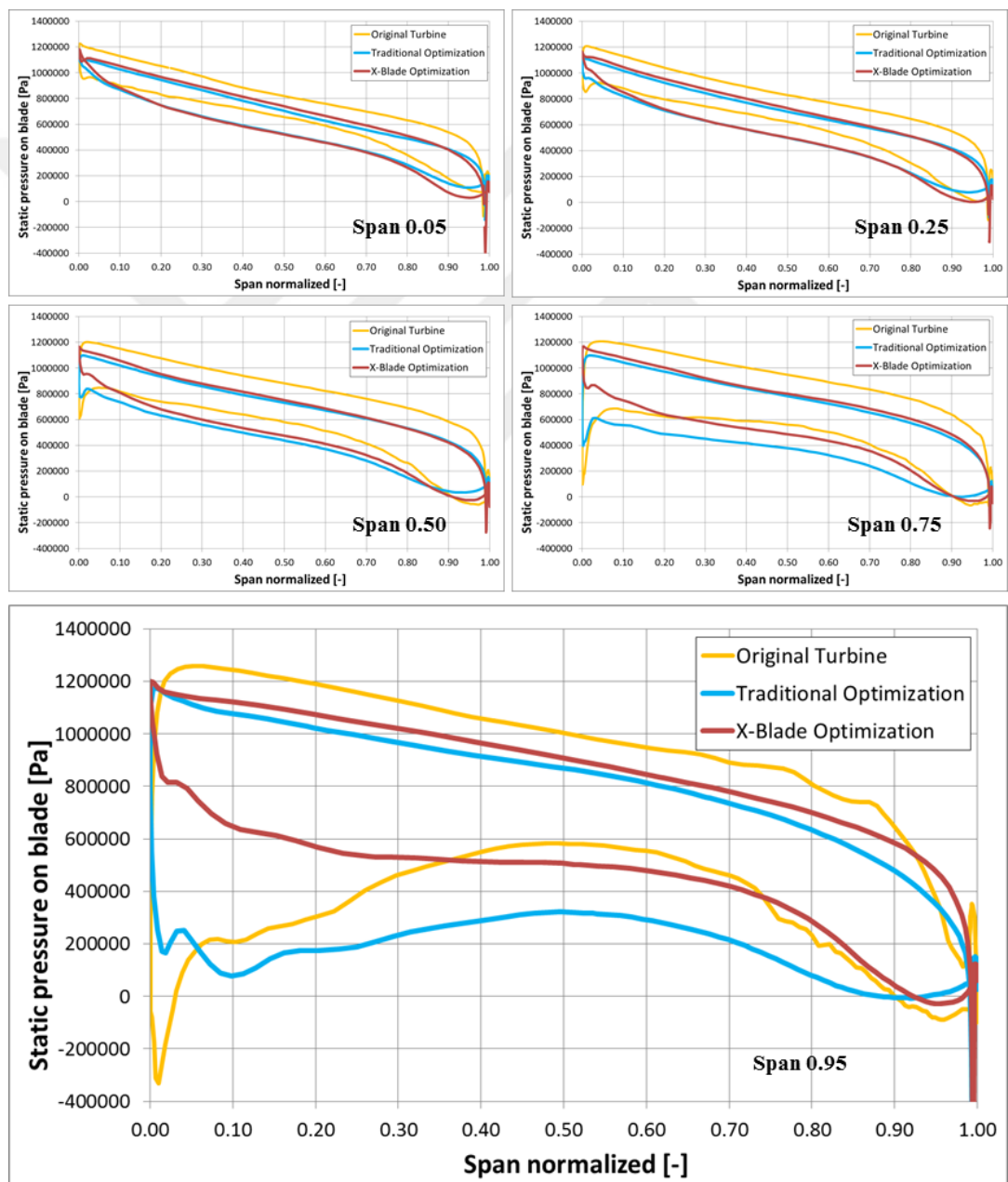


Figure 5.36 : Blade loading comparison of the original runner and optimization versions at their best efficiency points.

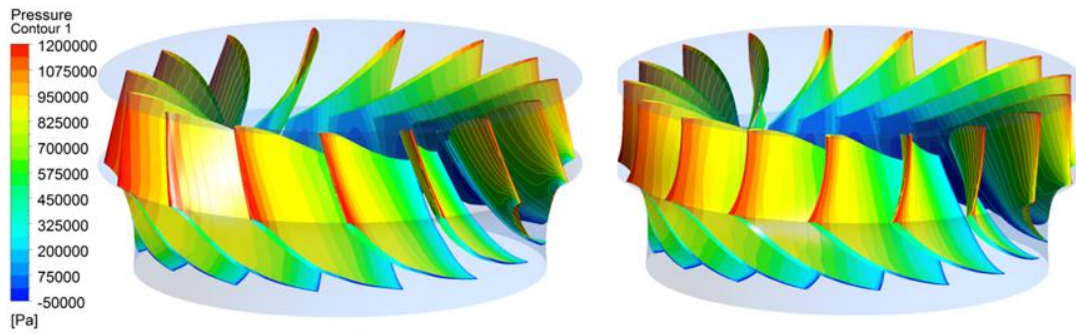


Figure 5.37 : Pressure contours of the original runner (left) and X-Blade optimization version (right) at their best efficiency points (view from upstream).

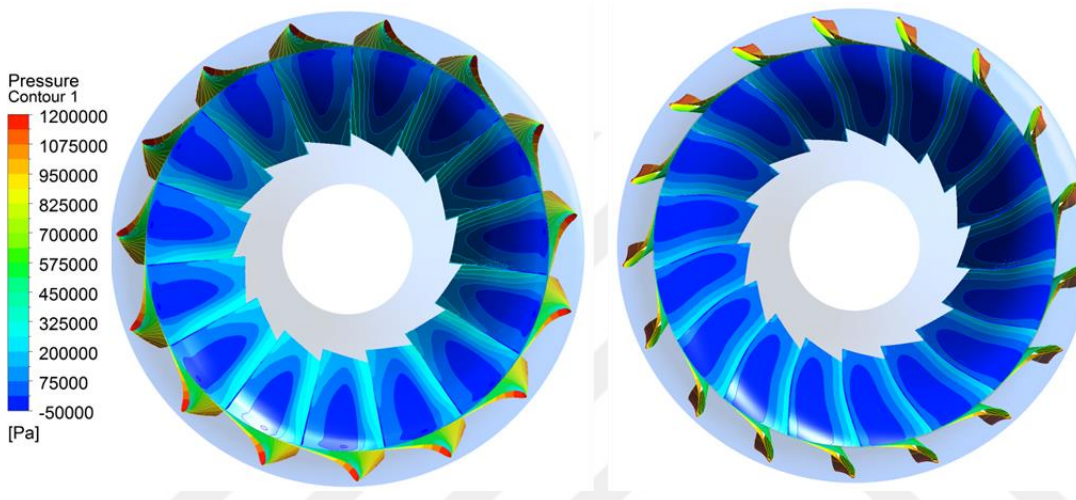


Figure 5.38 : Pressure contours of the original runner (left) and X-Blade optimization version (right) at their best efficiency points (view from downstream).

Figure 5.39 presents a comparison of the spanwise distribution of the c_m - and c_u -velocity components at the runner outlet between original blade and optimization versions, evaluated based on the numerical results at best efficiency point of each turbine. An analysis of the presented data shows that a more homogeneous distribution is reached for the c_m -component in the course of the X-Blade optimization. Nonetheless, inhomogeneous region close to shroud can not be eliminated with any of the optimization versions. On the other hand, although c_u -distribution is improved with X-Blade design, traditional optimization version shows slightly better performance with respect to the c_u . Figure 5.39 suggests that while traditionally optimized runner releases almost no swirl to draft tube, excessive power is tried to be taken from the water in X-Blade design. However, after 80 % span, situation starts to be in favor of X-Blade which deviates from the $c_u = 0$ line less than the conventional optimization.

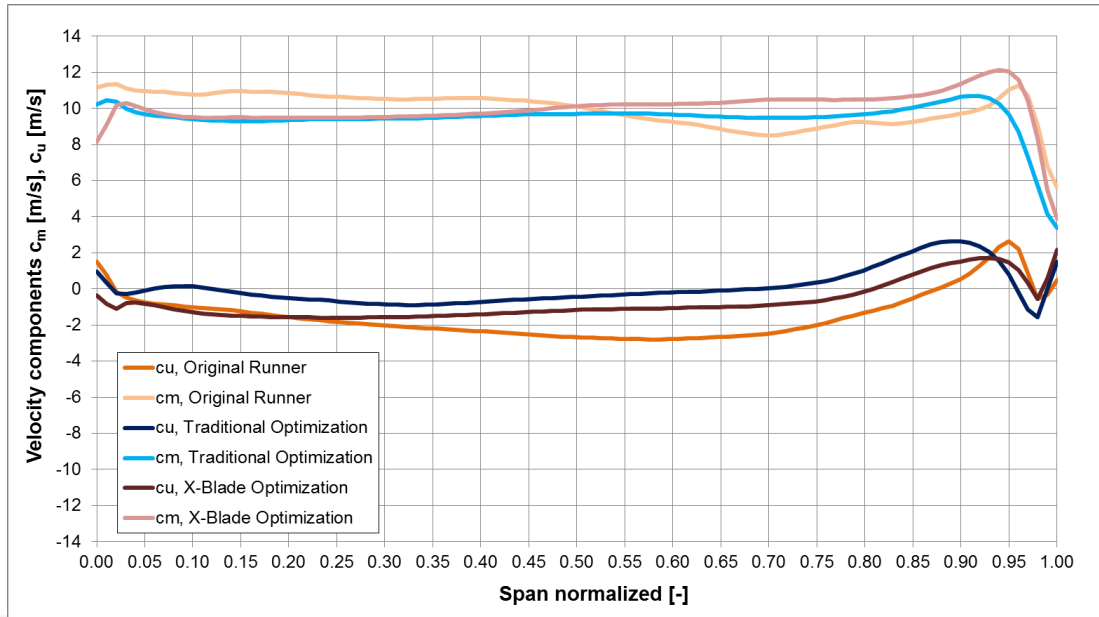


Figure 5.39 : Velocity distributions at the outlet of the runner for the original blade and optimization versions at their best efficiency points.



6. CONCLUSIONS AND RECOMMENDATIONS

This study represents the optimization methodology for a Francis turbine runner according to the operation conditions of the power plant by using CFD after the explanation of the design procedure for each mechanical component of a Francis turbine. In order to exemplify the expressed optimization steps, Kadincik I HPP is chosen as a case study and the runner of this hydropower plant is optimized by means of traditional methods and X-Blade technology.

Before the optimization, the weaknesses of the hydraulic shape of the Kadincik I turbine are revealed with the detail investigation of the main dimensions of the mechanical components and the runner blade angles. Comparison of these hydraulic parameters with the recommendations in the literature shows that horizontal part of the Kadincik I draft tube is extremely long; and therefore, it causes excessive friction losses. Moreover, whereas the inlet blade angles of existing runner around the shroud are higher than the suggestions in the literature, outlet blade angles around the hub are slightly lower with respect to the same references. Except from these points, no considerable perturbation is observed in the hydraulic designs of the mechanical components of Kadincik I HPP.

Comprehensive CFD analyses are conducted in the design net head (194 meter) for different discharge values, which is provided with the different guide vane openings, in order to investigate flow situation inside the unit and further verify the hydraulic design of Kadincik I HPP. First finding of this study is that although turbine attains its peak efficiency at 21 m³/s, minimum head loss point of each mechanical component occurs at different flow rates and none of them coincides with 21 m³/s. This suggests all mechanical components of the turbine are designed for different operation conditions, which violates the proper design procedure.

Although it is proved that spiral case of Kadincik I HPP does not achieve its maximum performance at 194 meter net head and 21 m³/s discharge, it shows a constant swirl design approach at this operation condition. Except from the cutwater region, mass flow is uniformly distributed along the circumferential direction with

the help of the stay vanes at the outlet of the spiral case. In the first stay vanes from the spiral case inlet, stagnation point of the flow is on the suction side of the vanes and consequently this causes wake regions behind the stay vanes; however, after the half of the stay vanes in the circumferential direction, the fluid flow starts to hit to the leading edges of the vanes. Therefore, it can be concluded the volute shows an adequate performance despite the fact that it is not design for this operation condition.

By considering the continuous increase in the guide vane efficiency with every increment in the flow rate, it is not surprising to see stagnation point of the fluid flow on the suction side of the wicket gates at 194 meter net head and 21 m³/s discharge. In fact, this situation is an indicator for the fact that best efficiency point of the guide vanes lies beyond the maximum discharge of the turbine. However, the main problem of the guide vane apparatus is it disturbs the homogenous flow reaching to the guide vane inlet although it reduces the cutwater effect. Amount of water passes between each guide vane varies considerably in the circumferential direction. Besides, peak and minimum mass flow rates happen at the opposite side of the machine, which can cause radial forces on the turbine shaft and therefore considerable vibration can be observed at this operation condition.

Although head loss analysis indicates that runner shows its best performance at higher flow rates for 194 meter net head, its velocity distributions at the inlet and the outlet of the domain are quite proper for the turbine design point. Nevertheless, negative circumferential velocity at the outlet suggests excessive amount of energy is taken from the water, which has a negative influence on the cavitation performance. Moreover, more constant meridional velocity distribution at the outlet is desired in the literature. Another weakness of the runner design shows itself in the static pressure distribution on the runner blade. Kadincik I HPP has a traditional Francis turbine runner design. This kind of runner designs mostly suffers from the low pressure regions at the leading edge around the shroud. Kadincik I HPP is a typical example of this situation and the literature recommends utilizing X-Blade technology to solve this problem.

Delivered negative circumferential velocity from the runner to draft tube causes swirl inside the draft tube cone at design point of the existing turbine. The oscillation of this swirl becomes critical at the end of the draft tube cone and gets contact with the

draft tube wall. This contact results in vibration at the power plant. Furthermore, CFD analyses at the design net head reveal the reason behind the extremely long horizontal part of the draft tube. According to the recommendations in the literature, absolute velocity at the outlet of the draft tube should not exceed $2 \text{ m}^3/\text{s}$ at the design operation point of the turbine. This statement could be satisfied with an extremely long draft tube at Kadincik I HPP.

Original turbine configuration of Kadincik I HPP shows a substantial performance with respect to the cavitation. It provides a cavitation free operation up to $25 \text{ m}^3/\text{s}$. When it is considered that maximum flow rate of the Kadincik I is $26 \text{ m}^3/\text{s}$, which is very rarely seen, almost no cavitation problem is faced in Kadincik I HPP.

In order to understand the whole performance of the existing unit, CFD analyses are conducted in different flow rates and different net heads, which covers the operation conditions of the hydro power plant. Consequently, hill chart of the turbine is obtained and compared with the operation conditions. Dramatic result of this study is although design net head of the turbine is designated as 194 meter by the turbine manufacturer, existing turbine achieves its peak efficiency at 155 meter net head and $17 \text{ m}^3/\text{s}$ discharge, as 94 %. By admitting the turbine has a satisfactory maximum efficiency, high efficiency values are so away from the design and operation points and therefore, turbine can only be operated at a maximum efficiency between 93.0 % and 93.5 %.

After detail investigation on the geometrical parameters, performance and the flow situation inside the unit, optimization targets are specified. First of all, peak efficiency of the turbine should be increased and the high efficiency values should be shifted to the operation conditions, i.e. design point of the turbine is aimed to change. Although original turbine shows a good cavitation performance, totally cavitation free operation should be guaranteed with the establishment of the optimization. Pressure distribution on the original runner blade is not favorable and open to improvement. Furthermore, negative circumferential velocity component at the outlet of the runner should be eliminated in order to enhance the cavitation performance and the flow situation at the draft tube.

In a hydraulic power plant with a Francis turbine, most of the time, spiral case and draft tube are embedded to the concrete, like Kadincik I HPP. Therefore,

modifications on their geometry or their replacements cost extremely expensive, which is the reason for their being out of the consideration in the refurbishment projects. Guide vane is another mechanical component whose replacement is not widely preferred in the rehabilitation projects because any changes in its design automatically change the moment acting on the guide vane shaft, which affects all the levers and the governing system. In brief, a small alteration in the guide vane geometry can cause a redesign of the whole governing system. However, it is proved in this thesis that all the optimization targets listed above can be achieved only with the optimization of the runner although other mechanical components are still designed for different operation conditions.

While the optimization process, two different optimization methods are followed, namely traditional design methodology and X-Blade technology, which has a negative leaning at the inlet of the runner. By taking the original runner geometry as base, several optimization versions are generated for both traditional optimization and X-Blade design. Among these alternatives, two optimization versions with best performances (one for each method) are chosen for further investigation.

As it is done for the original turbine, CFD analyses in different net head and discharge levels are conducted for the optimized turbines to verify the increase in peak efficiency and its position with respect to the operation conditions. The promising results are obtained and it is proved that modifications on the Francis turbine runner have a great influence on the value and the position of the best efficiency point of the turbine. While 94.8 % peak efficiency was attained with X-Blade optimization version around $Q = 20 \text{ m}^3/\text{s}$ and $H_{\text{net}} = 183 \text{ m}$, 94.3 % peak efficiency was achieved with traditional optimization version around $Q = 21 \text{ m}^3/\text{s}$ and $H_{\text{net}} = 174 \text{ m}$. Furthermore, X-Blade optimization version provides wider operation range with high efficiency values, which is also proposed in the literature after 1998.

Head loss analysis for the optimized turbines shows that spiral case and guide vane apparatus reach their best performances at different flow rates than the turbine itself. However, the advantage of these new designs is that maximum efficiencies of the runner and draft tube coincide with the best efficiency point of the turbine, which is obtained only with the changes in the hydraulic shape of the original runner.

While traditional optimization version provides cavitation free operation up to 29.0 m³/s with its more vertical leading edge and longer blade profiles, X-Blade guarantees no cavitation up to 28.0 m³/s with its increased blade angles at the outlet and the extension of the length of the blade profiles. In brief, both optimization versions seem adequate to solve the cavitation problem completely when maximum discharge value of the Kadincik I HPP is considered as 26 m³/s.

X-Blade optimization version makes its advantage strongly felt in the blade loading. Original runner suffers from the low pressure zones at the leading edge around the shroud. Although traditional optimization version improves the static pressure distribution on the blade, it can not bring an effective solution to this problem. On the other hand, homogenous pressure distribution on the runner blade is achieved with the establishment of the X-Blade technology.

Despite the inhomogeneity of meridional velocity at the outlet of the runner close to the shroud, X-Blade optimization version offers a more stable meridional velocity distribution than the original and traditionally optimized runners. However, traditional optimization version shows slightly better performance with respect to the circumferential velocity distribution at the runner outlet. Although the excessive amount of power taken from the water by original runner geometry are considerably reduced by both optimization versions, conventionally optimized runner provides a better circumferential velocity distribution, which less deviates from the $c_u=0$ line.

With all the findings of this study, it can be concluded that desired operation conditions can be achieved in a hydraulic power plant only with the replacement of the runner. The crucial issue in this kind of refurbishments is the turbine should be optimized according to the flow situation inside the unit and in this progress recommendations in the literature can be taken as a starting point. CFD is the most effective tool in the evaluation of the turbine performance and the relative improvements between the proposed designs because it considerably reduces the budget and the time of the project. This study also shows the advantages of X-Blade technology on the traditional design methods; therefore, it is more reasonable to prefer X-Blade in new designs.



REFERENCES

- [1] **TEİAŞ** (2016). *Yük Tevzi Dairesi Başkanlığı Kurulu Güç İstatistikleri*. Türkiye Elektrik İletim A.Ş.
- [2] **Madsen, M.G.** (2009). A Century of Turbine Research without Innovation? *Small Hydro Action for Promotion of Efficient Solutions R&D Actors Network Meeting*, Gdansk, September.
- [3] **Navthar, R.R., Tejas, J., Saurabh, D., Nitish, D. & Anand, A.** (2012). CFD Analysis of Francis Turbine. *International Journal of Engineering Science and Technology*. Vol. 4, pp. 3194-3199.
- [4] **Khare, R., Prasad, V., & Kumar, S.** (2010). Derivation of Global Parametric Performance of Mixed Flow Hydraulic Turbine Using CFD. *HYDRO Nepal*, July.
- [5] **Lorenz, H.** (1906). *Nue Theorie und Berechnung der Kreiselrader*. Munchen und Berlin, R.Oldenbourg.
- [6] **Bauersfeld** (1912). Die Konstruktion der Francis-Schaufel nach der Lorenzschen Turbinentheorie und ihre Eigenschaften. *Zeitschrift des vereines deutscher Ingenieure*, Vol. 56(51), pp. 2045-2051.
- [7] **Dreyfus, L. A.** (1946). A three dimensional theory of turbine flow and its application to the design of wheelvanes for Francis and propeller turbines. *Generalstabens litografiska anstalts förlag*.
- [8] **Wu, C.-H.** (1952). *A general theory of three-dimensional flow in subsonic and supersonic turbomachines of axial-, radial-, and mixed-flow types*. NACA.
- [9] **Katsanis, T., & W. McNally** (1969). Programs for Computation of Velocities and Streamlines on a Blade-to-Blade Surface of a Turbomachine. *ASME 1969 Gas Turbine Conference and Products Show*. doi:10.1115/69-gt-48.
- [10] **Kirsch** (1970). *A quasi-three dimensional design method for centrifugal pumps impeller*. Lecture Notes of Von Karman institute for fluid dynamic.
- [11] **Katsanis, T. & McNally, W.** (1974). *FORTTRAN program for calculating velocities and streamlines on the hub-shroud mid-channel flow surface of an axial-or mixed-flow turbomachine. 2 - Programmer's manual*, Lewis research center.
- [12] **Chauvin, J.** (1977). *Meridional flow in axial turbomachines*. Lecture Notes of Von Karman institute for fluid dynamics.

- [13] **Hirsch, C. & G. Warzee** (1978). An Integrated Quasi-3D Finite Element Calculation Program for Turbomachinery Flows. *J. Eng. Power Journal of Engineering for Power*, 101(1), 141. doi:10.1115/1.3446435.
- [14] **Keck, H. & W. Haas** (1982). *Finite element analysis of quasi-three dimensional flow in turbomachines*. John Wiley & sons ltd.
- [15] **Gjerde, K. M.** (1988). *Program-systemet turboest*, NTH.
- [16] **Billdal, J.T., Jacobsen, Ø., Bratsberg, K., Andersson, H.I., & Brekke, H.** (1993). Numerical Inviscid Flow Analysis of the GAMM Francis Runner. *3D-Computation of Incompressible Internal Flows*, 71-76. doi:10.1007/978-3-322-89452-6_5
- [17] **Andersson, H. I., & Gjerde, K. M.** (1988). *Viskøs og turbulent strømning I hydrauliske maskiner : numerisk del 1987*. Trondheim
- [18] **Jacobsen, Ø., & Brekke, H.** (1990). 3-D turbulent flow simulation in hydraulic machinery. *SINTEF Fluid Machinery*, Trondheim.
- [19] **Shukla, M.K., Jain, R., Prasad V., & Shukla, S.N.** (2011). CFD Analysis of 3-D Flow for Francis Turbine. *International Journal of Mechanical Engineering*. Vol. 1, pp 93 – 100, MIT Publications.
- [20] **Lain, S., Gracia, M., Quintero, B. & Orrego, S.** (2010). CFD Numerical simulations of Francis turbines. *Rev. Fac. Ing. Univ. Antioquia*. No:51.
- [21] **Čarija, Z., Mrša, Z. & Fucak, S.** (2008). *Validation of Francis Water Turbine CFD Simulations*. University of Rijeka Faculty of Engineering.
- [22] **Nilsson, H. & Davidson, L.** (2003). Validations of CFD against detailed velocity and pressure measurements in water turbine runner flow. *International Journal for Numerical Methods in Fluids*. Vol. 41, pp 863-879.
- [23] **Choi, H.J., Zullah, M.A., Roh, H.W., Ha, P.S., Oh, S.Y., & Lee, Y.H.** (2013). CFD Validation of Performance Improvement of a 500 kW Francis Turbine. *Renewable Energy*, 54, pp 111 – 123.
- [24] **Neopane, H.P., Dahlhaug, O.G., & Thapa, B.** (2007). Alternative Design of a Francis Turbine for Sand Laden Water. *International Conference on Small Hydropower - Hydro Sri Lanka*.
- [25] **Odesola, I.F., & Oriabre, J.I.** (2013). Development of a 5kw Francis Turbine Runner Using Computation Fluid Dynamics. *IAAAR 2013*.
- [26] **Patel, K., Desai, J., Chauhan, V., & Charnia, S.** (2011). Development of Francis Turbine using Computational Fluid Dynamics. *The 11th Asian International Conference on Fluid Machinery and The 3rd Fluid Power Technology Exhibition*.
- [27] **Okyay, G.** (2010). *Utilization of CFD Tools in the Design Process of a Francis Turbine (Master Thesis)*. Middle East Technical University.
- [28] **Hellström, J.G.I., Marjavaara, B.D., & Lundström, T.S.** (2007). Parallel CFD simulations of an original and redesigned hydraulic turbine draft tube. *Advances in Engineering Softwares*. Vol. 38, pp. 338 – 344.

- [29] **Henggeler, U., Krenn, J., Gentner, C., Angerer, C., Züger, A. & Züger, A.** (2012). Rehab of Low Specific Speed Francis Turbine. *17th International Seminar on Hydropower Plants – Pumped Storage in the Context of Renewable Energy Supply*.
- [30] **Viscanti, N., Pesatori, E. & Turozzi, G.** (2009). Improvement of a Francis Runner Design. *3rd IAHR International Meeting of the Workgroup on Cavitation and Dynamic Problems in Hydraulic Machinery and Systems*. Brno, Czech Republic.
- [31] **Derakhshan, S. & Mostafavi, A.** (2011). Optimization of GAMM Francis Turbine Runner. *World Academy of Science, Engineering and Technology*, Vol. 59, pp. 717-723.
- [32] **Ayancik, F., Aradag, U., Ozkaya, E., Celebioglu, K., Unver, O. & Aradag, S.** (2013). Hydroturbine Runner Design and Manufacturing. *International Journal of Materials, Mechanics and Manufacturing IJMMM*. pp.162-165. doi:10.7763/ijmmm.2013.v1.35.
- [33] **Wu, J., Shimmei, K., Tani, K., Niikura, K. & Sato, J.** (2007). CFD-Based Design Optimization for Hydro Turbines. *Journal of Fluids Engineering*. Vol. 129, pp. 159 – 168.
- [34] **Sallaberger, M., Michaud, C., Born, H., Winkler, S. & Peron, M.** (n.d.). *Design and Manufacturing of Francis Runners for Rehabilitation Projects*. VA TECH HYDRO.
- [35] **Huang, J., Ji, J., Tung, T. & Riley, M.** (2006). Francis Turbine Upgrade for the Lushui Generating Station by Using Computational Fluid Dynamics - A Case Study. *Great Wall World Renewable Energy Forum*.
- [36] **Thum, S. & Schilling, R.** (2002). Optimization of Hydraulic Machinery Bladings by Multilevel CFD Techniques. *International Journal of Rotating Machinery*. Vol. 2, pp. 161 – 167.
- [37] **Enomoto, Y., Kurosawa, S. & Kawajiri, H.** (2012). Design optimization of a high specific speed Francis turbine runner. *26th IAHR Symposium on Hydraulic Machinery and Systems*.
- [38] **Liu, S., Wu, Y., Wu, X., & Nishi, M.** (2011). Optimization of a Francis Turbine Through Flow Simulation with a RNG k- ω Turbulence Model. *International Journal Turbo Jet-Engines*. Vol. 28, pp. 53 – 58.
- [39] **Wang, Y.L., Li, G.Y., Shi, Q.H. & Wang, Z.N.** (2012). Hydraulic design development of Xiluodu Francis turbine. *26th IAHR Symposium on Hydraulic Machinery and Systems*.
- [40] **Kewnai, S. & Wongwises, S.** (2011). Improvement of the Runner Design of Francis Turbine using Computational Fluid Dynamics. *American Journal of Engineering and Applied Sciences*. Vol. 4, pp. 540 – 547.
- [41] **Sotnikov, A.A.** (n.d.). *Refurbishment projects of Francis turbines with runner replacement*. Hydraulic Turbine Laboratory, LMZ, Petersburg.
- [42] **Gray, D.** (2000). *Hydro Life Extension Modernization Guides – Volume 2: Hydromechanical Equipment*. Electric Power Research Institute.

- [43] **Cherny, S., Chirkov, D., Lapin, V., Lobareva, I., Sharov, S. & Skorospelov, V.** (n.d.). 3D Euler flow simulation in hydro turbines: Unsteady analysis and automatic design. *Notes on Numerical Fluid Mechanics and Multidisciplinary Design (NNFM) Advances in High Performance Computing and Computational Sciences*. pp. 33-51. doi:10.1007/978-3-540-33844-4_4.
- [44] **Billdal, J.T.** (2006). The X-Factor. *International Water Power and Dam Construction*. August. pp. 36-37.
- [45] **Casey, M.V., & Keck, H.** (1996). *Hydraulic turbines: Handbook of Fluid Dynamics and Fluid Machinery*. John Wiley.
- [46] **Krueger, R., & Bates, C.** (1976). *Selecting hydraulic reaction turbines* (Revised 1976. ed.). Washington, D.C.: United States Department of the Interior Bureau of Reclamation.
- [47] **Gubin, M.** (1973). *Draft tubes of hydro-electric stations*. New Delhi: Amerund Pub.
- [48] **Brekke, H.** (2001). *Hydraulic Turbines Design, Erection and Operation*. NTNU, Trondheim, Norway.
- [49] **Thomann R.** (1931). *Die Wasseturbinen und Turbinenpumpen*. Technische Universität Stuttgart, Stuttgart, Germany.
- [50] **Chapallaz, J., & Renaud, A.** (1995). *Wasserturbinen*. Bern: Bundesamt für Konjunkturfragen.
- [51] **Giesecke, J.** (2005). *Wasserkraftanlagen: Planung, Bau und Betrieb*. New York: Springer-Verlag Berlin Heidelberg.
- [52] **Raabe, J.** (1985). *Hydro Power: The Design, Use and Function of Hydromechanical, Hydraulic and Electrical Equipment*. Düsseldorf: VDI – Verlag GmbH.
- [53] **Leeb, K.** (2012). *Strömungsmaschinen - Francis-Turbine: Auslegung und Darstellung der Geschwindigkeitsdreiecke*. Lecture, Wien.
- [54] **Pfleiderer, C., & Petermann, H.** (1978). *Akım makinaları (Değ 4. bas. ed.)*. İstanbul: Matbaa Teknisyenleri Basımevi.
- [55] **Bovet, T. M.** (1961). *Contribution A L'etude Du Trace D'aubage D'une Turbine A Reaction Du Type Francis*. Information Techniques Charmilles. pp. 47-70.
- [56] **Miloş, T., & Bărglăzan, M.** (2004). CAD Technique Used to Optimize the Francis Runner Design. *The 6th International Conference on Hydraulic Machinery and Hydrodynamics*, Timisoara, Romania, October 21 - 22, 2004.
- [57] **Morales, M.** (2000). Diseño de Turbinas Francis en C Builder. *Ingenieria*. Vol. 10. pp. 125-136.
- [58] **Nourbakhsh, A., Razavi, O.S., Khodabakhsh, H., & Mehrabadi, A.** (2007). New Approach for Hydraulic Design of Francis Runner Based on Empirical Correlations. *International Conference on Small Hydropower - Hydro Sri Lanka*, 22-24 October 2007.

- [59] **De Siervo, F., & De Leva, F.** (1976). Modern Trends in Selecting and Designing Francis Turbines. *Water Power & Dam Construction*. August. pp. 28 – 35.
- [60] **Schweiger, F., & Gregori, J.** (1985). Developments in Francis Turbines. *Water Power & Dam Construction*. August. pp. 17 – 21.
- [61] **Lugaresi, A., & Massa, A.** (1987). Designing Francis Turbines: Trends in the Last Decade. *Water Power & Dam Construction*. August. pp. 23 – 28.
- [62] **Drtna, P., & Sallaberger, M.** (1999). Hydraulic turbines—basic principles and state-of-the art computational fluid dynamics applications. *Proc Instn Mech Engrs*. Vol. 213 Part C.
- [63] **Bodner, C.** (2013). *Entwicklung eines multidisziplinären Auslegungstools für Francis-Turbinen (Diplomarbeit)*. Institute of Hydraulische Strömungsmaschinen, Technische Universität Graz.
- [64] **Gjøsæter, K.** (2011). *Hydraulic Design of Francis Turbine Exposed to Sediment Erosion (Master Thesis)*. Norwegian University of Science and Technology, Department of Energy and Process Engineering.
- [65] **Brekke, H.** (2003). *Pumper og Turbiner*. Waterpower Laboratory NTNU.
- [66] **Brekke, H.** (2001). *State of the art in turbine design*. NTNU, Trondheim, Norway.
- [67] **Gogstad, P.J.** (2012). *Hydraulic Design of Francis Turbine Exposed to Sediment Erosion (Master Thesis)*. Norwegian University of Science and Technology, Department of Energy and Process Engineering.
- [68] **Brekke, H. & Huang, Y.** (2012). X-shape blade application for the Three Gorges project. *International Water Power And Dam Construction*. Vol. 64. pp. 17-19.
- [69] **Wang, F., Li, X., Ma, J., Yang, M., & Zhu, Y.** (2009). Experimental Investigation of Characteristic Frequency in Unsteady Hydraulic Behavior of a Large Hydraulic Turbine. *Journal of Hydrodynamics*, Ser. B, pp. 12-19.
- [70] **Demers, A.** (2009). Francis Turbine “X-Blade” Technology. *Hydro News, Magazine of Andritz Hydro*. Vol. 15 / 5-2009.
- [71] **Ayder, E.** (2015). Istanbul Technical University, Faculty of Mechanical Engineering, Personal Conversation.
- [72] **Hothersall, R.J.** (1988). Assessing the design of draft tubes. *Water power & dam construction*, April 1988, pp 55-57.
- [73] **Gulich, J.** (2010). *Centrifugal pumps*. (2nd ed.). Berlin: Springer-Verlag.
- [74] **Skorpik J.** (2014). Shapes of parts and materials of turbomachines. *Transformační technologie*, ISSN 1804-8293.
- [75] **Desai J., Roghelia A., Soni V., & Chauhan V.** (2010). Validation of Hydraulic Design of Spiral Casing and Stay Vanes of Francis Turbine Using CFD. *37th International & 4th National Conference on Fluid Mechanics and Fluid Power*.

- [76] **Kurokawa J., Nagahara H.** (1986). Flow Characteristics in Spiral Casing of Water Turbines. *IAHR Symposium Hydraulic Machinery and Systems*.
- [77] **Guo P., Luo X., Zheng X., & Liu S.** (2008). CFD – Based Match Design and Improving Performance for Francis Turbine Components. *2008 ASME Fluids Engineering Conference*, Jacksonville, Florida, USA.
- [78] **Meland, H.** (2010). *A new Design of a Francis Turbine in order to reduce Sediment Erosion (Master Thesis)*. Norwegian University of Science and Technology, Department of Energy and Process Engineering.
- [79] **Escaler, X., Egusquiza, E., Farhat, M., Avellan, F., & Coussirat, M.** (2006). Detection of cavitation in hydraulic turbines. *Mechanical Systems and Signal Processing*. Vol. 20. pp. 983-1007.
- [80] **IEC60041** (1991). - Field acceptance tests to determine the hydraulic performance of hydraulic turbines, storage pumps and pump-turbines. IEC Publications.
- [81] **Avellan, F.** (2004). Introduction to Cavitation in Hydraulic Machinery. *The 6th International Conference on Hydraulic Machinery and Hydrodynamics*. pp. 11 – 22.
- [82] **Brennen, C.E.** (1995). *Cavitation and Bubble Dynamics*. Oxford University Press.
- [83] **Liuzzi, D.** (2012). *Two-Phase Cavitation Modelling (Master Thesis)*. Faculty of Civil and Industrial Engineering, University of Rome – La Sapienza.
- [84] **Zhang, H. & Zhang, L.** (2012). Numerical simulation of cavitating turbulent flow in a high head Francis turbine at part load operation with OpenFOAM. *International Conference on Advances in Computational Modeling and Simulation*.
- [85] **Yao, Z., Xiao, R., Wang, F. & Yang, W.** (2015). Numerical Investigation of Cavitation Improvement for a Francis Turbine. *9th International Symposium on Cavitation, Journal of Physics: Conference Series* 656.
- [86] **Gohil, P.P., & Saini, R.P.** (2016). Numerical Study of Cavitation in Francis Turbine of a Small Hydro Power Plant. *Journal of Applied Fluid Mechanics*. Vol. 9. No. 1. pp. 357-365.
- [87] **Saeed, R.A.** (2015). Numerical Simulation of Three-Dimensional Cavitating Turbulent Flow in Francis Turbines with ANSYS. *International Journal of Mechanical, Aerospace, Industrial, Mechatronic and Manufacturing Engineering*. Vol. 9. No. 8. World Academy of Science, Engineering and Technology
- [88] **Susan, R., Muntean, S., & Anton, I.** (2002). Numerical Analysis of Cavitation Inception in Francis Turbine. *21th IAHR Hydraulic Machinery and System Symposium*. Lausanne.
- [89] **Schmidl, R.** (2007). *Contribution to the Cavitation Optimization of Kaplan Blades by Numerical Flow Simulation and Evolutionary Strategies (Doctorate Thesis)*. Institute of Hydraulic Fluid Machinery, Graz University of Technology.

- [90] **Gehrer, A., Egger, A., Benigni, H., Penninger, G., & Jaberg, H.** (2004). Dimensioning and Simulation of Process Pumps. *Karlsruhe Pump Users Technical Forum*.
- [91] **IEC60193** (1999). Hydraulic turbines, storage pumps and pump-turbines - Model acceptance tests. IEC Publications.
- [92] **Benigni, H., & Jaberg, H.** (2007). Stationary and Transient Numerical Simulation of a Bulb. *Proceedings of the 5th IASME / WSEAS International Conference on Fluid Mechanics and Aerodynamics*, Athens, Greece.
- [93] **Jost, D., Skerlavaj, A., Morgut, M., Meznar, P. & Nobile, E.** (2015). Numerical simulation of flow in a high head Francis turbine with prediction of efficiency, rotor stator interaction and vortex structures in the draft tube. *Journal of Physics: Conference Series* 579. doi:10.1088/1742-6596/579/1/012006.
- [94] **Ciocan, T., Susan, R., & Muntean, S.** (2014). Improving draft tube hydrodynamics over a wide operating range. *Proceedings of the Romanian Academy*. Vol. 15. pp. 182 – 190.
- [95] **Mauri, S.** (2002). *Numerical Simulation and Flow Analysis of an Elbow Diffuser (Master Thesis)*. Ecole Polytechnique Federale De Lausanne.
- [96] **Paik, J., Sotiropoulos, F., Asce, M., & Sale, M. J.** (2005). Numerical Simulation of Swirling Flow in Complex Hydroturbine Draft Tube Using Unsteady Statistical Turbulence Models. *Journal of Hydraulic Engineering J. Hydraul. Eng.* Vol.131(6). pp. 441-456. doi:10.1061/(asce) 0733-9429(2005)131:6(441).
- [97] **Eggenspieler, G.** (2012). *Turbulence Modeling*. ANSYS CFX Program Documentation and Help.
- [98] **Lopez, L.F.** (2006). *Surface Parametrization and Optimum Design Methodology for Hydraulic Turbines (Master Thesis)*. École polytechnique fédérale de Lausanne, Department of Mechanical Engineering.
- [99] **Souza, L.C.E.O., Moura, M.D., Junior, A.C.P.B., & Nilsson, H.** (n.d.). *Assessment of Turbulence Modelling for CFD Simulations into Hydroturbines: Spiral Casing*. Universidade de Brasília - Departamento de Engenharia Mecânica.
- [100] **Holo, A.L.** (2011). *CFD-Analysis of a High Head Francis Turbine (Master Thesis)*. Norwegian University of Science and Technology, Department of Energy and Process Engineering.
- [101] **Menter, F.R.** (1994). Two-Equation Eddy-Viscosity turbulence models for engineering applications. *AIAA Journal*. Vol. 32(8). pp. 1598-1605.
- [102] **Menter, F.R.** (2009). Review of the Shear-Stress transport turbulence model experience from industrial perspective. *International Journal of Computational Fluid Dynamics*. Vol. 23(4). pp. 305-316.
- [103] **Čarija, Z., & Mrša, Z.** (2003). Complete Francis turbine flow simulation for the whole range of discharges. *4th International Congress of Croatian Society of Mechanics*, Bizovac, Croatia.

- [104] **Luo, J.Y., Issa, R.I., & Gosman, A.D.** (1994). Prediction of Impeller-Induced Flows in Mixing Vessels Using Multiple Frames of Reference. *IChemE Symposium Series*. Vol. 136. pp. 549-556.
- [105] **ANSYS Fluent** (2006). *10.3.1. The Multiple Reference Frame Mode*. Fluent Inc.
- [106] **Homicz, G.F.** (2004). *Computational Fluid Dynamic Simulations of Pipe Elbow Flow*. Sandia National Laboratories. U.S. Department of Energy. doi:10.2172/919140.
- [107] **CFL3D User's Manual** (1999). *Chapter 6: Boundary Conditions*. NASA Langley Research Center, Hampton, VA.
- [108] **Basesme, H.** (2003). *Hidroelektrik Santrallar ve Hidroelektrik Santral Tesisleri* (2nd ed., p. 310). Ankara: EÜAŞ Genel Müdürlüğü Hidrolik Santraller Dairesi Başkanlığı.
- [109] **Schilling, R.** (2009). *Hydraulische Strömungsmaschinen und Anlagen*. Address at Fakultät für Maschinenwesen, Technische Universität München, Munich, Germany.
- [110] **Scheit, C., Karic, B. & Becker, S.** (2012). Effect of blade wrap angle on efficiency and noise of small radial fan impellers—A computational and experimental study. *Journal of Sound and Vibration*. Vol. 331. pp. 996-1010.
- [111] **Raabe, J.** (1989). *Hydraulische Maschinen und Anlagen*. VDI Verlag.

APPENDICES

APPENDIX A: Commissioning Tests Results of Kadincik I HPP

APPENDIX B: Mesh Statistics

APPENDIX C: Mesh Independency Studies

APPENDIX D: y^+ Values of the CFD Results with Medium Mesh

APPENDIX E: Numerical Hill Chart Data for Kadincik I HPP with Original Runner

APPENDIX F: Numerical Hill Chart Data for Kadincik I HPP with Traditionally Optimized Runner

APPENDIX G: Numerical Hill Chart Data for Kadincik I HPP with X-Blade Optimization

APPENDIX A

Load-ticket gates opening													
MW GENERATOR	HP TURBINE	WICKET GATES OPENING		UPSTREAM LEVEL m	DOWNSTREAM LEVEL m	Δ m	HEAD LOSSES m	NET HEAD m	PRESSURE				
		%	mm						UPSTREAM m	BALANCING PIPE BARS	CARBON SEAL BARS	DRAFT TUBE	
12	16700	30	72	406,5	206,7	198,8	1	198,8	203	1,6/2	0,8	0,6	
18	25100	40	99	406,3	206,8	199,5	1,5	198,0	200/200	1,6/2,2	1,0	0,5/1,5	
26	36200	50	131	406,3	206,9	199,4	2,6	196,8	198	1,9/2,2	1,1	0,8/0,7	
31	43200	60	152	406,3	207,0	199,3	3,7	195,6	198	2/2,4	1,4	0,5/0,6	
37,5	49300	70	178	406,2	207,0	199,2	4,8	194,5	192/195	2,4/2,9	1,7	0,5/0,8	
38/40	53000	80	201	406,2	207,0	199,2	5,5	193,7	187/197	2,4/2,9	1,8	0,4/1	
37/41	56500	85	too much cavitation							170/210	2/5		
43	60000	90	too much cavitation										

Figure A.1 : Commissioning test results of Kadincik I HPP (single unit operation).

MW TOTAL	MW GENER. 2	MW GENER. 1	WICKET GATE OPENING		LEVELS		Δ	HEAD LOSSES m	NET HEAD	PRESSURES			FLOWMETER %
			%	mm	UPSTREAM m	DOWNSTREAM m				UPSTREAM m	ABOVE RUNNER	DRAFT TUBE	
40	30	10	30	75	405,9	206,1	199,8	6,2	193,6	194	2,8/3	0,6	22
45	30	15	40	97	405,9	206,1	199,8	8	191,8	192	2,6/3,4	0,6/0,8	30
55	30	25	50	127	405,8	206,1	199,7	12	187,7	190	2,8/3,2	0,7/0,8	38
60	30	30	60	149	405,7	206,2	199,6	14,3	185,3	186	3,2/3,4	0,6	45
62	30	32	70	175	405,6	206,3	199,4	16,6	182,8	183	3,6/3,8	0,7	53
65,5	30	35,5	80	199	405,6	206,3	199,3	17,5	181,8	180	3,8	0,6/0,9	58
66	30	36	85	211	405,6	206,3	199,2	18	181,2	176,5	3,8/4	0,5/0,9	61
68,5	30	38,5	90	223	405,4	206,3	199,1	19,5	179,6	170/180	3,2/4	0,5/0,8	65
70	30	40	98	-	405,4	206,3	199,1	21	178,1	175 ±	-	-	

Figure A.2 : Commissioning test results of Kadincik I HPP (two unit operation).

APPENDIX B

Table B.1 : Mesh statistics of guide vanes.

Very Fine Mesh								
Opening [degrees]	# of nodes	# of elements	y+	# of inflation layer	Spanwise Elements	O-grid width factor	Min/Max face angles	Max edge length ratio
15.00	418912	396600	15	10	75	0	13° / 167°	13000
Fine Mesh								
Opening [degrees]	# of nodes	# of elements	y+	# of inflation layer	Spanwise Elements	O-grid width factor	Min/Max face angles	Max edge length ratio
7.50	239976	224835	25	10	65	0.1	7° / 174°	8500
10.00	233640	218790	25	10	65	0.1	9.5° / 171.5°	10500
12.50	233640	218790	25	10	65	0.1	11° / 169.5°	11000
15.00	231264	216450	25	10	65	0.1	15° / 164.5°	11000
17.50	223938	209430	25	10	65	0.1	18° / 163°	10300
20.00	240174	225810	25	10	65	0.1	16° / 163°	7500
22.50	240174	225810	25	10	65	0.1	21.5° / 158°	7500
25.00	220968	207480	25	10	65	0.1	20° / 161°	7000
27.50	335412	316875	25	10	65	0.1	12.5° / 169°	8000
Medium Mesh								
Opening [degrees]	# of nodes	# of elements	y+	# of inflation layer	Spanwise Elements	O-grid width factor	Min/Max face angles	Max edge length ratio
7.50	120902	111840	50	10	60	0.1	9° / 173°	5000
10.00	117852	108960	50	10	60	0.1	13.5° / 167°	5000
12.50	117852	108960	50	10	60	0.1	12.5° / 170°	5500
15.00	116876	108000	50	10	60	0.1	15.5° / 167°	5500
17.50	113826	105120	50	10	60	0.1	15° / 168°	5500
20.00	119194	110640	50	10	60	0.1	17° / 166°	4500
22.50	119194	110640	50	10	60	0.1	23° / 159.5°	4500
25.00	110776	102720	50	10	60	0.1	24.5° / 158.5°	4500
27.50	164578	153600	50	10	60	0.05	24° / 157.5°	4000
Coarse Mesh								
Opening [degrees]	# of nodes	# of elements	y+	# of inflation layer	Spanwise Elements	O-grid width factor	Min/Max face angles	Max edge length ratio
7.50	82156	75060	100	8	45	0.1	9° / 173°	2500
10.00	80040	73080	100	8	45	0.1	13.5° / 167°	2500
12.50	80040	73080	100	8	45	0.1	12.5° / 170°	2500
15.00	79304	72360	100	8	45	0.1	15.5° / 167°	2500
17.50	77004	70200	100	8	45	0.1	15° / 168°	2500
20.00	81604	74880	100	8	45	0.1	17° / 166°	2500
22.50	81604	74880	100	8	45	0.1	23° / 159°	2500
25.00	75440	69120	100	8	45	0.1	24.5° / 159°	2500
27.50	113252	104580	100	8	45	0.05	22° / 159°	2000

Table B.2 : Mesh statistics of runner.

Mesh Density	# of nodes	# of elements	y+	# of inflation layer	Spanwise Elements	O-grid width factor	Min/Max face angles	Max edge length ratio
Very Fine	792610	749250	15	10	90	0.2	12° / 170°	8000
Fine	400824	375300	25	10	75	0.2	11.5° / 169.5°	5500
Medium	269346	249795	50	10	65	0.2	10.5° / 169.5°	4000
Coarse	101898	92000	100	8	50	0.25	18.5° / 164°	2000

Table B.3 : Mesh statistics of draft tube.

Mesh Density	# of nodes	# of elements	First element distance	# of inflation layer	Height ratio
Very Fine	5420000	5350000	0.3	12	1.2
Fine	2542248	2504200	0.3	12	1.2
Medium	1182656	1161135	0.5	10	1.25
Coarse	631176	616605	0.75	10	1.35

Table B.4 : Mesh statistics of spiral case.

Mesh Density	# of nodes	# of elements	First element distance	# of inflation layer	Height ratio
Very Fine	4960000	12950000	0.2 - 0.35	10	1.15 - 1.40
Fine	3676773	10496883	0.2 - 0.35	9	1.15 - 1.40
Medium	1454952	4053164	0.3 - 0.5	8	1.35 - 1.5
Coarse	987650	3049308	0.4 - 0.65	6	1.5 - 1.75

APPENDIX C

As presented in Table B.1, Table B.2, Table B.3 and Table B.4, meshes with four different densities are generated for each domain. By conducting CFD analyses with same boundary conditions (194.1 meter net head, which is the design net head for the turbine), grid qualities are compared. Results are demonstrated in Figure C.1. As it is seen, beyond medium mesh set up it was hard to observe any improvement in the results. For the sake of the computational time, medium grid group is chosen for CFD analyses because the difference between medium and fine / very fine grid is on a minor level. Furthermore, in the optimization step again the same meshes are utilized and in the end relative improvement is discussed.

The CFD results in different guide vane openings for 194.1 meter net head show that turbine achieves its peak efficiency around $21 \text{ m}^3/\text{s}$, which corresponds to 15° guide vane angle. Consequently, hydraulic loss analysis are conducted at this net head and flowrate to see the change in the performance of the components. The results are visualized in Figure C.2, which also suggests that medium grid density is quite proper for the further CFD analysis with respect to accuracy and computational cost.

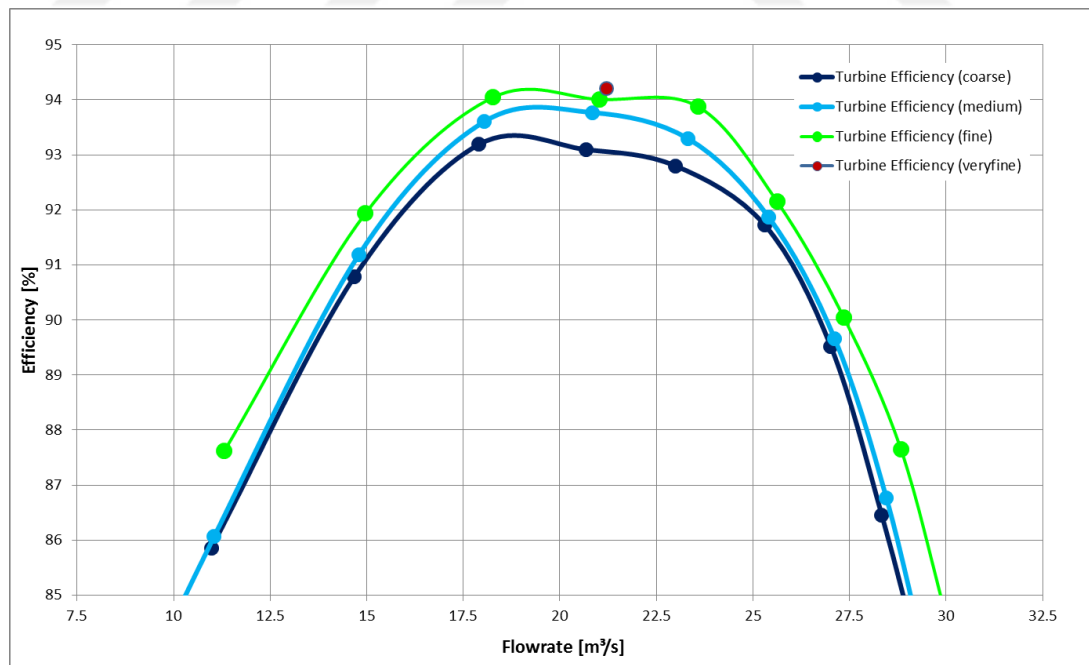


Figure C.1 : Mesh independency study for Kadincik I HPP.

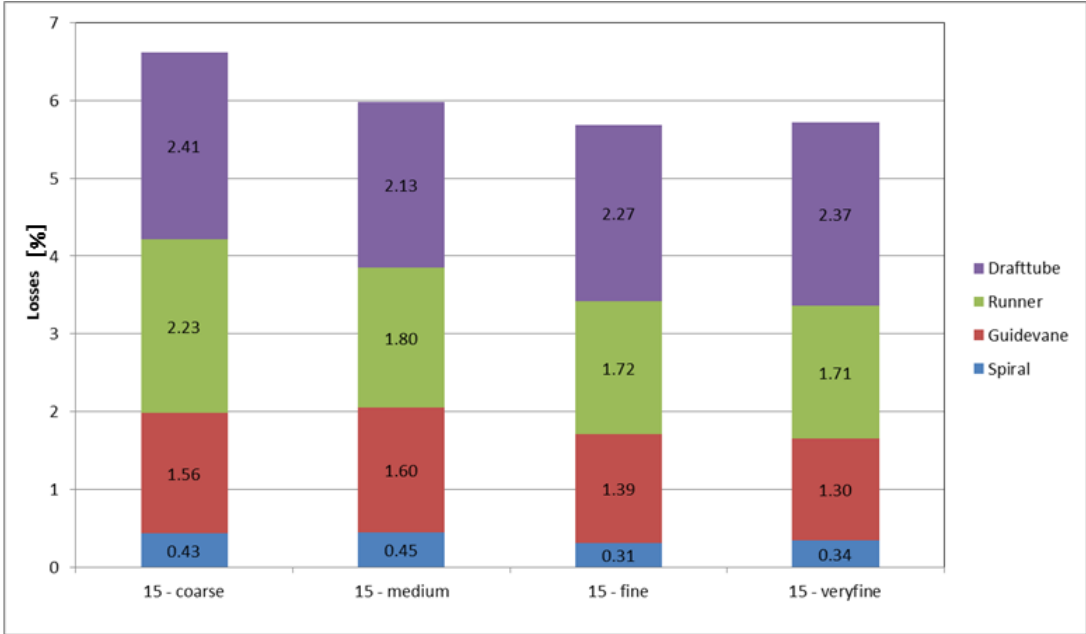


Figure C.2 : Hydraulic losses for different mesh densities.

APPENDIX D

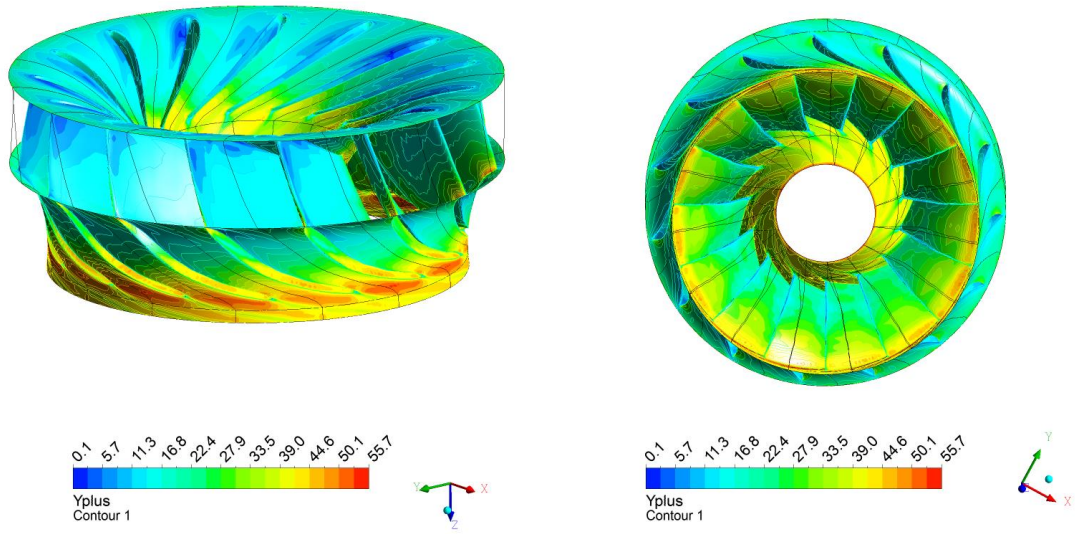


Figure D.1 : y^+ at runner for medium grid CFD results.

APPENDIX E

Table E.1 : Numerical hill chart data for Kadincik I HPP.

Discharge	Head	Power	Efficiency	Guide Vane Angle	Guide Vane Opening	Plant Thoma Number	Histogram Thoma Number
[m ³ /s]	[m]	[MW]	[%]	[°]	[mm]	[-]	[-]
15.4	122.6	16.9	90.6	15.0	85.6	0.180	0.082
16.3	132.8	19.8	92.7	15.0	85.6	0.166	0.077
12.0	143.0	15.2	89.6	10.0	58.1	0.154	0.044
17.2	143.0	22.7	93.6	15.0	85.6	0.154	0.078
20.7	143.0	26.3	89.9	20.0	112.2	0.154	0.098
6.0	153.2	7.1	76.8	5.0	29.4	0.144	0.069
12.5	153.2	16.9	89.3	10.0	58.1	0.144	0.030
17.9	153.2	25.5	93.9	15.0	85.6	0.144	0.077
21.5	153.2	29.0	89.1	20.0	112.2	0.144	0.078
24.8	153.2	32.8	87.3	25.0	137.6	0.144	0.149
6.3	163.4	7.9	77.6	5.0	29.4	0.135	0.054
13.2	163.4	19.3	90.7	10.0	58.1	0.135	0.038
18.7	163.4	28.3	93.6	15.0	85.6	0.135	0.073
22.7	163.4	33.5	91.2	20.0	112.2	0.135	0.100
25.8	163.4	36.4	87.3	25.0	137.6	0.135	0.139
6.6	173.6	8.8	77.9	5.0	29.4	0.127	0.041
13.7	173.6	21.2	90.0	10.0	58.1	0.127	0.036
19.4	173.6	31.1	93.2	15.0	85.6	0.127	0.071
23.7	173.6	37.2	91.5	20.0	112.2	0.127	0.105
26.7	173.6	40.0	87.1	25.0	137.6	0.127	0.136
6.8	183.9	9.7	78.0	5.0	29.4	0.120	0.028
14.2	183.9	23.4	90.4	10.0	58.1	0.120	0.039
20.1	183.8	34.1	93.0	15.0	85.6	0.120	0.072
24.6	183.8	41.0	91.6	20.0	112.2	0.120	0.112
27.6	183.9	43.6	86.6	25.0	137.6	0.120	0.133
7.1	194.1	10.8	79.3	5.0	29.4	0.113	0.029
11.0	194.1	18.1	85.1	7.5	43.9	0.113	0.027
14.8	194.1	25.6	90.2	10.0	58.1	0.113	0.046
18.0	194.1	32.1	92.6	12.5	72.0	0.113	0.065
20.8	194.1	37.1	92.8	15.0	85.6	0.113	0.074
23.3	194.1	41.3	92.3	17.5	99.0	0.113	0.094
25.4	194.1	44.3	90.9	20.0	112.2	0.113	0.110
27.1	194.1	46.2	88.7	22.5	125.0	0.113	0.122
28.5	194.1	46.9	85.8	25.0	137.6	0.113	0.128
29.6	194.1	46.9	82.5	27.5	149.9	0.113	0.135

APPENDIX F

Table F.1 : Numerical hill chart data for Kadincik I HPP with tradionally optimized runner.

Discharge	Head	Power	Efficiency	Guide Vane Angle	Guide Vane Opening	Plant Thoma Number	Histogram Thoma Number
[m ³ /s]	[m]	[MW]	[%]	[°]	[mm]	[-]	[-]
5.9	143.0	5.9	71.0	5.0	29.4	0.154	0.114
9.2	143.0	10.8	83.1	7.5	43.9	0.154	0.064
12.4	143.0	15.3	87.7	10.0	58.1	0.154	0.043
15.2	143.0	19.5	90.2	12.5	72.0	0.154	0.038
17.9	143.0	23.3	91.8	15.0	85.6	0.154	0.054
20.4	143.0	26.8	92.8	17.5	99.0	0.154	0.075
22.2	143.0	28.4	90.3	20.0	112.2	0.154	0.084
24.0	143.0	30.2	88.8	22.5	125.0	0.154	0.124
25.5	143.0	31.2	86.3	25.0	137.6	0.154	0.156
27.1	143.0	32.7	85.2	27.5	149.9	0.154	0.200
6.2	153.2	6.9	73.2	5.0	29.4	0.144	0.095
9.7	153.2	12.3	83.9	7.5	43.9	0.144	0.042
13.0	153.2	17.3	88.0	10.0	58.1	0.144	0.037
16.0	153.2	22.1	91.0	12.5	72.0	0.144	0.040
18.9	153.2	26.8	93.5	15.0	85.6	0.144	0.062
21.1	153.2	29.4	92.0	17.5	99.0	0.144	0.057
23.5	153.2	32.8	92.3	20.0	112.2	0.144	0.081
25.0	153.2	33.6	88.6	22.5	125.0	0.144	0.078
27.0	153.2	36.3	88.7	25.0	137.6	0.144	0.127
28.6	153.2	37.7	86.9	27.5	149.9	0.144	0.166
6.5	163.4	7.8	74.6	5.0	29.4	0.135	0.079
10.1	163.4	13.8	84.4	7.5	43.9	0.135	0.030
13.6	163.4	19.6	88.9	10.0	58.1	0.135	0.031
16.8	163.4	24.8	91.6	12.5	72.0	0.135	0.040
19.8	163.4	30.0	93.3	15.0	85.6	0.135	0.064
22.2	163.4	33.4	93.1	17.5	99.0	0.135	0.066
24.2	163.4	35.8	91.2	20.0	112.2	0.135	0.068
26.4	163.4	38.8	90.8	22.5	125.0	0.135	0.093
28.3	163.4	41.0	89.7	25.0	137.6	0.135	0.125
29.8	163.4	42.2	87.4	27.5	149.9	0.135	0.154

Table F.2 : Numerical hill chart data for Kadincik I HPP with traditionally optimized runner (continued).

Discharge	Head	Power	Efficiency	Guide Vane Angle	Guide Vane Opening	Plant Thoma Number	Histogram Thoma Number
[m ³ /s]	[m]	[MW]	[%]	[°]	[mm]	[-]	[-]
6.7	173.6	8.8	76.9	5.0	29.4	0.120	0.056
10.6	173.6	15.4	84.8	7.5	43.9	0.120	0.020
14.1	173.6	21.4	89.2	10.0	58.1	0.120	0.040
17.5	173.6	27.6	92.6	12.5	72.0	0.120	0.050
20.6	173.6	33.5	94.2	15.0	85.6	0.120	0.069
23.1	173.6	36.9	93.2	17.5	99.0	0.120	0.071
25.3	173.6	40.1	92.5	20.0	112.2	0.120	0.084
27.6	173.6	43.4	91.2	22.5	125.0	0.120	0.100
29.3	173.6	45.1	89.3	25.0	137.6	0.120	0.117
31.0	173.6	46.4	86.9	27.5	149.9	0.120	0.132
7.0	183.9	9.8	76.9	5.0	29.4	0.120	0.056
11.0	183.9	17.0	84.8	7.5	43.9	0.120	0.020
14.8	183.9	24.0	89.2	10.0	58.1	0.120	0.040
18.2	183.9	30.7	92.6	12.5	72.0	0.120	0.050
21.4	183.9	36.7	94.2	15.0	85.6	0.120	0.069
24.0	183.9	40.7	93.2	17.5	99.0	0.120	0.071
26.4	183.9	44.4	92.5	20.0	112.2	0.120	0.084
28.6	183.8	47.4	91.2	22.5	125.0	0.120	0.100
30.4	183.8	49.3	89.3	25.0	137.6	0.120	0.117
32.0	183.8	50.6	86.9	27.5	149.9	0.120	0.132
7.3	194.1	10.9	77.5	5.0	29.4	0.113	0.046
11.4	194.1	18.6	84.7	7.5	43.9	0.113	0.017
15.3	194.1	26.3	89.3	10.0	58.1	0.113	0.038
18.9	194.1	33.5	92.4	12.5	72.0	0.113	0.050
22.1	194.1	39.9	93.8	15.0	85.6	0.113	0.067
24.8	194.1	44.3	92.9	17.5	99.0	0.113	0.071
27.3	194.1	48.4	92.2	20.0	112.2	0.113	0.086
29.5	194.1	51.4	90.8	22.5	125.0	0.113	0.099
31.3	194.1	53.2	88.5	25.0	137.6	0.113	0.113
32.9	194.1	54.5	86.1	27.5	149.9	0.113	0.123

APPENDIX G

Table G.1 : Numerical hill chart data for Kadincik I HPP with X-Blade optimization.

Discharge	Head	Power	Efficiency	Guide Vane Angle	Guide Vane Opening	Plant Thoma Number	Histogram Thoma Number
[m ³ /s]	[m]	[MW]	[%]	[°]	[mm]	[-]	[-]
5.8	143.0	6.0	0.7	5.0	29.4	0.154	0.077
9.0	143.0	10.9	0.9	7.5	43.9	0.154	0.035
12.1	143.0	15.3	0.9	10.0	58.1	0.154	0.029
14.8	143.0	19.5	0.9	12.5	72.0	0.154	0.048
17.3	143.0	22.9	0.9	15.0	85.6	0.154	0.061
19.5	143.0	25.7	0.9	17.5	99.0	0.154	0.091
21.2	143.0	27.3	0.9	20.0	112.2	0.154	0.113
22.6	143.0	28.2	0.9	22.5	125.0	0.154	0.127
24.8	143.0	29.0	0.8	27.5	149.9	0.154	0.164
6.4	163.4	8.0	0.8	5.0	29.4	0.135	0.058
10.0	163.4	14.0	0.9	7.5	43.9	0.135	0.021
13.3	163.4	19.5	0.9	10.0	58.1	0.135	0.032
16.3	163.4	24.8	0.9	12.5	72.0	0.135	0.049
19.0	163.4	29.1	0.9	15.0	85.6	0.135	0.066
21.3	163.4	32.4	0.9	17.5	99.0	0.135	0.082
23.2	163.4	34.6	0.9	20.0	112.2	0.135	0.101
24.7	163.4	35.9	0.9	22.5	125.0	0.135	0.120
26.1	163.4	36.7	0.9	25.0	137.6	0.135	0.144
27.1	163.4	36.8	0.8	27.5	149.9	0.135	0.159
6.8	176.7	9.3	0.8	5.0	29.4	0.125	0.048
10.5	176.7	16.1	0.9	7.5	43.9	0.125	0.020
14.1	176.7	22.8	0.9	10.0	58.1	0.125	0.040
17.2	176.7	28.3	0.9	12.5	72.0	0.125	0.049
20.0	176.7	33.2	0.9	15.0	85.6	0.125	0.066
22.4	176.7	36.8	0.9	17.5	99.0	0.125	0.079
24.3	176.7	39.2	0.9	20.0	112.2	0.125	0.093
26.0	176.7	40.8	0.9	22.5	125.0	0.125	0.113
27.4	176.7	41.8	0.9	25.0	137.6	0.125	0.127
28.5	176.7	41.8	0.8	27.5	149.9	0.125	0.148

Table G.2 : Numerical hill chart data for Kadincik I HPP with X-Blade optimization (continued).

Discharge	Head	Power	Efficiency	Guide Vane Angle	Guide Vane Opening	Plant Thoma Number	Histogram Thoma Number
[m³/s]	[m]	[MW]	[%]	[°]	[mm]	[-]	[-]
7.0	183.9	10.0	0.8	5.0	29.4	0.120	0.043
10.9	183.9	17.3	0.9	7.5	43.9	0.120	0.020
14.5	183.9	24.4	0.9	10.0	58.1	0.120	0.038
17.7	183.8	30.4	0.9	12.5	72.0	0.120	0.052
20.5	183.8	35.4	0.9	15.0	85.6	0.120	0.067
22.9	183.8	39.1	0.9	17.5	99.0	0.120	0.076
24.9	183.8	41.7	0.9	20.0	112.2	0.120	0.089
26.6	183.8	43.3	0.9	22.5	125.0	0.120	0.107
28.0	183.8	44.2	0.9	25.0	137.6	0.120	0.125
29.3	183.8	44.6	0.8	27.5	149.9	0.120	0.150
7.2	194.1	11.0	0.8	5.0	29.4	0.113	0.036
11.3	194.1	18.9	0.9	7.5	43.9	0.113	0.023
15.1	194.1	26.7	0.9	10.0	58.1	0.113	0.037
18.4	194.1	33.3	0.9	12.5	72.0	0.113	0.054
21.3	194.1	38.7	0.9	15.0	85.6	0.113	0.067
23.7	194.1	42.4	0.9	17.5	99.0	0.113	0.074
25.7	194.1	45.2	0.9	20.0	112.2	0.113	0.084
27.5	194.1	47.0	0.9	22.5	125.0	0.113	0.100
30.2	194.1	48.6	0.8	27.5	149.9	0.113	0.133

CURRICULUM VITAE



Name Surname: Berk Can DUVA
Place and Date of Birth: Çorlu / Turkey – 01.01.1990
E-Mail: berkanduva@gmail.com

EDUCATION:

B.Sc.: Mechanical Engineering Department -
Middle East Technical University

PROFESSIONAL EXPERIENCE AND REWARDS:

2013 - 2016 TUBITAK Marmara Research Center - Energy Institute as researcher

2015 Most Successful Research Group of TUBITAK Marmara Research Center in 2014

2012 Erasmus Exchange Program Grant

PUBLICATIONS, PRESENTATIONS AND PATENTS:

- Özcan, A.Ö., Benigni, H., **Duva, B.C.**, Schiffer, J., Jaberg, H. & Mosshammer, M. (2015). Evaluation of the Refurbishment Potential for Francis Turbines Using CFD and Optimisation Techniques. *The 16th International Conference on Fluid Flow Technologies, Budapest, Hungary.*
- Benigni, H., Jaberg, H., Schiffer, J., Mosshammer, M., Özcan, A.Ö. & **Duva, B.C.** (2015). Rehabilitation of a Francis turbine using CFD and optimisation techniques – a case study in Turkey. *HYDRO 2015, Bordeaux, France.*